STUDIA

UNIVERSITATIS BABEŞ-BOLYAI

Chemia

CLUJ-NAPOCA 2006

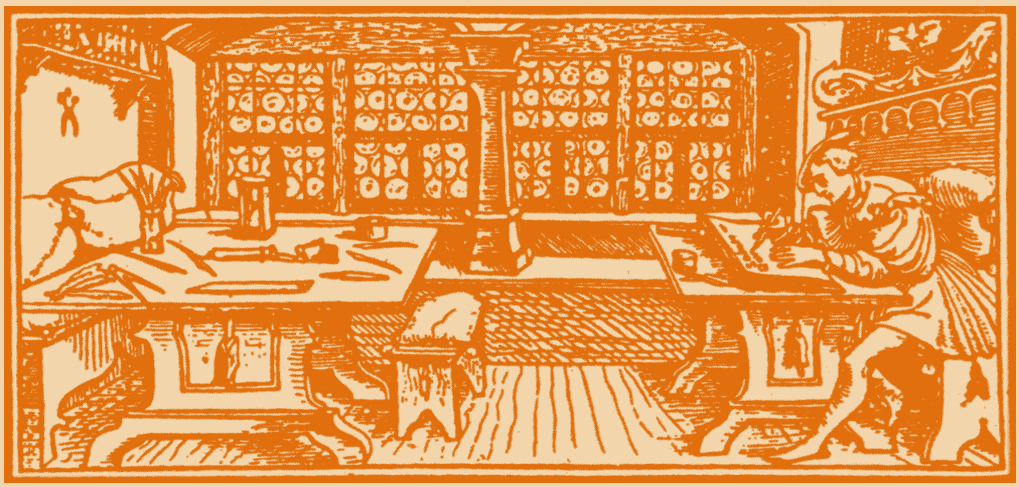

1

ANUL LI **2006**

S T U D I A

UNIVERSITATIS BABEŞ–BOLYAI

CHEMIA

1

Editorial Office: 400015 – Cluj–Napoca Republicii no. 24, Phone: 0264-405352

SUMAR - SOMMAIRE - CONTENTS - INHALT

BIOGRAPHY SORIN MAGER I

NICULINA BOGDAN, FLAVIA POP, ANDREI SERBAN GÂZ, ELENA BOGDAN, ANAMARIA TEREC, LUMINIȚA DAVID and ION GROSU, Synthesis And Structural Analysis of Some New Precursors of Macrocyclic Cyclophanes: 1,4-Bis(2-R-5,5-Dimethyl-1,3-Dioxan-2-Yl)Benzene 3

NICULINA BOGDAN, ANDREI SERBAN GÂZ, FLAVIA POP, ELENA BOGDAN, ANAMARIA TEREC, LUMINIȚA DAVID and ION GROSU, Synthesis And Structural Analysis of Some New Precursors of Macrocyclic Cyclophanes: 1,4-Bis(2-R-5-R^1-1,3-Dioxan-2-Yl)Benzene Derivatives 13

CLAUDIA MOLDOVAN, CASTELIA CRISTEA, IOAN A. SILBERG, ABDALLAH MAHAMOUD, SILVIA UDREA and JACQUES BARBE, Reactions of the 3-Cyano-10-Methyl-Pyrido[3,2-G]Quinolin-4-One. Ii 21

MIRCEA V. CRISTEA, MARIA CURTUI, CASTELIA CRISTEA, LUIZA GAINA, Modelling Uranium(Vi) Extraction Using Artificial Neural Networks 27

IOAN OPREAN, ANA AURELIA BOTAR, LUCIA GÂNSCĂ, IULIANA VASIAN, Synthesis of Cis - 7,8 - Epoxy- Octadecane, Species - Specific Component of the Sex Pheromone of Nun Moth Lymantria Monacha (Lepidoptera , Limantriidae) 33

ANIELA E. VIZITIU, MIRCEA V. DIUDEA, Conetori of High Genera 39

A. E. VIZITIU and M. V. DIUDEA, Retro Map Operations 49

CRISTIAN NEANU, FRANCISC PETER, IOANA ŞIŞU C, CSUNDERLIK and EUGEN ŞIŞU, Pseudoceramides and Their Derivatives. 3. Benzylidene Acetals of N-Acetyl-N-Methyl Glucamine – Preliminary Study 59

FLORINA POGACEAN, IOAN BALDEA and FLORIN TURBAT, The Inhibitory Effect of the Atenolol Upon the Enzyme Catalyzed Hydrogen Peroxide Decomposition 67

PETRONELA MARIA PETRAR, GABRIELA NEMES, IOAN SILAGHI-DUMITRESCU and LUMINITA SILAGHI-DUMITRESCU, New Halo Compounds of Silicon and Tin, Potential Precursors Of >E=C=P- Heteroallenic Systems. 77

M. JOENSSON, A. SILVESTRU and C. SILVESTRU, Bismuth(Iii) Complexes With Diorganodichalgogeno-Phosphinato Ligands. Synthesis and Spectroscopic Characterization 83

LADISLAU KÉKEDY-NAGY and EUGEN DARVASI, Flame Atomic Emission Spectrometry Determination of Cesium in Mineral and Well Waters Using a Methane-Air Flame 91

MONICA CULEA, SORIN HODISAN, ANAMARIA HOSU, CLAUDIA CIMPOIU, Analysis of Free Amino Acids From Plant Extracts by Chromatographic Methods 105

ADINA GHIRISAN, SIMION DRĂGAN, ALEXANDRU POP and VASILE MICLĂUŞ, Studies on the Natrium Sulphate Salting-Out Crystallization Ii. Crystallization Kinetics 115

IOANA IGNAT, SIMONA VARVARA and LIANA M. MURESAN, Study on the Inhibiting Behavior of a Non-Toxic Thiadiazole Derivative On Bronze Corrosion in Aqueous Electrolytes 127

OSSI HOROVITZ, ANCA-LIANA POPOVICIU, ELENA-MARIA PICA, Estimations of Surface Free Energies for Solid Metals 137

MARIA TOMOIA-COTISEL, Adsorption Kinetics of Stearic Acis at the Benzene/Watter Interface 159

ERRATUM G. C. BUCSA, I. BALDEA, Kinetics and Mechanism of P-Xylene Oxidation by Ce(Iv) in Aqueous Acid Medium. Lfer as an Argument to the Oxidation Mechanism 187

STUDIA UNIVERSITATIS BABEŞ-BOLYAI, CHEMIA, LI, 1, 2006

PROFESSOR SORIN MAGER

BIOGRAPHY

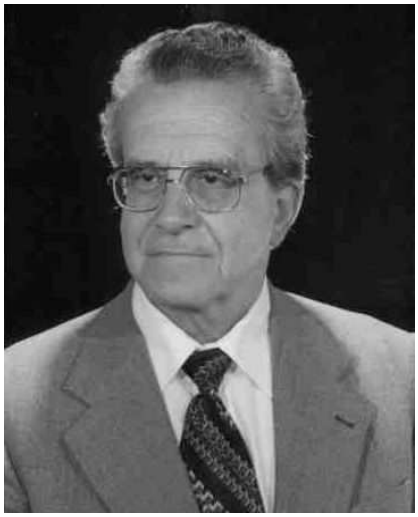

A brilliant scientist, the leader of the Organic Chemistry School of Cluj in the last decades, was the dean of the Faculty of Chemistry and Chemical Engineering for 8 years (1992-2000) in a difficult period of structural changes. At his 75 anniversary he is the same active, creative, exigent and productive professor as he is known by the academic community for nearly 50 years.

Borned on May 7th 1931 in Arad, a town charged with history in the western part of Transylvania, in a family with a strong attachment for the culture and national traditions. He distinguished himself already during his years as student in the lyceum and faculty, as an outstanding personality dedicated for study, with scientific curiosity and interest in organic chemistry.

He obtained the PhD degree in Organic Chemistry in 1964, at "Babeş" University, under the supervision of Professor Maria Ionescu with the thesis: "*o*-Nitrobenzylydene acetals of myoinositol".

He held different positions: 1953-1958 teaching assistant ("V. Babeş" University, Cluj-Napoca); 1958-1961 chemist in "Terapia" drug plant; 1961-1963 teaching assistant (Pedagogical Institute of Cluj-Napoca); 1963-1968 lecturer (Pedagogical Institute of Cluj-Napoca); 1968-1970 lecturer, 1970-1990 associated professor and from 1990-2001 professor and from 2001 consulting professor at "Babeş-Bolyai" University.

His creative scientific work was strongly influenced by the one year post-doctoral research stage spent at Notre Dame University at Notre Dame, Indiana, USA in 1971-1972 in the group of professor Ernest Eliel, the most important researcher in the field of stereochemistry and of saturated six membered ring heterocycles. After his return in Roumania he edited books and papers which are the first ones (in Roumania) in Stereochemistry and in Organic Structural Analysis and he is considered effectively as being the parent of these disciplines in our university.

Concerning his teaching activity, many series of graduates of our faculty strongly appreciated his clear, logic, systematic and enthusiastic

lectures. The colleagues and the academic community also appreciated his devotion towards Alma Mater Napocensis, his spirit of justice, his morality and collegiality. Professor Sorin Mager gave many lectures in important universities and International and National Conferences, he was visiting professor at University of North Carolina, Chapel Hill, North Carolina and Michigan State University, East Lansing, Michigan, USA (1994).

He published 6 books (one in a French Publishing House) and he was collaborator to the "Encyclopedia of Chemistry" volumes 2, 3, 6 - 123 papers (54 in foreign journals). in stereochemistry, organic structural analysis and fine organic synthesis.

Professor Mager was Member of American Chemical Society (ACS) and he is member of Romanian Chemical Society. He was advisor for 12 PhD Thesis and member in 64 PhD. Juries. His research works are cited in many important publications and he was awarded with C. D. Nenitzescu Prize of the Romanian Academy (1992).

STUDIA UNIVERSITATIS BABEŞ-BOLYAI, CHEMIA, LI, 1, 2006

SYNTHESIS AND STRUCTURAL ANALYSIS OF SOME NEW PRECURSORS OF MACROCYCLIC CYCLOPHANES: 1,4-BIS (2-R-5,5-DIMETHYL-1,3-DIOXAN-2-YL) BENZENE

NICULINA BOGDAN, FLAVIA POP, ANDREI SERBAN GÂZ, ELENA BOGDAN, ANAMARIA TEREC, LUMINIȚA DAVID AND ION GROSU*

Dedicated to Professor Sorin Mager
on the occasion of his 75th birthday

ABSTRACT. The synthesis and the stereochemistry of some new 1,3-dioxane derivatives of 1,4-diacetylbenzene are reported. The structural analysis carried out using NMR investigations revealed the anancomeric structure of the compounds. The favorable arrangement of the different functions for the participation to the macrocyclisation is insured by the axial orthogonal dispositions of the aromatic group with respect to both 1,3-dioxane rings.

Introduction

The investigations on the stereochemistry of 1,3-dioxane derivatives with aryl groups at position 2 of the heterocycle showed important structural aspects. The A value (free conformational enthalpy) of aryl groups at position 2 of the 1,3-dioxane ring are high (*e.g.* A_{Ph} = 13.04 kJ/mol [1,2]). The 2-aryl-1,3-dioxanes are anancomeric compounds and the conformational equilibrium between I and II is shifted toward I which exhibits the aryl group in the *equatorial* orientation (Scheme 1 [3-5]).

The conformational equilibrium of 2-alkyl,2-aryl-1,3-dioxanes (III, IV; *e.g.* 2-phenyl-2-methyl-1,3-dioxanes, Scheme 1) is shifted toward the conformer exhibiting the aryl group in the *axial* position [1,6-8].

* "Babeş-Bolyai" University, Organic Chemistry Department and CCOCCAN, 11 Arany Janos str., 400028, Cluj-Napoca, Romania

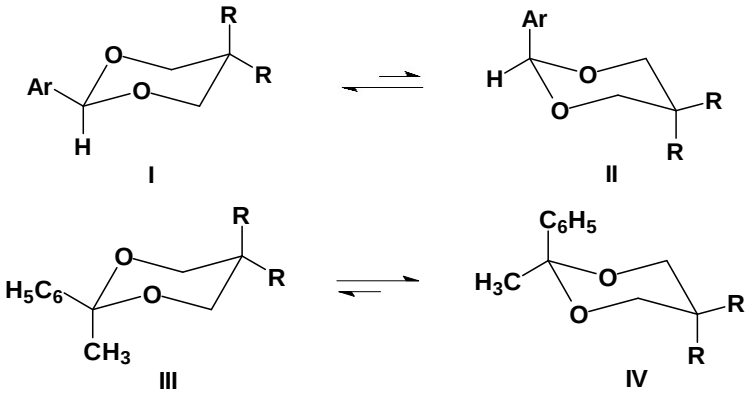

Scheme 1

The higher A value of the methyl group at position 2 (A_{Me} = 16.63 kJ/mol [1]) than the A value of the phenyl group (A_{Ph} =13.04 kJ/mol [1]) at the same position suggests the *axial* preference of the phenyl group. Thermodynamic measurements of 2-methyl-2-phenyl-1,3-dioxanes showed a considerably higher preference of the methyl group for the *equatorial* position ($\Delta G_{III\text{-}IV}^{0}$ = 10.11 kJ/mol [1]) than that calculated from the A- values of methyl and phenyl groups ($\Delta A = A_{Me} - A_{Ph}$ = 3.63 kJ/mol).

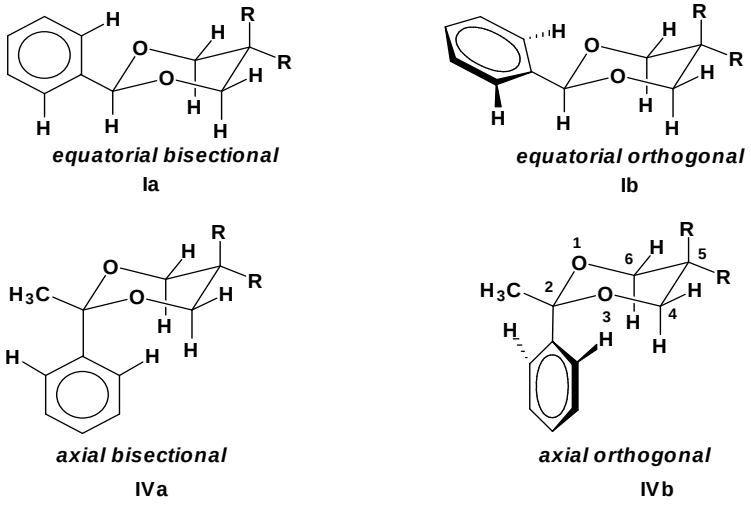

Scheme 2

The equatorial aryl groups exhibit a weak preference for the *bisectional* rotamer (I_a) [9-11] and the axial phenyl group shows the *orthogonal* orientation (IV_b, Scheme 2 [7,8,12-15]). This is consistent with the ^{1}H NMR shifts [7,8].

Investigations on the stereochemistry of compounds bearing two 1,3-dioxane rings on the same aromatic system, obtained from benzenedicarboxaldehydes, have revealed the *equatorial* orientation of the aromatic ring for both heterocycles [3-5], while the investigations of similar derivatives of 1,4-diacetylbenzene [16] and of 2,6-diacetylbenzene [17] showed the axial orientation of the aromatic group with respect to both heterocycles. Some of these 1,3-dioxane derivatives were already successfully used in the synthesis of macrocyclic cyclophanes [18, 19]

It was considered of interest to investigate the stereochemistry of new 1,3-dioxane derivatives of 1,4-diacetylbenzene bearing different substituents at the positions 2 and 5 of the 1,3-dioxane rings and to determine the conformational behaviour of the heterocycles, the orientation of the aromatic substituent in both heterocycles, and to identify the possibility to use these compounds for the synthesis of cyclophanes.

Results and Discussions

In order to obtain new bis(2-R-1,3-dioxan-2-yl) derivatives bearing the 1,4-phenylene unit the 1,3-dioxane derivative **1** [16] was brominated in good yields (Table 1) using the typical procedure for the bromination reaction of cyclic ketals (Scheme 3)[20,21].

The bromination reaction generated as side product the tribrominated derivative **3** (Scheme 4, Table 1), too.

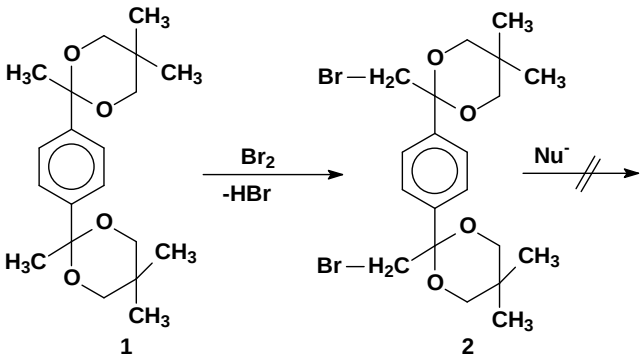

Scheme 3

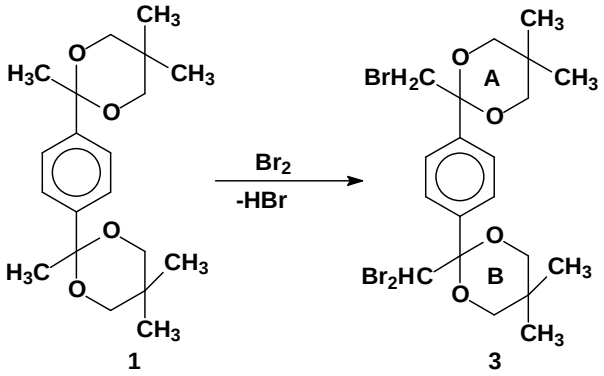

Scheme 4

Dibrominated derivative **2** was reacted with several nucleophyles (*e.g*. HO^-, $C_6H_5COO^-$) in order to have access to other derivatives with appropriate substitution for the macrocyclisation reaction. All the attempts failed and the conclusion was that the steric hindrance of the carbon atoms bearing the bromine substituents is very high and nucleophyle substitutions cannot take place in these positions.

Due to this result we changed our strategy and we decided to obtain first the desired derivatives of 1,4-diacetylbenzene and then to use these derivatives for the synthesis of the 1,3-dioxane rings.

In the first step we brominated in good yields 1,4-diacetylbenzene with bromine in acetic acid [22] and after that we carried out the substitution of bromine atoms of the dibrominated derivative **4** with $C_6H_5COO^-$ (Scheme 5, Table 1), and we obtained the diester **5**.

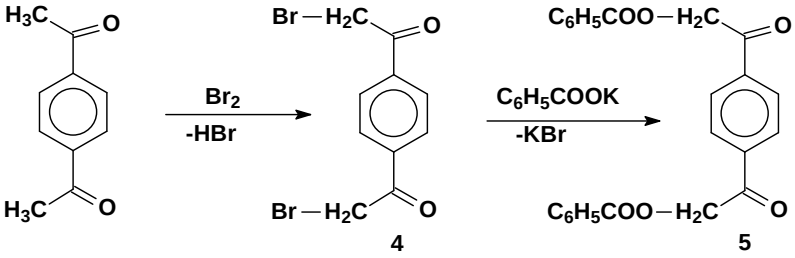

Scheme 5.

The dibenzoate derivative **5** was subjected to the condensation reaction with neopentylglycol or with dimethyl-bis(hydroxymethyl)malonate (Scheme 6, Table 1) in order to obtain the 1,3-dioxane diester **6** and hexaester **7**. The diester **6** was deprotected with LiOH at 0℃, to give diol **8**.

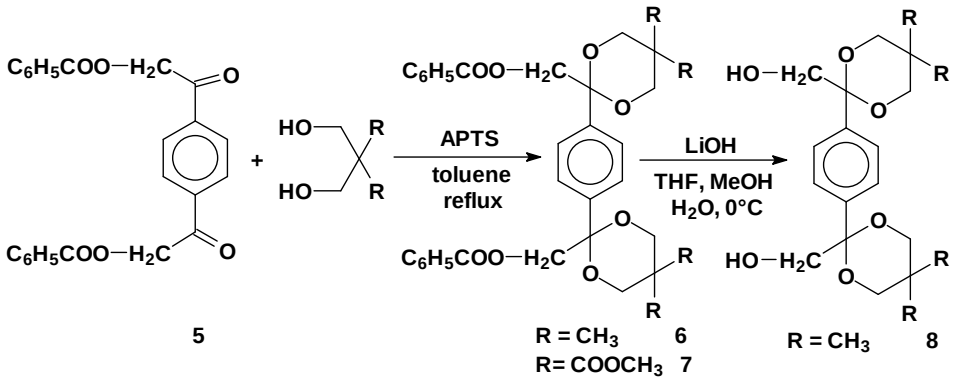

Scheme 6

Diol **8** was used to obtain the protected α,α'-dihidroxi-1,4-diacetylbenzene **10**, *via* the di-1,3-dioxane derivative **9** (Scheme 7, Table 1).

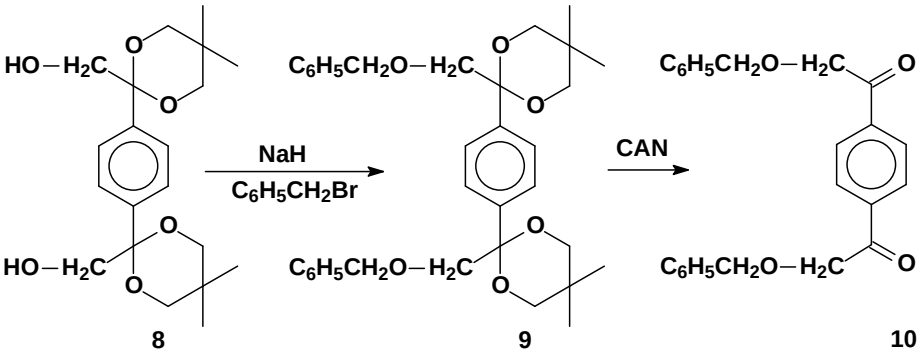

Scheme 7

Table 1.
Results of the synthesis of compounds **2**, **3** and **5-10**

Compound	**2**	**3**	**5**	**6**	**7**	**8**	**9**	**10**
Yields %	75	15	92	52	74	91	78	86

Compounds **2**, **3**, **7**, **9**, **10** are new ones, while compounds **5**, **6**, **8** were already reported [19].

The structural analysis was carried out using NMR investigations. The spectra of **2**, **3**, **6-9** exhibit different signals for the axial and equatorial protons of the 1,3-dioxane rings and for the similar groups located on it (Table 2).

Table 2.
NMR data for compounds **2**, **3** and **6**-**9**

Compound	4'(4")-H; 6'(6")-H		5'(5")-CH_3		5'(5")-$COOCH_3$	
	ax.	eq.	ax.	eq.	ax.	eq.
2	3.45	3.52	1.36	0.63	-	-
3	3.40	3.55	1.36	0.63	-	-
6	3.47	3.47	1.30	0.60	-	-
7	3.98	4.62	-	-	3.71	3.64
8	3.47	3.52	1.29	0.63	-	-
9	3.48	3.54	1.31	0.61	-	-

The NMR data suggest the anancomeric structure of these derivatives and the axial orthogonal orientation of the aromatic ring.

Conclusions

New 1,3-dioxane derivatives were obtained in good yields by condensation reactions or using the α, α' bromination reaction of cyclic ketals. The NMR based structural analysis of these derivatives revealed the rigid structure for all compounds and the axial orientation of the aromatic ring with respect to both saturated heterocycles. The reported derivatives are important precursors for the synthesis of cyclophane derivatives.

Experimental

^{1}H-NMR (300 MHz) and ^{13}C-NMR (75 MHz), COSY, HMQC, and HMBC spectra, were recorded at *rt* in $CDCl_3$ on a Bruker 300 MHz spectrometer, using the solvent line as reference. Mass spectra were recorded on an ATI Unicam Automass.

Melting points were measured with a Kleinfeld melting point apparatus and are uncorrected. Thin-layer chromatography (TLC) was conducted on silica gel 60 F_{254} TLC plates purchased from Merck. Preparative column (flash) chromatography was performed using PharmPrep 60 CC (40-63 μm) silica gel purchased from Merck. Chemicals were purchased from Aldrich or Acros and were used without further purification.

General Procedure for the Synthesis of Compounds 2 and 3

The 1,3-dioxane derivative (2.1 mmol) and dry dichloromethane (40 ml) were introduced into a three-necked flask equipped with a reflux condenser, a thermometer and a dropping funnel. Bromide (9.25 mmol) in 10 ml dry dichloromethane was added drop wise, under magnetically stirring, to this mixture cooled into an ice bath at 0-5ºC, the ensuing reaction being monitored initially by the fading of the solution color. After the addition of the bromide, the ice bath was removed and the stirring was continued for 1h,

the contents in the flask being allowed slowly to reach room temperature (20-25ºC). The mixture was evaporated *in vacuum* and the residue was crystallized from ethanol.

1,4-Bis(2'-bromomethyl-5',5'-dimethyl-1',3'-dioxan-2'-yl)benzene (2)
White solid, m.p.=164-5℃, yield 75% (flash chromatography, elution: DCM/pentane/diethyl acetate 1/3/0.1 v/v, Rf = 0.60). **^{1}H-NMR** (300 MHz,$CDCl_3$, δ ppm): 0.63 (6H, s), 1.36 (6H, s), 3.45 (4H, d, *J*=10.6 Hz), 3.46 (4H, s), 3.52 (4H, d, *J*=10.6 Hz), 7.51 (4H, s). **^{13}C-NMR** (75 MHz, $CDCl_3$, δ ppm): 21.9 (CH_3) 23.0 (CH_3), 30.2 (C_{quat}), 40.8 (CH_2), 72.2 (CH_2), 98.9 (C_{quat}), 128.44 (CH), 137.8 (C_{quat}). **MS** (EI, 70 eV); m/z (rel. int., %): 493 (2) $[M+H]^+$, 477 (10), 399 (100).

1-(2'-dibromomethylene-5',5'-dimethyl-1',3'-dioxan-2'-yl)-4-(2''-bromomethyl-5'',5''-dimethyl-1'',3''-dioxane-2''-yl)benzene (3)
White solid, m.p.=134-5℃, yield 15% (flash chromatography, elution: DCM/pentane : 3/1 v/v, Rf = 0.52). **^{1}H-NMR** (300 MHz,$CDCl_3$, δ ppm): 0.63 (6H, s), 1.36 (6H, s), 3.40 (4H, d, *J*=10.9 Hz), 3.46 (2H, s), 3.55 (4H, d, *J*=10.9 Hz), 6.88 (1 H, s) 7.63 (2H, d, *J*=8.3 Hz) 8.16 (2H, d, *J*=8.3 Hz) **^{13}C-NMR** (75 MHz, $CDCl_3$, δ ppm): 21.8 (CH_3) 22.9 (CH_3), 30.2 (C_{quat}), 49.6 (CH), 40.1 (CH_2), 72.3 (CH_2), 98.6 (C_{quat}), 128.6 (CH), 130.4 (CH), 131.4 (C_{quat}) 143.9(C_{quat}). **MS** (EI, 70 eV); m/z (rel. int., %): 475,477 (2.5), 391,393 (49), 314 (12), 305 (14), 209 (11), 104

General Procedure for the Synthesis of Compound 7

2,2-dicarboxymethyl-1,3-propanediol (11 mmol) and ketone **5** (5 mmol) with catalytic amounts of *p*-toluenesulphonic acid (0.1 g) were solved in 200 mL toluene. The mixture was refluxed and the water produced in the reaction removed using a Dean-Stark trap. When 80 % of the water had been separated, the mixture was cooled to room temperature and the catalyst was neutralized (under stirring 0.5 h) with CH_3-COONa powder in excess (0.2 g). The reaction mixture was washed twice with 100 mL of water. After drying over $MgSO_4$, the benzene was removed and **7** was purified by flash chromatography.

1,4-Bis[2'-benzoyloxymethyl-5',5'-bis(carboxymethyl)-1,3-dioxan-2'-yl]benzene (7)
White solid, m.p.= 245-6℃, yield 74% (flash chromatography, elution: DCM, Rf = 0.43. **^{1}H-NMR** (300 MHz,$CDCl_3$, δ ppm): : 3.64 (6H, s), 3.71 (6H, s), 3.98 (4H, d, *J*=11.3 Hz) 4.31 (4H, s) 4.62 (4H, d, *J*=11.6 Hz) 7.42 (4H, dd, overllaped *J*=7.2 Hz, *J*=7.5 Hz) 7.54 (2H, t, *J*=7.5 Hz) 7.60 (4H, s,) 8.0 (4H, d, *J* = 7.2 Hz). **^{13}C-NMR** (75 MHz, $CDCl_3$, δ ppm): 53.16 (CH_3) 53.19 (CH_3), 53.23 (C_{quat}), 63.8 (CH_2), 69.2 (CH_2), 100.4 (C_{quat}) 128.4 (CH), 128.6 (CH), 129.9 (C_{quat}), 130.0 (CH), 133.2 (CH) 136.5 (C_{quat}), 165.9 (CO), 166.9 (CO), 168.1 (CO). **MS** (EI, 70 eV); m/z (rel. int., %): 616(100) [M-134], 442 (40).

General Procedure for the Synthesis of Compound 9

To a suspension of NaH (8.4 mmol) in dry THF (50 mL), diol **8** (2.1 mmol) in 10 ml THF was added under argon. The mixture was heated to reflux and benzyl bromide (2.1 mmol) solved in 5 mL THF was added slowly to the

NaH solution. Reflux of the solvent was continued for 5h, after which the system was brought to room temperature and the solid phase removed by filtration. The solvent was evaporated and the crude product was solved in CH_2Cl_2 (20 mL) and then washed twice with water (20 mL). After drying over magnesium sulfate, the solvent was removed and the crude product was purified by crystallization from ethanol.

1,4-Bis(2'-benzyloxymethyl-5',5'-dimethyl-1,3-dioxan-2'-yl)benzene (9)
White solid, yield 76% **^{1}H-NMR** (300 MHz,$CDCl_3$, δ ppm): 0.61 (6H, s), 1.31 (6H, s), 3.48 (4H, d, *J*=10.6 Hz) 3.54 (4H, d, *J*=10.6 Hz), 3.56 (4H, s), 4.54 (4H, s) 7.11-7.23 (10H, m, overlapped signals), 7.50 (4H, s). **^{13}C-NMR** (75 MHz, $CDCl_3$, δ ppm): 22.05 (CH_3), 30.4 ($\underline{C}H_3$), 31.1 (C_{quat}), 71.6 (CH_2), 73.8 (CH_2), 77.25 (CH_2) 100.9 (C_{quat}), 127.38-127.42 (**CH**) 128.2 (CH), 132.3 (C_{quat} 1-C, 4-C), 137.5 (C_{quat}).

General Procedure for the Synthesis of Compound 10

To a stirred solution of **9** (6 mmol) in MeCN (3mL) and water (3mL) was added solid cerium ammonium nitrate (CAN, 18 mg, 4 mol %). The solution was heated at reflux for 2 h. After cooling at room temperature, water (10 mL) was added and the mixture was extracted with dichloromethane (3x20 mL). The organic layers were dried over $MgSO_4$, filtered and the solvent was evaporated *in vacuum*. The crude product was further purified by crystallization from acetone.

1,4-Bis(2'-benzyloxymethyl) benzene (10)
White solid, yield 86%. **^{1}H-NMR** (300 MHz,$CDCl_3$, δ ppm): 4.68 (4H, s), 4.74 (4H, s) 7.31 -7.37 (10H, overlapped signals) 7.98 (4H, s).

Acknowledgements: The financiar supports of PNCDI (CERES 4-37) and CNCSIS (A 1736) are strongly acknowledged.

REFERENCES

1. Anteunis M.J.O., Tavernier D., Borremans F., *Heterocycles* **1976**, *4*, 293
2. Kleinpeter E., *Advances in Heterocyclic Chemistry*, **1998**, *69*, 217
3. Grosu I., Mager S., Plé G., Plé N., Toscano A., Mesaroş E., Martinez E., *Liebigs Annalen/Recueil*, **1997**, *3*, 345
4. Grosu I., Mager S., Mesaroş E., Plé G., *Heterocyclic Commun*., **1998**, *4*, 53
5. Grosu I., Mager S., Toupet L., Plé G., Mesaroş E., Mihiş A., *Acta Chem. Scand*., **1998**, *52*, 366
6. Grosu I., Mager S., Plé G., Mesaroş E., Gegö C., Dulău A., *Rev. Roum. Chim*., **1999**, *44*, 467
7. Mager S., Grosu I., *Stud. Univ. "Babeş-Bolyai", Chemia*, **1988**,*33*, 47
8. Grosu I., Plé G., Mager S., Mesaroş E., Dulău A., Gegö C., *Tetrahedron*, **1998**, *54*, 2905
9. De Kok A.J., Romers C., *Recl. Trav. Chim. Pays-Bas*, **1970**, *89*, 313

10. Collins P.M., Travis A.S., Tsiquaye K.N., Lindley P.F., Perrat D., *J. Chem. Soc. Perkin Trans. 1*, **1974**,1895
11. Nader F.W., *Tetrahedron Lett*., **1975**, *14*,1207
12. Keller M., Langer E., Lehner H., *Monatsh. Chem*.,**1976**, *107*, 949
13. Kellie G.M., Murray-Rust P., Riddell F.G., *J. Chem. Soc. Perkin Trans. 2*, **1972**, 2384
14. Nader F.W., *Tetrahedron Lett.*, **1975**, *14***,**1591
15. Drewes S.E., Drewes M.W., McNaught I.J., *S. Afr. Tydskr. Chem*., **1985**, *38*,101
16. Grosu I., Muntean L.,Toupet L., Plé G., Pop M., Balog M., Mager S., Bogdan E., *Monatsh. Chem.* **2002**, *133*, 631
17. Balog M., Tötös S., Florian C.M., Grosu I., Plé G., Toupet L., Ramondenc Y., Dincă N., *Heterocyclic Commun.* **2004***, 10,* 139
18. Balog M., Grosu I., Plé G., Ramondenc Y., Condamine E., Varga R. A., *J. Org. Chem*., **2004**, *69*, 1337
19. Bogdan N., *manuscript in preparation*
20. Grosu I., Camacho B. C., Toscano A., Plé G., Mager S., Martínez R., Gavino R. R., *J. Chem. Soc. Perkin Trans. 1*, **1997**, 775
21. Bogdan E., Grosu I., Mesaroş E., Toupet L., Plé G., Mager S., Muntean L., *J. Chem. Soc. Perkin Trans. 1*, **2000**, 3635
22. Grosu I, Toupet L., Plé G., Mager S., Mesaroş E., Varga A., Bogdan E., *Monatsh. Chem*., **2000**, *131*, 277

STUDIA UNIVERSITATIS BABEŞ-BOLYAI, CHEMIA, LI, 1, 2006

SYNTHESIS AND STRUCTURAL ANALYSIS OF SOME NEW PRECURSORS OF MACROCYCLIC CYCLOPHANES: 1,4-BIS (2-R-5-R^1-1,3-DIOXAN-2-YL) BENZENE DERIVATIVES

NICULINA BOGDAN, ANDREI SERBAN GÂZ, FLAVIA POP, ELENA BOGDAN, ANAMARIA TEREC, LUMINIȚA DAVID AND ION GROSU*

Dedicated to Professor Sorin Mager
on the occasion of his 75th birthday

ABSTRACT. The synthesis and the stereochemistry of some new 2,5-substituted-1,3-dioxane derivatives of 1,4-diacetylbenzene are reported. The structural analysis carried out using NMR investigations revealed the anancomeric structure of the compounds and the *cis* or/and *trans* disposition of the substituents. These experiments showed the favorable arrangement of the different functions for the participation to the macrocyclisation reactions insured by the axial orthogonal disposition of the aromatic group with respect to both 1,3-dioxane rings.

Introduction

The studies on the conformational equilibriums of 2,2-disubstituted-1,3-dioxanes bearing alkyl and aryl groups in the ketal part of the heterocycle (I, II; *e.g.* 2-phenyl-2-methyl-1,3-dioxanes, Scheme 1) showed the shifting of these equilibriums toward the conformer exhibiting the aryl group in the *axial* position [1-3].

The *axial* preference of the phenyl group is suggested by the higher A value of the methyl group at position 2 (A_{Me} = 16.63 kJ/mol [1]) than the A value of the phenyl group (A_{Ph} = 13.04 kJ/mol [1]) at the same position. Thermodynamic measurements in 2-methyl-2-phenyl-1,3-dioxanes showed a considerably higher preference of the methyl group for the *equatorial* position (ΔG_{II-I}^0 = 10.11 kJ/mol [1]) than that calculated from the A-values of methyl and phenyl groups ($\Delta A = A_{Me} - A_{Ph}$ = 3.63 kJ/mol).

* "Babes-Bolyai" University, Organic Chemistry Department and CCOCCAN, 11 Arany Janos str., 400028, Cluj-Napoca, Romania

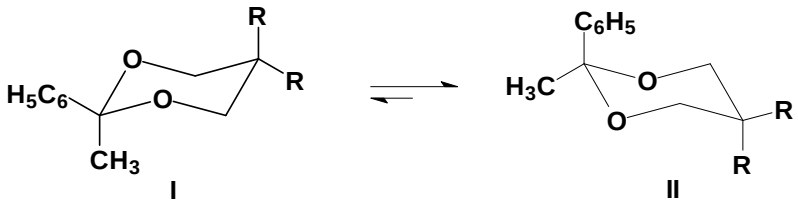

Scheme 1

Investigations on the stereochemistry of compounds bearing two 1,3-dioxane rings on the same aromatic system, obtained from benzenedicarboxaldehydes, have revealed the *equatorial* orientation of the aromatic ring for both heterocycles [4-6], while the investigations on the stereochemistry of derivatives of 1,4-diacetylbenzene [7] and of 2,6-diacetylpyridine [8] showed the axial orthogonal orientation of the aromatic ring with respect to both 1,3-dioxacyclohexane systems. The derivatives of these compounds bearing different substituents in positions 5' and 5" of the 1,3-dioxane rings show three diastereoisomers (*cis,cis*, *cis,trans,* and *trans,trans*) in agreement with the disposition of the groups with higher precedence at positions 5' (5") on the same side (*cis*) or on different sides (*trans*) with the aromatic group at position 2' or 2" (*e.g.* the derivatives of terephthaldialdehyde of scheme 2). Some *cis-cis* 1,3-dioxane derivatives of 1,4-diacetylbenzene and of 2,6-diacetylpyridine were already investigated and they were successfully used in the synthesis of macrocyclic cyclophanes [9, 10].

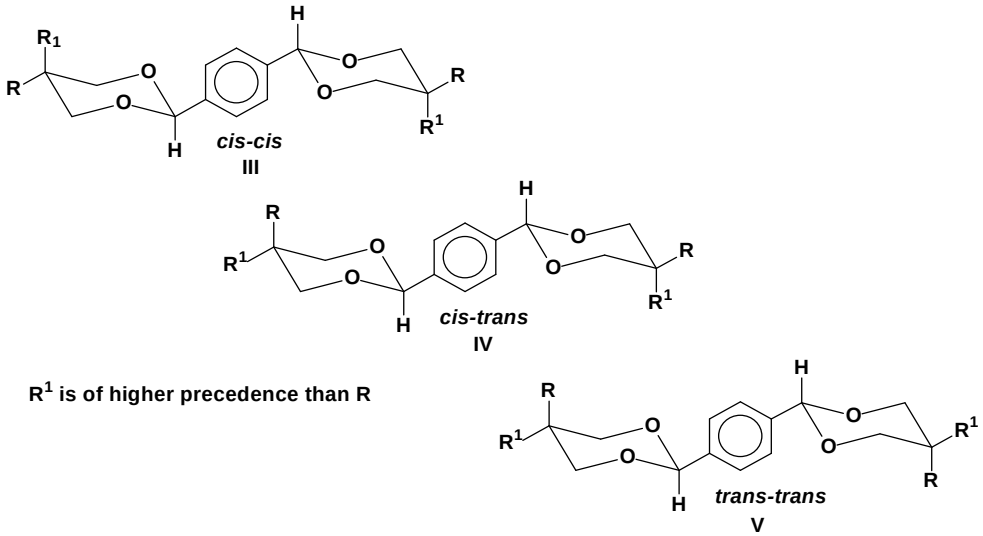

Scheme 2

It was considered of interest to investigate the stereochemistry of new 1,3-dioxane derivatives of 1,4-diacetylbenzene (or of some α, α' derivatives) bearing different substituents at the positions 2 and 5 of the 1,3-dioxane rings and to determine the conformational behaviour of the heterocycles, the orientation of the aromatic substituent for both heterocycles, and to identify and to characterize the possible *cis* and *trans* isomers.

Results and Discussions

New 1,3-dioxane derivatives of 1,4-diacetylbenzene having nonsymmetric substitution at the positions 5' and 5" of the heterocycles were obtained in good yields by the condensation reaction of 1,4-dicetylbenzene with several 1,3-propanediol derivatives (Scheme 3, Table 1).

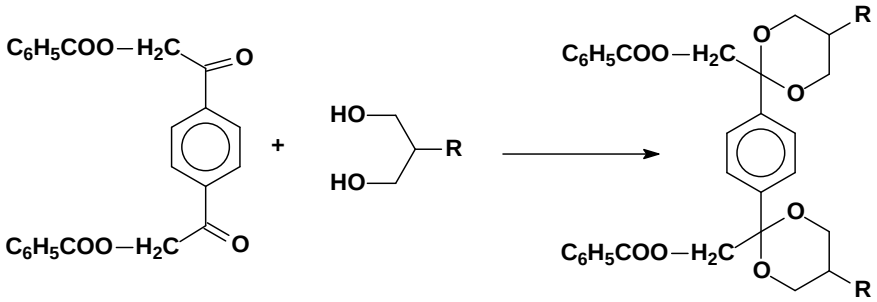

R= $COOCH_3$	**1**	**5**
R=$COOC_2H_5$	**2**	**6**
R = CH_2OH	**3**	**7**
R = CH_2OTs	**4**	**8**

Scheme 3

The yields for the reactions with esters were higher and for all cases the raw products were mixtures of isomers: *cis-cis, cis-trans* and *trans-trans*. The ratios and the yields are presented in table 1. At position 2 we considered as reference the ester group, which is of highest precedence.

Table 1.
Results of the synthesis of compounds **5-8**

Compound	**5**	**6**	**7**	**8**
Yields	45	49	53	36
Cis-cis/cis-trans/trans-trans	0 / 2 / 1	0 / 2 / 1	10 / 12 / 1	1 / 1.4 / 0

The *trans-trans* isomers of **5** and **6** and *cis-cis* isomer of **7** and **8** were separated by flash chromatography and were investigated as single compounds.

The *trans-trans* isomer of the tetrol **9** was synthesized (yields = 94 %) using the LAH reduction (Scheme 4) of the separated *trans-trans* isomer of **5**.

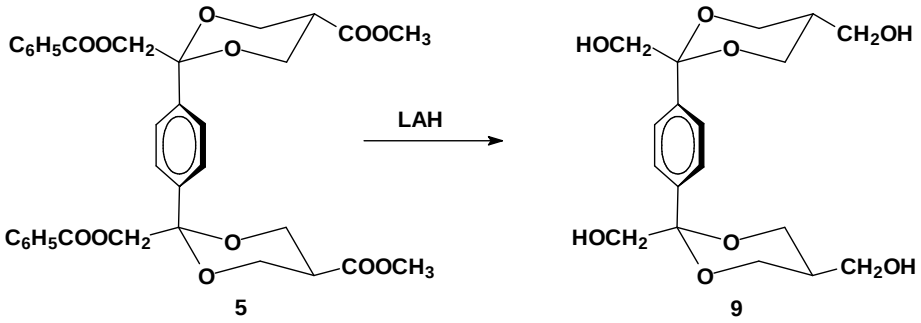

5 9

Scheme 4

The NMR investigation showed the anancomeric structure of the compounds. In all investigated compounds the aromatic substituent occupies the axial orientation for both 1,3-dioxane rings, while the substituents at positions 5' and 5" are either equatorial or axial and generate the *cis* and *trans* configurations. The anancomeric structure of the compounds is proved by the recording in the NMR spectra of different signals for the axial and equatorial protons of the dioxacyclohexane rings (Table 2). The axial or equatorial orientation of the substituents at positions 5' and 5" was deduced from the values of the coupling constants. If the substituent at position 5 of the 1,3-dioxane ring is equatorial, the axial proton at the same position exhibits a large coupling constant with the axial protons of positions 4 and 6. The signal belonging to the axial protons at positions 4 and 6 is in this case a doublet of doublets with two large coupling constants (many times overlapped into a triplet; the second coupling with large constant is due to the geminal equatorial proton). If the substituent at position 5 of the 1,3-dioxane ring is axial, the proton of the position exhibits couplings with small constants with the protons of positions 4 and 6, including the axial ones. The pattern for the signal belonging to the axial protons of positions 4 and 6 shows a doublet of doublets with a large coupling constant (due to the equatorial protons of the same positions) and another one with small value due to the coupling with the vicinal equatorial proton at position 5.

Table 2.
^{1}H NMR data (δ, ppm; J, Hz; $CDCl_3$) for compounds **4-8**

Compd.	Isomer	Position of R at 5'(5")	4'(4")-H, 6'(6")-H (δ)		J		
			ax	eq	4(6)eq-4(6)ax	4(6)ax-5ax	4(6)ax-5eq
5	*trans-trans*	3.61	3.84	4.20	11.7	11.7	-
6	*trans-trans*	1.18(t), 4.06(q)	3.84	4.19	11.7	11.7	-
7	*cis-cis*	3.95-3.96 (overlapped peak)		4.09	11.7	-	2.3
8	*cis-cis*	4.46	3.80 -3.92 (overlapped peak)				
9	*trans-trans*	3.22	4.53	4.96	11.3	11.3	-

Conclusions

The high yields synthesis of some new *cis-cis* and *trans-trans* bis-1,3-dioxane derivatives having as spacer between the two heterocycles an 1,4-phenylene unit is reported. The structural analysis carried out by NMR investigations reveals the axial orientation of the aromatic ring with respect to both dioxacyclohexane units. These derivatives are precursors for the synthesis of simple or layered cyclophanes.

Experimental

^{1}H-NMR (300 MHz) and ^{13}C-NMR (75 MHz), COSY and HMQC spectra, were recorded at *rt* in $CDCl_3$ or MeOD on a Bruker 300 MHz spectrometer, using the solvent line as reference. Mass spectra were recorded on an ATI Unicam Automass.

Melting points were measured with a Kleinfeld melting point apparatus and are uncorrected. Thin-layer chromatography (TLC) was conducted on silica gel 60 F_{254} TLC plates purchased from Merck. Preparative column (flash) chromatography was preformed using PharmPrep 60 CC (40-63 μm) silica gel purchased from Merck. Chemicals were purchased from Aldrich or Across and were used without further purification.

General Procedure for the Synthesis of Compounds 5-8

(5 mmol) diols **1-4** and (2 mmol) ketone (1,4-bis(2'-benzoyloxy-acetyl)benzene) with catalytic amounts of *p*-toluenesulphonic acid (0.1 g) were solved in 100 mL $CDCl_3$. The mixture was refluxed and the water produced in the reaction removed using a modified Dean-Stark trap. When 80 % of the water had been separated, the mixture was cooled to room temperature

and the catalyst was neutralized (under stirring 0.5 h) with CH_3-COONa powder in excess (0.2 g). The reaction mixture was washed twice with 100 mL of water. After drying over $MgSO_4$, the solvent was removed and the crude products were purified by flash chromatography or by crystallization.

***t*-1,*t*-4-Bis(*r*-2'-benzoyloxymethyl- *t*-5' – carboxymethyl-1,3-dioxan-2'-yl)benzene (5 *trans-trans*)**

White solid, m.p.=208-9℃, yield 24 % (flash chroma tography, eluent: DCM, Rf = 0.24. **^{1}H-NMR** (300 MHz,$CDCl_3$, δ ppm): 3.14 (2H, m), 3.61 (6H, s), 3.84 (4H, dd overlapped, *J*=*J'*=11.7 Hz), 4.20 (4H, dd, *J*=11.7 Hz, *J'*= 4.6 Hz), 4.36 (4H, s) 7.39 (4H, dd overlapped, *J*=8.7 Hz, *J'*=8.3 Hz), 7.54 (2H, t, *J*=8.7 Hz) 7.56 (4H, s), 7.95 (4H, d, *J* =8.3 Hz). **^{13}C-NMR** (75 MHz, $CDCl_3$, δ ppm): 40.0 (CH), 52.0 (CH_3), 62.1 (CH_2), 69.8 (CH_2), 100.0 (C_{quat}) 128.4 (CH), 128.7 (CH), 130.0 (C_{quat}), 129.8 (CH), 133.2 (CH) 136.8 (C_{quat}), 165.9 (CO), 170.3 (CO).

***t*-1, *t*-4-Bis(*r* -2'-benzoyloxyethyl-*t*-5'- carboxyethyl-1,3-dioxan-2'-yl)benzene (6 *trans-trans*)**

White solid, m.p.=141-2℃, yield 26 % (flash chroma tography, eluent: DCM, Rf = 0.27. **^{1}H-NMR** (300 MHz,$CDCl_3$, δ ppm): 1.18 (6H, t, *J*=7.2 Hz) 3.11 (2H, m), 3.84 (4H, dd overlapped, *J*=*J'*=11.7 Hz), 4.06 (4H, q, *J*=7.2 Hz) 4.19 (4H, dd, *J*=11.7 Hz, *J'*= 4.5 Hz), 4.36 (4H, s), 7.39 (4H, dd overlapped , *J*=7.9 Hz, *J'*=7.2 Hz) 7.52 (2H, t, *J*=7.9Hz) 7.57 (4H, s), 7.95 (4H, d, *J* =7.2 Hz).

***t*-1,*t* -4- Bis(*r*- 2'-benzoyloxymethyl- *c*-5'-hydroxymethyl-1,3-dioxan-2'-yl)benzene (7 *cis-cis*)**

White solid, m.p.= 154-5℃, yield 17% (flash chroma tography, eluent: DCM/ethanol = 2/0.1, Rf = 0.15. **^{1}H-NMR** (300 MHz,$CDCl_3$, δ ppm): 1.47 (2H, dt *J*=7.2*, J'*=2.3), 1.78 (2H, t, *J*=5.3 Hz), 3.95-3.96 (8H, overlapped picks), 4.08 (4H, dd, *J*= 11.7 Hz, *J*= 4.5 Hz), 4.33 (4H, s), 7.41 (4H, t, *J*= 7.1 Hz) 7.52 (2H, dd overlapped), 7.99 (4H, d, *J*= 7.1 Hz). **^{13}C-NMR (**75 MHz, $CDCl_3$, δ ppm): 36.2 (CH), 62.05 (CH_2), 62.12 (CH_2), 70.12 (CH_2), 100.3 (C_{quat}), 128.5 (CH), 128.6(CH), 129.8 (CH), 129.9 (C_{quat}), 133.2 (CH), 137.0 (CH), 166.0 (CO).

***t*-1,*t* -4- Bis(*r*- 2'-benzoyloxymethyl- *c*-5'-tosyloxymethyl-1,3-dioxan-2'-yl)benzene (8 *cis-cis*)**

White solid, m.p.=213-4℃, yield 14% (flash chromat ography, elution: diethyl ether/ pentane = 1/2, Rf = 0.21. **^{1}H-NMR** (300 MHz,$CDCl_3$, δ ppm):

1.69 (2H, m), 2.43 (6H, s),C 3.80-3.92 (8H, overlapped picks), 4.21 (4H, s), 4.46 (4H, d, *J*= 7.5 Hz), 7.31 (4H, d, *J*=8.3 Hz) 7.41 (4H, dd, *J*=8.3 Hz, *J*=7.2 Hz) 7.53 (4H, s) 7.55 (2H, t, *J*=7.2 Hz) 7.77 (4H, d, *J*=8.3 Hz) 7.97 (4H, dd, *J*=8.3 Hz) **^{13}C-NMR (**75 MHz, $CDCl_3$, δ ppm): 21.8 (CH_3), 33.9 (CH), 61.4 (CH_2), 68.9 (CH_2), 69.9 (CH_2), 100.4 (C_{quat}), 128.0 (CH), 128.56(CH), 128.62(CH), 129.8 (CH), 130.1 (CH) 132.8 (C_{quat}), 133.2 (CH), 136.7 (C_{quat}), 145.1 (C_{quat}), 165.9 (CO).

General Procedure for the Synthesis of Compound 9

A mixture of **5** (1mmol) and (5 mmol) of $LiAlH_4$ in 50 mL of THF was stirred under reflux for 5 h. Aqueous NaOH (5%; 10 mL) was very slowly

dropped into the stirred mixture at 0-5°C to destroy the excess $LiAlH_4$. After being stirred for 1 h, the mixture was filtered and washed several times with hot THF. The filtrate was evaporated, and the residue was purified by crystallisation from DCM.

***t*-1,*t* -4- Bis(*r*- 2'-benzoyloxymethyl- *t*-5'-hydroxymethyl-1,3-dioxan-2'-yl)benzene (9 *trans*-*trans*)**

White solid, m.p.= 218-9°C, yield 94%. **^{1}H-NMR (**300 MHz, MeOD , δ ppm): 2.2-2.35 (2H, m), 3.22 (4H, d, *J*= 6.4 Hz), 3.46 (4H, s) 3.53(4H, dd, *J*=*J'*=11.3 Hz), 3.96 (4H, dd, *J*=11.3 Hz, *J'*=4.6 Hz), 7.49 (4H, s). **^{13}C-NMR (**75 MHz, MeOD, δ ppm): 40.0 (CH), 62.7 (CH_2), 66.0 (CH_2), 72.4 (CH_2), 103.6 (C_{quat}), 130.8 140.4 (C_{quat}). **MS** (70 eV) (rel. int. %) m/z: 366 (M^+, 0.6), 179 (7), 147 (9), 117 (12), 89 (22), 71 (96), 59(100).

REFERENCES

1. Anteunis M.J.O., Tavernier D., Borremans F., *Heterocycles*, **1976**, *4*, 293
2. Mager S., Grosu I., *Stud. Univ. "Babeş-Bolyai", Chemia*, **1988**, *33*, 47
3. Grosu I., Plé G., Mager S., Mesaroş E., Dulău A., Gegö C., *Tetrahedron*, **1998**, *54*, 2905
4. Grosu I., Mager S., Plé G., Plé N., Toscano A., Mesaroş E., Martinez E., *Liebigs Annalen/Recueil*, **1997**, *3*, 345
5. Grosu I., Mager S., Mesaroş E., Plé G., *Heterocyclic Commun*., **1998**, *4*, 53
6. Grosu I., Mager S., Toupet L., Plé G., Mesaroş E., Mihiş A., *Acta Chem. Scand*., **1998**, *52*, 366
7. Grosu I., Muntean L.,Toupet L., Plé G., Pop M., Balog M., Mager S., Bogdan E., *Monatsh. Chem.* **2002**, *133*, 631
8. Balog M., Tötös, S., Florian C.M., Grosu I., Plé G., Toupet L., Ramondenc Y., Dincă N., *Heterocyclic Commun.* **2004***, 10,* 139
9. Balog M., Grosu I., Plé G., Ramondenc Y., Condamine E., Varga R. A., *J. Org. Chem*., **2004**, *69*, 1337
10. Bogdan N., *manuscript in preparation*

STUDIA UNIVERSITATIS BABEŞ-BOLYAI, CHEMIA, LI, 1, 2006

REACTIONS OF THE 3-CYANO-10-METHYL-PYRIDO[3,2-g]QUINOLIN-4-ONE. II*

CLAUDIA MOLDOVAN[1], CASTELIA CRISTEA[1], IOAN A. SILBERG[1], ABDALLAH MAHAMOUD[2], SILVIA UDREA[3] AND JACQUES BARBE[2]

Dedicated to professor Sorin Mager
at his 75th anniversary

ABSTRACT. The synthesis of 4-alkoxy-3-cyano-10-methyl-pyrido[3,2-g]quinoline derivatives is described. The structural assignments were performed by high resolution 2D NMR spectroscopy.

Introduction

The reaction of 3-cyano-10-methyl-pyrido[3,2-g]quinoline-4-one **1** with alkylhalides under PTC conditions, in strong alkaline media was previously described [1]. In the presence of KOH or NaOH, the hydration reaction of the cabonyl bond generates a stable gemminaldiol as the main reaction product and the target alkylation products are minor reaction products under these experimental conditions (scheme 1). The mixture of N-alkyl- and O-alkyl-3-cyano-10-methyl-pyrido[3,2-g]quinoline derivatives contains the two alkylated derivatives in 3:1 ratio.

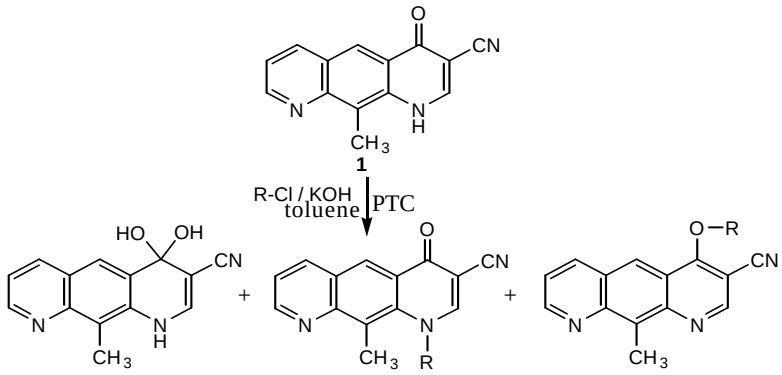

Scheme 1

---

* Part I [1]

[1] "Babeş-Bolyai" University, Faculty of Chemistry and Chemical Engineering, Organic Chemistry Department, Cluj-Napoca, RO- 400028, Romania
[2] Université de la Méditerranée, GERCTOP-UMR CNRS 6009, Marseille, France
[3] Institute of Organic Chemistry, National NMR Laboratory, Bucharest, Romania.

Another reaction strategy is thus required in order to obtain the O-alkyl-3-cyano-10-methyl-pyrido[3,2-g]quinoline derivatives in good yields.

Results and Discussions

The two steps reaction path proposed for the regioselective synthesis of 4-alkoxy-3-cyano-10-methyl-pyrido[3,2-g]quinolines **3** is presented in scheme 2.

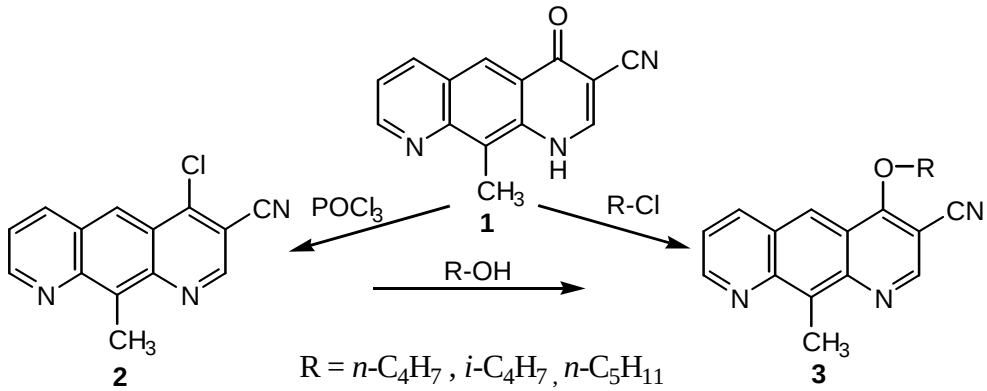

Scheme 2

As previously described, the chlorination of 3-cyano-10-methyl-pyrido[3,2-g]quinolin-4-one **1** with phosphorous oxychloride generated 4-chloro-3-cyano-10-methyl-pyrido[3,2-g]quinoline **2** in good yields [2]. The chlorine substituent in position *4* of the quinoline ring can be easily replaced by nucleophilic aromatic substitution. The reactivity of **2** is enhanced by the electron withdrawing effect of the nitrile group situated in position *3* of the heterocycle. For these reasons **2** was considered as an efficient intermediate for the synthesis of 4-alkoxy-3-cyano-10-methyl-pyrido[3,2-g]quinolines **3**.

The reaction of **2** with several alkoxides in the corresponding alcohols (such as *n*-butanol, *i*-butanol, amyl alcohol) were performed. The reaction conditions were summarized in table 1.

Table 1.
The reaction conditions for the alkylation of **2** with alkoxides.

Alkoxide	Reaction conditions Temperature [^{o}C]	Time [h]	Yield [%]
Sodium *n*-butoxide	110	2	42%
Sodium *i*-butoxide	110	2	48%
Sodium *n*-pentoxide	130	2	30%

The structures of the reaction products **3** were assigned by high resolution NMR experiments. 2D-NMR spectra were used for the complete structural assignments, as follows:

- The ^{1}H-^{1}H homocorrelations that generate the splitting pattern of the protons in the structure **3** were observed by the proton 2D COSY with gradients experiment (parameter set COSY 45gs-BBI). Figure 1 presents a detail of this 400 MHz 2D COSY spectrum, showing the cross peaks determined by the homogenous spin-spin couplings in the aromatic region and the corresponding structural assignments.

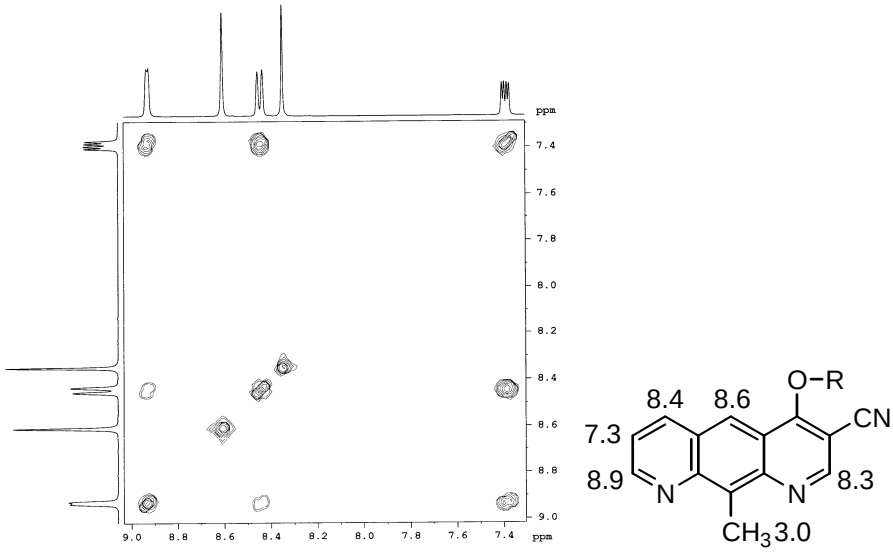

Fig 1.
400 MHz 2D NMR COSY spectrum of 3 (detail of the aromatic region) and the corresponding structural assignments

The tertiary carbon atoms of the heterocycle **3** were assigned according to the inverse ^{1}H-^{13}C correlation with z-gradients experiment (parameter set: HMQCgs-BBI). Figure 2 presents the 400 MHz 2D ^{1}H-^{13}C hetercorrelation spectrum, and the corresponding structural assignments.

The quaternary carbon atoms were assigned according to the ^{1}H-^{13}C inverse long range heterocorrelation with z-gradients experiment (parameter set: HMBCgs-BBI). In figure 3, the cross peaks in the HMBC spectrum show the ^{1}H-^{13}C heterocorrelations through two and three covalent bonds that enabled the structural assignments.

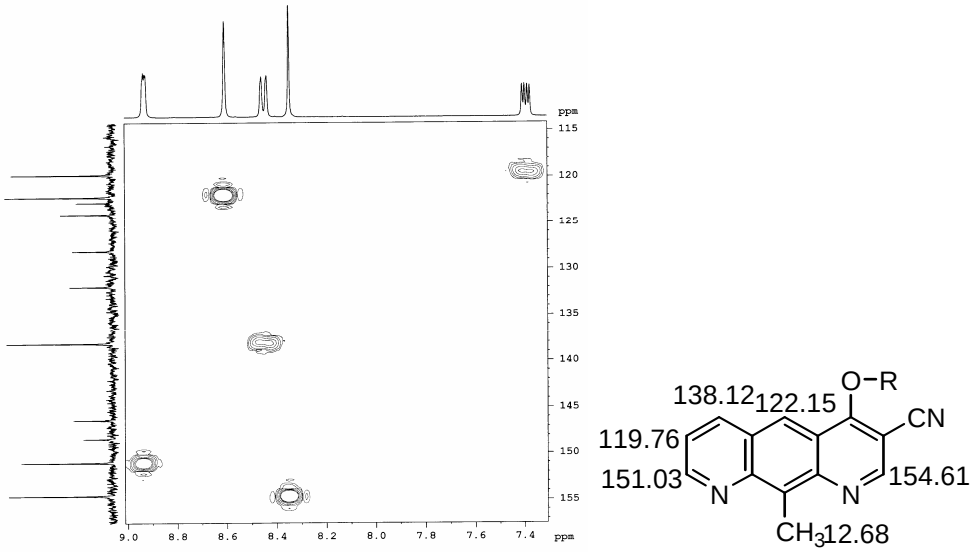

Fig 2.
400 MHz 2D NMR HMQC spectrum of 3 (detail of the aromatic region) and the corresponding structural assignments

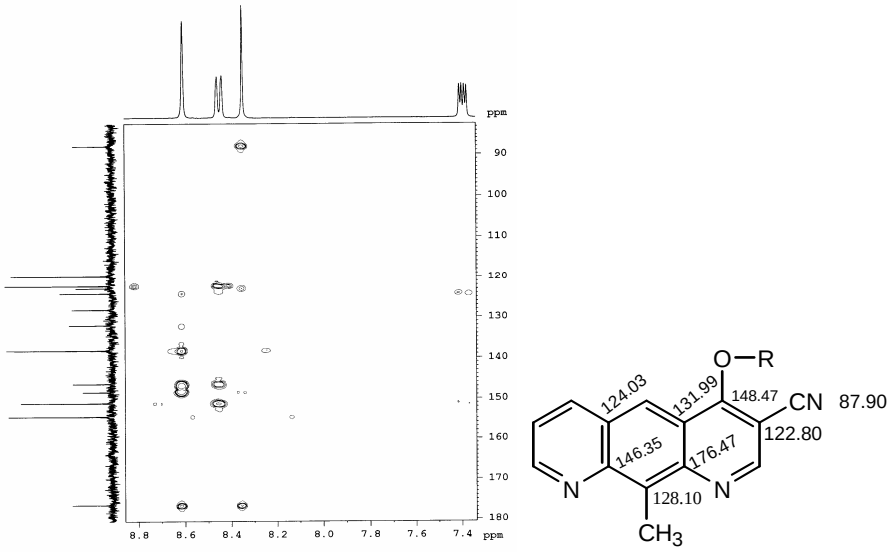

Fig.3.
400 MHz 2D NMR HMBC spectrum of 3 (detail of the aromatic region) and the corresponding structural assignments.

Conclusions

The reaction path proposed for the regioselective O-alkylation of 3-cyano-10-methyl-pyrido[3,2-g]quinoline-4-one afforded 4-alkoxy-3-cyano-10-methyl-pyrido[3,2-g] quinolines **3** in moderate yields.

Experimental

General procedure for 4-alkoxy-3-cyano-10-methyl-pyrido [3,2-g]quinolines preparations.

7 mL anhydrous alcohol was placed in a round bottom flask, treated with 0.04 g clean sodium (2 mmol) and warmed gently until all the sodium has reacted. 4-Chloro-3-cyano-10-methyl-pyrido[3,2-g] quinoline 0,25 g (1 mmol) were added and the solution was refluxed for 2 hours. The solution was cooled, then filtered. The filtrate was poured in water. The precipitate thus formed was filtrate and the solution was extracted with ether and then the solvent was evaporated. The product, a yellow powder, was recrystallised from ethanol.

4-(1-butoxy)-3-cyano-10-methyl-pyrido[3,2-g]quinoline
IR [cm^{-1}] 2850, 2900 (C-H stretching vibration), 2220 (C≡N stretching vibration), 1603, 1500 (aromatic C=C stretching vibration), 1220 (C-O stretching vibration).
^{1}H-RMN (400 MHz): δ_H (DMSO-d_6 solution): 8.93 (dd, 1H, J = 4Hz, J = 1.2 Hz, H_8) 8.60 (s, 1H, H_5), 8.44 (dd, 1H, J = 8.4 Hz, J = 1,2 Hz, H_6), 8.34 (s, 1H, H_2), 7.38 (dd, 1H, J = 8.4 Hz, J = 4 Hz, H_7), 4.40 (t, 2H), 3.44 (m, 4H), 3.02 (s, 3H), 1.06 (t, 3H).
^{13} C-RMN δ_C 176.45, 154.57, 151. 03, 148.37, 146.35, 138.13, 131.92, 128.07, 124.03, 122. 76, 122.17, 119.77, 87.92 (CN), 56.54, 19.06, 12.67.

4-(2-methyl-1-propoxy)-3-cyano-10-methyl-pyrido[3,2-g]quinoline
IR [cm^{-1}] 2215 (C≡N stretching vibration), 1603, 1565 (aromatic C=C stretching vibration), 1276, 1047 (C-O stretching vibration).
^{1}H-RMN (400 MHz): δ_H (DMSO-d_6 solution): 8.93 (dd, 1H, J = 4Hz, J = 1.2 Hz, H_8) 8.60 (s, 1H, H_5), 8.44 (dd, 1H, J = 8.4 Hz, J = 1,2 Hz, H_6), 8.34 (s, 1H, H_2), 7.38 (dd, 1H, J = 8.4 Hz, J = 4 Hz, H_7), 4.39 (d, 2H), 3.43 (m, 1H), 3.02 (s, 3H), 1.07 (d, 6H).
^{13} C-RMN δ_C 176.47, 154.61, 151.02, 148.47, 146.35, 138.12, 131.99, 128.10, 124.03, 122.80, 122.15, 119.76, 87.90 (CN), 56.54, 19.05, 12.69.

4-(1-pentoxy)-3-cyano-10-methyl-pyrido[3,2-g]quinoline
^{1}H-RMN (400 MHz): δ_H (DMSO-d_6 solution): 8.91 (dd, 1H, H_8) 8.58 (s, 1H, H_5), 8.42 (dd, 1H, H_6), 8.34 (s, 1H, H_2), 7.38 (dd, 1H, H_7), 4.2 (t, 2H), 3.5 (m, 2H), 3.02 (s, 3H), 1.07 (m, 5H).

REFERENCES

1. C. Moldovan, C. Cristea, I. A. Silberg, A. Mahamoud, C. Deleanu and J. Barbe *Studia Univ. Babes-Bolyai" Chem*ia, **2004,** *XLIX, 2* 118-122.
2. C. Moldovan , C. Cristea , I. A. Silberg , A. Mahamoud , C. Deleanu and J. Barbe, *Heterocyclic Communications,* **2004**, *10 (1)***,** 19-24.

STUDIA UNIVERSITATIS BABEŞ-BOLYAI, CHEMIA, LI, 1, 2006

MODELLING URANIUM(VI) EXTRACTION USING ARTIFICIAL NEURAL NETWORKS

MIRCEA V. CRISTEA, MARIA CURTUI, CASTELIA CRISTEA, LUIZA GAINA*

Dedicated to professor Sorin Mager
at his 75th anniversary

ABSTRACT. The use of ANN simulators for the mathematical modelling of the uranium(VI) extraction from an aqueous solution, using polar and/or nonpolar solvent containing the chelating agent di-(2-ethylhexyl)-ditiophosphoric acid, at different pH values is described. The ANN has been trained with experimental data using either 1-butanol or kerosene solvent. Good prediction results show the incentives of this modelling approach and the perspectives of its using for simulating processes with the aim of optimising both laboratory and industrial units.

Introduction

Artificial Neural Networks (ANNs) are founded on an idealized representation of the biological cell that processes information. ANNs can be represented as weighted directed graphs consisting in simple elements, neurons (grouped in layers) operating in parallel, and the connections between neurons. The weighted connection paths link every two neurons from adjacent layers such as the weighting structure is able to provide the overall network performance. As the ability to learn is a fundamental trait of intelligence, the ANNs may be considered simple but powerful artificial intelligence elements. In the ANNs context the learning process consists in updating the network architecture and connection weights so that the network can efficiently achieve a specific task. Usually, the tasks an ANN may effectively perform are: pattern classification, clustering or categorization, function approximation, prediction and associative memory applications [1].

But the main benefits of the ANN approach consist in their remarkable ability for generalization. The use of ANN models for control purposes has gained considerable attention in the field of modelling chemical process, being the subject of several scientific reports, and they are increasingly applied for system identification and simulation [2]. As a consequence, the ANNs may be successfully used for modelling systems in which detailed

* "Babeş-Bolyai" University, Faculty of Chemistry and Chemical Engineering, Cluj-Napoca, RO- 400028, Romania

governing rules are unknown or difficult to formalize under the form of first principle models [3, 4]. This last capability is exactly the type of application the present work is aimed to achieve.

The extraction of uranium(VI) from aqueous solutions with immiscible polar or nonpolar solvents using a dithiochelating agent was extensively studied. The choice of the proper solvent [5, 6] as well as the choise of the ligand [7, 8] and the optimal pH range were previously investigated.

This paper presents a first attempt to use Artificial Neural Networks for predicting the extraction of uranium(VI) from an aqueous solution, using mixtures of polar/nonpolar solvent of different ratio, in the presence of the chelating ligand di-(2-ethylhexyl)-ditiophosphoric acid. The chelate formation reaction is presented in scheme 1.

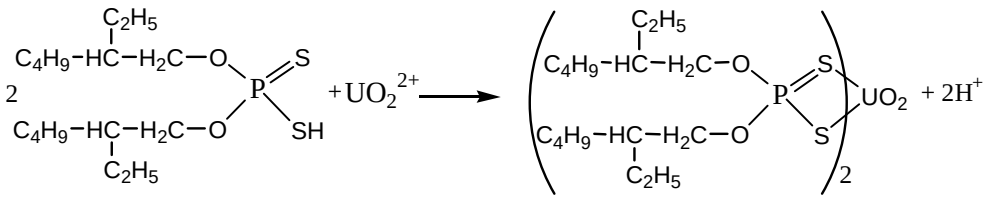

Scheme 1

Results and Discussions

The Artificial Neural Network employed in this study is of feedforward type and the backpropagation algorithm has been used for training the network's biases and weights. The network configuration is of multilayer structure and the quasi Newton Levenberg-Marquardt backpropagation algorithm has been used for learning.

The ANN architecture has been designed on the basis of heuristic methods. Its structure consists in an input layer of three neurons, a hidden layer of four neurons and a single-neuron output layer. The activation function of the first and second layer is of *tansig* (tan-sigmoid) form but the activation function of the output neuron is *linear*.

First, the ANN has been trained using the following input-output (input-target) pairs of data:

- ***Inputs*:** experimental data for the extraction of uranium(VI) from an aqueous solution having the uranium(VI) concentration of 0.1212 g/l, with either 1-butanol or kerosene solvent containing the chelatization ligand di-(2-ethylhexyl)-ditiophosphoric acid, at different pH values; these experimental data are presented in Table 1.

- ***Outputs*:** experimental data consisting in the percentage values of uranium(VI) extraction obtained for the above mentioned inputs, also presented in Table 1.

Table 1.
Experimental data for the extraction of uranium(VI) from an aqueous solution ($C_{U(VI)}$=0.1212 g/l), with either 1-butanol or kerosene solvent containing the chelatization ligand di-(2-ethylhexyl)-ditiophosphoric acid, at different pH values.

Sample no.	1-Butanol solvent		Kerosene solvent	
	Intputs pH	Outputs E [%]	Intputs pH	Outputs E [%]
1	1.2	94.5		
2	2.0	96.4		
3	4.1	99.2		
4	4.7	99.8		
5	5.6	99.9		
6			1.05	13.4
7			1.21	21.4
8			2.0	55.4
9			2.8	85.9
10			4.1	87.8
11			4.7	87.2
12			5.6	85.8

The ANN has been successfully trained. The simulation results produced by the trained network for modelling the percentage values of uranium(VI) extraction confirm this statement. The results (outputs) obtained by simulation for the already trained ANN, having as inputs the data presented in Table 1, are compared to the experimental outputs presented in the same table. The comparative results between experimental and ANN simulated data are shown in figure 1.

The relative errors between the ANN simulated data and the experimental data are considered to be small, as their offset is limited to ±1.4 %.

Second, as one of the most appreciated properties of the ANNs is their ability to make predictions, this was also the main purpose of the presented investigation. The predictions consist of the ANN's aptitude to provide values of the outputs for the inputs not yet seen during the training step.

During this second testing step the already trained ANN has been used for predicting the values for the percentage extraction of uranium(VI) from the aqueous solution ($C_{U(VI)}$=0.1212 g/l) containing 1-butanol *and* kerosene solvents with concentrations of various ratios, having totally different values compared to the ones used during the training step.

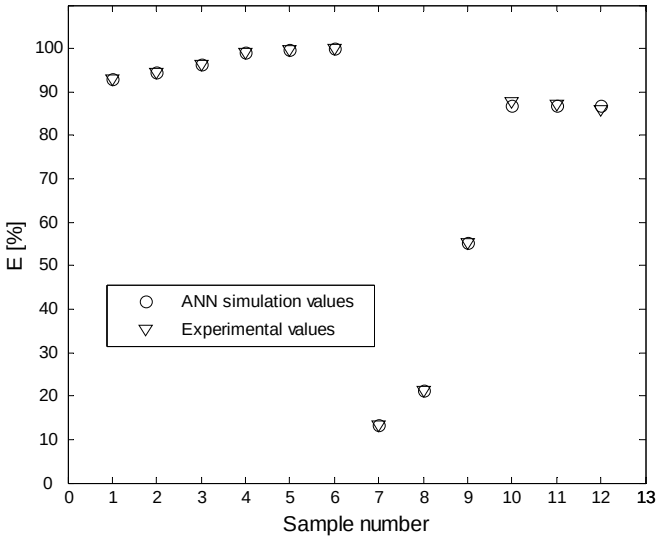

Fig. 1.
Comparative results between ANN simulated data and experimental data, for the set of input-output data used for training the ANN (*learning*)

In order to test the prediction capability of the trained ANN a new set of input-output experimental data has been used, as they are presented in Table 2.

Table 2.
Experimental data for the extraction of uranium(VI) from an aqueous solution ($C_{U(VI)}$=0.1212 g/l), using various 1-butanol-kerosene solvent mixtures containing the chelating ligand di-(2-ethylhexyl)-ditiophosphoric acid, at the pH values 2.5-3

Sample no.	$C_{butanol}$ [% vol. in kerosene]	E [%]
1	5	97.00
2	10	99.84
3	20	99.60
4	30	99.76

The values for the percentage extraction of the uranium(VI) obtained by ANN simulation are compared with the experimental values shown in Table 2 and the comparative results are presented in figure 2.

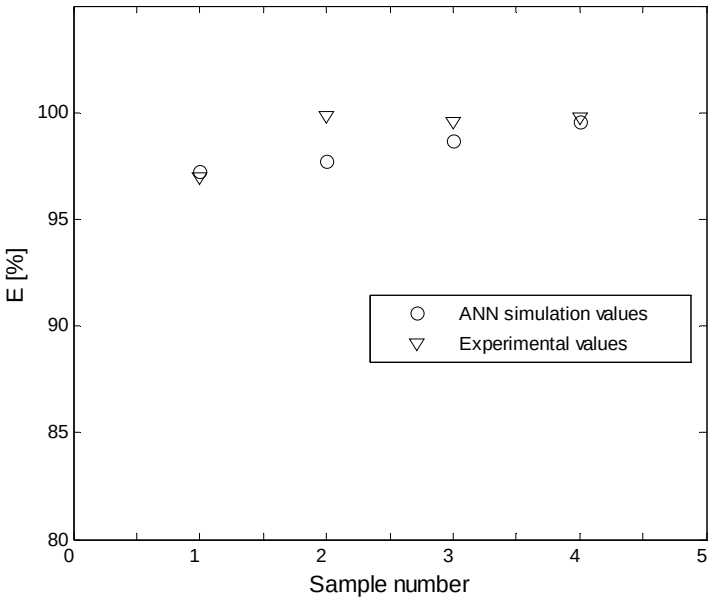

Figure 2.
Comparative results between ANN simulated data and experimental data, for the set of input-output data used for ANN testing (*prediction*).

As it may be noticed from figure 2, the ANN has good predictions capabilities proved by the errors situated in a narrow interval of ± 2.5%. Additionally it may be mentioned that testing has been performed on an input-output set of data not encountered during the ANN training procedure, and with the inputs having values very different to those used for training.

Conclusions

Although a relatively limited set of data has been used for training the results obtained on the basis of an ANN model for the simulation of the extraction of uranium(VI) from an aqueous solution ($C_{U(VI)}$=0.1212 g/l), using various 1-butanol-kerosene solvent mixtures containing the chelating ligand di-(2-ethylhexyl)-ditiophosphoric acid are very promising, The simulator may be used for getting new sets of data for uranium(VI) extraction using 1-butanol-kerosene solvent mixtures, sparing experimental time and costs. Further improvement of the model may be performed by the use of a more extended training set of data.

The use of ANN simulators for the mathematical modelling of the uranium(VI) extraction from an aqueous solution with 1-butanol - kerosene solvent mixtures containing the chelating ligand di-(2-ethylhexyl)-ditiophosphoric

acid may become a very useful tool for both laboratory and industrial scale optimisation of this investigated process.

REFERENCES

1. S. Haykin, *Neural Networks A Comprehensive Foundation*, MacMillan College Publishing Co., New York, **1994**.
2. M. V. Cristea, L. Toma, S. P. Agachi, *7-th World Congress of Chemical Engineering*, Glasgow, **2005**.
3. M.V. Cristea, S. Varvara, L. Muresan, I.C. Popescu, *Indian Journal of Chemistry.*, **2003**, *42A,* 764-768.
4. V. M. Cristea, I. Batiu, *Revue Roumaine de Chim*ie, **2005,** *50 (11-12)*, 1009-1012.
5. Haiduc, M. Curtui, I. Haiduc, *Journal of Radioanalytical and Nuclear Chemistry*, **2001**, *2*, 359-362.
6. M. Curtui, I. Haiduc, *Journal of Radioanalytical and Nuclear Chemistry. Letters,* **1984**, *86 (5)*, 281-290.
7. M. Curtui, Gh. Marcu, M. Diaconeasa, I. Haiduc, *Studia Univ. Babes-Bolyai" Chemia,* **1976**, *21*, 63-67.
8. M. Curtui, *Studia Univ. Babes-Bolyai" Chemia,* **1997**, *XLII, 1-2*, 95-100.

SYNTHESIS OF *CIS* - 7,8 – EPOXY - OCTADECANE, SPECIES - SPECIFIC COMPONENT OF THE SEX PHEROMONE OF NUN MOTH *LYMANTRIA MONACHA* (LEPIDOPTERA, LIMANTRIIDAE)

IOAN OPREAN[a,b], ANA AURELIA BOTAR[b], LUCIA GÂNSCĂ[b] AND IULIANA VASIAN[b]

ABSTRACT. The synthesis of *cis*-7,8-epoxy-octadecane, species-specific component of the sex pheromone of nun moth *Lymantria monacha* was based on a $C_{10}+C_2=C_{12}$ and $C_{12}+C_6=C_{18}$ coupling scheme, by acetylenic route, starting from 1-bromo-decane. The second coupling reaction took place between di-n-dodecyne mercury and 1-bromo–hexane in a transmetallation reaction.

Keywords: nun moth, *Lymantria monacha*, *cis*-7,8-epoxy-octadecane

Introduction

Nun moth (NM), *Lymantria monacha*, in Europe and gypsy moth (GM) *Lymantria dispar*, in Europe and North America are most important defoliators of coniferous and deciduous forests, respectively.

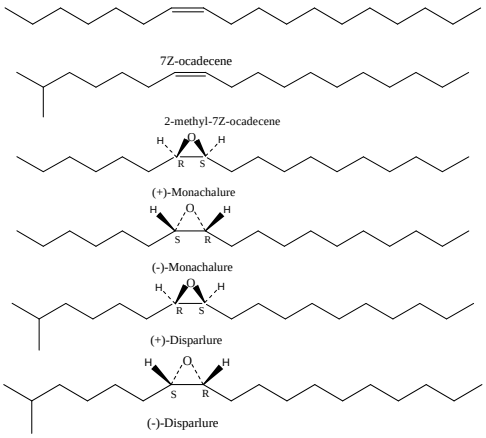

Figure 1

[a] „Babeş-Bolyai" University, Organic Chemistry Departament, 11 Arany Janos St. 400028, Cluj-Napoca, Romania
[b] "Raluca Ripan" Institute for Research in Chemistry, 30 Fântânele St., 400294, Cluj-Napoca, Romania

For sexual communication GM and NM females produce the pheromone disparlure; NM and GM males respond to the (+) - disparlure enantiomer [(7R, 8S)-cis-7,8-epoxy-2- methyloctadecane] as a single attractive but unspecific pheromone component [1-29].

Three epoxies [(-) - disparlure, (+) - and – (-) - monachalure] and two hydrocarbon volatile components [2- methyl- Z7- octadecene and Z7-octadecene] [30] synergistically prevented cross-attraction of coseasonal GM males and imparted specificity to NM sexual communication. Fig.1

In the literature are not mentioned the synthesis of cis-7,8-epoxy-octadecane, species-specific component of the sex pheromone of nun moth *Lymantria monacha.*

The paper presents a route for the synthesis of *cis*-7,8-epoxy-octadecane.

Results and Discussion

For the synthesis of *cis*-7,8-epoxy-octadecane (1) we explored the pathway outlined in Scheme 1, based on a $C_{10}+C_2=C_{12}$ and $C_{12}+C_6=C_{18}$ coupling scheme, by acetylenic route, starting from 1-bromo-decane.

In our variant, the first coupling reaction was effected in order to obtain 1-dodecyne (4) by adding 1-bromo-decane to monosodate acetylene, obtained in situ from acetylene in DMSO with sodium hydride. 1-Dodecyne (4) with mercuric chloride in an aqueous solution containing potassium iodide and sodium hydroxide (Nessler's reagent [31]) was quantitatively precipitated as di-n-dodecynyl mercury (5).

The key step in our acetylenic route consisted in transmetallation of di-n-dodecynyl mercury (5), which was directly lithiated by heating with lithium metal in diglyme and then alkylated with 1-bromo-hexane obtaining 7-octadecyne (7).

Z-7-Octadecene (8) was prepared from 7-octadecyne (7) by hydrogenation using Ni-P2/EDA catalyst, obtained by reducing nickel acetate with sodium borohydride and subsequent poisoning with ethylenediamine [32]. Using NiP-2 catalyst, the hydrogenation takes place quantitatively and with a very high degree of stereoselectivity.

To prepare *cis*-7,8-epoxy-octadecane (1) the olefine 8 was epoxidated with monoperphtalic acid.

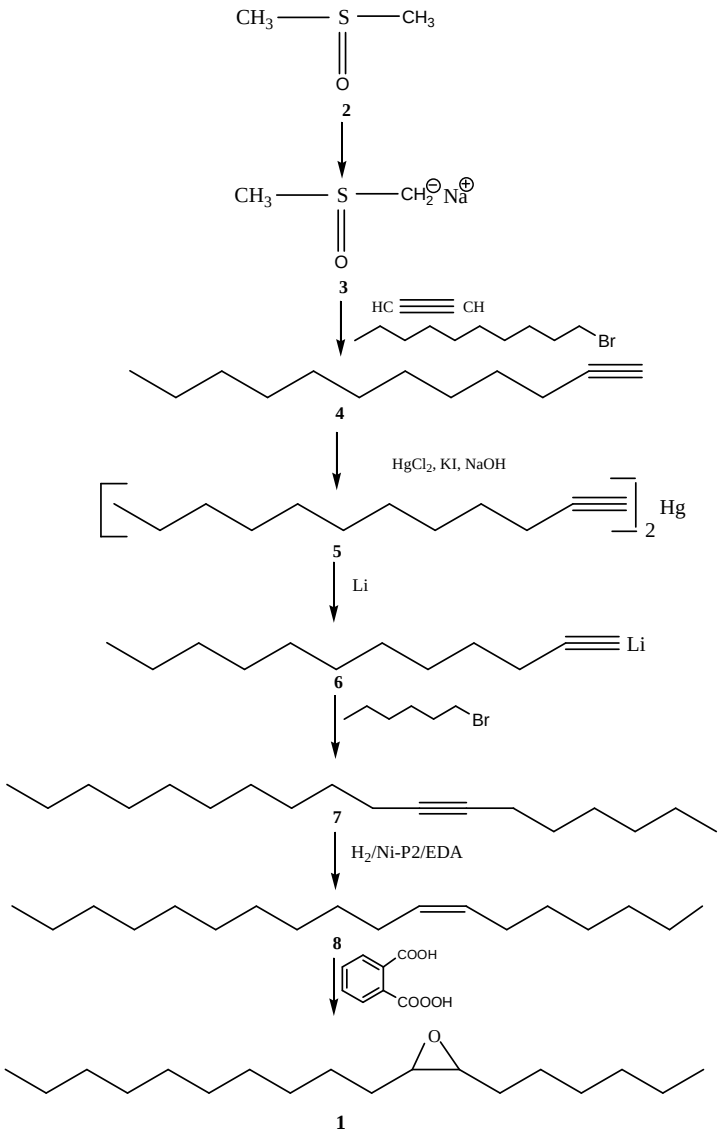

Scheme 1

Experimental

GC-MS analyses were performed on a Hewlett Packard GL-MSD 5890-5972 instrument, using a HP-5MS 30mX0.25mmX0.25µm capillary columm.

A Perkin Elmer Spectrometer Model 700 was used for IR spectra.

1-Dodecyne (4)

Aparatus: 1L reactor provided with a thermometer dipping into the liquid, a dropping funnel, a stirrer and a 20-30 cm long tube for preventing any splasting out of the reaction mixture.

All operations took place in inert atmosphere and under vigorous stirring.

4,41g (92 mmoles) of natrium hydride were added to 56 mL of dry DMSO. The temperature was risen up to 65^0-68^0. The conversion was finished when no more hydrogen was evolved.

Acetylene (freed from acetone) was introduced for 15 min. at a rate of about 2L/min with external cooling in order to moderate the reaction.

During this process the temperature is maintained between 20^0 and 30^0C.

28 mL of DMSO were added and afterwards, between 20^0-30^0, 8,17 g (37 mmoles) of 1-bromo-decane with external cooling.

The reaction was led to completion by stirring for 3 hours at room temperature. The reaction mixture was poured into 100 mL of ice-water and extracted with four portions of 100 mL petroleum ether.

The combined extract were washed with brine and dried over $MgSO_4$. A satisfactory purity could be achieved by vacuum distillation collecting the fraction at 92^0-94^0C/28 mmHg; yield: 6,14g (79%)

IR spectrum (film, cm^{-1}): 2160 s (-C≡C), 3280 vs (≡CH).

Mass spectrum (m/z; %): 151(<1), 137(<1), 123(1), 109(10), 95(40), 81(100), 67(77), 55(53), 41(85), 29(37).

Di-n-dodecynyl mercury (5)

18,4 g (110 mmoles) of 1-dodecyne (4) dissolved in 500 mL ethanol was added to a vigorous stirred solution of Nessler's reagent prepared according to the standard procedure [31].

The product 5 was obtained in yield of 93%, m.p.= 86^0-87^0.

7-Octadecyne (7)

16,33 g (30 mmoles) of di-n-dodecynyl mercury (5) in 84 mL diglyme was treated with 0,44 g of lithium under inert atmosphere at 100-110^0 for 2 hours.

11g (66 mmoles) of 1-bromo-hexane was added dropwise then the temperature raised to 120^0-130^0 under stirring for 6 hours. The mixture was left overnight, decanted, diluted with water and extracted with ethyl ether. The ethereal solution was washed to neutral and dried over $MgSO_4$.

After the removal of the solvent 12,1g (75%) of 7 were obtained, GC purity: 92%.

Mass spectrum (m/z; %): 250(<1), 235(<1), 221(<1), 207(<1), 180(1), 165(4), 152(2), 123(12), 109(29.9), 95(44.5), 81(53), 55(76.04), 67(54), 40(100), 29(24).

Z-7- Octadecene (8)

7-Octadecyne (7) was hydrogenated at Z-7-octadecene (8) in the presence of the NiP2/EDA catalyst, prepared in situ according to the standard procedure [32]. Z-7-octadecene (8) was obtained in yield of 93% , GC purity: 95%.

Mass spectrum (m/z, %): 252(10), 224(1), 196(<1), 182(<1), 168(1), 158(1.9), 125(11), 111(31.2), 97(59.8), 83(65.5), 69(73.4), 55(100), 41(99.5), 29(44.9).

Z-7,8-Epoxy-octadecane (1)

7,56g (30 mmoles) of Z-7-octadecene (8) was trated with 68 mL of ethereal solution of monoperphtalic acid (1 mL containing 93 mg of peracid) and kept at room temperature for 24 hours. The mixture was then filtered, the Synthesis of *cis* - 7,8 - epoxY- octadecane filtrate washed successively with 10% $NaHCO_3$, diluted NaOH and water. After drying over $MgSO_4$, the solvent was removed and the residium was **1**. Yield: 95%, GC purity: 95%.

Mass spectrum (m/z, %): M=268(<1), 252(<1), 225(<1), 211(<1), 197(<1), 183(12), 152(2.5), 141(<1), 127(15), 97(55.9), 83(40.9), 69(59), 55(100), 41(84), 29(45.5).

REFERENCES

1. B.A. Bierl, M. Beroza, C.W. Collier, *Science,* **1970**, *170*, 87
2. B.A. Bierl, M. Beroza, C.W. Collier, *J. Econ. Entomol.,* **1972**, *65*, 659
3. H.J. Bestmann, O. Vostrowsky, *Tetrahedron Letters,* **1974**, 207
4. H.J. Bestmann, O. Vostrowsky, W. Stransky, *Chem. Ber.,* **1976**, *109*, 3375
5. T.H. Chan, E. Chang, *J. Org. Chem.,* **1974**, *39*, 3264
6. S. Iwaki, S. Marumo, T. Saito, M. Yamada, K. Katagiri, *J. Am. Chem. Soc.,* **1974**, *96*, 7842
7. K. Mori, T. Takigawa, M. Matsui, *Tetrahedron Letters,* **1976**, 3953
8. J.H. Margraf, S.I. Lussking, E.C. McDonald, B.D. Volpp, *J.Chem.Ecol.,* **1983**, 9211
9. H.C. Brown, D. Basavaian, *Synthesis,* **1983**, 283
10. K. Koumaglo, H.T. Chan, *Tetrahedron Letters,* **1984**, *25*, 717
11. S. Tsuboi, H. Fukutani, A. Takeda, K. Kawazoe, S. Sato, *Bull .Chem. Soc. Japan,* **1987**, *60*, 2475
12. G.Q. Lin, B.C. Wu, L.Y. Liu, X.Q. Xian, W.S.Zhou, *Acta Chem. Sinica,* **1984**, 74
13. S. Pikul, M. Kozlowska, J. Jurezak, *Tetrahedron Letters,* **1987**, *28*, 2627
14. Y. Masaki, Y. Serizawa, K. Nagata, H. Oda, H. Nagashima, K. Kaji, *Tetrahedron Letters,* **1986**, *27*, 231
15. O. Jr. Achmatowich, A. Sadownik, R. Bielski, *Polish. J. Chem.,* **1985**, *59*, 553
16. V.B. Jigajimmi, R.H. Wightman, *Carbohydrate Res.,* **1986**, *147*, 145
17. A.G. Tolstikov, N.V. Kharhalina, V.N. Odinikov, *Zhur. Org. Khim.,* **1987**, *23*, 2469 and *Zhur. Org. Khim*., **1989**, *25*, 296
18. R.E. Rossiter, T. Katsuki, K.B. Sharpless, *J. Am. Chem. Soc.,* **1981**, *103*, 464
19. K. Mori, T. Ebata, *Tetrahedron Letters,* **1981**, *22*, 4281
20. K. Mori, T. Ebata, *Tetrahedron Letters,* **1986**, *42*, 3471
21. S. Marczak, M. Masnyk, J. Wicha, *Tetrahedron Letters*, **1989**, *30*, 2485
22. G.Q. Lin, Y. Jiang, W.S. Zhou, *Acta Chem. Sinica,* **1985**, 257
23. T. Satoh, T. Oohara, Y. Ueda, K. Yamakawa, *Tetrahedron Letters*, **1985**, *29*, 313
24. T. Satoh, T. Oohara, Y. Ueda, K. Yamakawa, *J. Org. Chem.,* **1989**, *54*, 3130
25. S. Tsuboi, H. Futurani, M. Utaka, A. Takeda, *Tetrahedron Letters*, **1987**, *28*, 2709

26. Bianchi, W. Cabri, P. Cesti, F. Francalanci, F. Rama, *Tetrahedron Letters*, **1988**, *29*, 2455
27. Otto, F. Stein, C.A. van der Willingen, *Agric. Ecosyst. Environ.,* **1988**, *21*, 121
28. T. Sato, T. Itoh, T. Fujisawa, *Tetrahedron Letters*, **1987**, *28*, 5677
29. Y. Ko. Soo, *Tetrahedron Letters*, **1994**, *35,* 3601
30. G. Gries, R. Gries, *Naturwissenschaffen,* **1996**, *83*, 382-385
31. E. Muller, J.K. Johnson, W.L. McEwen, *J. Amer. Chem. Soc*.,**1926**, *48*, 469
32. C.A. Brown and V.K. Ahnya, *Chem.Commun.,* **1973**, 553

STUDIA UNIVERSITATIS BABEŞ-BOLYAI, CHEMIA, LI, 1, 2006

CONETORI OF HIGH GENERA

ANIELA E. VIZITIU, AND MIRCEA V. DIUDEA*

Dedicated to Professor Sorin Mager, on his 75 years,
for his bright contribution to the Stereochemistry.

ABSTRACT. Nanocones are taken as starting structures for designing various 3D nanostructures. Toroidal objects of genera from one to five are built up by using conical zones and appropriate nanotubes. In the same sense, units derived by opening the Platonic solids operated by various map operations are used. The topology of the resulting objects is discussed in connection with the strain estimated at the POAV1 level of theory.

1. Introduction

A map *M* is a combinatorial representation of a closed surface.[1] Several transformations (*i.e.*, operations) on maps are known and used for various purposes.[2,3]

Let us denote in a map: *v* - number of vertices, *e* - number of edges, *f* - number of faces and *d* - vertex degree.

Recall some basic relations in a map:[4]

$$\sum d\, v_d = 2e \tag{2}$$

$$\sum s\, f_s = 2e \tag{3}$$

where v_d and f_s are the number of vertices of degree *d* and number of *s*-gonal faces, respectively. The two relations are joined in the famous Euler[5] formula:

$$v - e + f = \chi(M) = 2(1-g) \tag{4}$$

with χ being the Euler *characteristic* and *g* the genus[6] of a graph (*i.e.*, the number of handles attached to the sphere to make it homeomorphic to the surface on which the given graph is embedded; $g = 0$ for a planar graph and 1 for a toroidal graph). Positive/negative χ values indicate positive/negative curvature of a lattice.

If a graphene sheet is divided into six sectors, each with an angle of 60º (Figure 1), and if *m* of these sectors (with *m* varying from 1 to 5) are

* Faculty of Chemistry and Chemical Engineering, "Babes-Bolyai" University 400028 Cluj, Romania

selected sequentially with the dangling bonds being fused together (see below), a series of five single-walled nanocones is obtained, with a linear angle α at the cone apex equal to 112.9º, 83.6º, 60.0º, 38.9º, and 19.2º. These values correspond to the formula:[7]

$$\alpha = 2\arcsin(m/6) \qquad (1)$$

One can add two extreme cases: (i) the graphene sheet, with all m = 6 sectors being involved, corresponding to a "cone" with an angle of 180º; and (ii) when m = 6, one obtains a "cone angle" equal to zero, corresponding to a nanotube capped at one end with any combination of hexagons and six pentagons, *e.g*., a "half-buckminsterfullerene". Thus *nanotubes capped at one end can be considered to be a particular case of nanocones,* and indeed Ebbesen has observed by transmission electron microscopy how a blunt nanocone with m = 5 on adding a sixth 60º sector becomes converted into a nanotube.[8,9]

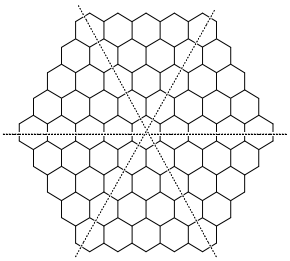

Figure 1.
The six sectors on a honeycomb lattice

In the hereafter text we will consider only cones ending in polygons of s = 3 to 5 with no other polygonal defect of the graphite sheet. The name of such objects includes: [tip polygon]CN_length of the cone body, in number of hexagon rows (Figure 2).

[3]CN_3; v = 48

Figure 2.
A nanocone ending in a trigon

2. Single Conetori

Conical zones may be involved in the construction of the so-called "distinct-walled tori" DWT, proposed by Nagy *et al*.[10] to appear by sealing a double-walled carbon nanotube DWNT in two distinct position, by an electron beam. Proposals of toroidal structures bearing polygonal defects are known since the pioneering times of nanoscience.[11-13]

Such structures, of genus 1, called hereafter conetori, are built up, in general, by two conical zones joined by two tubes, one internal and the other external, having corresponding distinct diameters. Their name includes: [cone tip polygon]CT_cone length_type and length of internal tube(tiling)_type and length of external tube(tiling), the length being given in number of hexagon rows. The tube is either an H (zig-zag) or V (armchair) one.[14]

Function of the composing parts the conetori are classified as follows.

2.2.1. Conetori with Internal H-tube, External V-tube

Even the small conetori (Figure 5) of this type are strained structures, it could be imagined that by increasing the number of atoms, they could become more relaxed molecules, as suggested in Figure 6. This huge object can be covered by disjoint coronenes (by the generalized map operation (2,2)[15]); it appears the opportunity to address the question of aromaticity of such total resonant molecular systems and consequently the possible increase of molecule stability.

[5]CT_2_H0(7)_V4(5,7,5)
v =360; S=5.44

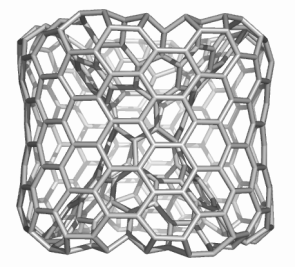

[5]CT_2_H1(7)_V5(5,7,5)
v =370; S=5.05

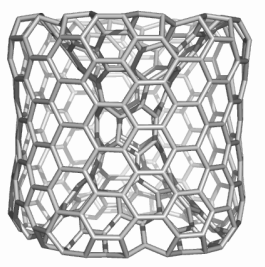

Figure 3.
Conetori with internal H-tube, external V-tube

(2,2)([5]CT_2_H0(7)_V4(5,7,5))
v =4320; S=0.52

DCor

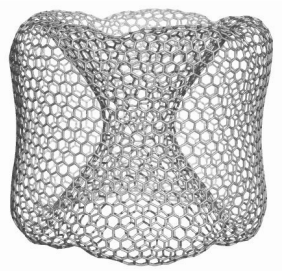

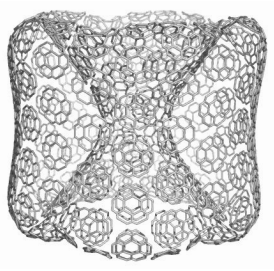

Figure 4.
Conetorus with disjoint coronenic units

2.2.2. Conetori with Internal V-tube, External V-tube

Cones of this type show (5,8,5) tiling at the junction with the inner tube while (5,7,5) at that with the outer tube (Figure 5a). The octagons can be eliminated by a Stone-Wales operation (*i.e*., edge rotation, specified by RO in Figure 5b). Systematic search on the stability of tori belonging to this type has been reported in ref.[10]

(a) [5]CT_2_V2(5,8,5)_V5(5,7,5)
V = 420; S=3.64

(b) [5]CT_2_V3(6,7)RO_V5(5,7,5)
V = 420; S=3.61

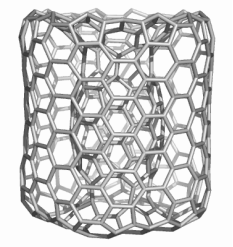

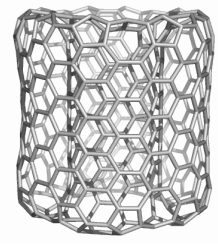

Figure 5.
Conetori with internal V-tube, external V- tube

3. Multi Tori

The torus of $g = 1$ is the simplest one in the series of objects of high genera. Such structures can be generated by opening the Platonic solids, operated by some map operations. In the following some of the most interesting classes of multi tori are illustrated and characterized from the topological point of view.

3.1. Tori of g =2 and g =3

By intersecting two simple tori in one or two points, multi tori of *g*=2 and *g*=3, respectively, can be constructed (Figure 6).

Systematic construction of such multi tori is based on the Platonic solids: they are operated by some map operations, *e.g.*, quadrupling *Q*, capra *Ca*, etc., and next every original face opened. In this way, repeat units in possible infinite lattices or finite multi tori, by joining every pair of open faces by an appropriate nanotube segment, can be constructed. The objects in Figure 7 originate in the tetrahedron T while those in Figures 8 to 11 in the cube C.

DT; v=936; e=1404; f_7=12; f_6=454; g=2; S=5.81

TT; v=984; e=1476; f_7=24; f_6=464; g=3=2x2-1; S=6.77

Figure 6.
Multi tori of genera g=2 and g=3

DT(T); v = 124; e = 186
f_7=12; f_6=48; g = 2; S = 14.44

Op(Ca(T)) ; v = 40; e = 54; f_7= 12;
g = 2; S = 10.432

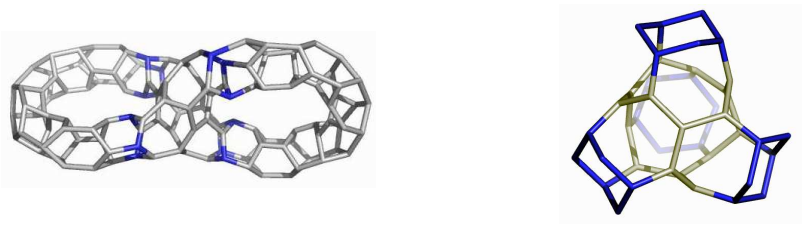

Figure 7.
Double torus of g=2, and its core derived from the tetrahedron T

Observe the objects in Figure 8 are isomers having the open faces of the cube ended as the “armchair” - V - tube (a) and “zig-zag” - H - tube (b). Clearly, the attached tubes have to have the same open ends. Also note the very low strain in the (b) object, which is further observed in the derived triple torus (Figure 9b, compared with Figure 9a). The both objects

in Figure 8 were inferred in the molecular realization of the celebrate Dyck graph,[16-18] on 32 vertices of valence 3, 48 edges, 12 octagons, girth 6, diameter 5, and chromatic number 2. It is non-planar and has the genus g = 1 (*i.e.*, there exists an embedding of the graph on the torus).[17] Cycle counting revealed 12 octagons and 16 hexagons.

(a) $E_{2a}(Q(C))$; v = 56; e = 72; f_8 = 12; g = 3 ; S =2.05

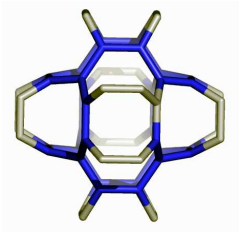

(b) $E_1(Q(C))$; v = 56; e = 72; f_8 = 12; g = 3 ; S = 0.50

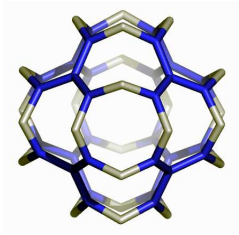

Figure 8.
Core units for m*ulti tori of high genera*, derived from the cube C

TT(C)_264V_CCA12A;
v = 264; e = 396; f_8=12; f_6=116; g = 3; S = 13.86

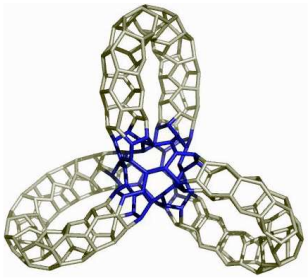

TT(C)_296H_CQSI7;
v = 296; e = 444; f_8=12; f_6=132; g = 3; S = 10.01

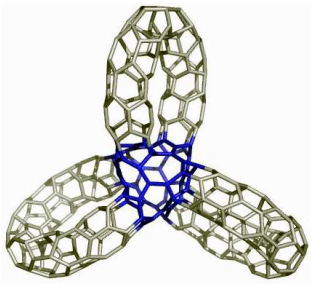

Figure 9.
Triple tori, g=3 with the core derived from the cube C

The strain S, in terms of the POAV1 theory,[19-22] of such objects of high genera[18] is relaxed as the number of atoms increases. It is evident, when compare the structures in Figures 10 (320 atoms) and 11 (2240 atoms), with a clear drop in their strain.

TT_320H_CA; v = 320;
e = 480; f_7=24; f_6=132; g = 3
S = 9.29

(b) *Op*(*Ca*(*C*)); S = 2.171
v = 80; e = 108; f_7 = 24; g = 3

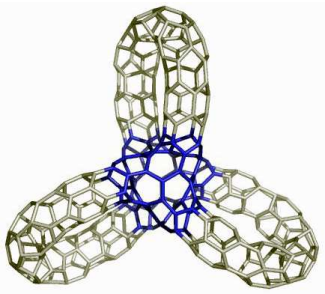

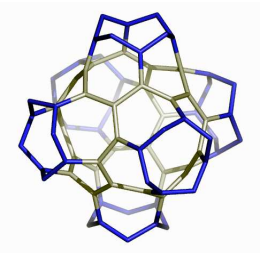

Figure 10.
Triple torus, g=3 and its core derived from the cube C

Ca_S(TTH_CA_R); v =2240; e = 3360; f_7=24; f_6=1092; g = 3; S = 2.54

Figure 11.
A more relaxed t*riple torus*, g=3, by Capra operation

3.2. Structures of High Genera

Structures of high genera can be generated, as above mentioned, by opening the Platonic solids, operated by some map operations. Units derived as above may form either infinite lattices of negative curvature[23-26] or closed cages, showing porous structure. Spongy carbons have been recently synthesized.[27] Objects like those in Figure 12, of genus 5, can be built up, on the unit derived by opening the chamfering/quadrupling transform of cube (see Figure 8), by closing together six cones emerging from the open faces. They are isomers comprising either a V or an H tubular inner unit.

(a) PTCV; v = 248; e = 372; f_8=24; f_6=92; g =5; S=5.47	(b) PTCH; v = 248; e = 372; f_7=24; f_8=12; f_6=80; g =5; S= 5.65 HF=17.74; Gap=4.56; D_{2h}
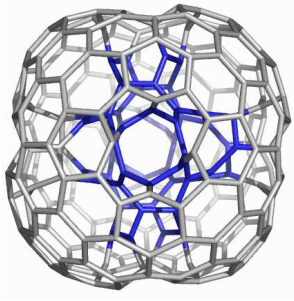	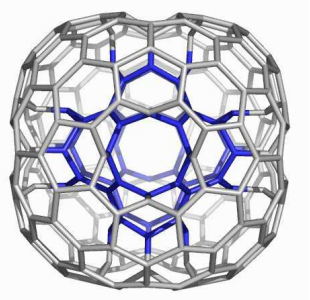

Figure 12.
Multi tori, g=5, with the core derived from the cube C

Objects of high genera have also been modeled by Lenosky et al.,[23,24] Terrones *et al*.[25,26] and more recently by Lijnen and Ceulemans.[18]

Structures have been optimized at the Amber MM HyperChem level (Polak-Ribiere conjugate gradient, at RMS = 0.005) and the strain computed by the JSChem software program.[28]

Conclusions

Conical zones are involved in several nanostructures, starting from the intersecting units of nanotubes to finite or infinite structures. Multi tori appear in zeolites or in spongy (carbon) structures, as parts of the infinite P- or FRD-type negatively curved surfaces. The toroidal objects including conical zones could appear as real molecular structures, as the nanotubes filled by spherical fullerenes turn in double walled nanotubes, the sealing of which enabling (elongated) toroidal structures with distinct walls.

REFERENCES

1. T. Pisanski , M. Randić, in *Geometry at Work*, M. A. A. Notes, **2000**, *53*, 174-194.
2. M. V. Diudea, P. E. John, A. Graovac, M. Primorac, T. Pisanski, *Croat*. *Chem*. *Acta*, **2003**, *76*, 153-159
3. M. V. Diudea, Covering Forms in Nanostructures, *Forma*, **2004**, *19* (3), 131-163.
4. L. Euler, *Comment. Acad. Sci. I. Petropolitanae*, **1736**, *8*, 128-140.
5. L. Euler, *Novi Comment*. *Acad*. *Sci*. *I*. *Petropolitanae*, **1758**, *4*, 109-160.
6. F. Harary, *Graph Theory*, Addison-Wesley, Reading, MA, **1969**.

7. A. T. Balaban, in: M. V. Diudea (Ed.), *Nanostructures-Novel Architecture*, Nova, N. Y., **2005**, 113-142.
8. A. Krishnan, E. Dujardin, M. M. J. Treacy, J. Hugdahl, S. Lynum, T. W. Ebbesen, *Nature*, **1997**, *388*, 451-454.
9. T. W. Ebbesen, *Acc. Chem. Res.,* **1998**, *31*, 558-566.
10. Csaba L. Nagy, Mircea V. Diudea, Teodor S. Balaban, in: M. V. Diudea (Ed.), *Nanostructures-Novel Architecture*, Nova, N. Y., **2005**, 35-81.
11. S. Itoh, S. Ihara, J-i. Kitakami, *Phys*. *Rev*., *B* **1993**, *47*, 1703-1704.
12. S. Ihara, S. Itoh , J-i. Kitakami, *Phys*. *Rev*., *B* **1993**, *47*, 12908-12911.
13. D. Babić, D. J. Klein, T. G. Schmalz, *J*. *Mol*. *Graphics Modell*. **2001**, *19*, 222-231.
14. M. V. Diudea, T. S. Balaban, E. C. Kirby, A. Graovac, *Phys*. *Chem*.,*Chem*.*Phys*., **2003**, *5,* 4210-4214.
15. M. V. Diudea, M. Ştefu, P. E. John, A. Graovac, *Croat*. *Chem*. *Acta,* **2005** (in press).
16. W. Dyck, *Math*. *Ann*., **1880**, *17*, 510-516.
17. A. Ceulemans, E. Lijnen, L. J. Ceulemans, P. W. Fowler, *Mol*. *Phys*., **2004**, *102*, 1149-1163.
18. E. Lijnen, A. Ceulemans, *J. Chem. Inf. Model.,* **2005**, CI0502496
19. R.C. Haddon, *J*. *Am*. *Chem*. *Soc*., **1990**, 112, 3385- 3389.
20. R.C. Haddon, K. Raghavachari, in: W.E. Billups and M. A. Ciufolini, *Buckminsterfullerenes*, VCH, **1993**, 185-215.
21. R.C. Haddon , S.-Y. Chow, *J*. *Am*. *Chem*. *Soc*., **1998**, 120, 10494-10496.
22. R.C. Haddon, *J*. *Phys*. *Chem*. *A*, **2001**, 105, 4164-4165.
23. T. Lenosky, X. Gonze, M. Teter, V. Elser, *Nature*, **1992**, *355*, 333-335.
24. S. J. Townsend, T. J. Lenosky, D. A. Muller, C. S. Nichols, V. V. Elser, *Phys*. *Rev*. *Lett*., **1992**, *69*, 921-924.
25. H. Terrones, A. L. Mackay, *Prog*. *Crystal Growth and Charact*., **1997**, *34*, 25-36.
26. H. Terrones , A. L. Mackay, *Chem*. *Phys*. *Lett*., **1993**, *207*, 45-50.
27. G. Benedek, H. Vahedi-Tafreshi, E. Barborini, P. Piseri, P. Milani, C. Ducati, and J. Robertson, *Diamond Relat*. *Mater*., **2003**, *12*, 768–773.
28. Cs. L. Nagy, M. V. Diudea, JSChem software program, "Babes-Bolyai" Univ., Cluj, **2005.**

STUDIA UNIVERSITATIS BABEŞ-BOLYAI, CHEMIA, LI, 1, 2006

RETRO MAP OPERATIONS

A. E. VIZITIU AND M. V. DIUDEA*

ABSTRACT. Operations on maps are well known theoretical tools for transforming a given polyhedral tessellation. Several properties of fullerenes, such as their π-electronic structure and stability, need information on their associate graph, which eventually resulted by a map operation applied on a smaller molecular graph. In this respect, retro-operations, particularly those of the most used leapfrog, chamfering and capra operations, appear particularly useful in searching the properties of fullerenes. A series of analyzed fullerenes proved to be leapfrog transforms of smaller cages. This helped in understanding their closed π-electronic structure and stability.

Introduction

Fullerenes are carbon allotropes, with finite cage associate graphs, that already entered in the realm of real chemistry: they have been functionalized or inserted in supramolecular assemblies.[1-7]

A fullerene is, according to a classical definition, an all-carbon molecule consisting entirely of pentagons (exactly 12) and hexagons (*N*/2-10). Non-classical fullerene extensions may include rings of other sizes.[8-10]

A map *M* is a combinatorial representation of a closed surface.[11] Several transformations (*i.e.*, operations) on maps are known and used for various purposes.

Operations on maps are topological-geometrical transformations enabling modification of a polyhedral tessellation. Basic simple map operations, such as dualization, truncation, stellation, etc., are supposed known. About this subject, the reader is referred to. [11-13]

Let us recall some basic relations in a map:[14]

$$\sum d\, v_d = 2e \tag{1}$$

$$\sum s\, f_s = 2e \tag{2}$$

In the above, *v* is the number of vertices, *e* - number of edges, *f* - number of faces, *d* - vertex degree, v_d - number of vertices of degree *d* and f_s - number of *s*-gonal faces, respectively. The two relations are joined in the famous Euler formula:[15]

$$v - e + f = \chi(M) = 2(1-g) \tag{3}$$

* Faculty of Chemistry and Chemical Engineering "Babes-Bolyai" University, 400028 Cluj, Romania

with χ being the Euler *characteristic* and *g* the genus[16] of a graph (*i.e*., the number of handles attached to the sphere to make it homeomorphic to the surface on which the given graph is embedded; *g* = 0 for a planar graph and 1 for a toroidal graph).

This paper presents three of the most used map operations and their retro-pairs and their possible use in investigating π-electronic structure and stability of some fullerenes.

Leapfrog

Leapfrog *Le* is a composite operation,[12,17-20] which can be written as:

$$Le(M) = Du(P_3(M)) = Tr(Du(M)) \quad (4)$$

A sequence of stellation-dualization P_3-*Du* rotates the parent *s*-gonal faces by π/s. Leapfrog operation is illustrated, for a pentagonal face, in Figure 1.

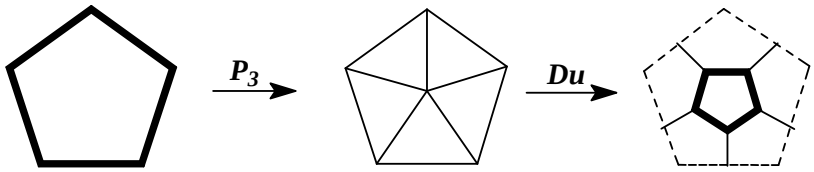

Figure 1.
Le operation on a pentagonal face

The map transformed parameters are as follows:

Le(*M*): $$v = s_0 f_0 = d_0 v_0 \; ; \; e = 3e_0 \; ; \; f = v_0 + f_0 \quad (5)$$

Retro-leapfrog *RLe* operation is based on the following sequence:

$$RLe = -P_3(Du(Le(M))) \quad (6)$$

performed by cutting all vertices in the dual (of leapfrogged map) with degree lower than the maximal one (Figure 2). As a 3D realization, *RLe* is illustrated in Figure 3.

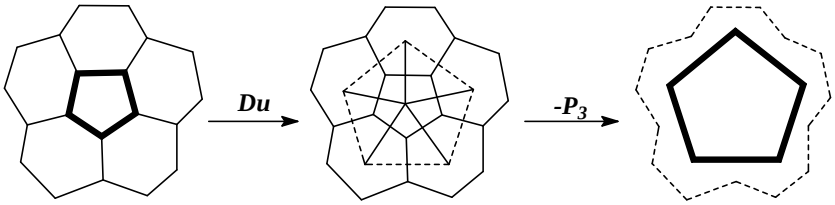

Figure 2.
Retro-Leapfrog *RLe* operation on a pentagonal face

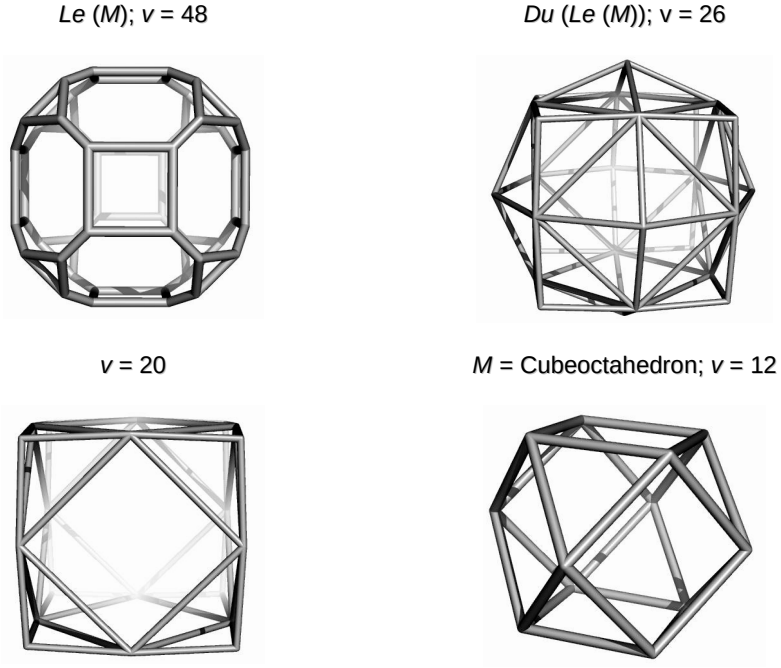

Figure 3.
Retro-Leapfrog operation

Quadrupling

Quadrupling *Q* is another composite operation, achieved by the sequence:[12]

$$Q(M) = -E(Tr_{P_3}(P_3(M))) \tag{7}$$

where *-E* means the (old) edge deletion (dashed lines, in Figure 4) of the truncation Tr_{P3} of each central vertex of P_3 capping.

The complete transformed parameters are:

$Q(M)$: $$v = (d_0 + 1)v_0;\ e = 4e_0;\ f = f_0 + e_0 \quad (8)$$

Q operation leaves unchanged the initial orientation of the polygonal faces.

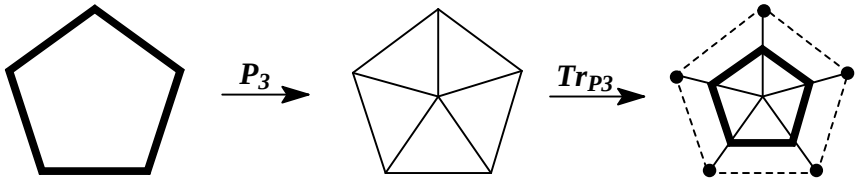

Figure 4.
Q operation on a pentagonal face

Retro-quadrupling *RQ* operation is based on the sequence:

$$RQ(M) = E(-Tr_{P_3}(P_3(M))) \quad (9)$$

performed by adding new edges parallel to the boundary edges of the parent faces (Figure 5) and deletion of these faces. As a 3D realization, *RQ* is illustrated in Figure 6.

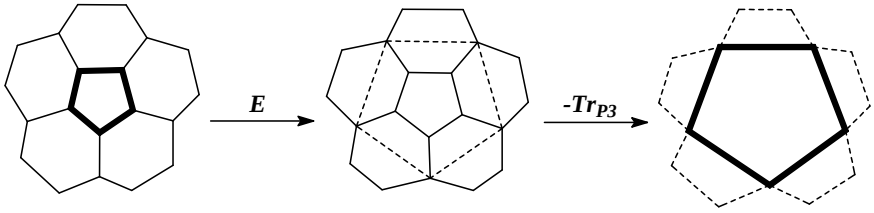

Figure 5.
Retro-Quadrupling *RQ* operation on a pentagonal face

Figure 6.
Retro-Quadrupling operation

Capra

Capra *Ca* - the goat, is the Romanian corresponding of the *leapfrog* English children game. It is a composite operation,[13,21,22] necessarily coming from the Goldberg's[23] multiplying factor *m*:

$$m = (a^2 + ab + b^2);\ a \geq b;\ a + b > 0 \tag{10}$$

that predicts *m* (in a 3-valent map) as follows: *Le*, (1, 1), *m*= 3; *Q*, (2, 0), *m*= 4; *Ca*, (2, 1), *m*= 7. By this reason, *Le* is also called *tripling* and *Ca septupling*. *Q* was originally called *chamfering*.[23]

Capra is achieved by truncating the vertex located in the center of parent faces of a pentangulation P_5 transform (Figure 7). Note that, P_5 involves an E_2 (*i.e*., edge trisection). This operation results in a map that preserves the original vertices while the parent *s*-gonal faces are twisted by $\pi/(3/2)s$.

The transformation can be written as:

$$Ca(M) = Tr_{P_5}(P_5(M)) \tag{11}$$

with Tr_{P5} meaning the truncation of each vertex where P_5 capping faces of a parent face are incident. *Ca* insulates any face of *M* by its own hexagons, which are not shared with any old face (in contrast to *Le* or *Q*).

The complete transformed parameters by *Ca* are:

Ca(*M*): $$v_1 = v_0 + 2e_0 + s_0 f_0 = (2d_0 + 1)v_0;\ e_1 = 7e_0;\ f_1 = s_0 f_0 + f_0 \tag{12}$$

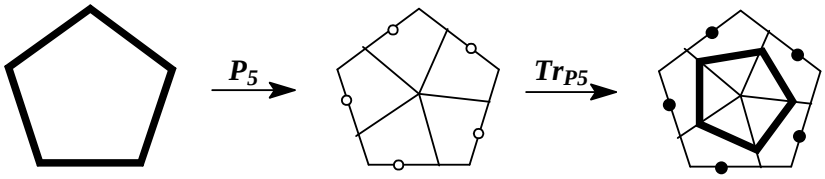

Figure 7.
Ca operation on a pentagonal face

Retro-capra *RCa* operation is achieved by the sequence:

$$RCa(M) = -E_2(-Tr_{P5}(M)) \tag{9}$$

In words, delete the smallest faces of the actual map and continue with - E_2 (Figure 8). As a 3D realization, *RCa* is illustrated in Figure 9.

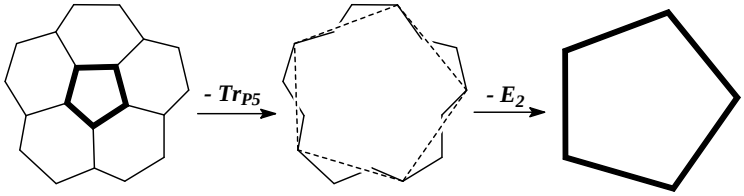

Figure 8.
Retro-Capra R*Ca* operation on a pentagonal face

C_{140} - Tr_{P_5} (*D*); *N* = 80

Figure 9.
Retro-Capra operation

Discussion

The properly closed PC shell *fz*-tubulenes[24] (*i.e.*, cages having fullerene halves as caps for a "zig-zag" tube) obey a true leapfrog rule, but written for zig-zag cylinders, Z-LER: $N = 13k + 3km;\ k = 4,6,8,...;\ m = 1,2,...$.

A closed structure of π-electronic shell was found[25] to be a general property of cages derived by *Le* operation from smaller objects. We just confirmed this hypothesis by drawing the parent small cages (with non-trivalent atoms corresponding to the polar rings different from hexagon) by the retro *RLe* operation (Figure 10).

The closed shell π-electronic structure of these cages is reflected in the HOMO-LUMO gap, in both simple Hűckel level of theory and PM3 calculations (Table). The heat of formation HF values of the cages with the polar ring between k = 6 and 10 are pretty low (note that the PM3 energy for C_{60} is about 13.5 kcal/mol).

Observe the Hückel gaps close in LUMO being NBO (for 0(mod(k,4) cages, Table, entries 1 and 3). Also note the cap $C_{13k/2(k\,(56)^{k/2}(665)^{k/2}-Z[3k,0])}$; k = 6, is C_{60} deducible, by taking a hexagon as the polar ring. The subscripts name is given in terms of the spiral code.[24]

The strain energy SE, in terms of POAV1 theory,[26-29] decreases as the cage size increases (Table). For comparison, SE for C_{60} is about 8.26 kcal/mol.

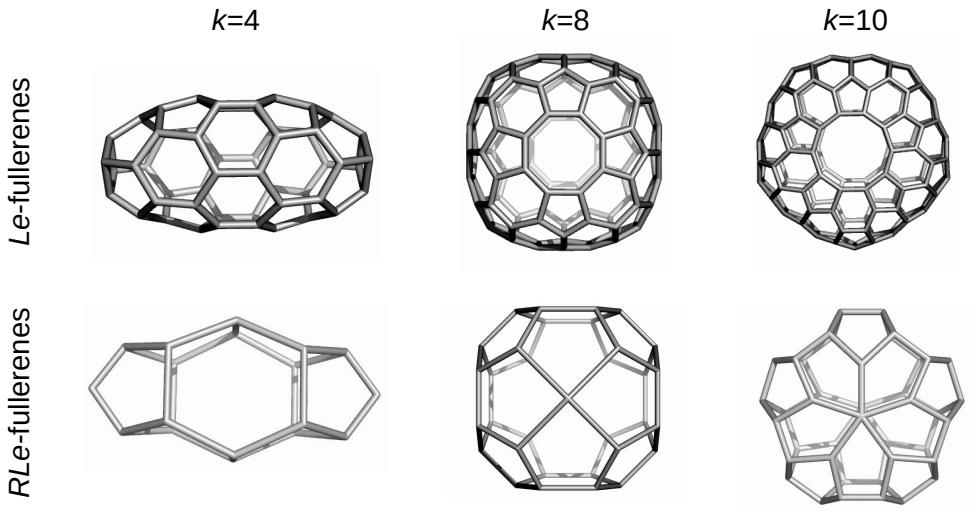

Figure 10.

*Fullerene*s of general formula $C_{N(k\,(56)^{k/2}(665)^{k/2}-Z[3k,0])}$

Table.

Data for *fz*-tubulenes $C_{N(k\,(56)^{k/2}(665)^{k/2}-Z[3k,0])}$

	Cage *k*	*v*	Sym.	PM3 HF/at. (kcal/mol)	PM3 Gap (eV)	SE POAV1 (kcal/mol)	Hűckel Data HOMO	LUMO	Gap (|β| units)	Shell
1	4	52	D_{2h}	21.585	5.533	12.526	0.256	0	0.256	PC
2	6	78	C_{3h}	12.294	6.083	6.794	0.516	-0.118	0.634	PC
3	8	104	C_{4h}	11.453	5.730	5.218	0.256	0	0.256	PC
4	10	130	C_{5h}	12.518	5.998	4.999	0.458	-0.087	0.545	PC

It is quite strange that, for the cage with *k*=8, both the heat of formation HF (Table, row 3) and strain energy SE (in POAV1 terms, Table 2, row 3, column 2) data show lower values than for the cage with *k*=6, suggesting a higher stability for the former. However, the HOMO-LUMO gap for the cage with *k*=8 is lower than for the cage with *k*=6, both at Hűckel and PM3 level of theory (Table), indicating a kinetic instability, which is supplementary supported by the non-bonding character of the LUMO orbital, in Hűckel theory.

Conclusions

Operations on maps and their retro-transformations, particularly those of the most used leapfrog, chamfering and capra operations, proved to be useful in investigating the properties of fullerenes, particularly their π-electronic structure and stability. Thus, a series of Z-LER cages proved to be leapfrog transforms of smaller cages. Among these, the cage with *k* = 6, was described as the most stable among the discussed structures, which indeed, corresponds to the isolated fullerene C_{78}.

REFERENCES

1. H. Zorc, Lj. P. Tolić, S. Martinović and D. Srzić, *Fuller*. *Sci*. *Technol*. **1994**, *2*, 471-480.
2. F. Diedrich and C. Thilgen, *Science*, **1996**, *271*, 317-323.
3. I. S. Neretin, K. A. Lyssenko, M. Yu. Antipin, Yu. L. Slovokhotov, O. V. Boltalina, P. A. Troshin, A. Yu. Lukonin, L. N. Sidorov and R. Taylor, *Angew*. *Chem*. *Int*. *Ed*. **2000**, *39*, 3273-3276.
4. W. Qian and Y. Rubin, *Angew*. *Chem*. *Int*. *Ed*. **2000**, *39*, 3133-3137.
5. K. Lee, Ch. H. Lee, H. Song, J. T. Park, H. Y. Chang and M.-G. Choi, *Angew*. *Chem*. *Int*. *Ed*. **2000**, *39*, 1801-1804.

6. T. F. Fässler, R. Hoffmann, S. Hoffmann and M. Wörle, *Angew. Chem. Int. Ed.* **2000**, *39*, 2091-2094.
7. J.-Y. Zheng, Sh. Noguchi, K. Miyauchi, M Hamada, K. Kinbara and K. Saigo, *Fullerene Sci. Technol.* **2001**, *9*, 467-475.
8. A. L. Mackay and H. Terrones, *Nature*, **1991**, *352*, 762.
9. Gao, Y. D.; Herndon, W. C. *J. Amer. Chem. Soc.* **1993**, *115*, 8459-8460
10. P. W. Fowler, T. Heine, D. E. Manolopoulos, D. Mitchell, G. Orlandini, R. Schmidt, G. Seiferth and F. Zerbetto, *J. Phys. Chem.* **1996**, *100*, 6984-6991.
11. T. Pisanski and M. Randić, in: Geometry at work: a collection of papers showing applications of Geometry (Gorini, C. A., Ed.) *Math. Assoc. Amer.*, **2000, 53**, 174-194.
12. M. V. Diudea, P. E. John, A. Graovac, M. Primorac, and T. Pisanski, *Croat. Chem. Acta*, **2003**, **76**, 153-159.
13. M. V. Diudea, *Forma* (Tokyo), **2004**, **19**, 131-163.
14. L. Euler, *Acad. Sci. I. Petropolitanae* **1736**, *8*, 128-140.
15. L. Euler, *Novi Comment. Acad. Sci. I. Petropolitanae*, **1758**, **4**, 109-160.
16. F. Harary, *Graph Theory*, Addison-Wesley, Reading, MA, **1969**.
17. V. Eberhard, Zur Morphologie der Polyeder, Leipzig,Teubner,**1891**.
18. P. W. Fowler, *Chem. Phys. Lett.* **1986**, *131*, 444-450**.**
19. P. W. Fowler and J. I. Steer, *J. Chem. Soc. Chem. Commun*. **1987**, 1403-1405.
20. J. R. Dias, *MATCH*,*Commun. Math. Comput. Chem.*, 1996, *33*, 57-85.
21. M. V. Diudea, *Studia Univ. "Babes-Bolyai"*, 2003, **48**(2), 3-16.
22. M. V. Diudea, *J. Chem. Inf. Model.,* **2005**, *45,* 1002-1009.
23. M. Goldberg, *Tôhoku Math. J.* **1937**, *43*, 104-108.
24. M. V. Diudea, *Phys. Chem., Chem. Phys.***, 2004**, *6*, 332-339.
25. P. W. Fowler and T. Pisanski, *J. Chem. Soc. Faraday Trans.* **1994**, *90*, 2865-2871.
26. R.C. Haddon, *J. Am. Chem. Soc.* **1987**, *109*, 1676-1685.
27. R.C. Haddon, *J. Am. Chem. Soc.* **1990**, *112*, 3385- 3389.
28. R.C. Haddon, *J. Am. Chem. Soc.* **1997,** *119,* 1797-1798.
29. R.C. Haddon and S.-Y. Chow, *J. Am. Chem. Soc.* **1998**, *120*, 10494-10496.

STUDIA UNIVERSITATIS BABEŞ-BOLYAI, CHEMIA, LI, 1, 2006

PSEUDOCERAMIDES AND THEIR DERIVATIVES. 3. BENZYLIDENE ACETALS OF N-ACETYL-N-METHYL GLUCAMINE – PRELIMINARY STUDY.

CRISTIAN NEANU[1], FRANCISC PETER[2], IOANA ŞIŞU[1], CAROL CSUNDERLIK[2] AND EUGEN ŞIŞU[1]*

ABSTRACT. Acetalization of N-acetyl-N-methyl-1-amino-1-deoxy-D-glucitol with 2.5 equivalents of 1,1-dimethoxybenzaldehide in N,N-dimethylformamide at reflux temperature with camphorsulphonic acid as catalyst yielded 5,6-O-benzylidene-N-acetyl-N-methyl-glucamine as the major product. 2,3:4,6-di-O-benzylidene-N-acetyl-N-methyl-glucamine, 4,6-O-benzylidene-N-acetyl-N-methyl-glucamine and a mixture of 2,3:5,6- and 3,4:5,6-di-O-benzylidene-N-acetyl-N-methyl-glucamine byproducts have been also isolated. Separation and purification conditions of these new products are described. The structures have been assigned by ^{13}C-NMR and MS-EI.

Keywords: aminoalditol acetals, pseudoceramide, flash chromatography, 5,6-O-benzylidene-N-acetyl-N-methyl-glucamine, 2,3:4,6-di-O-benzylidene-N-acetyl-N-methyl-glucamine, 4,6-O-benzylidene-N-acetyl-N-methyl-glucamine, 2,3:5,6-di-O-benzylidene-N-acetyl-N-methyl-glucamine, 3,4:5,6-di-O-benzylidene-N-acetyl-N-methyl-glucamine.

Introduction

The development of new biocompatible and biodegradable surfactants based on natural feedstocks is subject of an increasing scientific and industrial interest [1]. Aminoalditol derivatives represent a class of compounds that can be used both as surfactants as well as pseudoceramides [2, 3]. The use of N-methyl-glucamine (an accessible and cheap aminoalditol) allows two strategies in order to obtain a compound with amphiphatic character that could exhibit ceramide properties:

a) attachment of a nonpolar tail to the amine function followed by the attachment of a second nonpolar tail to the alcohol function

b) creation of an amide bond at the amine function (by acylation) followed by the attachment of two nonpolar tails at the alcohol functions.

[1] Academia Română - Institutul de Chimie Timişoara, Bd. Mihai Viteazul 24, 300223 Timişoara, România

[2] „Politehnica" University of Timişoara, Faculty of Industrial Chemistry and Environmental Engineering, C. Telbisz 6, 300001 Timişoara, România

* E-mail: esisu@mail.dnttm.ro; esisu@acad-icht.tm.edu.ro

These two options can be realized with biocatalysts, using the catalytic capacity and the specificity of lipases [4, 5]. A new approach in the synthesis of these compounds starts from N-acetyl-N-methyl glucamine and consists in the enzymatic attachment of fatty acids by esterification or transesterification reactions catalyzed by lipases [6]. The reaction monitorization can easily performed by HPLC or GC, whether mono- and di-esters of N-acetyl-N-methyl-glucamine are available as standard compounds. The selective esterification of each alcohol function in the aminoalditol requires acetal derivatives as intermediates. This paper presents the results of acetalization of N-acetyl-N-methyl-1-amino-1-deoxy-D-glucitol with dimethoxy benzaldehyde in acid catalysis.

Results and Discussion

The condensation of aldehydes and ketones with alcohols is one of the first reactions studied in organic chemistry. E. Fischer obtained in 1895 for the first time, fructose acetals and then glucose acetals, in acid catalysis [7]. Acetals can be obtained in acidic, basic or neutral conditions or using other methods [8]. A series of well documented reviews present results of the acetalization reaction for alditols [9], aldoses, aldosides [10,11] and ketoses [12] but not of aminoalditols.

The acetalization of N-acetyl-N-methyl-glucamine was performed by transacetalization reaction in acidic media using dimethoxy benzaldehyde (see the experimental part). The reaction was monitorized by TLC.and the inspection of the plate showed 5 spots at the following Rf values: spot 1 (0.73), spot 2 (0.67), spot 3 (0.55), spot 4 (0.24) and spot 5 (0.15) (AcOEt :MeOH = 90:10).

Considering the TLC plate polarity and the eluent polarity we used, the spots on the TLC plate can be assigned as follows: spots 1, 2 and 3 for di-benzylidene derivatives and spots 4 and 5 for mono-benzylidene derivatives. After separation by flash chromatography, the compounds have been analyzed by MS-EI. Spots 1, 2 and 3 are di-benzylidene derivatives and have the molecular peak at m/z= 413($M^{+\cdot}$) for a 22 eV ionization energy, thus confirming the proposed assignments. Spot 1 was characterized as acetylated derivative, having the molecular peak at m/z= 455 ($M^{+\cdot}$), 24 eV.

The analysis of ^{1}H-NMR spectra is difficult because the 8 protons in the linear side chain are localized in the 3.5-4.3 ppm interval and the coexistence of cis-trans conformers of the amide bond (Figure 1) determines the doubling of the total number of signals.

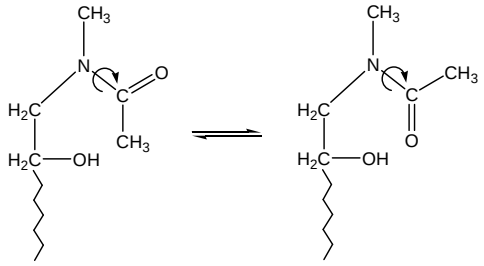

trans (t) cis (c)

Figure 1.
Cis-trans conformers of N-acetyl-N-metyl-glucamine and derivatives

The ^{13}C-NMR spectroscopy offers valuable data concerning the nature of the acetal rings as well as their positions [13, 14]. Buchanan and coworkers [15, 16] observed that the chemical shift of the acetal carbon atom is strongly influenced by the size of the ring and is situated in the following intervals:

108.1-115.7 ppm for 1,3-dioxolane rings
97.1-101.1 ppm for 1,3–dioxane rings
100.8-102.3 ppm for 1,3-dioxepane rings

The ^{13}C-NMR spectra analysis of spot 1 show 8 signals in the169.4 - 171.2 ppm interval, which indicate the existence of 2 isomers, each one with 2 conformers. The 4 signals situated in the 103.7 – 104.2 ppm interval correspond to 4 acetalic C atoms from 1,3-dioxolanic rings and belong to 2 dibenzylidene isomers, both with 2 conformers. These chemical shifts are deshielded (they are present at lower ppm values: 103.7 - 104.2 ppm) comparing with literature data (108.1 - 115.7 ppm for 3-dioxolanic rings [15, 16]) because of the influence of Ph. Hereby the 2 isomers from spot 1 can be only the compounds **2** and **3** from Figure 2: 2,3:5,6-di-O-benzylidene-N-acetyl-N-methyl-glucosamine and 3,4:5,6-di-O-benzylidene-N-acetyl-N-methyl-glucosamine. Assigning position 5,6 to one of the benzylidene groups will be explained below.

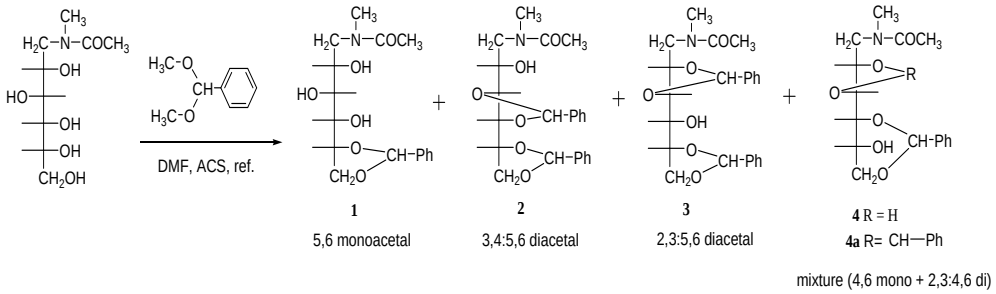

Figure 2.
Mono- and diacetal reaction products

^{13}C-NMR spectra analysis of spot 2 relieves 4 signals:

- at 103.7 and 104.5 ppm the signals correspond to an acetalic C from 1,3-dioxolane ring (the signals are shifted to a higher value of the magnetic field because of the influence of the phenyl group comparing with the literature data [15, 16])

- at 100.7 and 101.0 ppm the signals correspond to an acetalic C from 1,3-dioxane ring.

Admitting that the initial and kinetically more stable 5, 6-benzylidene derivative is stabilized during time to the thermodynamically more stable 4,6-benzylidene isomer, results that spot 2 can be assigned solely to compound **4a** (Figure 2) namely 2,3:4,6-di-O-benzylidene-N-acetyl-N-methyl-glucamine. The 3,5:4,6 and 2,5:4,6 isomers are excluded because the chemical shifts of acetalic C at 105.0 and 104.1 ppm are clearly assigned to a dioxolanic ring.

Although isopropyliden and cyclohexyliden aminoalditol acetals have been already described [20, 21] there are no data about benzylidene acetals, consequently the position of benzylidene group had to be established. The analysis of ^{1}H-NMR spectra is difficult and doesn't give any valuable information. To spread the hydrogen atom attached on carbon atom with free hydroxyl groups from compound of spot 4 the free hydroxyl groups were derivatized by acetilation and than analysed by ^{1}H-NMR.

The type of ring was deduced from chemical shifts of the acetalic C atom from the ^{13}C-NMR spectra. There are 2 signals at 103.5 ppm and 103.9 ppm which indicate a 1,3-dioxolane ring and thereby the spot 4 correspond to compound **1** (Figure 2)**:** 5,6-O-benzyliden-N-acetyl-N-methyl-glucamine. The position of the 1,3-dioxolane ring on the linear side chain was determined by NMR experiments: monodimesional APT and bidimensional COSY and HETCOR. The assignment of C atoms from the linear side chain was established by HETCOR and APT experiments only for C1 and C6.

The presence of cis-trans conformers was proved previously by our group [20, 21]. Obtaining mainly 5,6-O-acetals of N-acetyl-N-methyl-glucamine

is in agreement with the literature concerning kinetic acetalization of diethyl-dithioacetals of glucose, galactose and arabinose [17-19] and for isopropyliden and cyclohexyliden acetals of N-acetyl-N-methyl-glucosamine [20, 21].

The ^{13}C-NMR spectra analysis of spot 5 relieve the existence of 1,3-dioxane ring (100.4 and 100.5 ppm) and it was assigned to compound **4** from Figure 2 (4, 6-benzilidene isomer of N-acetyl-N-methyl-glucamine). The benzylation of compound **1** (spot 4) (NaH, BnBr) followed by hydrolysis of benzyliden acetal (I_2/MeOH) leads finally to 2,3,4-tri-O-benzyl-N-acetyl-N-methyl-glucozamine. This compound was also obtained from 5,6-isopropilydene-N-acetyl-N-methyl-glucozamine [21] and from 5,6-cyclohexylidene-N-acetyl-N-methyl-glucozamine[22], their structure were previously established [21]. These compounds were obtained by the same reaction path, the obtained compounds presenting identical IR spectra. Therefore the assigning structure of compound **4** (spot 5) were confirmed also by chemical way.

The procedure and the complete description of the ^{13}C-NMR spectra are presented in the experimental part. The description of structure was done for both conformers together and the notation used is: (cis, trans), meaning that both signals are present and also that the number of signals is double.

Equipment and Methods

NMR spectra were recorded on a Varian Gemini 300 MHz apparatus against the line of the solvent ($CDCl_3$). Chemical shifts are expressed in ppm. Mass spectra were recorded on a Varian Finnigan Mat 212 mass spectrometer. TLC analysis was performed on Kieselgel Merck plates with fluorescence indicator. Separation by flash chromatography was performed on 220-400 mesh silica (Aldrich). Visualization of the chromatograms was accomplished with UV lamp and by developing with a 20% H_2SO_4 in ethanol solution, then heating the plate at 120ºC. Anhydrous solvents have been used.

Experimental

2 g (8.4 mmol) N-acetyl-N-methyl-glucamine is solved in 5 ml DMF (kept on 4Å molecular sieves) and a catalytic amount of camphorsulphonic acid is added under stirring. The reaction mixture is cooled to 0ºC and 3.6 ml (24 mmol) dimethoxy benzaldehyde are drop by drop added under argon atmosphere and stirring. The reaction mixture is stirring at reflux temperature (48 h) until TLC control (AcOEt:MeOH = 90:10) indicates the disappearance of the starting material. The reaction is stopped by adding 0.5 ml Et_3N and the solvents are vacuum distilled with toluene. The mixture is then separated and purified by flash chromatography (Table 1).

The 5,6-O-benzyliden-N-acethyl-N-methyl glucosamine was obtained in 52% yield. All products are as consistent clays at room temperature.

Table 1.
Flash chromatography and TLC separation and analysis conditions of the acetalization products

Spots separation	FC elution system	TLC control system
1+2+3 spots by 4+5 spots	Tol:AcOEt=22:78	AcOEt :MeOH=95:10
1+2 spots by spot 3	Tol:AcOEt=22:78	AcOEt :MeOH=95:10
spot 1 by spot 2	Tol:AcOEt=22:78	AcOEt :MeOH=95:10
spot 3 by spot 2	Tol:AcOEt=25:75	AcOEt :MeOH=95:5
spot 4 by spot 5	Tol:AcOEt=25:75	AcOEt :MeOH=95:5
spot 5 by 4+5 spots	Tol:AcOEt=25:75	AcOEt :MeOH=95:5

Spot 1: *2,3:5,6- di-O-benzylidene-(4-O-acetyl)-N-acetyl-N-methyl-glucosamine* + *3,4:5,6-di-O-benzylidene-(2-O-acetyl)-N-acetyl-N-methyl-glucosamine* (compounds **2** and **3**, Figure 2)
MS(EI), 22eV, (characterized as monoacetylated derivative $C_{25}H_{29}NO_7$) m/z= 455($M^{+\cdot}$)
^{13}CRMN (75MHz, $CDCl_3$)
171.25, 171.19, 170.82, 170.40, 169.96, 169.64, 169.52 (4C, 2X $\underline{C}H_3$-CO, (cis, trans), (the isomers 2 and 3))
137.34, 136.80 (4C, 2x $\underline{C}$ from Ph, (cis, trans), the isomers 2 and 3))
129.71, 129.66, 129.38, 129.28, 129.07, 128.34, 128.29, 128.20, 126.30, 126.21, 126.16, 126.09, (20C, 10x $\underline{C}$H from Ph, (cis, trans), the isomers 2 and 3))
104.20, 104.01, 103.90, 103.74, (4C, 2x $\underline{C}$H-Ph, (cis, trans), the isomers 2 and 3)),
77.42, 76.99, 76.57, 74.98, 74.37, 74.24, 70.33, 70.28, 70.20, 70.06, 69.88, 68.09, 68.03, (8C, $\underline{C}$2, $\underline{C}$3, $\underline{C}$4, $\underline{C}$5, (cis, trans), the isomers 2 and 3))
67.37, 67.25, 67.10, 66.59, (2C, $\underline{C}$6, (cis, trans), the isomers 2 and 3))
50.77, 50.45, (2C, $\underline{C}$1, (cis, trans), the isomers 2 and 3))
37.19, 37.07, 33.52, 33.41, (2C, $\underline{C}H_3$-N, (cis, trans), the isomers 2 and 3))
21.54, 21.50, 21.10, 20.75, 20.71, 20.67, 20.58, 20.53, 20.45, 20.38, (4C, $\underline{C}H_3$-CO, (cis, trans) the isomers 2 and 3))

Spot 2: *2,3 :4 6-di-O-benzylidene-N-acetyl-N-methyl-glucosamine* (compound **4a**, Figure 2)
MS(EI), 22eV, ($C_{23}H_{27}NO_6$), m/z= 413($M^{+\cdot}$)
^{13}CRMN (75MHz, $CDCl_3$)
171.97, 171.46, (1C, N-$\underline{C}$=O, (cis, trans))
137.97, 137.90, (2C, $\underline{C}$ from Ph, (cis, trans))
129.61, 129.57, 129.41, 129.35, 129.09, 128.99, 128.38, 128.28, 128.27, 128.17, 126.71, 126.61, 126.55, 126.43, 126.34, 125.92, (10C, $\underline{C}$H from Ph, (cis, trans))
104.52, 104.33, 103.70, (1C, $\underline{C}$H-Ph, (cis, trans)), from dioxolane ring
101.02, 100.90, 100.76, (1C, $\underline{C}$H-Ph, (cis, trans)), from dioxane ring
78.69-68.56 (multiple signals), (4C, $\underline{C}$2, $\underline{C}$3, $\underline{C}$4, $\underline{C}$5, (cis, trans))
67.91, 67.55, (1C, $\underline{C}$6, (cis, trans))
49.02, 48.91, (1C, $\underline{C}$1, (cis, trans))
38.42, 38.16, (1C, $\underline{C}H_3$-N, (cis, trans))
21.75, 21.63, (1C, $\underline{C}H_3$-CO, (cis, trans))

Spot 4: *5, 6-O-benzylidene-N-acetyl-N-methyl-glucosamine* (compound **1**, Figure 2)
MS(EI), (24eV) ($C_{16}H_{23}NO_6$), m/z=325, ($M^{+\cdot}$)
^{13}CRMN (75MHz, $CDCl_3$)
173.06, (1C, N-C=O, (cis, trans))
137.87, 137.29, (1C, C from Ph, (cis, trans))
129.28, 129.13, 128.26, 128.19, 126.54, 126.44, 126.33, 126.31, 126.03, (5C, CH from Ph, (cis, trans))
103.98, 103.57, (1C, CH-Ph, (cis, trans))
74.02, 73.60, 72.47, 72.43, 70.09, 69.74, 69.67, 68.17, (4C, C2, C3, C4, C5, (cis, trans))
68.71, (1C, C6, (cis, trans))
53.77, 51.63, (1C, C1, (cis, trans))
38.11, 37.95, (1C, CH_3-N, (cis, trans))
21.63, 21.58, (1C, CH_3-CO, (cis, trans))

Spot 5: *4, 6-O-benzylidene-N-acetyl-N-methyl-glucosamine* (compound **4,** Figure 2)
MS(EI), (24 eV) ($C_{16}H_{23}NO_6$), m/z=325, ($M^{+\cdot}$)
^{13}CRMN (75MHz, $CDCl_3$)
172.18, (1C, N-C=O, (cis, trans))
137.73, 137.33, (1C, C from Ph, (cis, trans))
128.38, 128.27, 128.20, 126.75, 126.67, 126.56, 126.42, 126.23, 125.97, (5C, CH from Ph, (cis, trans))
100.59, 100.47, (1C, CH-Ph, (cis, trans))
79.53, 79.09, 78.40, 78.34, 78.04, 72.38, 72.24, 70.13, 69.57, 69.30, (4C, C2, C3, C4, C5, (cis, trans))
63.44, 62.71, (1C, C6, (cis, trans))
49.50, 49.11, (1C, C1, (cis, trans))
38.47, 38.41, (1C, CH_3-N, (cis, trans))
21.72, 21.59, (1C, CH_3-CO, (cis, trans))

Conclusions

The reaction between N-acetyl-N-methyl-glucamine and dimethoxy benzaldehyde in acid catalysis (camphorsulphonic acid) gives mainly the 5,6-monobenzylidene acetal (compound **1**, Figure 2) with 52% yield. The new compounds: 5,6-O-benzylidene-N-acetyl-N-methyl-glucosamin (as main product), 2,3:4,6-di-O-benzylidene-N-acetyl-N-methyl-glucosamine, 4,6-O-benzylidene-N-acetyl-N-methyl-glucosamine and a mixture of 2,3:5,6- with 3,4:5,6-di-O-benzylidene-N-acetyl-N-methyl-glucosamine (not previously described in the literature), were characterized by MS-EI, ^{1}H-NMR, and ^{13}C-NMR. The identity of products was confirmed by MS and the ring type was established by ^{13}C-NMR, COSY and HETCOR experiments. The careful study of the spectra indicates the existence of cis-trans conformers. The existence of conformers makes difficult their characterization by ^{1}H-NMR, therefore they were characterized mainly by ^{13}C-RMN. The optimal conditions for reaction monitorization and for flash chromatography separation and purification have been also established.

REFERENCES

1. K. Hill, K. O. Rhode, *Fett/Lipid*, **1999**, *101*, 1999, 25-33.
2. T. Maugard, M. Remaud-Simeon, D. Petre, P. Monsan, *Biocatalysis Biotransform.,* **1998,** *16*, 383-393.
3. H. Möller, W. Knörr, M. Weuthen, B. Guckenbiehl, A.Wachter, *Fett/Lipid*, **1997**, *99*, 120-129.
4. M. Woudenberg-van Oosterom, F. van Rantwijk, R.A. Sheldon, *Fett/Lipid*, **1996**, *98*, 390-393.
5. T. Maugard, M. Remaud-Simeon, D. Petre, P. Monsan, *J. Mol. Cat. B: Enzymatic*, **1998**, *5*, 13-17.
6. F. Peter, A. Mirescu, E. A. Oostveen, J. van Haveren, G. Preda, "The IVth International Symposium of Interdisciplinary Regional Research", Timişoara, **2000**, 711-718.
7. E.Fischer , Ber., **1895**, *28*, 1145.
8. P. Calinaud, J. Gelas, "Preparative Carbohydrate Chemistry" (S. Hanessian, ed.), Marcel Dekker, New York, **1997**, 3.
9. S. A. Barker, E. J. Bourne, *Adv. Carbohydr. Chem*., **1952**, *7***,** 1952, 137-187
10. A. N. de Belder, *Adv. Carbohydr. Chem*., **1965**, *20*, 219-301
11. A. N. de Belder, *Adv. Carbohydr. Chem. Biochem*., **1977**, *34*, 179-209
12. J.Sugihara, *Adv. Carbohydr. Chem. Biochem*., **1953**, *8*, 1-44
13. I. J. Burden, J. F. Stoddart, *J. Chem. Soc., Perkin Trans.I*, **1975**, 675-682.
14. J. P. Clayton, R. S. Oliver, N. H. Rogers, T. J. King, *J. Chem. Soc., Perkin Trans. I*, **1979**, 838-846.
15. J. G. Buchanan, M. E. Chacon-Fuertes, A. R. Edgar, S. M. Moorhouse, D. I. Rawson, R. H. Wightman, *Tetrahedron Lett*., **1980**, *21*, 1793-1796.
16. J. G. Buchanan, A. R. Edgar, D. I. Rawson, P. Shahidi, R. H. Wightman, *Carbohydr. Res*., **1982,** *100*, 75-86.
17. G. W. Schnarr, D. M. Vyas, W. A. Szarek, *J. Chem. Soc., Perkin Trans. I*, **1979**, 496-503.
18. 18. D. Horton, J. D. Wander, *Carbohydr. Res.,* **1968**, *10***,** 279-288.
19. S. J. Angyal, R. Lefur, *Carbohydr. Res.,* **1980**, *84*, 201-209.
20. E. Şişu, C. Neanu, M. Căproiu, I. Şişu, A. Lascu, F. Peter, V. Rusu, C. Csunderlik , Rev. Chim. (Bucharest), 2002, 53, 750-754.
21. E. Şişu, C. Neanu, M. Căproiu, I. Şişu, A. Lascu, F. Peter, V. Rusu, C. Csunderlik, *Rev. Chim. (Bucharest),* 2002, *53*, 815-818.

STUDIA UNIVERSITATIS BABEŞ-BOLYAI, CHEMIA, LI, 1, 2006

THE INHIBITORY EFFECT OF THE ATENOLOL UPON THE ENZYME CATALYZED HYDROGEN PEROXIDE DECOMPOSITION

FLORINA POGACEAN, IOAN BALDEA* AND FLORIN TURBAT

ABSTRACT. The reaction of decomposition of hydrogen peroxide in the presence of catalase has been investigated by means of a Clark oxygen sensor, in the presence and absence of various concentrations of Atenolol – a β-blocker drug - having an inhibiting role. The Michaelis – Menten kinetic parameters have been determined from Lineweaver-Burk plots. The inhibition pattern we have deduced, suggested by the Lineweaver - Burk plots, corresponds to a fully mixed inhibition mechanism. Inhibition constants K_I and K_I' were determined. A kinetic method for the determination of Atenolol has been suggested.

Keywords: Atenolol, Catalase, Hydrogen peroxide decomposition, Inhibition mechanism, Kinetic methods.

Introduction

Catalase, an oxidoreductase EC 1.11.1.6, is a tetrameric haemin-enzyme consisting of a 4 identical tetrahedrally arranged subunits of 60000 g/mol each [1]. Catalase is widely distributed in nature It is found in all aerobic microorganism, in plant and animal cell [2]. The enzyme, when located in organelles, acts as a regulator of the H_2O_2 level, while in erythrocytes, catalase provides) a protection for hemoglobin against the oxidizing agents like H_2O_2 together with gluthathione peroxidase [3].

The enzyme - catalyzed reaction:

$$2H_2O_2 \xrightarrow{catalase} 2H_2O + O_2 \quad (1)$$

has been the subject of extensive investigations, both in regard to the kinetics and to the mechanism of the decomposition [4, 5, 6, 7, 8].

Similar reaction were also observed for other organic peroxides [9, 10] Well-known inhibitors of these reactions are ions like azide, cyanide and fluoride [11, 12, 13], or some organic compounds compounds like 3-amino-1,2,4-triazole [14] and atenolol[15].

Atenolol is a cardioselective β-adrenoceptor blocking agent (β-blocker).

* *Department of Chemistry and Chemical Engineering, Babes-Bolyai* University of Cluj, 11 Arany Janos Str.,Cluj-Napoca 400028

Atenolol ($C_{14}H_{22}N_2O_3$) according to European Pharmacopeia (±)-2-[4-(2-hydroxi-3-izopropylaminopropoxil)]-phenyl]-acetamide[16]

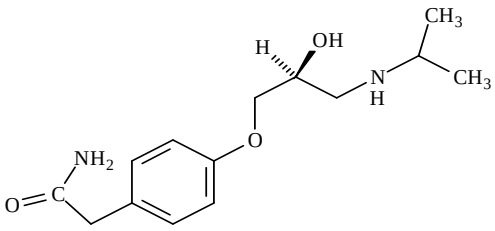

Atenolol has a chiral center, and is clinically used as a racemate [15]. B-adrenoceptor antagonists are a group of compounds that competitively inhibit the effects of catecholamines at β- adrenergic receptors [17]. These agents are used widely in clinical medicine for the treatment of varios deseases including hypertension, angina pectoris [18] cardiac arrythmias, hypothyroidism and glaucoma.

The main aim of this paper is the description of the inhibition mechanism. It would permit to develop a kinetic method of the determination of the drug Atenolol in very low concentration, based on the inhibitory effect on the rate of hydrogen peroxide decomposition.

Experimental

Equipment. The measurements were undertaken with a Clark oxygen sensor, attached to a Multiline P4 multimeter with automatic data acquisition on a PC. The sensors cover a measuring range from 0 up to 19.99 mg/L for the dissolved oxygen, with a resolution of 0.01 mg/L and an accuracy of ±0.5% from 5.30 ℃. All experiments were performed in a v essel provided with a water jacket. The temperature was maintained constant at 20±0.1 ℃, by means of a Falc 90 recirculatory water bath. The reaction mixtures were stirred with a magnetic stirrer, always with the same frequency.

Reagents and Solutions. We used bacterial catalase from *Micrococcus Lysodeikticus* 176340 U/ml (where the enzyme unit 1U is the amount of enzyme needed to transform 1 μmol of the substrate within 1 min, under standard conditions), from FLUKA with a purity index of 0.85, which came from the ratio of absorbances at 405 nm and 280 nm, $A_{405}/_{A280.}$

The molar concentration of catalase was determined spectrophotometrically at 407 nm, where the extinction coefficient is known to be $4x10^5$ mol^{-1} dm^3 cm^{-1} [19].

All the other reagents were of analytical reagent grade. The solutions were prepared with de-ionized, four-times distilled water in order to avoid the interference of heavy metals. Stock solutions of catalase ($9x10^{-10}$

mol/L), H_2O_2 (4.9 x 10^{-2} mol/L) and atenolol (10^{-5} mol/L) in phosphate buffer of pH=7.0 were freshly prepared before each set of experiments. Hydrogen peroxide has been standardized against potassium permanganate in acidic media.

Procedure

The reaction mixture of 10 mL volume was prepared directly in the reaction vessel connected to a thermostate, where the solutions of the reagents were kept. Measured volumes of buffer and atenolol stock solution were placed in the vessel, and the change in the concentration of oxygen was monitored while the mixture was continuously stirred. The oxygen concentration became constant after about 50 s, when a known volume of H_2O_2 stock solution was added to the mixture. After about 50 s the concentration of oxygen reached a constant value again, so that the catalyzed reaction was started by the injection of 2 ml of the stock solution of the enzyme. A typical oxygen concentration versus time curve obtained by monitoring the reaction with a Clark sensor is presented in Fig. 1.

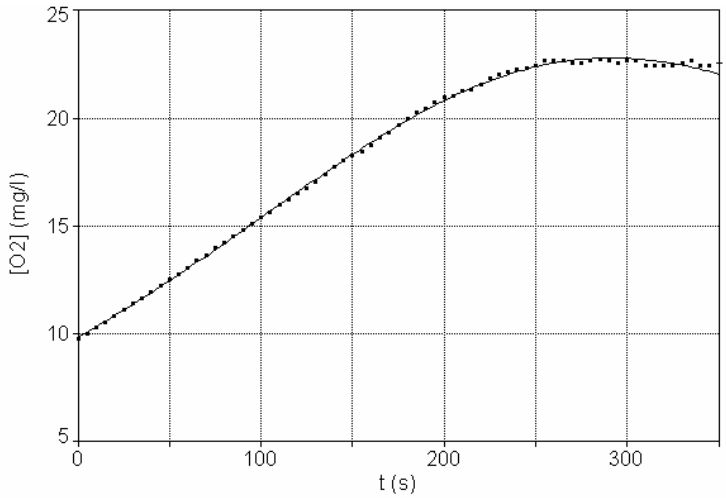

Fig. 1.
A typical curve for O_2 evolution, recorded with the Clark sensor in the reaction mixture pH=7 at 20^0C

The rate has been measured after the introduction of the enzyme solution into the mixture as the slope of the oxygen concentration increase with time. Only the starting period, within 25 – 30 % of reaction, with a linear dependence has been considered. The degree of H_2O_2 transformation was calculated from the experimental measured oxygen concentration as

$$X = \frac{2[O_2]_t - [O_2]_0}{[H_2O_2]_0} \quad (1)$$

where $[O_2]_t$ is the actual concentration of O_2, and $[O_2]_0$ is the constant value of $[O_2]$ obtained after the addition and consumption of all amount of H_2O_2.

Results and Discussion

A large amount of information is available in literature about the kinetics and the mechanism [5, 20- 22] of the reaction in the absence of inhibitor

The initial reaction rates, r_0, were determined from the slopes of the early part of the O_2 evolution curves, after catalase addition. Although the catalytic cycle seems to be quite complicate [23] because of the various oxidation states of Fe in heme, our data of initial rates fitted well to Michaelis-Menten equation [24]

$$r_0 = \frac{k[E_0][S]}{K_M + [S]} = \frac{r_{max}[S]}{K_M + [S]} \quad (2)$$

where $[E]_0$ and [S] stand for the initial concentration of the enzyme and for the substrate concentration respectively, K_M and r_{max} are the Michaelis-Menten parameters, and k is the rate constant of breakdown of the enzyme substrate complex to the product. This equation can be brought into the double-reciprocal form:

$$\frac{1}{r_0} = \frac{1}{r_{max}} + \frac{K_M}{r_{max}} \cdot \frac{1}{[S]} \quad (3)$$

and used to obtain the Lineweaver-Burk plots [25]. The value of the Michaelis-Menten constant K_M= 3.94x10^{-4} mol/L and the maximum velocity r_{max}=4.64x10^{-2} mol L^{-1} s^{-1}, obtained by us, are comparable to those mentioned in literature [26].

The Influence of Atenolol on the Enzyme-Catalyzed Decomposition of Hydrogen Peroxide

Several kinetic runs performed in the presence of different concentrations of atenolol proved the inhibitory effect of this compound. When the concentration of H_2O_2 was varied at several fixed concentrations of atenolol, Lineweaver-Burk plots for the inhibited reaction

$$\frac{1}{r_{o(I)}} = \frac{1}{r_{max(I)}} + \frac{K_{M(I)}}{r_{max(I)}} \cdot \frac{1}{[S]} \qquad (4)$$

resulted in a family of straight lines (Fig. 2), which have a common intersection point on the left side of the ordinate and below the abscissa.

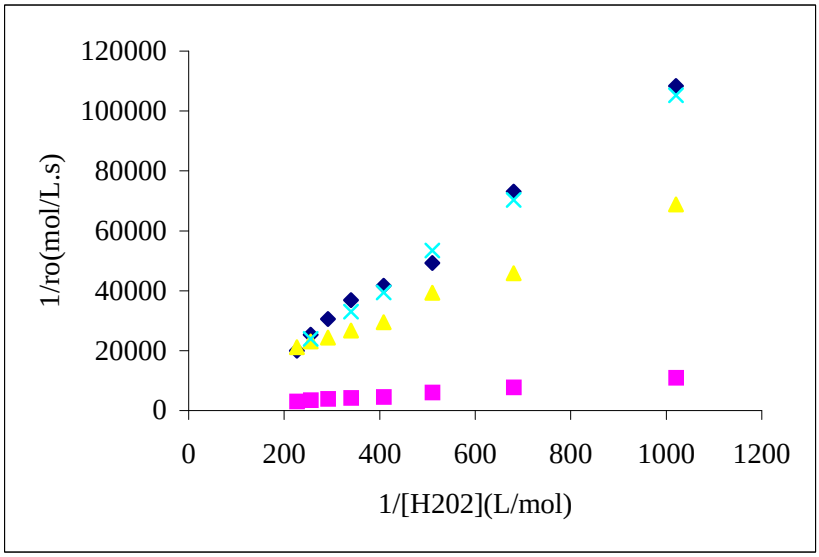

Fig.2.
Lineweaver Burk plots obtained for different concentration of atenolol

As the slopes of Lineweaver- Burk plots depend on the inhibitor concentration, a systematiuc study could lead to a kinetic method of determination of this inhibiting agent concentration.

The Michaelis-Menten parameters in the presence of the inhibitorI were determined from the parameters of the lines in figure 2. Their values are:

$$r_{max(I)} = r_{max} \frac{1 + \beta \frac{[I]}{K'_I}}{1 + \frac{[I]}{K'_I}} \quad \text{and} \quad K_{M(I)} = K_M \left(\frac{1 + \frac{[I]}{K_I}}{1 + \frac{[I]}{K'_I}} \right) \qquad (5)$$

where: $K_{M(I)}$ is the apparent Michaelis constant in the presence of inhibiting agent, K'_I and K_I are the dissociation constants of the enzyme – substrate - inhibitor complex, ESI, and the enzyme inhibitor complex, EI, respectively.

The constant β is equal to zero for full inhibition, while for partial inhibition 0< β≤1. Lineweaver-Burk plots of Fig. 2 correspond to the inhibition pattern of full or partial mixed inhibitors [26].

In order to distinguish between full and partial inhibition, the slopes and intercepts from the primary Lineweaver- Burk plots were re-plotted against the corresponding inhibitor concentration. They are presented in figure 3 Both

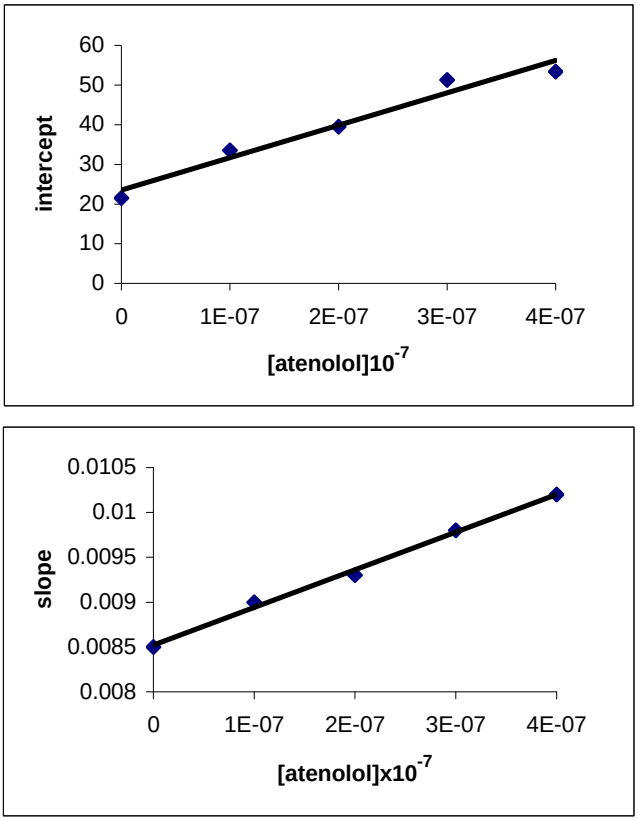

Fig 3.
The plots of intercepts and slopes versus the inhibitor concentration

these plots gave straight lines with good correlation coefficients. The straight lines equations are intercept: $y = (8{,}0 \pm 2.07) \cdot 10^{7}\, x + (23{,}55 \pm 5{,}08)$, and slope: $y = (42 \pm 7.76) \cdot 10^{2}\, x + (85 \pm 1{,}9) \cdot 10^{-4}$. This behavior is considered as typical for full inhibition [26]. Considering the possibility of a

Table 1.
Mean values or the maximum velocity $r_{max(I)}$ and Michaelis Menten constant in the presence of the inhibitor $K_{M(I)}$

$[atenolol]_0 \times 10^7$ (mol/l)	$r_{max(I)} \times 10^2$ (mol/ls)	$K_{M(I)} \times 10^4$ (mol/l)
1.00	2.98	2.68
2.00	2.53	2.35
3.00	1.94	3.19
4.00	1.87	1.66

partial inhibition, a non-linear fit of the intercept $1/r_{max(I)}=f([I]$ and the slope $K_{M(I)}/r_{max(I)}=f\ [I]$ gave negative values for β.

Therefore it is very likely that atenolol acts as a reversible full mixed inhibitor according to the reaction scheme:

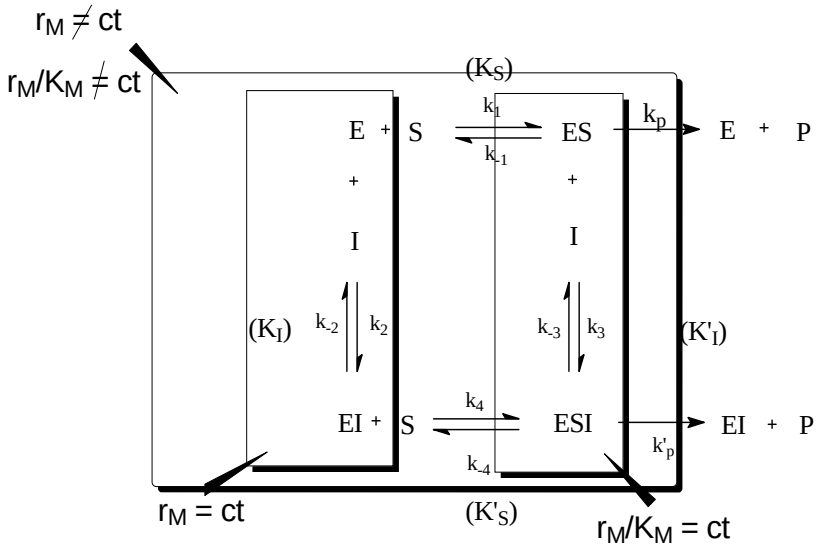

Scheme 1.
Mixed inhibition mechanism for atenolol, where E stands for catalase, S for hydrogen peroxide and I for atenolol.

The plot (Fig.3) of slopes and intercepts respectively against the inhibitor concentration were used to determine the dissociation constants mentioned in the scheme above, $K_I=(2.023\pm0,2)\times10^{-6}$ M of EI and $K'_I=(2.94\pm0,2)\times10^{-7}$ M Of ESI . The constant K_I was obtained from the slope of the $K_{M(I)}/r_{max(I)}$ versus [atenolol] graph:

$$K_I = \frac{K_M}{r_{max} \cdot slope} \quad (6)$$

while the K'_I constant was determined from the slope of the $1/r_{max(I)}$ versus [atenolol] graph:

$$K'_I = \frac{1}{r_{max} \cdot slope} \quad (7)$$

Conclusions

The catalase –catalyzed decomposition of hydrogen peroxide in phosphate buffer was studied in presence of atenolol. The atenolol acts like a fully mixed inhibitor, as observed from Lineweaver-Burk plots.

Michaelis Menten parameters were determined for the decomposotion of H_2O_2 in the presens of catalase yielding the values of $K_M = 3.94 \times 10^{-4}$ mol/L and $r_{max} = 4.64 \times 10^{-2} mol/L^{-1}s^{-1}$

REFERENCES

1. B.Chance , H.Sies, A. Boveris, Hydroperoxide Metabolism in Mammalian Organs, *Physiol Rev*., **1979**, 59, 527-605.
2. A. Deisseroth, A.L.Dounce, Physical and Chemical Properties, Mechanism of Catalysis and Physiological Role*, Physiol Rev*. **1970**, 50, 319-375.
3. B. Chance H.Sies, A. Boveris, *Physiol Rev*., **1979**, 59, 527-605.
4. B.Chance, *Acta Chem Scand*, **1947**, 1, 236-267.
5. P. Jones, A Suggett, *Biochem J*., **1968**, 110, 617-620.
6. P.George, *Biochem J*., **1949**, 44, 197-205.
7. B. Chance , D. Herbert, *Biochem J*., **1950**, 46, 402-414.
8. OM. Lardinois, MM. Mestdagh, PG. Rouxhet, *Biochim Biophys Acta*, **1996**, 1295, 222-238.
9. K.Kikuchi, Y. Kawamura-Konishi, H.Suzuki, *Arch. Biochem. Biophys*, **1992**, 296, 88-94.
10. M.L.Kremer, *J.Chem. Soc., Faraday Trans*. **1985**, 1, 81,91-104.
11. M.L.Kremer, *J.Phys Chem*. **1981**, 85, 835-839.
12. . B.Chance, *J. Biol. Chem*., **1949**, 179, 1299-1309.
13. Y. Ogura, Y. Tonomura, S.Hino, H. Tamiya, *J. Biochem*-Tokyo, **1950**, 37, 153-177; Y. Ogura, I. Yamazaki , idem, **1983,** 94, 403-408.
14. E. Margoliash, A. Novogrodsky, *Biochem J*, **1958**, 468-475.
15. K. Yoshihiro, S.Yoshiyuki, H. Jingyi, K. Takahiro, *J. Chem.Soc. Perkin Trans*, **1995** ,2, 1749-1759

16. ***Pharmacopee Europeene,3-rd Ed. **1997**.
17. M.A. Barret, in Beta-adrenoceptive agonist;in Recut Advances in Cardiology , ed Churchill Livingstone , **1973**, p 289.
18. B.N. C. Pritchard, G.S. Avery, Cardiovascular Drug , β-AdrenoceptorBloking Drug, **1977**, p 85
19. P. Jones, A. Sugget*, Biochem J*., **1968**, 108, 833-838.
20. DP. Nelson, LA. Kiesow, *Anal. Biochem*, **1972**, 49, 474-478.
21. P.Jones, Wynnes-Jones WFK, *T.Faraday Soc*.,**1972**, 49, 474-478.
22. ML Kremer, *J. Chem. Soc Farad T* ,**1983**, 79, 2125-2131.
23. P.Nicholls, P. Loewen, I. Fita Enzymology and structure of catalases in Meme – Fe Proteins,Advances in Inorg. Chem. Ed A.G.Sykes and G. Mauk Vol 51, pp 52-106, **2001**
24. L. Michaelis ,M. Menten, *Biochem.Z*, **1913**, ,49, 33-369.
25. H.Lineweaver, D. Burke, J*. Am. Chem. Soc* ,**1934**, 56, 658-666.
26. JL. Gelpi, JJ.Aviles, M. Busguets, S.Imperial, A. Mazo, A. Cortes, *J. Chem Educ*. ,**1993,** 70,805-816.

STUDIA UNIVERSITATIS BABEŞ-BOLYAI, CHEMIA, LI, 1, 2006

NEW HALO COMPOUNDS OF SILICON AND TIN, POTENTIAL PRECURSORS OF >E=C=P- HETEROALLENIC SYSTEMS

PETRONELA MARIA PETRAR, GABRIELA NEMES, IOAN SILAGHI-DUMITRESCU* AND LUMINITA SILAGHI-DUMITRESCU

ABSTRACT. New halo compounds of Si and Sn potential precursors of doubly-bonded derivatives of type >E=C=P- (E = 14 main group elements) have been synthesized. Compounds **1**-**3** (bearing a 2,4,6-tri-*tert*-butylphenyl group bound to phosphorus and one 2,4,6-tri-methylphenyl radical bonded to Si) are stabilized by the large steric hindrance which prevents the approach of monomers to form dimers or oligomers.

Introduction

The chemistry of the –P=C< phosphaalkenes has been intensively studied since the synthesis of the first such compound [1] in 1965. Its stabilization was then achieved by resonance effects; however, it was found that bulky organic groups, such as 2,4,6-tri-tert-butylphenyl (Mes*), 2,4,6-*tri-iso*-propylphenyl (Tip), 2,4,6-*tri*-metylphenyl (Mes), *tert*-butyl (t-Bu), etc offer a supplementary stabilization through their sterically protective effect .

The general available synthetic route to make a bond of an E 14 group element to the C=P moiety is shown in Scheme 1:

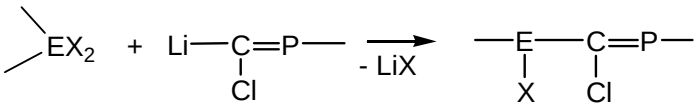

Scheme 1

Due to the pronounced π–electron accepting effect, phosphaalkenes containing low coordinated phosphorus atoms have been investigated in various catalytic processes (polymerization of ethylene, hydroformylation reactions, direct conversion of allylic alcohols) [2-5] and proved also to be useful synthons in organoelement chemistry [6].

Several metal complexes of phosphaalkenes in different coordination modes have been already synthesized and have been recently reviewed [6, 7].

* Department of Chemistry, "Babes-Bolyai" University, 1, Kogalniceanu str., Cluj-Napoca, RO-400084, Romania

Silylated and stannylated phosphaalkenes are described in the literature [8-12]. The presence of group 14 elements in the phosphaalkene molecule could induce interesting electronic effects that would allow the fine tuning of the metal centre properties of the complexes. Their use as building block of new polymeric materials could also lead to interesting outcomes.

We report herein the synthesis and characterization of three novel phosphaalkenes substituted with group 14 organometallic groups starting from the sterically hindered Mes*$PCCl_2$.

Results and Discussion

The treatment of the dihalogenated phosphaalkene Mes*$PCCl_2$ with one equivalent of n-BuLi at -85℃ leads to the form ation of Mes*PC(Cl)Li, which can be used as a nucleophilic agent in the synthesis of silylated and stannylated compounds.

Thus, compounds **1** and **2** were obtained following the route shown in Scheme 2.

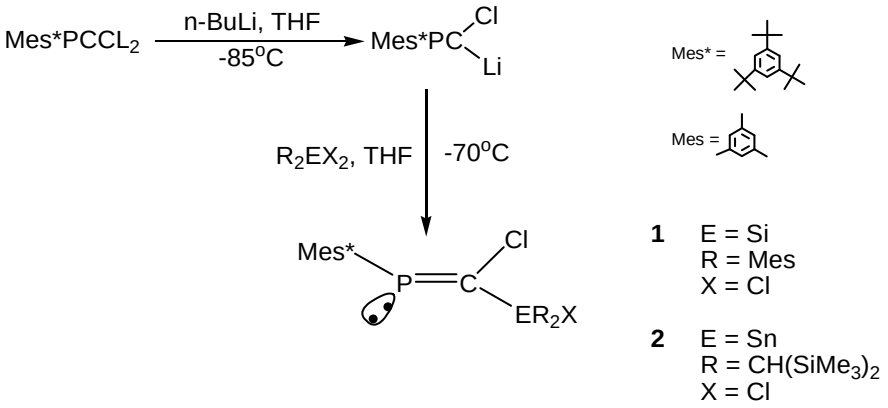

Scheme 2

Although these compounds were not completely purified, they were characterized through multinuclear NMR spectroscopy, and relevant data are given in Table **1**. The phosphorus and carbon chemical shifts of **1** are in the expected region for a P=C system [13,15].

In case of compound **2** the presence of a diastereotopic carbon atom (Me_3SiCH) leads to two different signals in ^{1}H-NMR for the methyl groups.

Compound **2 (**the E isomer) show a doublet at 43.6 ppm ($^3J_{P\text{-}Sn}$=363.74 Hz) in the ^{119}Sn-NMR spectra and a singlet in the ^{31}P spectra [13,14].

A byproduct in the synthesis of **2** was the Z geometrical isomer, which gives signals at 306.07 ppm in ^{31}P NMR spectra and 12.06 ppm (d, $^3J_{P\text{-}Sn}$=374.93

Hz) in ^{119}Sn NMR respectively. The relative proportion of the E/Z stereoisomers as shown by ^{31}P-NMR is 4/1.

Compound **2** has also been characterized through ^{29}Si-NMR spectroscopy and gives a doublet at -5.65 ppm with a silicon-phosphorus coupling constant of 58 Hz.

Table 1.
Relevant NMR data for compounds**1** and **2**

Compound	**^{1}H NMR**	**^{31}P NMR**	**^{13}C NMR**
1	1.34 ppm (d, $^{5}J_{HP}$ = 0.33 Hz, 18H, *o*-t) 1.44 ppm (s, 9H, *p*-tBu) 2.25 ppm (s, 12 H, *o*-Me) 2.41 ppm (s, 6H, *p*-Me) 7.41 ppm (s, 2H, H_{arom})	323.8 ppm ($^{2}J_{PSi}$ =58 Hz)	173 ppm (dd, C=P)
2	0.24 ppm (s, 9H, Me_3Si) 0.27 ppm (s, 9H, Me_3Si) 1.33 ppm (s, 9H, *p*-tBu) 1.49 ppm (s, 18H, *o*-tBu) 7.40 ppm (s, 2H, H_{arom})	305.490 ppm ($^{2}J_{PSn}$ = 365.66 Hz)	4.40 ppm (wide signal, $\underline{C}H_3Si$) 174.25 ppm (d, $^{2}J_{PC}$ =102,85 Hz) 14.42 ppm (s, $\underline{C}HSn$) 135.09 ppm (d, $^{2}J_{CP}$ = 71.61 Hz, ipso C Mes*)

The reaction of $MeSiCl_3$ with two equivalents of Mes*PC(Cl)Li (Scheme 3) lead to the formation of the sterically hindered silylated phosphaalkene **3**:

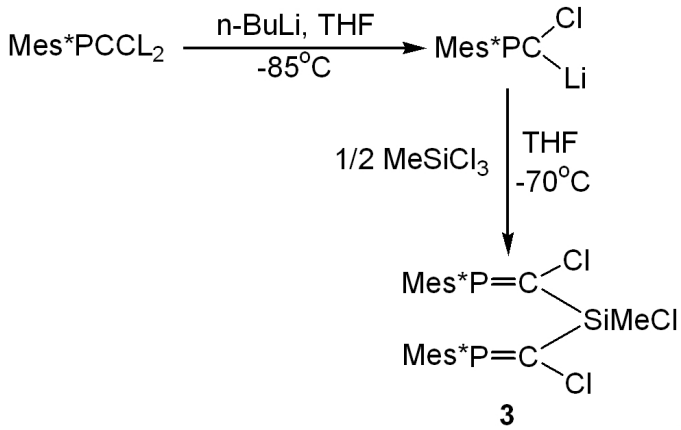

3

Scheme 3

NMR data for **3** are given in Table 2.

Table 2.
NMR chemical shift and coupling constants for **3**.

Compound	^{1}H NMR	^{31}P NMR	^{13}C NMR
3	0.88 ppm (s, 3H, Me) 1.33 ppm (s, 9H, *p*-tBu) 1.44 ppm (s, 18H, *o*-tBu) 7.41 ppm (s, 2H, Harom)	313.57 ppm ($^{2}J_{PSi}$ = 44.63 Hz)	162.90 ppm (dd, $^{2}J_{CP}$ = 75.46 Hz, $^{3}J_{CP}$ = 5,5 Hz) 134.37 ppm (d, $^{2}J_{CP}$ = 64.14 ppm, ipso C Mes*)

The ^{29}Si NMR spectrum shows a triplet at -1.61 ppm, with a $^{2}J_{SiP}$ coupling constant of 47.7 ppm, which is close to that observed in the ^{31}P NMR spectrum.

In the analogues halosilylphosphaalkenes Mes*PC(Cl)SiPhTipX (X = Cl, F) the silicon atom appears more shielded (-6.8 ppm and -10 ppm respectively), but the $^{2}J_{PSi}$ coupling constant is comparable (54 Hz in both cases).

The reactivity of these new compounds is under current study. Their potential application in the synthesis of new, stable heteroallenes of >E=C=P- type is also currently investigated. An approach to the obtaining of such unsaturated derivatives would be the reaction of **1**-**3** with t-BuLi, followed by intramolecular elimination of LiCl (Scheme 4):

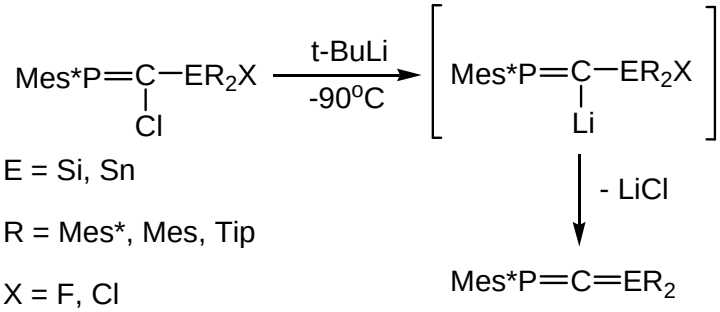

Scheme 4

Conclusions

Three new compounds containing –P=C(Cl)-E(Cl)< (E = Si, Sn) skeleton stabilized by bulky substituents at phosphorus and E have been synthesized.
The use of these dihaloderivatives for the synthesis of heteroallenes containing low coordinated phosphorus atoms is under current investigation.

Experimental

All manipulations were carried out using Schlenk techniques under inert atmosphere. Solvents were dried and freshly distilled from sodium/benzophenone.

NMR Spectra were recorded in $CDCl_3$ on a Bruker AC 200 instrument at 200.1, 50.1, 81.01 MHz (for ^{1}H, ^{13}C and ^{31}P respectively) and an AC 300 instrument at 100.6 MHz for ^{13}C, ^{29}Si and ^{119}Sn.

$MeSiCl_3$ and MesH were available commercially (Aldrich). 1.6 M solution of n-BuLi and t-BuLi (Aldrich) in hexane were used throughout.
Mes*$PCCl_2$ has been prepared according to the literature procedure [16].

Synthesis of {Chloro-[chloro-bis-(2,4,6-trimethyl-phenyl)-silanyl]-methylene}-(2,4,6-tri-tert-butyl-phenyl)-phosphane (1):
To a solution of 1 g Mes*$PCCl_2$ (2.7 mmols) in 20 mL THF 1.9 mL of n-BuLi 1.6M were added at -90°C. The reaction mixture was stirred for an hour at -85°C and than added dropwise to a solution of 0.98 g Mes_2SiCl_2 (2.7 mmols) in 30 mL THF, cooled at -70°C. The solution was allowed to warm up at room temperature and the solvent was removed under vacuum and replaced with pentane. LiCl was removed by filtration.
MS(m/z): 624 (M+), 609 (M^+-Me), 491 (M^+-Mes-Me), 379 (M^+-Mes*), 119 (Mes)

Synthesis of {[Bis-(bis-trimethylsilanyl-methyl)-chloro-stranyl]-chloro-methylene}-(2,4,6-tri-tert-butyl-phenyl)-phosphane (2):
To a solution of 2.12 g Mes*$PCCl_2$ (5.9 mmols) in 30 mL THF 3.3 mL of n-BuLi 1.6M were added at -90°C. The reaction mixture was stirred for an hour at -85°C and than added dropwise to a solution of 3 g of Bis_2SnCl_2 (5.9 mmols) in 30 mL THF, cooled at -70°C. The solution was allowed to warm up at room temperature and the solvent was removed under vacuum and replaced with pentane. LiCl was removed by filtration. Several attempts to obtain a crystalline product failed but by eliminating the pentane, a white solid mixture was obtained from which compound **2** was identified through the NMR data. MS(m/z): 796 (M), 681 (M-2 t-Bu+1); 637 (M-Bis); 602 (M-Bis-Cl)

Synthesis of Bis[1-chloro-2-(1,3,5-*tri-tert*-butyl-phenyl)phosphaalkene] methylchlorosilane (3):
To a solution of 2 g Mes*$PCCl_2$ (5.4 mmols) in 30 mL THF 3.8 mL of n-BuLi 1.6M were added at -90°C. The reaction mixture was stirred for an hour at -85°C and than added dropwise to a solution of 0.40 g Me_3SiCl (2.7 mmols) in 15 ml THF, cooled at -70°C. The solution was allowed to warm up at room temperature and the solvent was removed under vacuum and replaced with pentane. LiCl was removed by filtration. Attempts to obtain crystalline product failed. By removing the pentane a light-yellow solid mixture was obtained from which compound **3** was identified through NMR data.

Acknowledgment. Drs. Jean Escudie and Henri Ranaivonjatovo from Paul Sabatier University Toulouse, are thanked for their hospitality and for useful discussion on this manuscript. We thank the Ministry of Education and Research Bucharest (CEEX project) for partial financial support of this work.

REFERENCES

1. R. Allman, *Angew. Chem.,* **1965**, *77*, 134.
2. L. Weber, *Angew. Chem, Int. Ed. Engl*., **2002**, *41*, 563.
3. O. Daugulis, M. Brookhart, P.S. White, *Organometallics*, **2002**, *21*, 5935.
4. F. Ozawa, H. Okamoto, S. Kawagishi, S. Yamamoto, T. Minami, M. Yoshifuji, *J. Am. Chem. Soc*., **2002**, *124*, 10968.
5. S. Ikeda, F. Ohhata, S. Kawagishi, S. Yamamoto, T. Minami, F. Ozawa, M. Yoshifuji, *Angew. Chem, Int. Ed. Engl*., **2000**, *39*, 4512.
6. L. Weber, *Coord. Chem. Revs.*, **2005**, *249(7-8),* 741.
7. H. Liang, S. Ito, M. Yoshifuji, *Youji Huaxue*, **2004**, *24(10),* 1310.
8. R. Appel, C. Casser, M. Immenkeppel, *Tetrahedron Lett.,* **1985**, *26(30),* 3551.
9. M. van der Sluis, V. Beverwijk, A. Termaten, E. Gavrilova, F. Bickelhaupt, H. Kooijman, N. Veldman, A. L. Spek, *Organometallics*, **1997**, *16(6),* 1144.
10. L. Rigon, H. Ranaivonjatovo, J. Escudie, A. Dubourg, J. Declercq, *Chem.-A Eur. J.*, **1999**, *5(2),* 774.
11. L. Baiget, M. Bouslikhane, J. Escudié, G. Cretiu Nemes, I. Silaghi-Dumitrescu, L. Silaghi-Dumitrescu, *Phosphorus, Sulfur, Silicon and Relat. Elem.,* **2003**, *178(9),* 1949.
12. G. Cretiu Nemes, H. Ranaivonjatovo, J. Escudie, I. Silaghi-Dumitrescu, L. Silaghi-Dumitrescu, H. Gornitzka, *Eur. J. Inorg. Chem*., **2005**, 1109.
13. R. Appel, *Multiple Bonds and Low Coordination in Phophorus Chemistry* (eds. M. Regitz, O.J. Scherer), Thieme, Stuttgart, **1990**, p. 157.
14. L.M. Markovski, V.D. Romaneko, *Tetrahedron*, **1989**, *45(19),* 6019.
15. S. Loschschmidt, A. Schmidpeter, *Phosphorus, Sulfur Relat. Elem*., **1986**, *29*, 73.
16. S. J. Goede, F. Bickelhaupt, *Chem. Ber*., **1991**, *124*, 2677.

STUDIA UNIVERSITATIS BABEŞ-BOLYAI, CHEMIA, LI, 1, 2006

BISMUTH(III) COMPLEXES WITH DIORGANODICHALCOGENO-PHOSPHINATO LIGANDS. SYNTHESIS AND SPECTROSCOPIC CHARACTERIZATION

M. JOENSSON[1], A. SILVESTRU[2] AND C. SILVESTRU[2]

ABSTRACT. Metathesis reactions between $BiCl_3$ or OBiCl with alkali metal salts of diorganodichalcogenophosphinato ligands, in stoechiometric ratio, led to tris(diorganophosphinato)bismuth, $Bi(O_2PR_2)_3$ (R = Me, Ph, Cy, Pr^n, Bz), tris(diorganomonothiophosphinato)bismuth, $Bi(OSPPh_2)_3$, as well as the diphenyldithiophosphinato derivatives $Bi(S_2PPh_2)_3$ and $OBi(S_2PPh_2)$. The compounds were characterized by multinuclear NMR (^1H, ^{13}C, ^{31}P), IR and mass spectrometry. The spectroscopic data allowed us to predict a polymeric structure with anisobidentate ligands in case of the dioxo derivatives, while for the other species either monomeric or polymeric structures may be proposed.

Keywords: bismuth complexes, organophosphorus ligands, spectroscopic characterization

Introduction

Diorganophosphorus ligands of type $[R_2PXY]^-$ (R = alkyl or aryl, X, Y = O, S) and their metal complexes have attracted much interest for several years, due both to the diversity of their structural features and their potential applications (*i.e.* biological or catalytic activity). In compounds with such ligands different coordination patterns were observed, *i.e.* monodentate or bidentate (chelating or bridging two or more metal centers) as a consequence of *(i)* the ability of the ligand to involve one or both chalcogen atoms in interactions with metal centers, and *(ii)* the tendency of many Main Group or transition metals to increase their coordination number [1-4]. Several solid state structural types were established for different metal complexes by single-crystal X-ray diffraction studies. Related to the applications of these species, a special interest is concerned to their solution behavior and structure. Even if a large number of metal complexes with $[R_2PXY]^-$ (X, Y = O, S) ligands were already described, only few bismuth complexes containing dithiophosphinato groups were so far studied and structurally characterized by single-crystal X-ray diffraction, *i.e.* $Bi(S_2PMe_2)_3$ [5], $Bi(S_2PEt_2)_3$ [6], $Bi(S_2PPh_2)_3$ [7], and

[1] Hochschule Vechta, Institut für Didaktik der Naturwissenschaften, der Mathematik und des Sachunterrichts, D-49377 Vechta, Germany

[2] Faculty of Chemistry & Chemical Engineering, "Babes-Bolyai" University, RO-400028 Cluj-Napoca, Romania. Fax: 0040-264-590818; Tel: 0040-264-593833; E-mail: ancas@chem.ubbcluj.ro

$MesBi(S_2PPh_2)_2$ [8]. Our studies, reported here, were focused on some bismuth(III) inorganic species with dioxo-, monothio- or dithiophosphinato ligands. Spectroscopic data (multinuclear NMR, MS) are also included for $Bi(S_2PPh_2)_3$, only IR data [9] and the crystal structure [7] being previously reported.

Experimental

Solvents were pre-dried over activated 4 Å molecular sieves and then distilled from potassium (THF), magnesium (methanol), calcium chloride (acetonitrile), Na_2CO_3 (acetone) under a continuous stream of argon. $BiCl_3$ and OBiCl were commercially products. All other starting materials were obtained according to literature methods: R_2PO_2Na (R = Me [10], Bz [11], Cy [12], Ph, Pr^n [13]), $Ph_2PS_2NH_4$, Ph_2PSONH_4 [13].

^1H, ^{13}C and ^{31}P NMR spectra were recorded on a VARIAN GEMINI instrument operating at 300, 75.4 and 121.4 MHz respectively, relative to TMS (^1H and ^{13}C) and H_3PO_4 85 % (^{31}P). Mass spectra were obtained using either a VARIAN CH7 (A) MAT instrument (EI) or a JEOL SX-102A spectrometer (FAB). IR spectra were recorded either as KBr pellets or Nujol mulls on a SPECORD IR UR 20 instrument.

Preparation of tris(dimethylphosphinato)bismuth(III), $Bi(O_2PMe_2)_3$ (1)

A mixture of 0.5 g (1.6 mmol) $BiCl_3$ and 0.68 g (4.8 mmol) $Me_2PO_2Na{\cdot}1.5\ H_2O$ in acetonitrile (50 ml) was refluxed for 2 hours under argon atmosphere. The resulted NaCl was filtered off and the solvent was removed in vacuum, leaving the title compound as a white solid. Yield 0.54 g (70%). M.p. 71-73°C. IR:(KBr, cm^{-1}): 1295s, 1255m, 1150vs (asym PO_2); 960vs (sym PO_2); 870vs (P-CH_3); 750m, 700s (P-C). ^1H NMR ($CDCl_3$): 1.42 (d, 18H, C*H*$_3$, $^2J_{PH}$ 16.7 Hz). ^{13}C NMR ($CDCl_3$): 16.50 (d, $^1J_{PC}$ 102.5 Hz). ^{31}P NMR ($CDCl_3$): 51.9 (s). FAB+ MS [*m/z* (%)]: 1371 (5) $[Bi_3(O_2PMe_2)_8^+]$, 976 (8) $[Bi_2(O_2PMe_2)_6^+]$, 488 (17) $[Bi(O_2PMe_2)_3^+]$, 395 (58) $[Bi(O_2PMe_2)_2^+]$, 302 (10) $[Bi(O_2PMe_2)^+]$, 93 (100) $[O_2PMe_2^+]$, 77 (7) $[OPMe_2^+]$.

Preparation of tris(diphenylphosphinato)bismuth(III), $Bi(O_2PPh_2)_3$ (2)

A mixture of 0.98 g (3.1 mmol) $BiCl_3$ and 2.23 g (9.3 mmol) $Ph_2PO_2Na{\cdot}$in methanol (100 ml) was stirred under argon atmosphere, for 2 hours, at room temperature. The white precipitate containing NaCl and the desired product was filtered off and washed with water to remove NaCl. The unsoluble white solid was dried to yield 2.07 g (77%) of the title compound. M.p. 237°C. IR (KBr, cm^{-1}): 1435vs (P-Ph); 1135s, 1085vs, 1065m (asym PO_2); 1030m, 1010vs, 990vs (sym PO_2); 745vs, 725vs, 690vs (PC). ^1H NMR (Me_2CO-*d*$_6$): 7.52 (m, 18H, C_6H_5-*meta+para*); 7.84 (m, 12H, C_6H_5-*ortho*). For ^{31}P NMR, see subsequent discussion.

General method for the NMR tube scale reactions

$BiCl_3$ and the sodium salt of the appropriate diorganophosphinic acid were mixed in a 1:3 molar ratio in $CDCl_3$, directly in the NMR tube, at room temperature, according to the data in Table 1, and the NMR spectra were recorded.

*Tris(di-n-propylphosphinato)bismuth(III), $Bi(O_2PPr^n_2)_3$ (**3**)*: ^{1}H NMR ($CDCl_3$): 1.02 (m, 18H, C*H*$_3$); 1.64 (m, 24H, C*H*$_2$-C*H*$_2$). ^{13}C NMR ($CDCl_3$): 15.46 (s, C_α); 15.59 (d, C_β, $^2J_{PC}$ 19.2 Hz); 31.22 (d, C_γ, $^1J_{PC}$ 90.6 Hz). ^{31}P NMR ($CDCl_3$): 58.4 (s).

*Tris(dicyclohexylphosphinato)bismuth(III), $Bi(O_2PCy_2)_3$ (**4**)*: ^{1}H NMR ($CDCl_3$): 1.22-1.82 (m, 33H, C_6H_{11}). ^{13}C NMR ($CDCl_3$): 24.61 (s, C_4); 25.92 (s, C_3); 26.19 (d, C_2, $^2J_{PC}$ 13.5 Hz); 34.99 (d, C_1, $^1J_{PC}$ 90.6 Hz); ^{31}P NMR ($CDCl_3$): 62.3 (s).

*Tris(dibenzylphosphinato)bismuth(III), $Bi(O_2PBz_2)_3$ (**5**)*: ^{1}H NMR ($CDCl_3$): 2.84 (s, br, 12H, C*H*$_2$); 7.17 (s, br, 30H, C_6H_5). ^{13}C NMR ($CDCl_3$): 36.21 (d, *C*H$_2$, $^1J_{PC}$ 88.6 Hz); 126.68 (s, C_p); 128.49 (s, C_m); 130.01s (C_o); 131.78 (d, C_i, $^2J_{PC}$ 6.6 Hz). ^{31}P NMR ($CDCl_3$): 48.5 (s).

Table 1.
Preparation details for $Bi(O_2PR_2)_3$ (NMR tube scale reactions).

$BiCl_3$ g (mmol)	NaO_2PR_2 g (mmol)	
0.0305 (0.1)	R = Pr^n	0.0499 (0.3)
0.0228 (0.07)	R = Cy	0.0547 (0.21)
0.0228 (0.07)	R = Bz	0.0551 (0.21)

***Preparation of tris(diphenylmonothiophosphinato)bismuth(III), $Bi(OSPPh_2)_3$* (6)**

A mixture of 0.31 g (1.0 mmol) $BiCl_3$ and 2.26 g (3.0 mmol) $Ph_2P(S)ONH_4$·in acetone (50 ml) was refluxed under argon atmosphere for 2 hours. NH_4Cl was filtered off and the solvent was removed in vacuum. The resulting colorless solid was recrystalized from benzene. Yield 0.5 g (55%). M.p. 180^{o}C. IR (KBr, cm^{-1}): 1437vs (P-Ph); 1128s, 1109s; 1033m, 1013m, 994m (P-O) 656m (P=S); 770s, 748s, 732s, 693s (PC). ^{1}H-NMR ($CDCl_3$): 7.36 (m, 12H, C_6H_5-*meta*); 7.46 (m, 6H, C_6H_5-*para*); 7.83 (m, 12H, C_6H_5-*ortho*). ^{13}C NMR ($CDCl_3$): 128.31 (m, C_m, $^3J_{PC}$ 13.9 Hz); 131.45 (m, C_o, $^2J_{PC}$ 12.8 Hz) 132.10 (s, C_p); 134.10 (d, C_i, $^1J_{PC}$ 113.1 Hz). ^{31}P NMR ($CDCl_3$): 80.9 (s). EI MS [*m/z* (%)]: 908 (5) [M^+], 675 (10) [$Bi(OSPPh_2)_2^+$], 442 (17) [$Bi(OSPPh_2)^+$], 233 (5) [$SOPPh_2^+$], 217 (59) [$SPPh_2^+$], 201 (17) [$OPPh_2^+$], 154 (100) [Ph_2^+].

***Preparation of tris(diphenyldithiophosphinato)bismuth(III), $Bi(S_2PPh_2)_3$* (7)**

A mixture of 0.63 g (2 mmol) $BiCl_3$ and 1.6 g (6 mmol) $Ph_2PS_2NH_4$·in THF (50 ml) was stirred under argon atmosphere, for 3 hours, at room temperature. The solvent was removed in vacuum and the remained solid was treated with chloroform. NH_4Cl was filtered off and the solvent was removed in vacuum to give a yellow crystalline product. Yield 1.37 g (72%). M.p. 127^{o}C. ^{1}H NMR ($CDCl_3$): 7.38 (m, 18H, C_6H_5-*meta+para*); 7.87 (ddd, 12H, C_6H_5-*ortho*, $^3J_{PH}$ 14.5, $^3J_{HH}$ 8.0, $^4J_{HH}$ 1.2 Hz); ^{13}C NMR ($CDCl_3$): 128.19 (d, C_m, $^3J_{PC}$ 13.3 Hz); 130.55 (d, C_o, $^2J_{PC}$ 12.1 Hz); 131.06 (s, C_p); 139.29 (d, C_i, $^1J_{PC}$ 83 Hz); ^{31}P NMR ($CDCl_3$): 60.1 (s). EI MS [*m/z* (%)]:707 (96) [$Bi(S_2PPh_2)_2^+$], 458 (22) [$Bi(S_2PPh_2)^+$], 249 (55) [$S_2PPh_2^+$], 217 (100) [$SPPh_2^+$], 154 (5) [Ph_2^+], 77 (5) [Ph^+].

Preparation of oxo(diphenyldithiophosphinato)bismuth(III), OBi(S_2PPh_2) **(8)**

A mixture of 1.3 g (5.0 mmol) OBiCl and 1.335 g (5.0 mmol) $Ph_2PS_2NH_4$ in acetone (50 ml) was refluxed for 2 hours. NH_4Cl was filtered off and the yellow solution was concentrated in vacuum. The resulting yellow solid was recrystalized from acetic acid. Yield 2.2 g (93%). M.p. 76°C. IR (KBr, cm^{-1}): 1436s (P-Ph); 610s, 660s (asym PS_2); 555vs (sym PS_2). ^{1}H NMR ($CDCl_3$): 7.32 (m, 4H, C_6H_5-*meta*); 7.40 (m, 2H, C_6H_5-*para*); 7.78 (dm, 4H, C_6H_5-*ortho*, $^2J_{PH}$ 14.4 Hz). ^{13}C NMR ($CDCl_3$): 128.46 (d, C_m, $^3J_{PC}$ 13.9 Hz), 131.95 (d, C_o, $^2J_{PC}$ 10.8 Hz), 132.23 (s, C_p), 132.88 (d, C_i, $^1J_{PC}$ 76.1 Hz). ^{31}P NMR ($CDCl_3$): 71.0 (s).

Results and Discussion

Synthesis

Inorganic bismuth derivatives of type $Bi(X_2PR_2)_3$ (X = O, R = Me, Ph, Pr^n, Cy, Bz; X = S, R = Ph), $Bi(OSPPh_2)_3$ and $OBi(S_2PPh_2)$ were obtained by salt metathesis reactions between either $BiCl_3$ or OBiCl and an alkali metal or ammonium salt of the appropriate phosphorus-containing acid, according to equations (1) – (4):

$$BiCl_3 + 3\ NaO_2PR_2 \longrightarrow Bi(O_2PR_2)_3 + 3\ NaCl \quad (1)$$

R = Me (**1**), R = Ph (**2**)
R = Pr^n (**3**), R = Cy (**4**)
R = Bz (**5**)

$$BiCl_3 + 3\ NH_4OSPPh_2 \longrightarrow Bi(OSPPh_2)_3 + 3\ NH_4Cl \quad (2)$$

6

$$BiCl_3 + 3\ NH_4S_2PPh_2 \longrightarrow Bi(S_2PPh_2)_3 + 3\ NH_4Cl \quad (3)$$

7

$$OBiCl + NH_4S_2PPh_2 \longrightarrow OBi(S_2PPh_2) + NH_4Cl \quad (4)$$

8

Compounds **1**, **2** and **6**–**8** were isolated as solid products, while compounds **3**–**5** were generated in solution, directly in the NMR tube, and investigated spectroscopically without further isolation.

Some data concerning the new compounds and related bismuth(III) dithiophosphinates, already described in literature, are given in Table 2.

All compounds were investigated by NMR spectroscopy. Compounds **1**, **2** and **6**–**8** were also characterized by infrared spectroscopy and mass spectrometry (EI or FAB).

NMR Spectroscopy

The dioxo derivatives exhibit a poor solubility in $CDCl_3$. For compound **2** the NMR spectra could be obtained only in presence of more polar solvents, *i.e.* acetone-d_6 or DMSO-d_6. This suggests a possible polymeric structure for these compounds.

Table 2.
Analitical data for the new Bi(III) compounds and related derivatives.

Compound	M.p. [^oC]	^{31}P NMR ($CDCl_3$)	Structure data
$Bi(O_2PMe_2)_3$ (**1**)	71-73	51.9	NMR, MS, IR[a]
$Bi(O_2PPh_2)_3$ (**2**)	237	12.5[b]	NMR, MS, IR[a]
$Bi(O_2PPr^n_2)_3$ (**3**)		58.4	NMR[a]
$Bi(O_2PCy_2)_3$ (**4**)		62.3	NMR[a]
$Bi(O_2PBz_2)_3$ (**5**)		48.5	NMR[a]
$Bi(OSPPh_2)_3$ (**6**)	180	80.9	NMR, IR[a]
$Bi(S_2PPh_2)_3$ (**7**)	127	60.1	NMR, MS,[a] IR [9], X-ray [7]
$OBi(S_2PPh_2)$ (**8**)	76	71.0	NMR, IR[a]
$Bi(S_2PMe_2)_3$	242	60.4 (C_6D_6)	NMR, X-ray [5]
$Bi(S_2PEt_2)_3$			NMR, X-ray [6]
$MesBi(S_2PPh_2)_2$	180 (dec)	-	NMR, MS, X-ray [8]

[a] This work; [b] In DMSO-d_6.

In a mixture of $CDCl_3$ – DMSO-d_6, the ^{31}P NMR spectrum of **2** exhibits two resonances, at δ 28.4 and 24.8 ppm, respectively. The resonance at lower field (δ 28.4 ppm) is very close to that observed for the free acid in $CDCl_3$ (δ 28.6 ppm). However, the ^{31}P NMR spectrum in pure DMSO-d_6 for compound **2** contains only one resonance (δ 12.5 ppm), different from the values observed in the same solvent for $Ph_2P(O)OH$, (δ 24.7 ppm) or Ph_2PO_2Na (δ 17.4 ppm), which clearly suggests the formation of a Bi(III) species, probably a DMSO adduct, with a monomeric structure. The strong coordination ability of DMSO to the bismuth atom is well known [14,15].

In order to investigate the influence of the organic group attached to phosphorus upon the solubility of bismuth derivatives, some related species, *i.e.* $Bi(O_2PR_2)_3$ (R = Pr^n, Cy, Bz), were generated directly in the NMR tube, in $CDCl_3$. For all dioxo derivatives the ^1H and ^{13}C resonances are not significantly shifted compared to the free acids, but in all cases the ^1H resonance for the O*H* group, characteristic for the free acids, is absent, as well as the corresponding OH stretching vibration in the region 2600 - 1600 cm^{-1}, in the IR spectra (for compounds **1** and **2**). In contrast to the free acids, the proton resonances for the dioxo derivatives exhibit a broad aspect and the proton-proton and phosphorus-proton couplings are not resolved. The ^{31}P resonances for the Me and Bz substituted derivatives are enough shifted

to conclude the formation of the desired complexes [*i.e.* δ 48.5 ppm for $Bi(O_2PBz_2)_3$ in contrast to δ 51.4 ppm for $Bz_2P(O)OH$, and δ 51.9 ppm for $Bi(O_2PMe_2)_3$ in contrast to δ 48.6 ppm for $Me_2P(O)OH$].

The Bi(III) compounds containing monothio or dithio ligands are soluble in common organic solvents and the NMR spectra in $CDCl_3$ solution are consistent with the formation of the desired compounds (**6**–**8**). The ^{1}H and ^{13}C NMR spectra exhibit the expected resonances for the organic groups attached to phosphorus, split by the proton-proton and phosphorus-proton couplings, and phosphorus-carbon couplings, respectively. The ^{31}P NMR spectra show only one sharp resonance.

Mass Spectra

The FAB+ MS spectrum of compound **1** contains the molecular ion in a relatively high abundance (12%), but peaks with higher mass are also present (*i.e. m/z* 1371 $[Bi_3(O_2PMe_2)_8^+]$, *m/z* 976 $[Bi_2(O_2PMe_2)_6^+]$), thus consistent with the formation of molecular associations, at least of a trimeric species $[Bi(O_2PMe_2)_3]_3$.

For the monothio and dithio derivatives, peaks of low intensity, corresponding to the molecular ions, were observed in the EI spectra, along with different other peaks corresponding to ions formed by fragmentation. For compound **7**, even if the single-crystal X-ray studies revealed a dimeric structure [7], no fragments with m/z values higher than corresponding to a monomeric species were observed in the EI MS spectrum, which is consistent with weak intermolecular Bi···S interactions.

Infrared Spectra

The infrared spectra of the dioxo derivatives **1** and **2** are consistent with a coordination of the phosphinato ligands through both oxygen atoms to the metal center (*e.g.* vasym(PO_2) 1135s, 1085vs, 1065m, and $\nu_{sym}(PO_2)$ 1030m, 1010vs, 990vs for **2** *vs.* vasym(PO_2) 1035m, 1010s, and $\nu_{sym}(PO_2)$ 1142vs, 1133vs for $Ph_2SbO_2PPh_2$, for which a polymeric structure, with *O,O'*-bridging ligand, was established by single-crystal X-ray diffraction [16]). Taking into account the low solubility of this type of bismuth compounds and the observation in mass spectrum of compound **1** of fragments with a higher mass than expected for a monomeric species, polymeric structures with bridging ligand units might be considered. The difference in solubility might be due to a higher association degree for the phenyl substituted compound.

The strong IR absorptions observed for the compound **6** in the region 1130-1000 cm^{-1} and at 656 cm^{-1} are indicative for single P-O and double P=S bonds in the monothiophosphinato ligand [c.f. $Ph_2P(S)OH$ [17]: v(P-O) 892vs, v(P=S) 633vs; $Ph_2SbOSPPh_2$ [16]: v(PO) 1061vs, 1050vs, v(PS) 593vs; for which a polymeric structure, with *O,O'*-bridging ligand, was

established by single-crystal X-ray diffraction). This behaviour is consistent with the primary coordination of the monothio ligands to the metal centre through the oxygen atom, while the sulfur doubly bonded to phosphorus is probably involved in secondary intramolecular bonding, thus resulting in a distorted octahedral Bi(*O,S*)$_3$ core. Additional increase in coordination number of the metal centre through intermolecular bismuth chalcogen interactions, as observed in the related dimeric antimony derivative, [Sb(OSPPh$_2$)$_3$]$_2$ [18], cannot be excluded.

It was suggested that the difference Δ = vasym(PS$_2$) - vsym(PS$_2$) might be used for estimation of the coordination pattern of the dithiophosphorus ligands in metal complexes, *i.e.* Δ = 50-70 cm^{-1}, Δ = 70-90 cm^{-1} and Δ > 95 cm^{-1} indicates isobidentate, anisobidentate and monodentate coordination, respectively [18]. Indeed, for Bi(S$_2$PPh$_2$)$_3$ (**7**) the Δ = 75 cm^{-1} [9] is consistent with the bidentate pattern of the dithio ligand found by single-crystal X-ray diffraction studies [7]. For the bismutyl derivative OBi(S$_2$PPh$_2$) (**8**) the difference Δ of 105 cm^{-1} would suggest a monodentate coordination of the dithio ligand. However, taking into account that in all bismuth(III) complexes investigated so far by single-crystal X-ray diffraction [5-8] the dithiophosphorus ligands are coordinated through both sulfur atoms thus resulting in higher coordination number of the metal centre, molecular associations in solid state for compound **8** can not be excluded.

REFERENCES

1. I. Haiduc in *Comprehensive Coordination Chemistry II - From Biology to Nanotechnology*, Vol.1 (Vol. Ed. A. B. Lever), Elsevier Ltd., Oxford, UK, **2004**, p. 349-376.
2. C. Silvestru, I. Haiduc, *Coord. Chem. Rev.*, **1996**, *147*, 117.
3. I. Haiduc, R. B. King, M.G. Newton, *Chem. Rev.*, **1994**, *94*, 301.
4. I. Haiduc, L. Y. Goh, *Coord. Chem. Rev.*, **2002**, *224*, 151.
5. F.T. Edelmann, M. Noltemeyer, I. Haiduc, C. Silvestru, R. Cea Olivares, *Polyhedron*, **1994**, *13*, 547.
6. G. Svensson, J. Albertsson, *Acta Chem. Scand*., **1989**, *43*, 511.
7. M.J. Begley, D.B. Sowerby, I. Haiduc, *J. Chem. Soc., Dalton Trans.*, **1987**, 145.
8. K.H. Ebert, R.E. Schulz, H.J. Breunig, C. Silvestru, I. Haiduc, *J. Organomet. Chem.*, **1994**, *470*, 93.
9. A. Mueller, V.V. Krishna Rao, G. Klinksiek, *Chem Ber*., **1971**, *104*, 1892.
10. H. Reinhardt, D. Bianchi, D. Mölle, *Chem Ber*., **1957**, *90*, 1656.
11. R.C. Miller, J.S. Bradley, L.A. Hamilton, *J. Am. Chem. Soc*., **1956**, *78*, 5299.
12. K. Issleib, A. Brack, *Z. Anorg. Allg. Chem*., **1954**, *277*, 258.

13. W.A. Higgins, P.W. Vogel, W.G. Craig, *J. Am. Chem. Soc.*, **1955**, *77*, 1864.
14. P.G. Jones, D. Henschel, A. Weitze, A. Blaschette, *Z. Anorg. Allg. Chem.*, **1994**, *620*, 1037.
15. A. Weitze, A. Blaschette, D. Henschel, P.G. Jones, *Z. Anorg. Allg. Chem.*, **1995**, *621*, 229.
16. M.J. Begley, D.B. Sowerby, D.M. Wesolek, I. Haiduc, C. Silvestru, *J. Organomet. Chem.*, **1986**, *316*, 281.
17. G.E. Coates, R.N. Mukherjee, *J. Chem. Soc.,* **77**, 1955, 1864.
18. I. Haiduc, I. Silaghi-Dumitrescu, R. Grecu, R. Constantinescu, L. Silaghi-Dumitrescu, *J. Mol. Struct.*, **114**, 1984, 467.

STUDIA UNIVERSITATIS BABEŞ-BOLYAI, CHEMIA, LI, 1, 2006

FLAME ATOMIC EMISSION SPECTROMETRY DETERMINATION OF CESIUM IN MINERAL AND WELL WATERS USING A METHANE-AIR FLAME

LADISLAU KÉKEDY-NAGY* AND EUGEN DARVASI

ABSTRACT. Effects of flame composition, the observation height and the spectral bandpass of the monochromator on the emission of Cs in methane-air flame were studied and optimized. The best results were obtained using the 852.19 nm Cs line at the observation height of 11 mm, with the flame composition of 1.12 (relative stoichiometric units) and the slit width of 0.8 mm. The effect of Li, Na, K, Rb, Mg, Ca, Sr, Zn, Al and PO_4^{3-} on the emission of Cs was studied too. The detection limit of 3 ± 1.4 $\mu g.L^{-1}$ was obtained, in the presence of 200 $mg.L^{-1}$ K, at a significance level of 0.05. The Cs content of mineral and well waters was determined without prior concentration by using both the external calibration and standard addition method. The results of these methods show good agreement implying the use of background correction.

Keywords: Cs, FAES, Water analysis

1. Introduction

Cesium is one of the widespread trace elements of the environment, its relative quantity in the Earth crust being of 7.10^{-5} %. It is distributed unequally in different environmental compartments; the mean Cs content of the rocks is of 0.7 $mg.kg^{-1}$, of the soils is of 3 $mg.kg^{-1}$. The seawater contains in average only 50 $ng.L^{-1}$ while the surface waters of 200 $ng.L^{-1}$, respectively. Higher concentrations of Cs occur in minerals (as pollutite, $CsAlSi_2O_6$), in certain volcanic rocks (in avogadite as $CsBF_4$) or can accompany certain minerals, as biotite and leopoldite, Cs content of which could reach 4.5 % of Cs.

Cs has no special physiological role. Plants (as barley, lichens), wild mushrooms and microorganisms (as *Escherichia coli*, *Anabaena.variabilis, Chlorella salina, Saccaromyces cerevisiae, Streptomyces lividans* etc.*)* accumulate primarily Cs *via* K^+ transport in their organisms [1–6]. More harmful, with high biological risks, are the radioisotopes of Cs (^{134}Cs and ^{137}Cs), the main by-products of nuclear fission, being γ emitters with the half-life of 3 h and 33 years, respectively. Therefore, the main accent falls on the quantification of the Cs radioisotopes, most of the papers in this field workout

* Corresponding author. Tel.: +40-264-593833; fax: +40-264-590818. E-mail address: lkekedy@chem.ubbcluj.ro
"Babeş-Bolyai" University, Faculty of Chemistry and Chemical Engineering400028 Cluj-Napoca, Arany J. 11, Romania

radio-analytical method. Flame atomic absorption spectrometry (FAAS) is the standard method for the determination of the total Cs content of different samples, including natural waters, regardless of their origin. The determinations are carried out at 852.19 nm atomic line; the detection limits are in the order of magnitude of $\mu g.L^{-1}$ [7]. Due to the low Cs content of natural waters, the analyte is usually separated and preconcentrated prior measurements by passing through a Dowex 50–X8 resign column, followed by either an ammonium hexacyanocobalt ferrate or potassium hexanitrocobaltate column [8]. Flame atomic emission spectrometry (FAES) is also used for the quantification of Cs. The determinations are carried out either at the Cs 455.54 or the 852.19 nm atomic line; the detection limits being of order of 0.1 $\mu g.L^{-1}$. The common feature of these methods consists of the use of high temperature C_2H_2–air or C_2H_2–N_2O flames wherein Cs easily excites and ionizes, due to its low excitation and ionization energies, of 1.386 and 3.89 eV, respectively. The ionization is suppressed by adding KCl solution in 1 % final concentration in the sample [8–10]. From this point of view the cooler flames, as H_2–air, propane–butane–air (PB–A), natural gas–air (NG–A) or methane–air (M–A) flames seems to be more advantageous for the direct quantification of Cs in low concentrations. So the lowest detection limits, of 30 $fg.mL^{-1}$, have been obtained in hydrogen and propane flames using the electron avalanche amplification of the laser enhanced two-step ionization of Cs [11].

The PB–A and NG–A flames are used in low performance commercial flame–photometers for the determination of alkaline metals designated for routine analyses. The M–A flame has similar properties (temperature, burning velocity etc) with the former ones [12, 13]. To our best knowledge the behaviour of Cs in the M-A flame has not yet been studied, nor the determination of Cs content of natural waters using this flame. The aim of this work is to study the behaviour of this element in the M–A flame, to optimize instrumental parameters and to determine the Cs content of natural waters, respectively.

2. Experimental

The optimal flame and instrumental parameters were established as follows: first, the emission spectrum of Cs was identified in the M-A flame; then the flame parameters (flame composition, observation height over the burner head (h)) have been optimized. In the following step the detection limit was determined under optimized conditions. Finally, the Cs content of some natural waters was determined.

2.1. Instrumentation

A HEATH–701 (Heath Co., Benton Harbour, MI, USA) spectrophotometer with a HEATH EU–700 scanning monochromator, a HEATH EU–700–30 type photomultiplier module and a M12FC51 (NARVA,

Germany) photomultiplier (–1200 V) was used. The photomultiplier signal was introduced via a home made A/V converter/amplifier unit and data acquisition card (Decision–Computer International Co. Ltd., USA) into an IBM Pentium II PC (120 MHz, 32 Mb RAM) and processed using a home written Qbasic software program. The boxcar average technique was used, with data sampling interval of 0.33 ms. One measurement point was the average of 1500 consequent individual readings. The final data represented the mean value of the 50 measurement points. The other instrumental setup was the same as described earlier [14].

2.2. Chemicals

Stock solutions of Cs, Na, K, Li, Rb, Ca, Sr, Zn, Al, Mg and PO_4^{3-} were of 1000 $mg.L^{-1}$, prepared from RbCl, CsCl, Li_2CO_3, H_3PO_4 (Merck, Darmstadt, Germany), NaCl, KCl (Reactivul, Bucuresti, Romania), $CaCO_3$, $SrCO_3$, Mg, Zn and Al (Specpure, Johnson Matthey Chemicals Limited, England), respectively. The calibration solutions were obtained daily by diluting a given volume of stock solution with double distilled water.

2.3. Sampling and Sample Handling

The well water samples were collected in village Săvădisla (county Cluj), located 24 km's north-west from Cluj-Napoca city. The waters were sampled, handled and conserved in accordance with the EPA-recommendations [7]. The determinations were carried out within 72 hours after sampling. The mineral waters (commercial available, "Harghita", "Tuşnad", "Dorna", "Izvorul Minunilor") were analyzed after the sealed bottles were opened and degassed by shaking. All water samples were sprayed directly into the flame-photometer without any other treatment.

2.4. Procedure

The behaviour of Cs in the M-A flame was studied up to h = 18 mm over the burner head in 1 mm steps, at three different flame compositions: 0.88; 1.00; 1.12 (expressed in relative stoichiometric unit - RSU). Four replicate measurements were made; the mean and the standard deviation, the S/N and the S/B ratios were calculated for each h and flame composition. The homogeneity of the means was tested too by the F test at the significance level of 0.05. The sensitivity of the amplifier was set properly for each spectral domain, depending on the intensity of the emission lines and the background observed. For a given set of determinations, the sensitivity was kept constant.

3. Results and Discussion

3.1 The Emission Spectrum of Cs, Determination of the Analytical Emission Line

First the emission spectrum of Cs was determined by recording the spectrum of the flame alone, then that of the flame in the presence of Cs by spraying a solution of 100 mg.L^{-1} Cs in the flame. The spectra were recorded in the 300–900 nm domain with a scanning rate of the monochromator of 0.02 nm.sec^{-1}. The composition of the flame was kept constant, of 1.12 RSU. Using spectral tables the emission lines with wavelengths of 455.54 nm, 459.32 nm, 852.19 nm and 894.35 nm were identified [10]. These are all atomic lines, the most intensive ones being of 852.19 nm and 455.54 nm, respectively.

The change of the analytical signal versus h at the formerly detected wavelengths was studied further. The concentrations of the calibration solutions were different, in function of the intensity of Cs emission line under study. The background intensity was measured in all cases in the presence of Cs, at the wavelengths of 457.0 nm, 461.0 nm, 854.0 nm and 896.0 nm, respectively. The variation of the net emission signal of different Cs lines versus h over the burner head is represented in Fig.1.

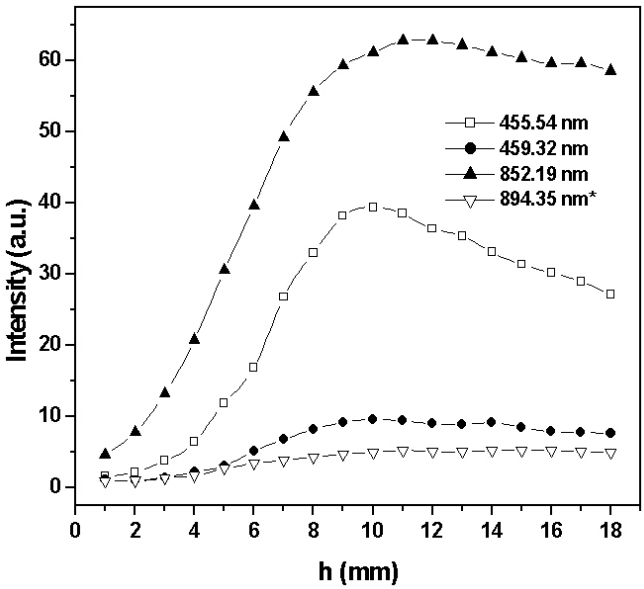

Figure 1. Variation of the net emission signal of the Cs lines vs. h.
* not in scale (5 x magnification)

For the quantitative comparison of the results obtained at different wavelengths only the maximum value of the net analytical signal (I) for each line was selected. The relative intensity (I_{rel}) for each line was calculated too. The reference concentration was of 100 $mg.L^{-1}$, the sensitivity the highest value used and the reference line was the weakest one. The S/B ratio was determined in the same way, the reference concentration being the highest one used. The results are summarized in Table 1.

Table 1. The relative intensities of the emission lines of Cs in the M–A flame

Wavelength (nm)	I (a.u.)	h (mm)	I_{rel}	S/N	S/B
455.54	39.4	10	75.76	296.5	6.9
459.32	9.6	10	18.46	72.2	2.0
852.19	62.8	11	120.76	468.7	157.0
894.35	0.52	11	1.00	4.2	2.5

The most intensive Cs line is that of 852.19 nm, superimposed on the low value of the background (high S/B ratio). For analytical purposes the 455.54 nm line could be used too, but in less favorable conditions than the former. The intensity of each Cs line varies in the same manner as the translational temperature of the flame, the maximum intensity being at 10–11 mm over the burner head [15] (see Fig.1.). In conclusion the analytical emission line for Cs in the M-A flame is that of 852.19 nm at h = 11 mm.

3.2. Determination of the Optimal Values of the Flame Composition and the Height of Observation Over the Burner Head

The influence of the flame composition, on h, on the analytical signal and S/N ratio for the most sensitive line was studied, at the concentration level of 10 $mg.L^{-1}$. The data were processed using the MicroCal Origin™ Software package, version 5 (MicroCal Software Inc., MA, USA) and plotted as 2D contour map (Fig.2).

The results show that the maximum intensity is obtained in all cases at the same h = 11 mm over the burner head, regardless of the flame composition. The analytical signal decreases slightly with the decrease of the methane content in the flame. The standard deviations of all means are homogeneous; therefore the magnitude of the S/N ratio is decided by the magnitude of the mean. In conclusion, the optimal conditions for the quantitative determination of Cs in the M–A flame are λ = 852.19 nm, h = 11 mm, flame composition of 1.12.

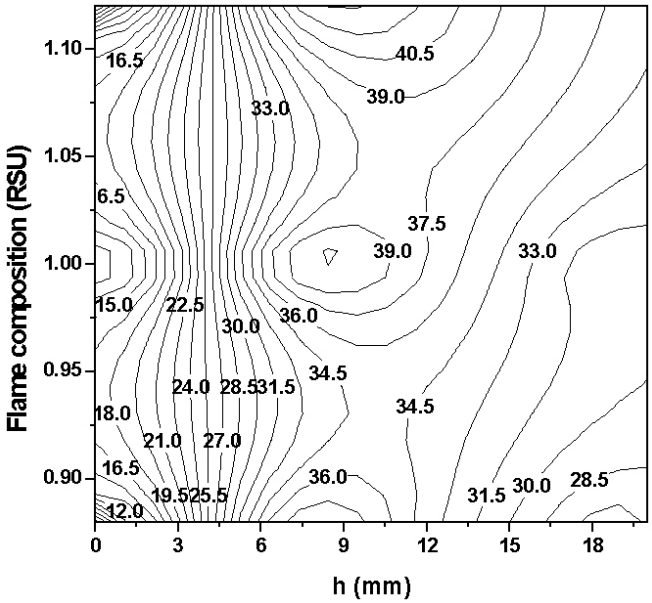

Figure 2. The 2D contour map of the emission of the 852.19 nm Cs line vs. observation height and flame composition. The data labels on the plot indicate the grid matrix values.

3.3. The Influence of the Spectral Bandpass of the Monochromator on the Analytical Signal, S/N and S/B Ratio

The spectral bandpass of the monochromator, determined by its width of the slit (SW), influences in different manner the amplitude and the fluctuations of the emission signal. Therefore the optimal width of the slit for which the S/N ratio is maximum can be determined. The flame and instrumental parameters used were the optimal ones, determined earlier. The influence of the width of slit over I and S/N ratio was studied in the 0.1–1.5 mm domain in steps of 0.1 mm. The analytical signal exhibits a linear variation with the slit width up to 1.5 mm, the I–SW relationship could be approximated with a linear function ($I = -43.986 + 0.7608\ SW$, $R^2 = 0.9994$). The standard deviation of the means is homogeneous up to a width of 0.8 mm and then they differ significantly. The highest value for the S/N ratio was found at a value of the width of 0.8 mm. In conclusion, the width of the slit could be increased up to 0.8 mm without decay of the S/N ratio.

3.4. Interferences

The effect of Li, Na, K, Rb, Mg, Ca, Sr, Zn, Al and PO_4^{3-} ions on the emission signal of Cs of 1 $mg.L^{-1}$ was investigated, up to a concentration of the interferent of 500 $mg.L^{-1}$. Some of these elements are potential inorganic interferents, present in natural waters at higher concentrations. The optimal experimental conditions were described in a previous paragraph. The background signal was measured at 854.0 nm in the presence of the interferent. The variation of the emission signal of Cs versus the concentration of the interferents is represented in Fig. 3.

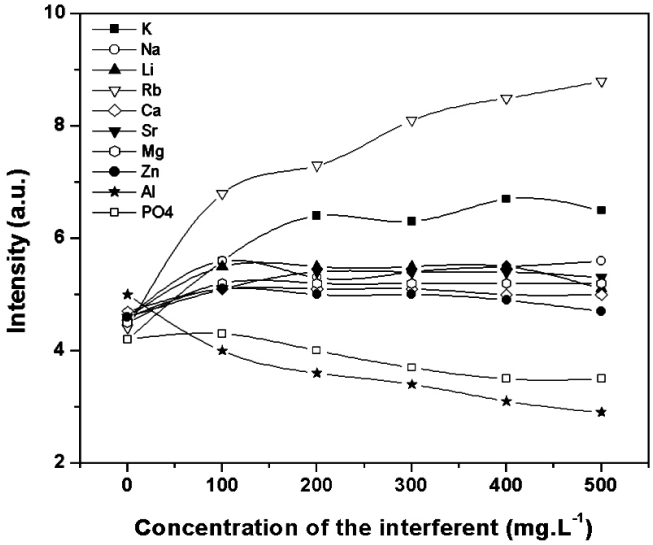

Figure 3. Influence of Li, Na, K, Rb, Ca, Sr, Mg , Zn, Al and PO_4^{3-} on the emission of Cs of 1 $mg.L^{-1}$

The alkaline metals K and Rb, acting as ionization suppressors, enhance the emission signal of Cs up to an excess of 200 and 100 times, respectively. Both Al and PO_4^{3-} decrease significantly the emission signal of Cs, probably due to a low evaporation rate of Cs from the condensed phase in the M–A flame. The other interferents do not influence the Cs emission, even at higher concentrations.

3.5. Calibration, Determination of the Detection Limit

For the determination of the detection limit the variation of the analytical signal versus concentration was studied. Five calibration curves were plotted, in the $10–10^{-2}$ $mg.L^{-1}$ Cs concentration range. Each calibration curve was established by using six standard solutions and covers only one

order of magnitude of concentration. Six replicate measurements were made at each concentration level. There were tested the homogeneity of means and the linearity of the calibration curve, the equation of the regression line, the confidence limits and the coefficient of correlation (R^2), with the least squares method were calculated. The detection limit was calculated using the two-step Neyman-Pearson criteria at the significance level of 0.025 [16,17]. The results are summarized in Table 2.

Table 2. Calibration curves and detection limits (n = 6)

No. eq.	Concentration range Cs ($mg.L^{-1}$)	Slit width (mm)	Equation of the calibration curve	Detection limit ($mg.L^{-1}$)
1	1 – 10	0.1	$I = -1.0407 + 1.7398C$ $R^2 = 0.9991$	0.4 ± 0.14
2*	1 – 10	0.1	$I = 0.6355 + 3.0495C$ $R^2 = 0.9994$	0.2 ± 0.09
3@	1 – 10	0.1	$I = 0.4992 + 2.8415C$ $R^2 = 0.9992$	0.3 ± 0.24
4*	0.1 – 1	0.1	$I = -0.0226 + 3.6297C$ $R^2 = 0.9983$	0.15 ± 0.06
5*	0.01 – 0.1	0.8	$I = 0.0287 + 38.727C$ $R^2 = 0.9964$	0.003 ± 0.0014

* with K added, in final concentration of 200 $mg.L^{-1}$
@ with Rb added, in final concentration of 100 $mg.L^{-1}$

Cs exhibits linear dynamic range in the 1–10 $mg.L^{-1}$ concentration domain in the presence of K of 200 $mg.L^{-1}$, used as ionization suppressor. Rubidium has the same effect (Table 2, Eq.(3)), but in lesser extent. On the other hand the presence of Rb increases the noise level of the determinations, namely the instability of the flame, as compared with K. The increased slit width up to 0.8 mm allows the signal enhancement and the extension of the usable concentration about one order of magnitude. The detection limit obtained for each concentration range is also summarized in Table 2. The lowest detection limit, of 3 ± 1.4 $\mu g.L^{-1}$, obtained with the M–A flame is the same order of magnitude with those obtained with the hotter (C_2H_2–air and C_2H_2–N_2O) flames.

4. Determination of Cs in Water Samples

The Cs content of the water samples was determined by calibration and the standard addition method, the latter being used as reference method for the method validation, in the absence of certified reference material. The determinations were carried out with the SW of 0.8 mm. The other parameters were the optimal ones. Four parallel measurements (n = 4) were made in

all cases. Two sets of standard calibration solutions were prepared. One set contained the analyte in the presence of K of 200 $mg.L^{-1}$. In order to ensure the same evaporation conditions with the well water samples, the other set contained K, Na, Ca, Mg, as matrix, in the same concentration level as the well waters (K, Na of 100 $mg.L^{-1}$ and Ca, Mg of 50 $mg.L^{-1}$, respectively). The K, Na, Ca, Mg content of these samples has been determined earlier [18, 19]. In the case of standard addition method 100 µL of Cs stock standard was added to the 20 mL of sample. Three additions of standard were made, in 0.025 $mg.L^{-1}$ concentration steps. Using the data set, the reproducibility of the standard addition method was tested first. The recoveries found were within 88.2–132.3%, the slope of regression lines being close to that obtained by standard calibration. The results obtained with the standard calibration using K of 200 $mg.L^{-1}$ are systematically lower with 10–66 % than those obtained with the synthetic well water. This fact suggests the presence of the evaporation interference in the flame due to the high salinity of the well waters. For further considerations only the last case values were taken into account. The results of the two methods (Table 3) agree within the error of determinations for the given water. The confidence limits are wide due to the high noise level of the determinations close to the detection limit. The calibration method using synthetic well water could be used for quantification.

Table 3. Results of analysis of water samples (n = 4)

Sample		Concentration ($\mu g.L^{-1}$, by calibration)	Concentration ($\mu g.L^{-1}$, by standard addition)
Mineral water	"Harghita"	11 ± 1.6	12 ± 1.5
	"Tuşnad"	8 ± 1.7	7 ± 2.1
	"Dorna"	4 ± 1.6	4 ± 1.9
Well water	no.1	< 3 ± 1.4	< 3 ± 1.4
	no.2	3 ± 1.7	3 ± 1.4
	no.3	5 ± 1.6	6 ± 0.9
	no.4	5 ± 1.6	7 ± 1.1
	no. 5	7 ± 1.7	7 ± 1.4
	no. 6	10 ± 1.5	8 ± 1.9

The mineral water "Harghita" and "Tuşnad" have close Cs content, originating from the same volcanic region of the country (as indicated on the label of the bottles).

The well water samples nos.1–4 have practically the same Cs content, the wells being sunk very close one to the other (about 20 meters).

The other samples (nos.5–6), collected from another site of the village, have significantly higher Cs contents. The potassium and rubidium

content of these samples are higher too as well as the K/Rb and K/Cs concentration-ratios [14, 19]. These facts show that the wells from different sites are supplied from other ground water sources, being sunk in rocks with different geological structure and chemical composition. The high alkaline metal content of the waters suggests the presence of rock salt bulbs or layers stratified among the sedimentary structures.

In conclusion, the Cs content of mineral and well waters can be determined directly in the M–A flame with acceptable precision by calibration method using synthetic well waters and background correction.

5. Conclusions

In the M–A flame Cs exhibits only an atomic spectrum. The most intense line is at 852.19 nm. The optimal excitation zone is at 11 mm over the burner head, in fuel rich conditions. The observation height for the maximum intensity is independent of the flame composition. In order to increase the S/N ratio, and to make the detection limit lower, the width of the slit of the monochromator could be increased till 0.8 mm without decay of the S/N ratio. The calibration curves for the 852.19 nm Cs line are linear in the 10–0.001 $mg.L^{-1}$ concentration range; the detection limit obtained is of 3 ± 1.8 $\mu g.L^{-1}$ Cs. The ionization of Cs most efficiently is suppressed with 200 $mg.L^{-1}$ K. The Cs content of mineral and well waters can be determined with acceptable precision using the calibration method and background correction.

REFERENCES

1. E.F. Elstner, R. Fink, W. Holl, E. Lengfelder, H. Ziegler, *Oecologia*, **1989**, *80*, 173
2. D. Bossemeyer, A. Schlosser, E.P. Bakker, *J. Bacteriol*.,**1989**, *171,* 2219
3. S.V. Avery, G.A. Codd, G.M. Gadd, FEMS *Microbiol. Lett*., **1992**, *95,* 253
4. S.V. Avery, G.A. Codd, G.M. Gadd, *Biochem. Soc. Trans*., **1995**, *23*, 468S
5. M.J. Hoptroff, S. Thomas, S.V. Avery, Can. *J. Microbiol*., **1997**, *43*, 954
6. F. Kato, C. Kuwahara, A. Oosone *at.al*., *J. Health Sci*., **2000**, *46*, 259
7. Standard Methods for examination of water and wastewater, 19th Edition, Ed. M.A.H. Franson, A.D. Eaton (AWWA), L.S. Clesceri (WEF), A.E. Greenberg (APHA), 1995, p. 3-13
8. K. Güçlü, R. Apak, E. Tütem, G. Atun, *J. Radioanal Nucl. Ch*., *2004*, **259**, 209
9. J.D. Winefordner, Spectrochemical methods of analysis, New York., Wiley Interscience, 1971, p. 131
10. R. Mavrodineanu, H. Boiteux, Flame spectroscopy, John Wiley, New York, 1965, p. 369

11. J.P. Temirov, O.I. Matveev, B.W. Smith, J.D. Winefordner, *Appl. Spectrosc*., *2003*, **57**, 729
12. A.G. Gaydon, H.G. Wolfhardt, Flames, their Structure, Radiation and Temperature, Chapman and Hill, New York, 1970
13. C.S. Mc.Enally, L.D. Pfefferle, R.K. Mohammed, M.D. Smoke, M.B. Colket, *Anal. Chem.*, **1999**, *71*, 364
14. L. Kékedy-Nagy, E.A. Cordoş, *Talanta*, **2000**, *52*, 645
15. E. Cordoş, L. Kékedy-Nagy, *Studia Universitatis Babeş-Bolyai, Chemia*, **1992**, *37*, 61
16. C. Liteanu, I. Rîcă, Statistical Theory and Methodology of Trace Analysis, John Wiley, New York, 1980.
17. D.L. Massart, B.G.M. Vandeginste, S.N. Deming, Y. Michotte, L. Kaufman, Chemometrics: a textbook, Elsevier, New York, 1988
18. L. Kékedy-Nagy, E.A. Cordoş, *Studia Universitatis Babeş-Bolyai, Chemia*, **1999**, *44*, 183
19. L. Kékedy-Nagy, E.A. Cordoş, *Studia Universitatis Babeş-Bolyai, Chemia*, **2000**, *45*, 263

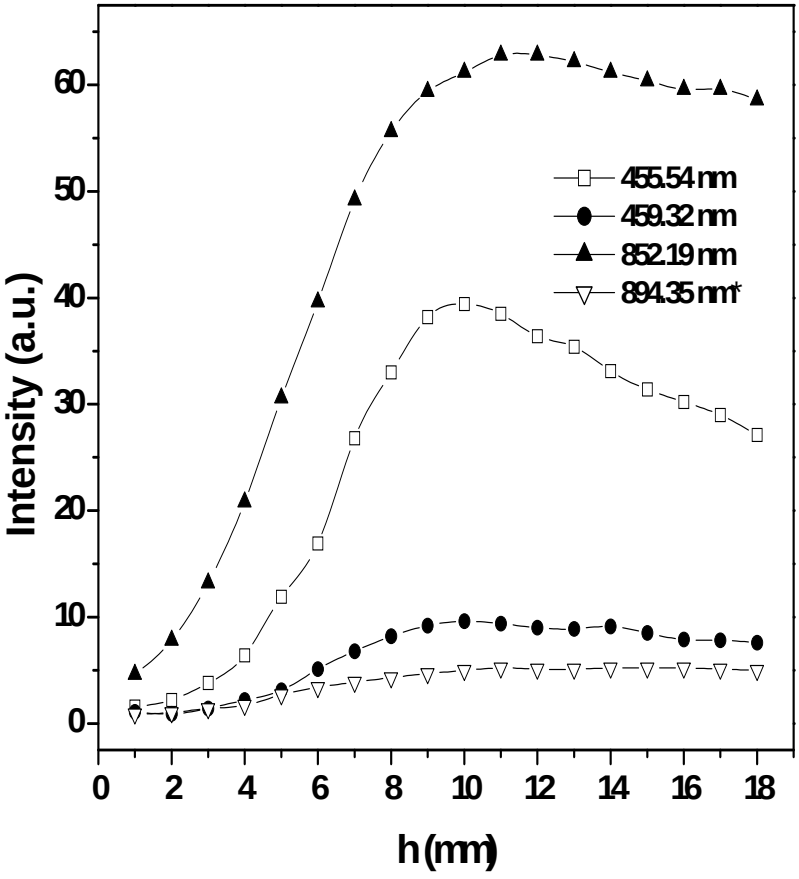
Intensity (a.u.)
h (mm)
455.54 nm
459.32 nm
852.19 nm
894.35 nm*
0
10
20
30
40
50
60
0
2
4
6
8
10
12
14
16
18

Figure 1.

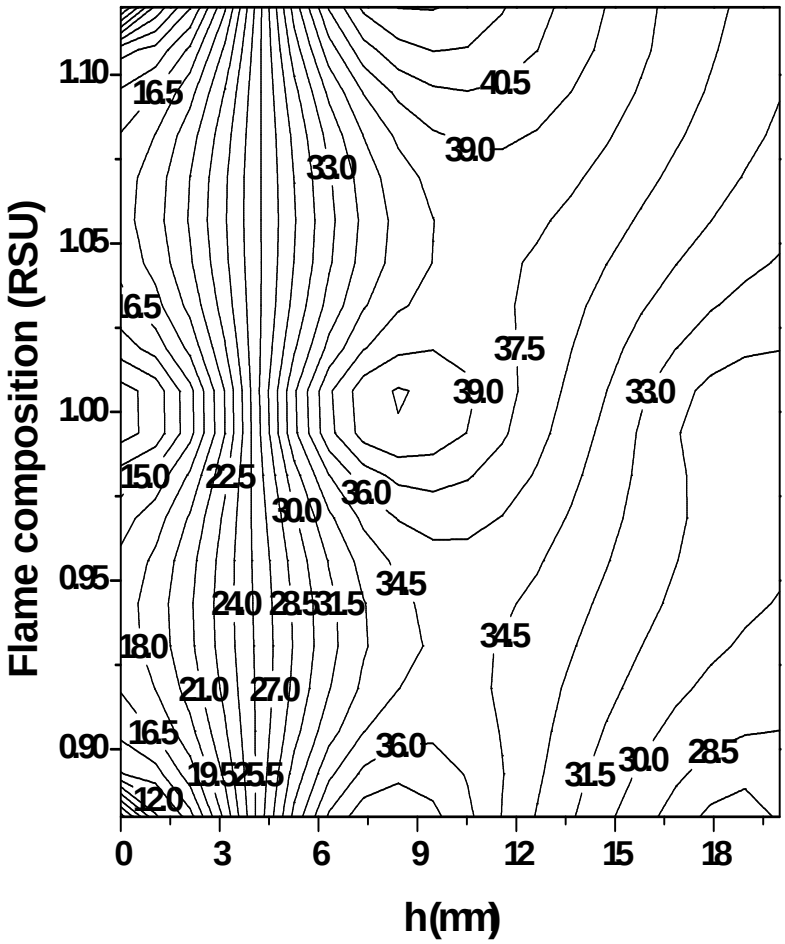
Flame composition (RSU)
h(mm)
1.10
1.05
1.00
0.95
0.90
0
3
6
9
12
15
18
16.5
40.5
39.0
33.0
6.5
37.5
39.0
33.0
15.0
22.5
30.0
36.0
34.5
24.0
28.5
31.5
18.0
34.5
21.0
27.0
16.5
36.0
19.5
25.5
31.5
30.0
28.5
12.0

Figure 2.

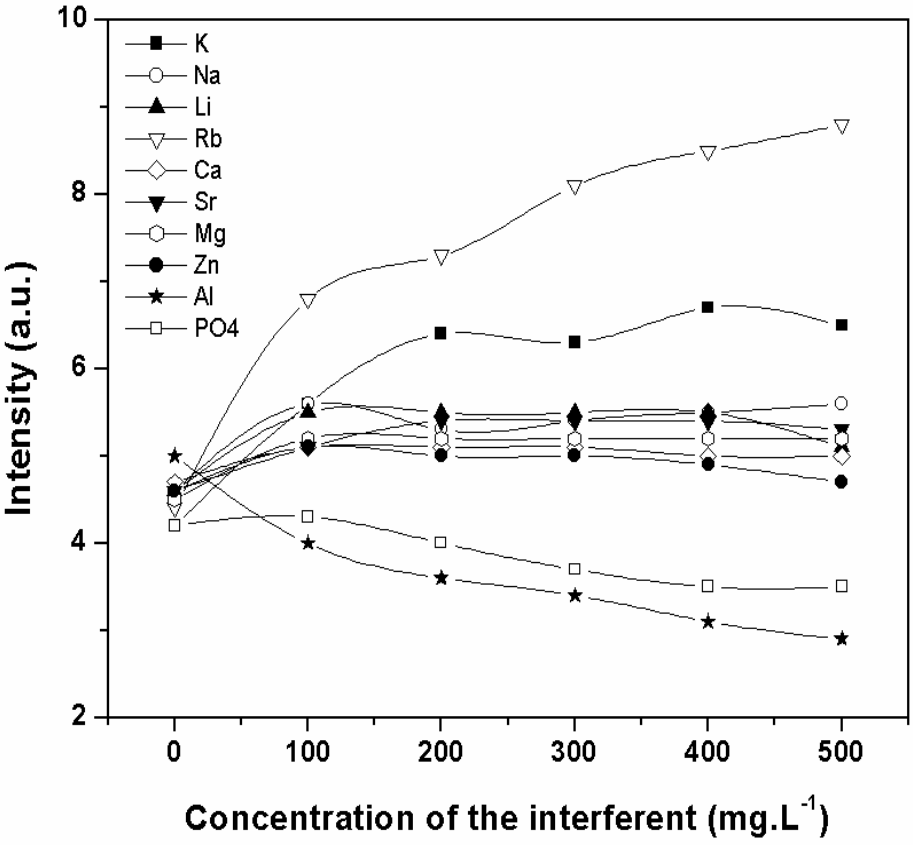
K
Na
Li
Rb
Ca
Sr
Mg
Zn
Al
PO4
Intensity (a.u.)
10
8
6
4
2
0
100
200
300
400
500
Concentration of the interferent (mg.L-1)

Figure 3.

STUDIA UNIVERSITATIS BABEŞ-BOLYAI, CHEMIA, LI, 1, 2006

ANALYSIS OF FREE AMINO ACIDS FROM PLANT EXTRACTS BY CHROMATOGRAPHIC METHODS

MONICA CULEA[1], SORIN HODISAN[2], ANAMARIA HOSU[3], CLAUDIA CIMPOIU[3,*]

Dedicated to Professor Sorin Mager
on the occasion of his 75th birthday

ABSTRACT. Three modern techniques: thin-layer chromatography (TLC), high performance liquid chromatography (HPLC), and gas chromatography-mass spectrometry (GC-MS) have been used for separation, identification and quantitative determination of free amino acids from *Equisetum arvense* and *Ocimum basilicum*. The results of this research explain the utilization of *Equisetum arvense* and *Ocimum basilicum* leaf extracts in phytopharmaceutical and cosmetic products.

Keywords: plant extract; chromatographic methods; separation; identification; quantitative determination

1. Introduction

Natural compounds offer without doubt the richest resources of chemical diversity. In the last decade the pharmaceutical and cosmetic industries have been extensively using medicinal plant. Isolation, identification and quantitative determination of the active compounds from plant extracts are some of the oldest fields for the application of chromatographic methods for studying the structure-activity relationship.

Chromatographic methods allow separation and identification of biological active compounds such as: amino acids, peptides, flavones, sugars, tannins, organic acids etc., their metabolites and intermediaries which do not display biological activity [1].

Thin-layer chromatography (TLC) is advantageous in separation and identification of amino acids from plant extracts because multiple samples can be analyzed simultaneously in a short time, with low detection limits. A variety of adsorbents such as silica gel [2], modified silica gel [3, 4], polyamide [5], alumina and cellulose [6] can be used for one- or two-dimensional separation of

[1] "Babeş-Bolyai" University, Faculty of Physics, 1 M. Kogalniceanu, 400084 Cluj-Napoca, Romania
[2] University of Oradea, Faculty of Sciences, 5 Armata Română, 410087 Oradea, Romania
[3] "Babeş-Bolyai" University, Faculty of Chemistry and Chemical Engineering, 11 Arany Janos, 400028 Cluj-Napoca, Romania
[*] Corresponding author: email: ccimpoiu@chem.ubbcluj.ro

amino acids. The most frequently used mobile phase systems are n-butanol-acetic acid-water, phenol-water, and n-butanol-acetic acid-acetone-water.

Separation of amino acids can be achieved by high performance liquid chromatography (HPLC) on C-18 stationary phase using mixtures of acetonitrile-acetate, phosphate, and citrate or borate buffer as mobile phases [7, 8].

The detection has been done under UV light if the adsorbent had a fluorescent indicator or after derivatization with ninhydrine, dansyl chloride, phtalic anhydride, dimethylamino azobenzene isothiocyanate (DABITC), etc [9, 10].

The best results for the quantitative determination of amino acids have been obtained using the gas chromatography-mass spectrometry (GC-MS) technique [11, 12].

The aim of this paper is the analysis of free amino acids from *Equisetum arvense* and *Ocimum basilicum* leaf extracts using TLC, HPLC, and GC-MS techniques.

Equisetum arvense is an excellent astringent genito-urinary system. It is useful mild diuretic and it is use in the treatment of kidney and bladder problems, cystitis, urethritis, prostate disease and internal bleedings such as urinary bleeds and stomach ulcer [13]. *Equisetum* has been found to ease the pain of rheumatism and stimulate the healing of chilblains. It is restorative to damage pulmonary tissue after pulmonary tuberculosis and other lung disease. In cosmetic, it is good for splitting nails and lifeless hair [14].

Ocimum basilicum is use as a culinary and medicinal herb. It acts principally on the digestive and nervous systems: easing flatulence, stomach cramps, colic and indigestion, poor digestion, nausea, gastro-enteritis, in treatment of feverish (especially colds and influenza), migraine, insomnia, depression and exhaustion [13]. Externally, it is use to treat acne, loss of smell, insect stings, snake bites and skin imperfections [14].

2.Experimental

2.1. Materials

Standard amino acids, $Na_3P(W_3O_{10})_4$ and trifluoroacetic acid were obtained from Merck (Darmstadt, Germany). Acetyl chloride and ion exchange resins Amberlite IR 120H and Dowex 50W-X8 were from Fluka (Buchs, Switzerland). ^{15}N-glycine (Gly 98.9%) was obtained from ITIM (Cluj-Napoca). Thin-layer chromatographic separation of amino acids was achieved on 20x20 cm, 0.1 mm thick cellulose plates CEL 300-10UV254 (Macherey Nagel). All other chemicals obtained from Comchim Bucharest were analytical grade.

2.2. Extraction of Free Amino Acids

The isolation of amino acids can be done, from dry plants, using different extraction methods, such as: extraction with 5% NaCl solution, 75% ethanol,

0.25% NaOH, 0.25M HCl, metasiliconic acid or a CH_3COOH-HCl-H_2O (18:1:1 v/v/v) mixture [12].

In our experiments the isolation of amino acids from dry plant has been done using two different extraction methods. For TLC and HPLC experiments 0.5g dry plants were extracted in 10mL 1% HCl solution. Then a 10% $Na_3P(W_3O_{10})_4$ solution was used for removing proteins from the extract by precipitation. After centrifugation the clear solution was passed through an ion exchange Amberlite IR120H column eluted with 40mL ammonia solution. The obtained solution was evaporated to dryness and the residue was redissolved in 1mL aqueous solution 30% (v/v) iso-propanol. For GC-MS experiments 0.5g dry plant were extracted in ethanol. The amino acids were purified on a Dowex 50W-X8 exchange resins, in a 2x40 mm column and eluted with 3M ammonia solution.

2.3. TLC

Aliquot (1μL) of standard solutions of 17 essential amino acids (1ng/mL) and the extract solutions were applied as spots to the cellulose plates with a micropipette.

The separation and identification of the free amino acids from the standard samples and extracts were achieved by bidimensional TLC (2D-TLC). The compositions of mobile phase were optimized by "Prisma" method. The plate was eluted on the first direction with n-butanol-acetone (35:35, v/v) and acetic acid-water (7:23, v/v) prepared and mixed (1:1, v/v) before elution. The second mobile phase was methanol-water-pyridine (80:20:5, v/v/v). The elutions have been done in unsaturated N-chamber and the elution distance was 18 cm. After the elution the plates were dried in hot air. The detection has been done by spraying the plates with a 0.5% ninhydrine solution in ethanol then dried at 110^0C for 10-15 min. The identification of the amino acids was achieved by comparing the R_f values and the colors of the spots.

2.4. HPLC

The HPLC analysis amino acids from standard solution and from plant extracts were converted into their phenyl-thiocarbamilic derivatives.

The standard mixtures, the plant extracts (10μL) were analyzed by HPLC using a HPLC apparatus (Merck Hitachi D-2000) with a Spherisol 5 ODS-2 column (250 mm x 4.6 mm i.d.) and a mixture of 0.15M sodium acetate (pH 6.5)-acetonitrile, concentration gradient 5-22%, 1 mL/min, temperature 55^0C, and UV detection at 254 nm. The identification of derivatized amino acids was achieved by comparing the retention time values.

2.5. GC-MS

The amino acids were transformed into N-trifluoroacetil n-butyl ester to increase their volatility. Asparagine and glutamine were transformed into aspartic acid and glutamic acid, respectively. Hystidine and arginine were difficult to analyze by gas chromatography. [^{15}N]-glycine was used as the internal standard (10 μg/mL).

2.5.1. Derivatization

The amino acids were derivatized using two step derivatization procedure. The dry samples were esterified with 0.5mL distilled butanol-acetyl chloride (4:1, v/v) for 1h at 110^{0}C. The excess reagent was removed by bubbling nitrogen through the mixture. The amino group was acetylated with a 200μL mixture of trifluoroacetic anhydride (TFAA)-methylene chloride (1:1, v/v) at 60^{0}C for 30 min. After cooling, the excess reagent was removed by bubbling nitrogen then 1mL ethyl acetate was added.

2.5.2. GC-MS

A trace DSQ ThermoFinnigan quadrupol mass spectrometer coupled with a Trace GC was used. The amino acids derivatives were separated on Rtx-5MS capillary column, 30m x 0.25mm, 0.25μm film-thickness, using a temperature program from 50^{0}C to 300^{0}C (3 min) at 10^{0}C/min. The following conditions were followed: transfer line temperature 250^{0}C, injector temperature 200^{0}C, and ion source temperature 250^{0}C, splitter 10:1. Electron energy was 70eV and emission current 100μA. The flow rate of helium was 2mL/min. 40μg of each samples was injected into the column.

The identification of amino acids was carried out by comparing the MS spectra with those from Wiley spectra library.

The quantitative determination of glycine was performed by selected ion monitoring (SIM). The following peaks were monitored for quantitative analyses: 154, 155 m/z from glycine.

3.Results and Discussion

3.1. Separation and Identification of Free Amino Acids by TLC

The R_f values of standards amino acids eluted with two mobile phase systems are presented in Table 1. Some of these amino acids were separated using the first mobile phase. The second mobile phase system could separate the amino acids that are unseparated by the first one. Therefore, the bidimensional elution is recommended.

Table 1.
The R_f values of standard amino acids.

Amino acid	**R_{f1}** **BuOH-Acetone-HAc-H_2O** **(35 : 35 : 7 : 23, v/v)**	**R_{f2}** **MeOH-H_2O-Py** **(80 : 20 : 5, v/v)**
Glutamine (Glutamic acid)	0.77	0.68
Alanine	0.44	0.72
Proline	0.42	0.53
Tyrosine	0.33	0.14
Lysine	0.56	0.73
Phenylalanine	0.83	0.82
i-Leucine	0.85	0.92
Histidine	0.72	0.60
Serine	0.53	0.57
Valine	0.51	0.68
Asparagine (aspartic acid)	0.24	0.36
Methionine	0.81	0.78
Glycine	0.38	0.30
Arginine	0.50	0.43
Leucine	0.88	0.89
Threonine	0.51	0.68

The chromatographic results of bidimensional TLC analysis of studied plant extracts (Table 2) show the presence of glutamine, alanine, proline, glycine, lysine, phenylalanine, iso-leucine, asparagine, serine, threonine, methionine, valine and leucine in both *Equisetum arvense* and *Ocimum basilicum* extracts.

Table 2.
The R_f values of amino acids from plant extracts

Amino acid	***Equisetum arvense***		***Ocimum basilicum***	
	R_{f1}	**R_{f2}**	**R_{f1}**	**R_{f2}**
Glutamine	0.75	0.67	0.73	0.66
Alanine	0.43	0.73	0.42	0.74
Proline	0.41	0.55	0.42	0.54
Glycine	0.31	0.13	0.32	0.13
Lysine	0.55	0.74	0.54	0.73
Phenylalanine	0.82	0.84	0.83	0.83
i-Leucine	0.84	0.94	0.84	0.93
Asparagine	0.31	0.29	0.30	0.30
Serine	0.54	0.58	0.55	0.59
Threonine	0.52	0.70	0.51	0.70
Methionine	0.79	0.79	0.80	0.79
Valine	0.50	0.43	0.50	0.42
Leucine	0.86	0.91	0.87	0.90

The identification was made on the basis of R_f values. The intensity of spot colors is only informative because it is different for different amino acids due to different quantity of compounds or probably to differences between the sensitivity of the reaction with ninhydrine.

3.2. Separation and Identification of Free Amino Acids by HPLC

The separation of standard amino acids is presented in Figure 1 and HPLC separations of plant extracts are presented in Figure 2.

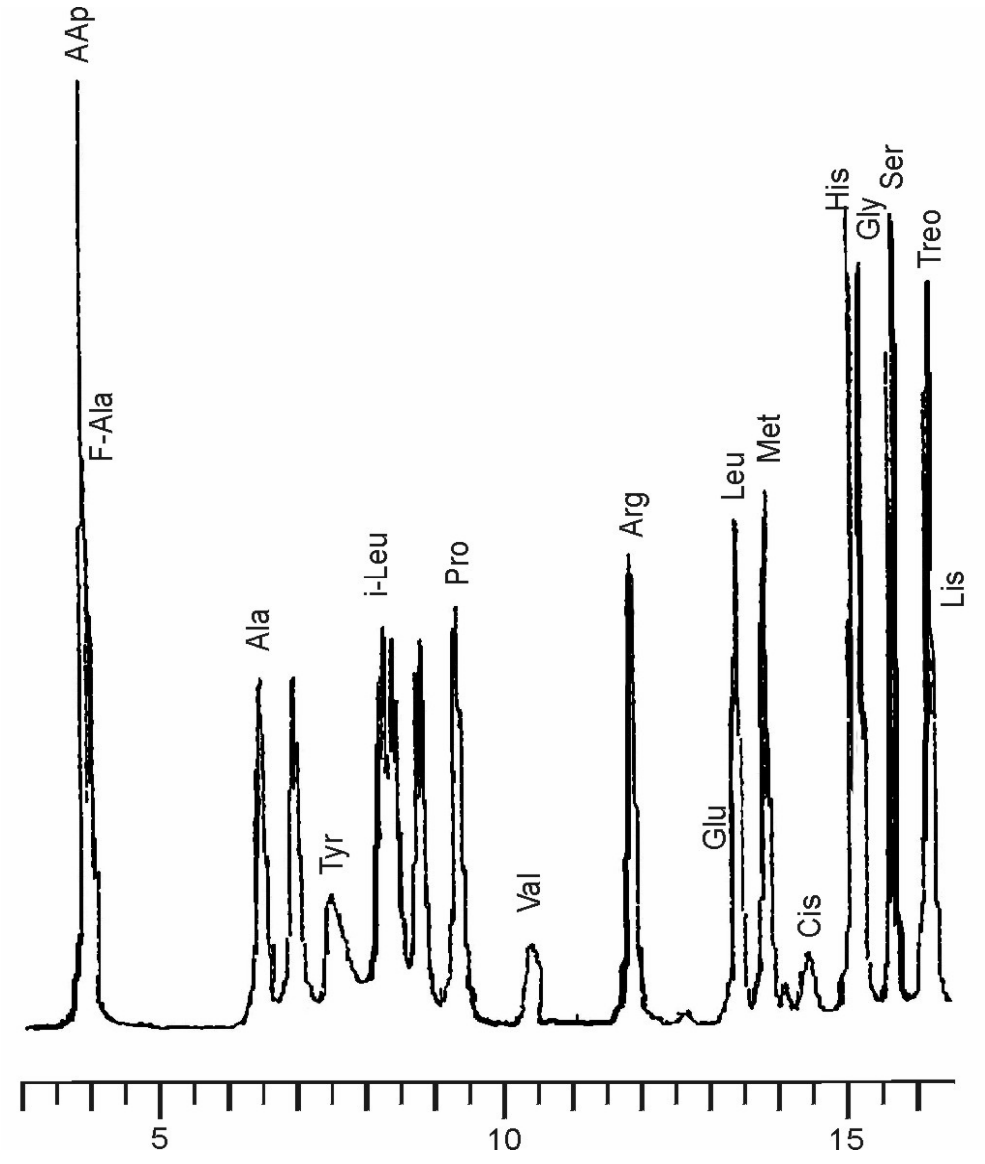

Figure 1.
The HPLC chromatogram of standard amino acids.

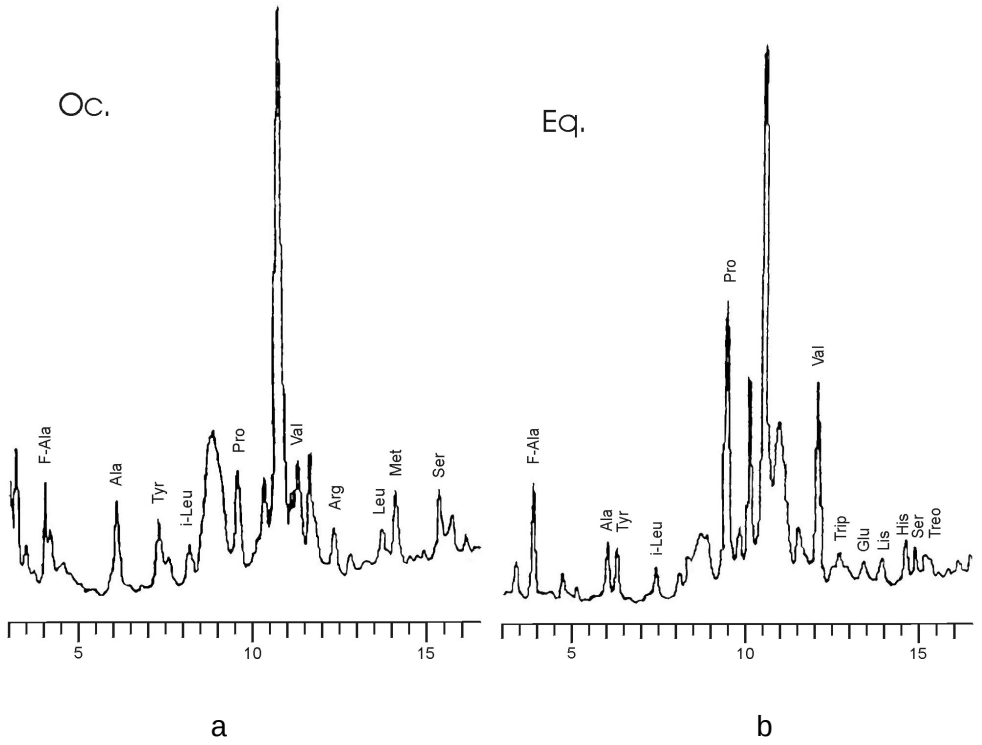

Figure 2.
The HPLC chromatograms of: a – *Ocimum basilicum*; b – *Equisetum arvense*

These figures show that the amino acids present are those identified by TLC: glutamine, alanine, proline, lysine, phenylalanine, iso-leucine, serine, threonine and valine in the *Equisetum arvense* extract and alanine, proline, phenylalanine, iso-leucine, serine, methionine, valine, and leucine in the *Ocimum basilicum* extract.

3.3. Separation, Identification and Quantitative Determination of Free Amino Acids by GC-MS

The results of quantitative determination are presented in Table 3. By GC-MS the presence of the same amino acids are confirmed. Glutamine, alanine, proline, glycine, lysine, phenylalanine, iso-leucine, asparagine, serine, threonine, methionine, valine, leucine, histidine, and tyrosine are the free amino acids from *Equisetum arvense* and *Ocimum basilicum* extracts determined by this method.

Table 3.
The GC results of quantitative determination of amino acid from plants extracts

Amino acid	**t_R**	**F**	***Equisetum arvense***		***Ocimum basilicum***	
			A (mm^2)	**C (μg/g)**	**A (mm^2)**	**C (μg/g)**
Alanine	12.75	0.77	1.04	8.65	0.96	8.27
Glycine	13.40	0.80	0.90	7.56	0.87	7.32
Threonine	14.81	0.20	0.05	1.65	0.11	3.51
Serine	15.28	0.20	0.09	3.01	0.38	12.82
Valine	15.76	0.84	0.89	7.09	1.20	9.56
Leucine	17.82	0.80	1.04	8.69	0.91	7.58
i-Leucine	18.11	0.80	0.49	4.12	0.37	3.06
Tyrosine	19.90	0.95	0.55	3.85	0.27	1.90
Proline	21.54	0.84	1.15	9.09	1.24	9.81
Metionine	24.91	0.39	0.08	1.36	0.45	7.69
Asparagine	27.73	0.88	1.07	8.07	2.35	17.84
Phenilalanine	27.90	0.82	1.30	10.53	2.38	19.34
Glutamine	30.90	1.00	2.07	13.77	2.81	18.75
Lysine	30.96	0.43	0.68	10.47	0.69	10.75
Histidine	35.93	0.51	0.07	0.98	0.23	3.02

4. Conclusions

The chromatographic methods allow the separation, the identification, and the quantitative determination of free amino acids from *Equisetum arvense* and *Ocimum basilicum* extracts. The important amino acids from *Equisetum arvense* and *Ocimum basilicum* are phenylalanine, asparagine, and lysine, which have an essential role in protein syntheses and in tissue regeneration, even if their concentration are small.

REFERENCES

1. V. A. Davankov, *Zavod. Lab.* **1992**, *58*, 1.
2. M. Ali, J. S. Qedry, *J. Ind. Hem. Soc.* **1987**, *64*, 230.
3. R. Bhusmsn, I. Ali, *J. Planar Chromatogr.-Mod. TLC*, **1990**, *3*, 85.
4. E. V. Brazhnikova, V. V. Pomazonov, *Zavod. Lab.* **1993**, *59*, 22.
5. M. DeLos Angelos Barcelona, *J. Chromatogr*., **1982**, *238*, 175.

6. R. Bhushan, J. Martens, in: *Handbook of Thin-Layer Chromatography*, J. Sherma, B. Fried (Eds.), Marcel Dekker Inc., New York 2003, pp. 373.
7. S. L. Da, X. Y. Li, Z. H. Wang, *Sepn*. **1992**, *10*, 248.
8. Y. Tsuruta, Y. Date, K. J. Kohashi, *J. Chromatogr*. **1990**, *502*, 178.
9. T. Cserhati, Z. Illes, *Chromatographia* **1993**, *36*, 302.
10. S. A. Cohen, *J. Chromatogr*. **1990**, *512*, 283.
11. M. Culea, S. Neamtu, N. Palibroda, M. Borza, S. J. Nicoara, *J. Mol. Struct*. **1995**, *348*, 377.
12. T. Hodisan, M. Culea, C. Cimpoiu, A. Cot, *J. Pharm. Biomed. Anal*. **1998**, *18*, 319.
13. FDA. Guidance for industry: Botanical drug products. Draft guidance. August 2000; www.fda.gov/cder/guidance/1221dft.htm
14. Romanian Pharmacopoeia 10, Bucharest, 2003.

STUDIA UNIVERSITATIS BABEŞ-BOLYAI, CHEMIA, LI, 1, 2006

STUDIES ON THE NATRIUM SULPHATE SALTING-OUT CRYSTALLIZATION II. CRYSTALLIZATION KINETICS

ADINA GHIRISAN, SIMION DRĂGAN, ALEXANDRU POP AND VASILE MICLĂUŞ*

ABSTRACT. The kinetic of nucleation and growing of the crystal nuclei in the salting-out crystallization of natrium sulphate were studied. The influence of kinetic parameters (energy consumption or *agitator power input*, temperature and growth rate) on the second nucleation was determined. The influence of the hydrodynamic conditions and of the temperature on the average size of the obtained crystals was discussed. A value of activation energy of $5.4 \bullet 10^4$ J/mol for the nucleation process was determined.

Introduction

A crystallization operation consists of three basic steps: supersaturation (or supercooling), formation of crystal nuclei, and the subsequent growth of these nuclei into crystals [1]. Supersaturation may be achieved by cooling, evaporation of the solvent, addition of a precipitating agent, as a result of a chemical reaction, etc.

The conventional process of natrium sulphate crystallization through evaporation has many disadvantages: the high-energy requirement, the complexity of the installation with many steps and the complex process of separation of the obtained Glauber salt [2].

By the salting-out crystallization, by adding organic alcohol (methanol or ethanol) the solubility of the solute in the solvent supersaturated solution was reduced [3]. The equilibrium study of the salting-out crystallization has shown several advantages [3]:

a). The process can be operated at low temperature without output or input of energy in the crystallizer;

b). The construction of the installation is simple with lower cost of equipment and

c). Very pure crystals can be obtained because of high retention for the impurities of the mixed-solvent mother liquor.

To have a complete information about the process evolution in the case of salting-out crystallization of natrium sulphate the equilibrium data obtained in the first part of our study [3] are not enough. It is necessary to know more about the factors that can influence the nucleation and the crystal

* Faculty of Chemistry and Chemical Engineering "Babeş-Bolyai" University, 400028 Cluj-Napoca, Romania

growth kinetics: intensity of mixing between organic and inorganic phases, concentration of the sulphate in aqueous solution, crystal size evolution, etc.

Nucleation

The generation of ultramicroscopic particles in the process of nucleation is the sum of contributions by primary and secondary nucleation. Primary nucleation occurs in the absence of crystals, while secondary nucleation is attributed to the influence of existing crystals.
The rate of primary nucleation has been modelled by the power law expression [4]:

$$B = \frac{dN}{dt} = k_n (C - C^*)^n \quad (1)$$

where *B* is the number of nuclei formed per unit volume per unit time, *N* – the number of new nuclei per unit volume, k_n – the rate constant, *C* – the instantaneous solute concentration, and *C** the solute concentration at saturation. The *(C-C*)* term is the driving force of the crystallization process, called the *supersaturation*. The exponent n is typically in the range of 3 to 4 [5].
When a supersaturated solution is in contact with particles of the crystallizing compound, secondary nucleation occurs. Experimental data from industrial crystallizers have indicated that secondary nucleation usually predominates. There are two types of secondary nucleation: shear nucleation and contact nucleation [3]. *Shear nucleation* occurs as a result of fluid shear on growing crystal faces, and *contact nucleation* happens because of crystal collision with each other and with the impeller and other vessel internal surfaces. The most widely used relation for the rate of secondary nucleation in crystallization is the following [6]:

$$B = \frac{dN}{dt} = k_B \cdot \rho_L{}^l \cdot (C - C^*)^b \quad (2)$$

where k_B is the rate constant and ρ_L is the suspension density. The exponent "*l* " ranges up 1.5, with 1 being the more probable value, the exponent *b* can be range up to 5 but has a most probable value of 2 [5].

Crystal growth

Crystal growth is the post nucleation process in which molecules are deposited on the surface of existing crystals. If crystal size is characterized by a characteristic dimension, *L*, it is convenient to express its linear growth rate by the equation [4]:

$$G \equiv \frac{dL}{dt} = k_g (C - C^*)^g \quad (3)$$

where L is a characteristic dimension of the crystal and k_g is an overall mass transfer coefficient; k_g is in general depended on the crystal size, hydrodynamic conditions, temperature, the nature of the ions and the presence of impurities.

Crystal growth is actually a process that consists of two steps in series. In the fist step the solute molecules or ions must reach the crystal surface by means of diffusion. In the second one, at the surface, the solute must be integrated into the crystal lattice. These two processes may be described as:

Diffusion: $$G = k_d (C - C_i)^d \quad (4)$$

Surface integration: $$G = k_r (C_i - C^*)^r \quad (5)$$

where C_I is the concentration at the interface between the liquid and the solid phase, k_d and k_r are the mass transfer coefficients. If surface integration is very fast compared with bulk diffusion, $k_r >> k_d$ and $k_g \approx k_d$.

In conclusion, the formation of a stable crystal nucleus in a homogeneous or a heterogeneous system is not an easy process. Not only must the requisite number of molecules agglomerate, but also they must become oriented into a fixed lattice.

In this research study we have tried to establish the crystal formation rate during salting-out crystallization of natrium sulphate considering the influence of different factors as density of suspension, power input as the specific consumption of energy for mass unit, and crystal growth rate and the efficiency of the separation process.

Experimental

The experimental research was carried out in a batch isothermal stirred vessel of 0.5 l, type MSMPR (Mixed Suspension, Mixed Product Removal), with a device for the measuring and controlling of the temperature. The used agitator is an impeller with diameter blade of 4 cm.

The growth rates were obtained through granulometric analysis. For the granulometric analysis the suspension samples collected in time were filtered, washed with alcohol, dried and then analysed by sieving. The nucleation rates were obtained from the induction time, defined as the time between realisation of the known supersaturation and the appearance of the visible crystal [7]. The numbers of the crystals were determined for a diluted sample using a Coulter-Counter device [7].

The intensity of the hydrodynamic conditions was evaluated by the energy consumption or power input.

The following parameters were investigated:

- the residence time in crystallizer 5 – 180 min,
- the consumption energy (agitator power input) 0.18 – 1.64 W/kg,
- the temperature 30 – 70 ^{0}C.

Results and Discussion

The Efficiency of Crystallization

In this paper the efficiency of crystallization is defined as the ratio between the experimental obtained mass and the theoretical mass of the crystals. The data obtained from Fig. 1 have pointed out that the efficiency of the crystallization depends on the temperature and residence time in the crystallizer at constant energy consumption. The diagram from Fig. 1 shows that at a *specific energy consumption* of 0.18 W/kg a higher than 90 % efficiency can be obtained only by a residence time of 120 minutes and a temperature of 70 ^{0}C. To explain this dependence we have performed some kinetic studies.

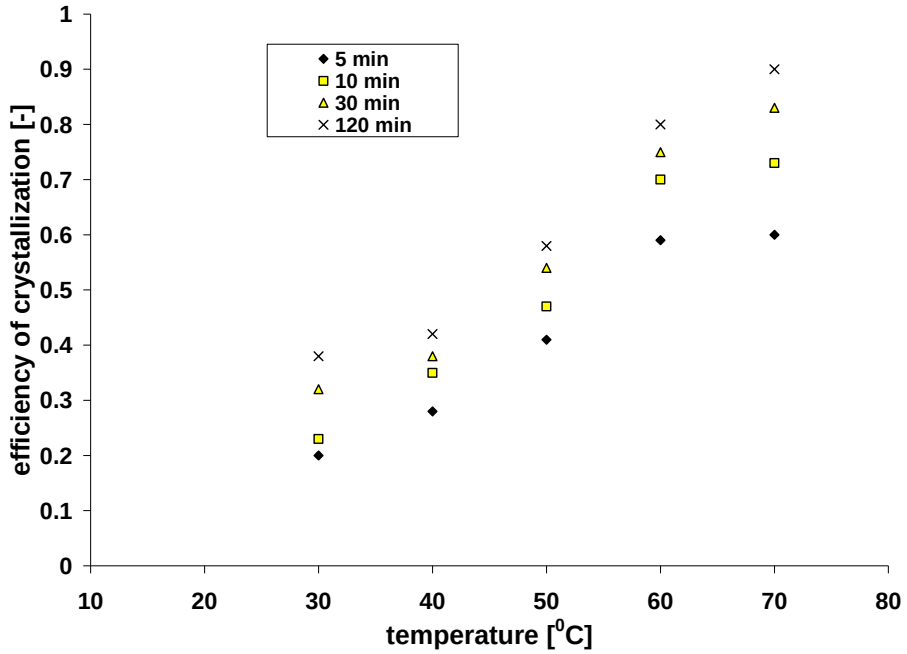

Fig. 1.
Efficiency of crystallization versus temperature at different residence timefor a power input of 0.18 W/kg.

Crystallization Kinetics

Estimates of nucleation and growth rates during crystallization can be obtained from the population balance analysis by batch experiments [4]. By making a mass balance on the number of crystals within a given size range between *L* and *L* +*ΔL*, the population balance equation for size independent growth in a perfectly mixed batch crystallizer with negligible breakage and agglomeration is:

$$\frac{\partial(nV)}{\partial t}+\frac{\partial(nVG)}{\partial L}=0 \tag{6}$$

where *n* is the population density defined as the number of crystals of specific size per unit volume of crystallizer (number/m^3m^1), *L*- size of crystals at time t (m), *G* – overall linear growth rate of crystals (m/s).

The mass balance in the MSMPR crystallizer with ideal mixing can be obtained using the equation data (solubility curve) and definition of the moments of distribution as pointed by Randolph [8]. For an MSMPR crystallizer with ideal mixing, with constant volume, without agglomeration and breakage, which means that the growth rate independent of the size of the crystal is, operating at steady state, a solution of population balance (equation 6) is:

$$n = n_0 \exp\left(-\frac{L}{G\cdot\tau}\right) \tag{7}$$

When $L \rightarrow 0$ the solution of equation (6) will be:

$$B_0 = n_0 \cdot G_0 \tag{8}$$

The equation (8) suggests that the secondary nucleation rate B_0 (number/m^3s^1) is the product of population density n_0 (number of crystals/m^4) and the crystal growth rate G_0 (m/s), is defined as equation (3) has already shown.

There are many empirical expressions that correlate the second nucleation rate with the crystallization parameters. The mostly used for the contact nucleation is given by the next equation [9]:

$$B_0 = k_B \cdot \rho_L^{\ l} \cdot \varepsilon^r \cdot G_0^{\ p} \tag{9}$$

The analysis of equation (9) shows the dependence of the nucleation process on the suspension density (ρ_L) to a power exponent "*l*", on power input (ε) to a power exponent "*r*" and on growth rate (G_0) to a power exponent "*p*".

By operating on MSMPR crystallizer at steady state for different systems Mersmann [10] it has been concluded that the value of the exponent "*l*" = 1.

Because the effective nucleation rate B_0 is influenced by the crystal mass in crystallizer the density of the suspension will be replaced by the retention degree Φ defined by the equation:

$$\Phi = \frac{\rho}{\rho_S} \tag{10}$$

where ρ is the suspension density and ρ_S – the solid density.

So, the new equation of modified nucleation rate is:

$$\frac{B_0}{\Phi} = k_B \cdot \rho_S \cdot \varepsilon^r \cdot G_0{}^p \tag{11}$$

For the determination of the power exponents we have assumed that the equation (11) can be simplified to the form:

$$\frac{B_0}{\Phi} = K_1 \cdot G_0{}^p \tag{12}$$

A straight line on the double log scale can represent this equation for all used consumption energy (Figure 2). The slope of the straight line corresponds to the value of the power exponent "*p*". The average value is 1.045, which corresponds to the literature values (1 – 3) [11].

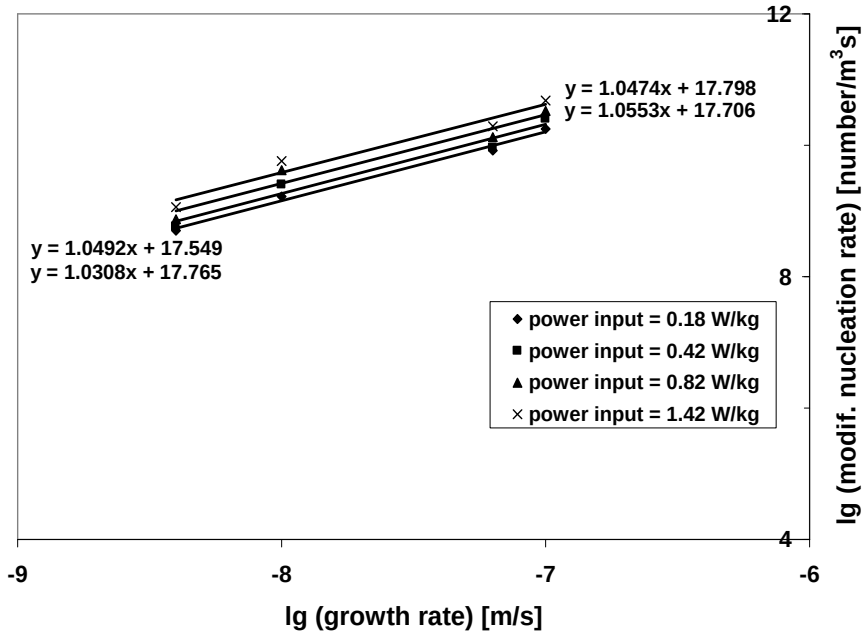

Fig 2.
Determination of the power exponent “p”.

In order to obtain the value of the power exponent “*r*” the equation (11) was simplified to the form:

$$\frac{B_0}{\Phi} = K_2 \cdot \varepsilon^r \tag{13}$$

From the slope of the curves log B_0/Φ versus log ε an average value of r = 0.61 was obtained (Figure 3), which corresponds to the literature values (0.6 – 0.7) [11]. The results have shown the maintenance of a constant slope at different power input of stirrer.

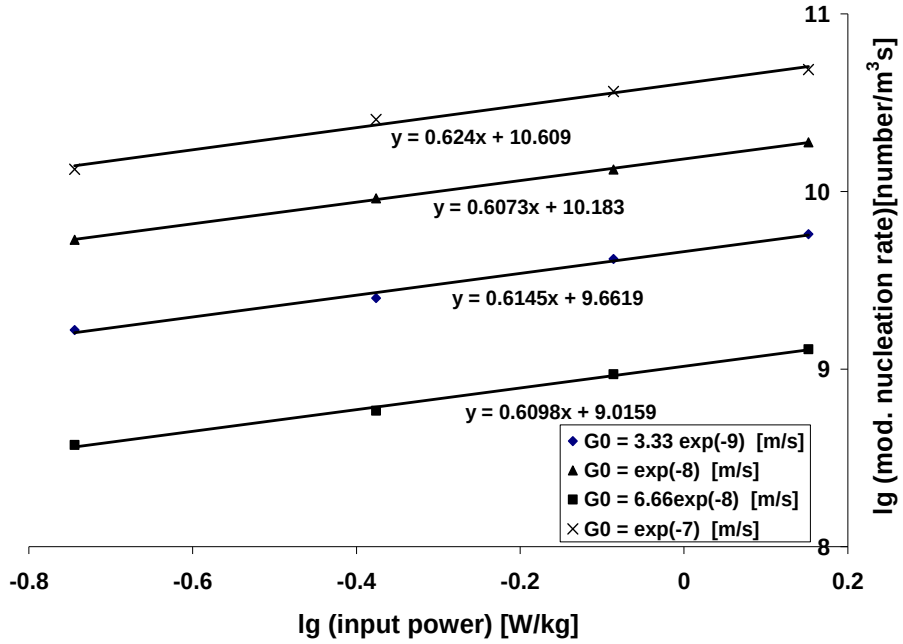

Fig. 3.
Determination of the power exponent "r".

The influence of the temperature on the nucleation rate is represented by the constant rate for secondary nucleation k_B:

$$k_B = \frac{B_0}{\rho_S \cdot \Phi \cdot \varepsilon^{0.61} \cdot G_0^{1.045}} \tag{14}$$

as the equation of Arrhenius shows:

$$k_B = k_0 \cdot e^{-\frac{E_a}{RT}} \tag{15}$$

The plot log k_B versus (1/T) leads to a straight line with a constant slope for different linear growth rates (Figure 4). From the slope of the straight line the activation energy $E_a = 5{,}4\ 10^4$ J/mol was obtained.

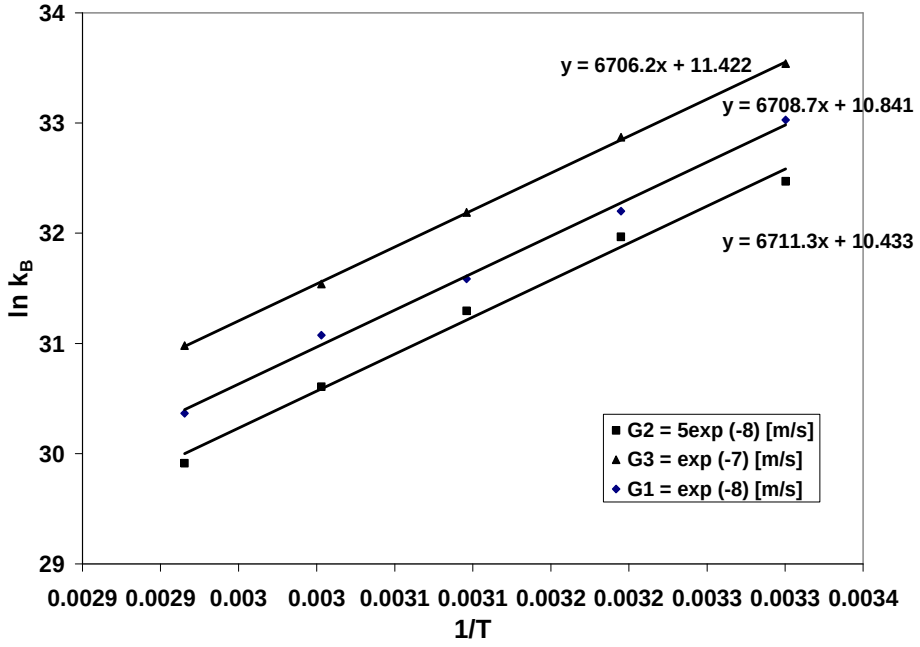

Fig. 4.
The influence of the temperature on the nucleation rate.

Crystal size

The granulometric analysis of the obtained natrium sulphate has shown that the average diameter of the crystals lies in the range 150 - 500 μm depending on the crystallization conditions. Sometimes the size of the crystal increases up to 1 mm, because of the agglomeration process that can be observed from the polycrystalline form of the particles visible only by microscopic analysis.

The analysis of the dependence of the average diameter of the crystals on the growth rate at a constant residence time can be calculated by the equation (16):

$$x_{50} = K \cdot G_0 \tag{16}$$

where G_0 is defined by the equation (3). The equation (3) has shown that the linear growth rate depends on hydrodynamic conditions and temperature by means of the k_g coefficient.

In Figure 5 the experimental values of the average size of the crystals x_{50} (mm) are plotted versus power input per unit mass ε (W/kg) at different temperatures. The linear dependence of the average diameter of the crystal on the power input at constant temperature was observed. At the same time the dependence of the crystal size on the temperature has shown that with the increase of the temperature, the average size of the crystals decreases for the same consumption of energy. The decrease of the average size of the particles simultaneously with the increase of the temperature can be explained through the decrease of the crystallization potential (C - C*), supersaturation having a higher influence on the growth rate than constant K.

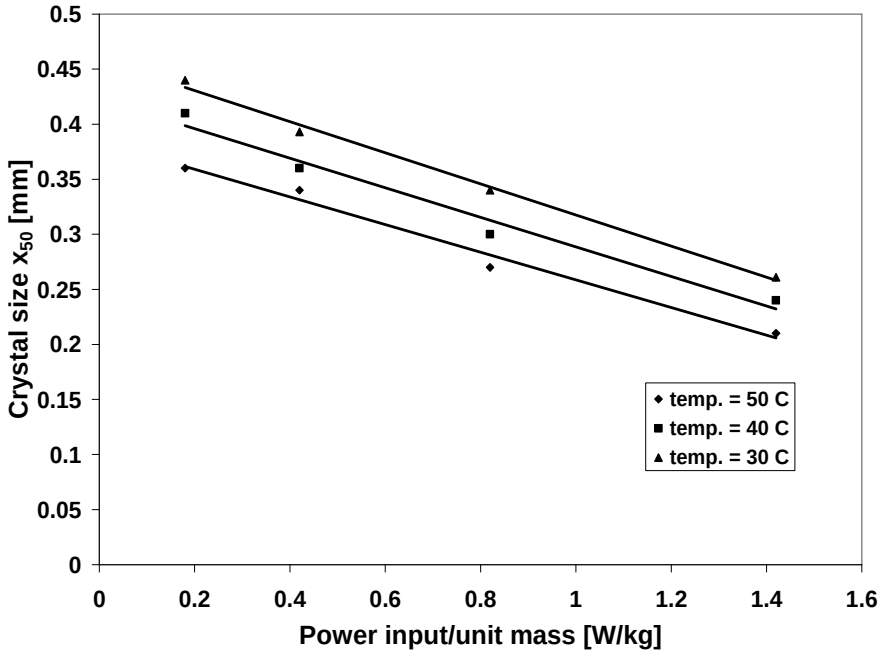

Fig. 5.
Crystal size versus specific consumption of energy.

Conclusions

The kinetic results have shown that the efficiency of the crystallization can be improved with the increase of the residence time and with the variation of the temperature in crystallizer.

By using the equation of population balance it was made possible to determine the specific influence of each parameter on the crystallization process.

The experimental measurements have shown that the second nucleation constant k_B decreases with the increase of the temperature. From the Arrhenius equation the activation energy of nucleation E_a = 5,4 10^4 J/mol was determined.

The dependence of the average diameter of the crystals on the power input ε was also determined.

The obtained results have shown that the salting-out crystallization leads to superior sizes of the crystal comparing the classical evaporation process and to a rigorous control of the process.

REFERENCES

1. Kirk-Othmer, "*Encyclopedia of Chemical Technology*", Second Edition, Ed. Wiley and Sons, Inc., **1965**
2. H. Poppe, *Chem. Proc. Eng*., **1968**, 12, 61 - 71
3. Al. Pop, A. Ghirişan, S. Drăgan and V. Miclăuş*, Studia Univ. Babeş-Bolyai, Chemia*, **2004**, 49(2), 195 - 201
4. N.S. Tavare, "*Industrial Crystallization*", Plenum Press, New York, **1995**
5. R.G. Harrison, P. Todd, Scott R. Rudge and D.P. Petrides, "*Bioseparations Science and Engineering*", N.Y. Oxford, Oxford Univ. Press, **2003**
6. W.J. Genck, "*Crystallization from solutions. In Handbook of Separations Techniques for Chemical Engineers*", 3nd, Ed. McGrow-Hill, New York, **1977**
7. L. Filipescu, M. Crețu, M. Mocioi and A. Zaharia, *Revista de Chimie*, **1981**, 32(4), 347 - 351
8. A. Randolph şi M. Larson, "*Theory of Particulate Process*", 2nd, Ed. Academic Press, San Diego, **1988**
9. J. Nyvlt, O. Sohnel, M. Matuchova and M. Broul, "*Kinetics of Industrial Crystallization*", Ed. Academic Praque, **1985**
10. A. Mersmann, *Chem. Ing.Tech*., **1982**, 54 (7), 631-643
11. M. Giulietti, M.M. Seckler, S. Derenzo, M. I. Re and E. Cekinski, *Braz. J. Chem. Eng*., **2001**, 18(4), 423 - 440

STUDIA UNIVERSITATIS BABEŞ-BOLYAI, CHEMIA, LI, 1, 2006

STUDY ON THE INHIBITING BEHAVIOR OF A NON-TOXIC THIADIAZOLE DERIVATIVE ON BRONZE CORROSION IN AQUEOUS ELECTROLYTES

IOANA IGNAT[1], SIMONA VARVARA[2] AND LIANA M. MURESAN[1*]

ABSTRACT. The efficiency of a new non-toxic thiadiazole derivative (2 mercapto-5-R-acetylamino-1, 3, 4-thiadiazole) as bronze corrosion inhibitor in various aqueous electrolytes (sodium chloride, sodium sulphate and sodium hydrogen carbonate) was studied by electrochemical polarization measurements. The calculated corrosion parameters suggest that the thiadiazole derivative reduces the rate of bronze corrosion, acting as a mixed-type inhibitor in all the investigated electrolytes. The best inhibiting efficiency of the thiadiazole derivative was observed in sodium chloride solution.

Keywords: bronze corrosion; corrosion inhibitor; thiadiazole derivatives

1. Introduction

Copper and copper-based alloys are widely used in a great variety of applications, such as heat exchangers, building construction, electronics, coinage, art works etc. [1]. In spite of the fact that copper is a relatively noble metal, it corrodes easily in oxygen-containing electrolytes [2]. The corrosion behavior of copper and its alloys in various environments (acidic, alkaline and neutral) has been explored for several decades and, in all cases the dissolution of copper was balanced by the oxygen reduction [3].

Since copper and its alloys are not stable in oxygen-containing electrolytes, substantial improvement in their passivity is needed [4]. To this regard, a range of organic compounds can offer a good protection against corrosion to the exposed copper and bronze surfaces in different aggressive environments. Thus, it is well-known that, on copper and bronze, heterocyclic compounds containing nitrogen, oxygen or sulfur [5-10] are efficient corrosion inhibitors due to the chelating action of heterocyclic molecules and the formation of a physical blocking barrier on the surface [7]. In particular, benzotriazole and its derivatives are among the most effective inhibitors for

[1] "Babes-Bolyai" University, Department of Physical Chemistry, 11 Arany Janos St., 400028 Cluj-Napoca, ROMANIA.
* E-mail: limur@chem.ubbcluj.ro
[2] "1 Decembrie 1918" University, Systemic Archaeology Institute, 11-13 Nicolae Iorga St., 510009 Alba-Iulia, ROMANIA

copper and copper alloys corrosion over a wide temperature and pH range [7, 11-13], but because they are highly toxic [10, 14] they should be replaced with other environmentally friendly inhibitors.

In an attempt to find non-toxic alternatives to the conventional benzotriazole, recent works showed that 2-amino-5-mercapto-1,3,4-thiadiazole is an excellent corrosion inhibitor for copper and bronze in citric acid [15, 16]. In this context, the present work was carried out to investigate the effect of a new thiadiazole derivative, *i.e.* 2 mercapto-5-R-acetylamino-1, 3, 4-thiadiazole on bronze corrosion in different aqueous electrolytes. The efficiency of the inhibitor was studied by electrochemical polarization measurements.

2. Experimental

Materials

Experiments were carried out in different 0.01 M aerated electrolytes (Table 1), at room temperature.

Table 1.
Characteristics of the corrosive media

Electrolyte	NaCl	Na_2SO_4	$NaHCO_3$
pH	5.46	5.76	8.77
λ 10^{-3} (S/cm)	1.243	2.058	1.073

2 mercapto-5-R-acetylamino-1, 3, 4-thiadiazole was synthetized in the laboratories of the Faculty of Pharmacy from Cluj-Napoca, Romania and its molecular structure is presented in figure 1.

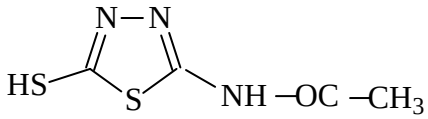

Figure 1.
Molecular structure of the inhibitor

In all the investigated aqueous electrolytes, the concentration range of the inhibitor was 10^{-5} to 10^{-3} M.

All the other chemicals were of analytical grade and used as received.

Methods

Potentiodynamic polarization measurements were conducted using an electrochemical analyzer (Autolab-PGSTAT 10, EcoChemie, Utrecht, Netherlands) connected to a PC for potential control and data acquisition.

Chronopotentiometry was used for the open-circuit potential (O.C.P) measurements.

The electrochemical experiments were performed in a three-electrode cell with a separate compartment for the reference electrode connected with the main compartment *via* a Luggin capillary. The working electrode was made of bronze (see its composition in Table 2), the reference electrode was a saturated calomel electrode (SCE) and the counter electrode was a platinum foil.

Table 2.
Weight % composition of the bronze electrode

Cu	**Sn**	**Pb**	**Zn**	**Sb**	**Ni**	**Fe**	**Mn**	**As**	**S**
87.975	6.014	4.020	1.172	0.299	0.181	0.11	0.002	0.033	0.19
Si	**P**								
0.004	0.004								

Prior to all the polarization runs, the bronze electrode was polished with grit paper of 600, rinsed with distilled water and ethanol, and immersed for 60 minutes in the electrolyte. Anodic and cathodic curves were recorded in a potential range of $E = E_{corr} \pm 200$ mV with a scan rate of 0.25 mV s^{-1}. The rotation speed of the working electrode was fixed at 2000 rpm.

3. Results and Discussion

3.1. Open-Circuit Potential (O.C.P) Measurements

The way in which a metal changes its O.C.P. with time upon immersion in a solution could bring information about the reactions taking place at the metal solution interface. In general, a shift of potential towards positive direction denotes passivation behaviour, whilst a shift in the negative direction signifies activation behaviour.

The open-circuit potentials evolution in time for the bronze electrode, recorded immediately after 60 minutes immersion in different electrolytes are presented in Figure 2.

In the absence of the inhibitor, the O.C.P values for the sulphate and hydrogen carbonate electrolytes gradually increase in the positive direction during the first minutes to reach a stationary state characterized by -0.102 V *vs.* SCE and -0.069 V *vs.* SCE, respectively. This passive behaviour could be most probably attributed to the chemisorption of the dissolved oxygen and its reduction together with possible formation of oxide layers and/or hydroxysulfate or hydroxycarbonate on the surface of the electrode [17].

In the chloride medium, the OCP stabilized very quickly after the immersion at -0.379 V *vs.* SCE. Cuprite (Cu_2O), nantokite (CuCl) and tin species (hydroxides and/or hydroxychlorides) could be produced in this case on the bronze surface [16].

Disregarding the electrolyte composition, more anodic values of the O.C.P. are observed in the presence of thiadiazole derivative. The positive potential shift could be associated with the formation of protective film at the electrode surface. This behaviour suggests that, probably, 2 mercapto-5-R-acetylamino-1, 3, 4-thiadiazole is adsorbed on the bronze surface, acting mainly as an inhibitor for bronze corrosion in all the investigated aqueous media.

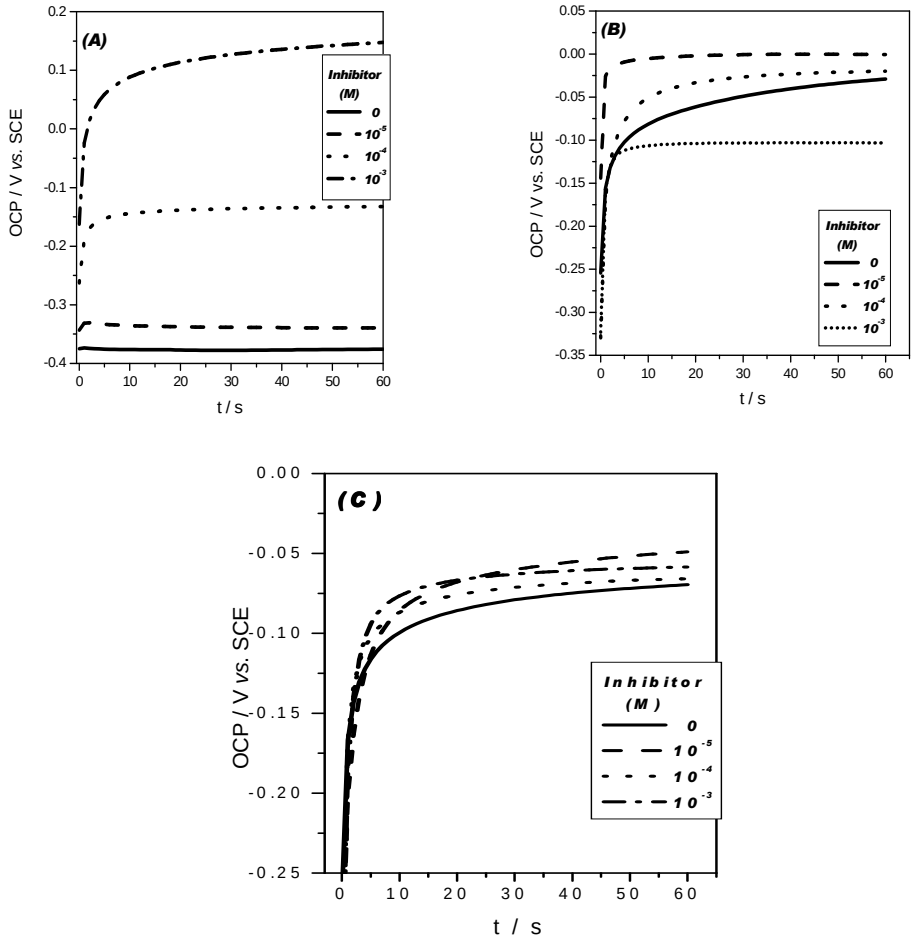

Figure 2.

Open-circuit potentials evolution for the bronze electrode immersed in various 0.01 M aqueous electrolytes without and with different concentrations of 2 mercapto-5-R-acetylamino-1, 3, 4-thiadiazole: (A) NaCl; (B) Na_2SO_4; (C) $NaHCO_3$.

3.2. Potentiodynamic Polarization Measurements

The cathodic and anodic polarization curves of bronze electrodes recorded after its immersion during 60 minutes in different electrolytes in the absence and in the presence of 2 mercapto-5-R-acetylamino-1, 3, 4-thiadiazole are shown in Figure 3.

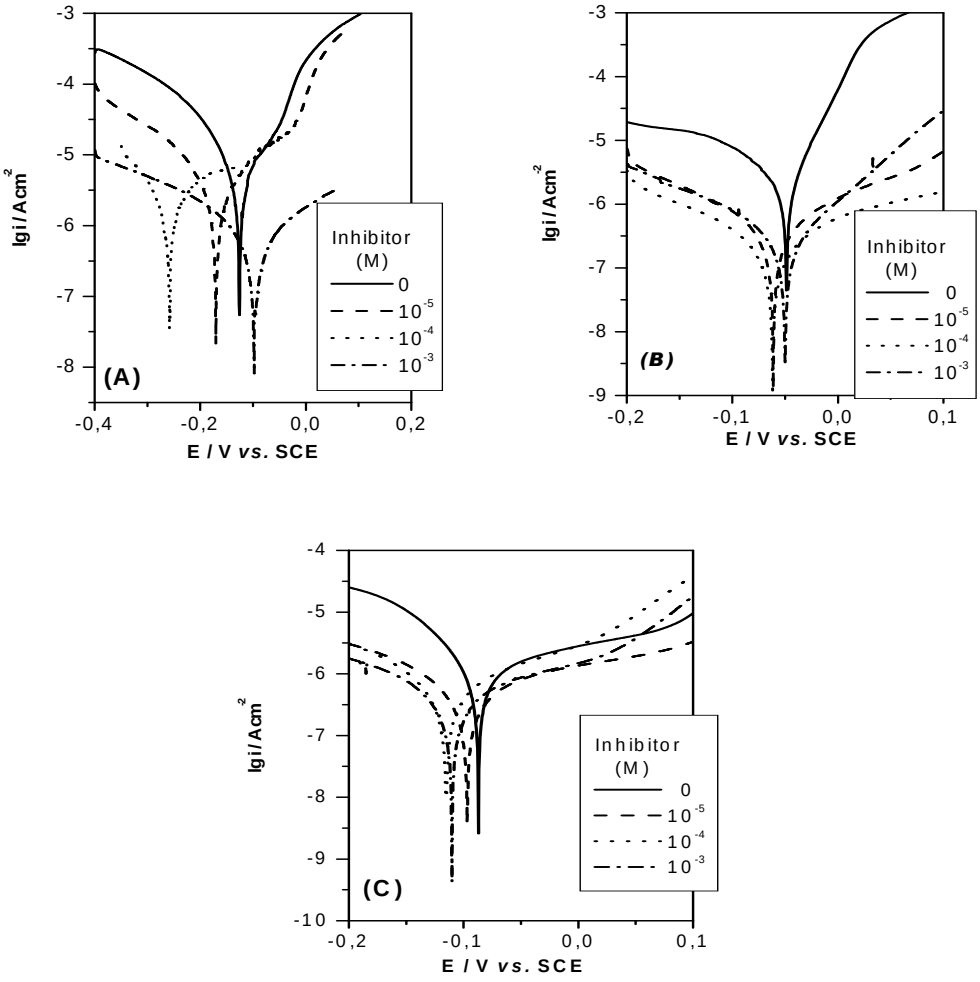

Figure 3.
Influence of thiadiazole derivative concentration on the anodic and cathodic polarization curves of bronze in various aqueous 0.01 M electrolytes: (A) NaCl; (B) Na_2SO_4; (C) $NaHCO_3$.

As can be observed, the anodic curves in NaCl solution are characterized by the presence of a shoulder, which has been attributed to the formation of CuCl on the metal surface [19], according to the reactions [20]:

$$Cu + Cl^- \leftrightarrow CuCl + e^-$$
$$CuCl + Cl^- \leftrightarrow CuCl_2^-$$

It is generally accepted that, in the apparent Tafel region, the corrosion process is controlled by the electrodissolution of copper and the diffusion of soluble $CuCl_2^-$ from outer Helmholtz plane into the bulk solution (mixed control) [21].

Disregarding the electrolyte composition, the addition of the inhibitor determines a considerably decrease both in the anodic and cathodic current density values with respect to the blank solutions. This indicates that the tested thiadiazole derivative cannot be designed exclusively as anodic or cathodic inhibitor. It acts as a mixed-type inhibitor that protects the electrodic surface, and hinders both the anodic dissolution of copper and the cathodic oxygen reduction. However, the slight shift of the corrosion potential values in the negative direction observed in the presence of the inhibitor points to a small predominance of the cathodic reaction.

The corrosion parameters were calculated directly from the potentiodynamic polarization measurements on the basis of the Tafel extrapolation, according to the equation:

$$i = i_0 \exp\left[\frac{2{,}303}{b_a}\left(E - E_{corr}\right)\right] - \exp\left[-\frac{2{,}303}{b_c}\left(E - E_{corr}\right)\right] \quad (1)$$

where b_a and b_c are anodic and cathodic Tafel slopes, $E_{corr\ is}$ the corrosion potential and the other parameters have the usual meaning.

The corrosion inhibition efficiency (IE) in the presence of the inhibitor was calculated from the relation:

$$IE = \frac{i_{corr} - i'_{corr}}{i_{corr}} \cdot 100\,[\%] \quad (2)$$

where i_{corr} and i'_{corr} are the corrosion current densities in the absence and in the presence of the inhibitor, respectively.

The values of the corrosion potential (E_{corr}), corrosion current density (i_{corr}), inhibition efficiency (IE) and of the anodic and cathodic Tafel

slopes (b_a and b_c) for bronze in different electrolytes as a function of the inhibitor concentration are presented in Table 3.

As it can be seen, the corrosion potentials dependence on the inhibitor concentration is not a monotonic one: at very low concentrations (below 10^{-3} M), the inhibitor shifts the corrosion potential slightly to the cathodic direction, while at higher inhibitor concentrations, the corrosion potential shifts to the anodic direction. These variations of the corrosion potential values are probably due to a competition between the anodic and the cathodic inhibiting reactions and/or to the metal surface condition. Moreover, in the presence of 2 mercapto-5-R-acetylamino-1, 3, 4-thiadiazole both the anodic and cathodic Tafel slopes change with the inhibitor concentration, indicating once more that both reactions are influenced by the inhibitor presence.

Relatively high values of the corrosion inhibition efficiency are observed in all solutions. However, it should be noticed that the thiadiazole derivative has a better inhibition effect on bronze corrosion in chloride electrolyte as compared to sulphate or hydrogen carbonate solutions. For chloride and sulphate electrolytes, the optimum concentration for the investigated thiadiazole derivative with the corresponding inhibiting efficiency was 10^{-4} M. In the case of hydrogen carbonate solution, the optimum concentration of inhibitor was 10^{-3} M for an efficiency of around 82 % (table 3).

Table 3.
Corrosion parameters for bronze in different electrolytes in the absence and in the presence of 2 mercapto-5-R-acetylamino-1, 3, 4-thiadiazole at room temperature.

Electrolyte (0.01 M)	**Inhibitor conc.** (M)	**E_{corr}** (mV/SCE**)**	**i_{corr}** (10^7 Acm^{-2})	**b_c** ($V\ dec^{-1}$)	**b_a** ($V\ dec^{-1}$)	**IE** (%)
NaCl	0	-96	41.14	0.115	0.057	-
	10^{-5}	-170	4.28	0.096	0.047	89.60
	10^{-4}	-256	3.43	0.109	0.045	91.66
	10^{-3}	-98	3.72	0.124	0.109	90.95
Na_2SO_4	0	-48	23.30	0.109	0.037	-
	10^{-5}	-60	7.89	0.098	0.049	66.13
	10^{-4}	-62	4.30	0.110	0.032	81.54
	10^{-3}	-50	4.38	0.149	0.077	81.20
$NaHCO_3$	0	-87	7.31	0.122	0.045	-
	10^{-5}	-97	3.02	0.104	0.080	58.68
	10^{-4}	-116	3.53	0.125	0.083	51.71
	10^{-3}	-110	1.31	0.116	0.073	82.08

A possible explanation for the inhibiting action of 2 mercapto-5-R-acetylamino-1, 3, 4-thiadiazole on the bronze corrosion could be found in the covering of the electrodic surface with a protective film made of a polymeric Cu(I)-inhibitor complex. According to [15], the efficiency of the organic inhibitors could be associated to the extent to which they adsorb and cover the metal surface. Their adsorption depends on the structure of inhibitors, on the surface charge of the metal, and on the type of the electrolyte. 2 mercapto-5-R-acetylamino-1, 3, 4-thiadiazole acts as a bidentate ligand both through the aminic and the closed ring nitrogen in the complex.

4. Conclusions

The results of electrochemical investigation show that 2 mercapto-5-R-acetylamino-1, 3, 4-thiadiazole has fairly good inhibiting properties for bronze corrosion in all the investigated electrolytes. It behaves as a mixed-type inhibitor.

The maximum inhibition efficiency of 2 mercapto-5-R-acetylamino-1, 3, 4-thiadiazole was observed in chloride electrolytes. Its inhibiting action can be attributed mainly to the blockage of the bronze surface by a protective film consisting of a polymeric Cu(I)-inhibitor complex in which the inhibitor acts as a bidentate ligand through the aminic nitrogen atom and the closed ring nitrogen.

Acknowledgements

The authors thank Prof. Dr. Robert Sandulescu, from the "Iuliu Hatieganu" University of Medicine and Pharmacy of Cluj-Napoca for supplying us the thiadiazole derivative. The financial support from EGIDE (Project ECO-net No. 10279NA/2005) is gratefully acknowledged.

REFERENCES

1. D-Q. Zhang, L-X. Gao, G-D. Zhou, *J. Appl. Electrochem*., **2003**, 33, 361–366.
2. M. Pourbaix, "Atlas of Electrochemical Equilibria in Aqueous Solutions'", Pergamon Press, Inc., New-York, 1966.
3. S. Magaino, *Electrochim. Acta*, **1997**, 42, 3, 377-382
4. M. Metikos-Hukovic, R. Babic, I. Paic, *J. Appl. Electrochem*., **2000**, 30, 617-624.
5. H. Otmacic, E. Stupnisek-Lisac, *Electrochim. Acta*, **2003**, 985-991.
6. R. Tremont, C.R. Cabrera, *J. Appl. Electrochem*., **2002**, 32, 783–793.
7. H. Ma, S. Chen, L. Niu, S. Zhao, S. Li, D. Li, *J. Appl. Electrochem*., **2002**, 32, 65–72.
8. J. B. Matos, L. P. Pereira, S. M. L. Agostinho, O. E. Barcia, G. G. O. Cordeiro, E. D' Elia, *J. Electroanal. Chem*., **2004**, 570, 91–94.
9. S. A. Abd El-Maksoud, *Electrochim. Acta*, **2004**, 49, 4205–4212.
10. E. Stupnisek-Lisac, A. Gazivoda, M. Madzarac, *Electrochim. Acta* **2002**, 47, 4189-4194.

11. G. Quartarone, G. Moretti, T. Bellomi, G. Capobianco, A. Zingales, *Corrosion*, **1998**, 54, 606-618.
12. N. Huynh, S. E. Bottle, T. Notoya, D. P. Schweinsberg, *Corros. Sci*., **2000**, 42, 259-272.
13. J. L. Guinon, J. Garcia-Anton, V. Perez-Herranz, *J. Appl. Electrochem*., **2000**, 30, 379-384.
14. E. Stupnisek -Lisac, N. Galic, R. Gasparac, *Corrosion*, **2000**, 56, 1105-1111.
15. L. Ying, F. Haitao, Z. Yifan, W. Wuji, *J. Mat. Sci.*, **2003**, 38, 407-411.
16. R. B. Faltermeier, *Studies in Conservation,* **1998,** 44, 121-128.
17. N. Souissi, L. Bousselmi, S. Khosrof, E. Triki, *Mat. Corr.*, **2003**, 54, 318–325.
18. M. Pourbaix, *Corros. Sci.*, **1990**, 30, 963-978.
19. M. Itagaki, M. Tagaki, K. Watanabe, *Corros. Sci.,* **1996**, 38, 1109-1125.
20. C. Deslouis, B. Tribollet, G. Mengoli, M. M. Musiani, *J. Appl. Electrochem*., **1988**, 18, 374-393.
21. A. L. Bacarella, J. C. Griess, *J. Electrochem. Soc.,* **1973**, 120, 459-467.

STUDIA UNIVERSITATIS BABEŞ-BOLYAI, CHEMIA, LI, 1, 2006

ESTIMATIONS OF SURFACE FREE ENERGIES FOR SOLID METALS

OSSI HOROVITZ[1], ANCA-LIANA POPOVICIU[1], ELENA-MARIA PICA[2]

ABSTRACT. Experimental methods rarely give reliable values of the free surface energies/surface tensions for solid metals and just few data exist. Therefore correlations between surface and bulk thermodynamic properties are important in order to obtain estimated values for the surface quantities. From experimental values, molar free surface energies are calculated on the basis of molar volumes or atomic radii of metallic elements. The bulk properties considered here are melting point, enthalpy of atomization, free enthalpy of atomization and inner free enthalpy of atomization. Different correlations are investigated and the results are discussed and compared with the predictions of the rule of broken bonds between first neighbour atoms. The deviations of some elements from the regression lines are examined. From the correlations, a set of calculated free surface enthalpies for 69 solid elements is proposed.

Keywords: metals, surface free energy, enthalpy of atomization, correlations

Introduction

Surface free energy is one of the most important properties of solid state and particularly of solid metals. It determines the equilibrium shape of crystals and plays a decisive role in surface phenomena and processes, such as surface faceting, roughening, surface segregation in binary alloys, crystal growth, formation of grain boundaries, growth and stability of thin films, the shape of small crystallites in a supported catalyst, adsorption, sintering. The surface free energies between two interacting surfaces control processes like the stability of aqueous colloidal suspensions, the dynamics of molecular self-assembly, wetting, spreading, deinking, adhesion. Many mineral processing techniques, e.g. froth flotation, selective flocculation, filtration and thickening depend on the solid/liquid interfacial interaction [1].

Surface free energy, γ is defined as the excess Helmholtz energy (free energy), or the excess Gibbs energy (free enthalpy) per unit area:

$$\gamma = F_s = G_s = \Delta F/A_s = \Delta G/A_s \quad (1)$$

For liquids it is numerically and dimensionally equal to the *surface tension* (*interfacial tension*), Some authors consider the two notions to be synonymous for solids too and related to the work spent in forming the surface,

[1] Department of Physical Chemistry, "Babes-Bolyai" University Cluj-Napoca, Romania
[2] Department of Chemistry, Technical University Cluj-Napoca, Romania

and introduce the *surface stress* or *stretching tension* in order to describe the work spent in stretching the surface [2, 3]. The first is a scalar quantity, the second - a tensor. The difference comes from the reduced mobility of atoms in solids, which prevents them to quickly rearrange to an equilibrium position when a new surface is created, while liquids cannot maintain a strain. However, this mobility is increased near the melting point, where this difference should disappear. As the temperature is approaching the melting point, a roughening of the surface occurs and even a "surface melting" can take place.

The temperature dependence of the surface free energy is related to the surface entropy, $S_s = \Delta S/A_s$, A_s being the surface area, the entropy variation involved in the creation of the unit area of the solid-vapour interface, by the obvious relation:

$$S_s = -\left(\frac{\partial G_s}{\partial T}\right)_p = -\left(\frac{\partial \gamma}{\partial T}\right)_p \tag{2}$$

and the surface enthalpy (or energy) can be obtained from the Gibbs-Helmholtz equation:

$$H_s = \gamma - T\frac{\partial \gamma}{\partial T} \tag{3}$$

So-called "molar" surface quantities are defined as products of the above functions with the "molar" surface, $V_M^{2/3}$ (V_M – the molar volume of the solid), e.g. the "molar" surface free energy $\gamma V_M^{2/3}$. For liquids, a linear decrease of surface tension with temperature increase is generally assumed, i.e. surface entropy is constant, independent of temperature. In the case of solid metals, exact measurements on the temperature dependence of surface free energy are missing, but here also a decrease of γ with increasing temperature is observed.

Since experimental methods rarely give reliable values of the free surface energies for solid metals and just few data exist, there were many attempts to calculate the surface energy. They range from empirical correlations between this quantity and some bulk properties of the metal to the use of *ab-initio* techniques, passing through semi-empirical methods, among them many applications of the law of corresponding states and statistical mechanics [4].

Empirical Correlations Between Free Surface Energy and Other Properties of Solid Metals

In order to find correlations between free surface energies and other properties of the metals, experimental values were used (Table 1), taken mostly from the compilation of Kumikov and Khokonov [5]. The authors

have selected, compared and evaluated experimental values, obtained by various methods. These measurements were made at different, most of

Table 1.
Surface free energies and other properties of solid metals

Element	γ^{exp} [mJ.m^{-2}]	γ^{TM} [mJ.m^{-2}]	T_m[K]	ΔH_a [kJ/mol]	V[cm^3]	R [pm]
Li	---	472	454	159.4	13.096	156
Be	1000	1298	1551	324.3	4.875	113
Na	---	234	370.9	108.4	23.686	186
Mg	---	688	922	147.7	13.981	160
Al	1140	1020	933.5	326.4	9.985	143
Si	1200	940	1683	455.6	12.051	117
K	---	129	337	89.2	45.348	231
Ca	---	425	1112	178.3	25.851	197
Sc	---	---	1814	377.8	15.033	161
Ti	1938	1749	1941	469.9	10.546	145
V	2900	2301	2173	514.2	8.782	131
Cr	2090	2006	2130	396.6	7.230	125
Mn	1400	1298	1518	280.7	7.393	137
Fe	2170	2123	1808	416.3	7.095	125
Co	2424	2218	1768	424.7	6.621	125
Ni	1940	2080	1726	429.7	6.594	124
Cu	1520	1566	1356.4	338.3	7.123	128
Zn	868	896	693	130.7	9.158	133
Ga	767	845	302.9	277	11.70	122
Ge	820	748	1210.4	376.6	13.64	123
Rb	---	104	312.2	80.9	55.856	243
Sr	---	358	1041	164.4	33.7	215
Y	---	---	1795	421.3	19.888	180
Zr	1850	1687	2125	608.8	14.055	161
Nb	2400	2313	2741	725.9	11.059	147
Mo	2630	2510	2883	658.1	9.405	136
Tc		---	2445	678	8.513	135
Ru	3400	2655	2607	642.7	8.217	132
Rh	2800	2325	2239	556.9	8.298	134
Pd	2000	1743	1825	378.3	8.868	138
Ag	1205	1086	1235	384.6	10.272	144
Cd	675	698	594.1	112	12.995	149
In	633	658	429.3	243.3	15.869	163
Sn	673	661	505	302	16.306	140
Cs	---	84	301.6	76.1	70.955	265
Ba	---	326	998	180	39.122	210
La	---	---	1193	427	20.731	187
Nd	---	812	1297	328	20.605	181
Pm	---	---	1312	301	22.380	183
Sm	---	---	1345	206.7	19.941	180
Eu	---	---	1095	178	28.895	204
Gd	900	---	1586	398	19.936	179
Yb	---	---	1097	152	24.790	194

Lu	---	---	1936	428	17.781	174
Hf	---	1923	2495	669	13.521	154
Ta	2480	2493	3269	782	10.900	143
W	2900	2765	3683	849.4	9.476	137
Re	2200	3133	3453	769.9	8.854	138
Os	---	2950	3327	790.8	8.492	134
Ir	---	2655	2637	665.2	8.573	136
Pt	1950	2203	2045	565.3	9.094	139
Au	1410	1333	1337.6	369	10.210	144
Tl	562	550	576.7	182.2	17.710	170
Pb	560	540	601	196	18.271	175
Bi	501	446	544.5	207.1	21.324	155
Ra	---	---	973	161.9	44.403	132
Th	---	---	2023	598.3	19.832	181
Pa	---	---	1873	606.7		161
U	---	1780	1405	535.6	12.494	138

γ^{exp} – experimental values for free surface energy [5], γ^{TM} – Tyson and Miller values [6], T_m – melting point, ΔH_a – enthalpy of atomization, V – molar volume, R – metallic radius

them at relatively high, temperatures, near the melting point of the metal. The preferred values are mostly those obtained by the compensated zero-creep method. The scatter of the values is important, the relative errors of the measurements reach 10-20%, but only 1-3% in the zero-creep method. We selected the most probable values (most of them recommended by the authors) along with some values from other sources. Insofar as possible, we selected values obtained at lower temperature, where the peculiarities of the solid metals are more pronounced.

In literature the „experimental“ values of Tyson and Miller [6] are often used. As a matter of fact, these are extrapolated from the values for liquid metals at the melting point, γ_L which are reasonable well known quantities. They inferred that the ratio of free surface energies for solids γ_S and for liquids should be approximately constant for metallic elements:

$$\gamma_S / \gamma_L = 1.18 \pm 0.03 \quad (4)$$

The values given by Tyson and Miller are also included in Table 1.

Since surface free energy of a pure solid is determined by the strength of cohesive forces between the adjacent particles, it seems logically to expect correlations between it or other surface properties and some physico-chemical bulk properties of the materials, that are also the result of forces of this kind. Of course, this should apply only to pure materials, inasmuch as even the smallest amounts of surface active contaminants have a strong influence on the values of surface tension, while the bulk properties are only

slightly modified. The bulk properties considered here are melting temperatures and standard enthalpies of atomization.

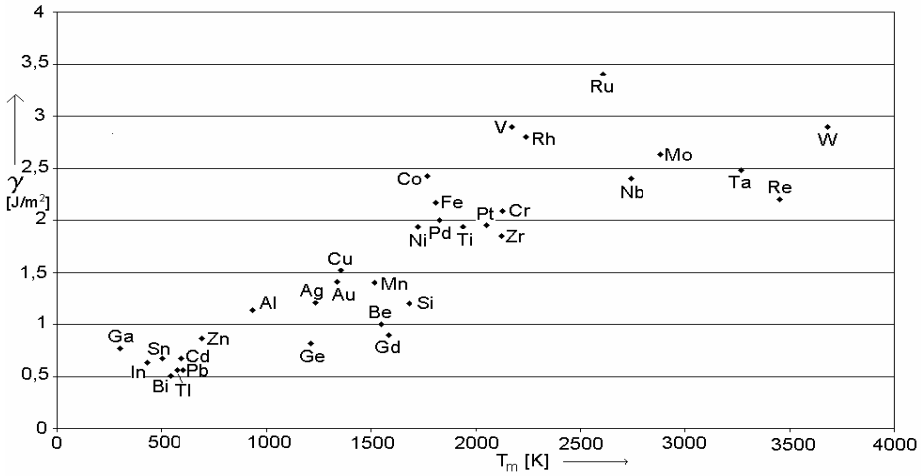

Figure 1.
Surface free energies of solid metals versus melting temperatures

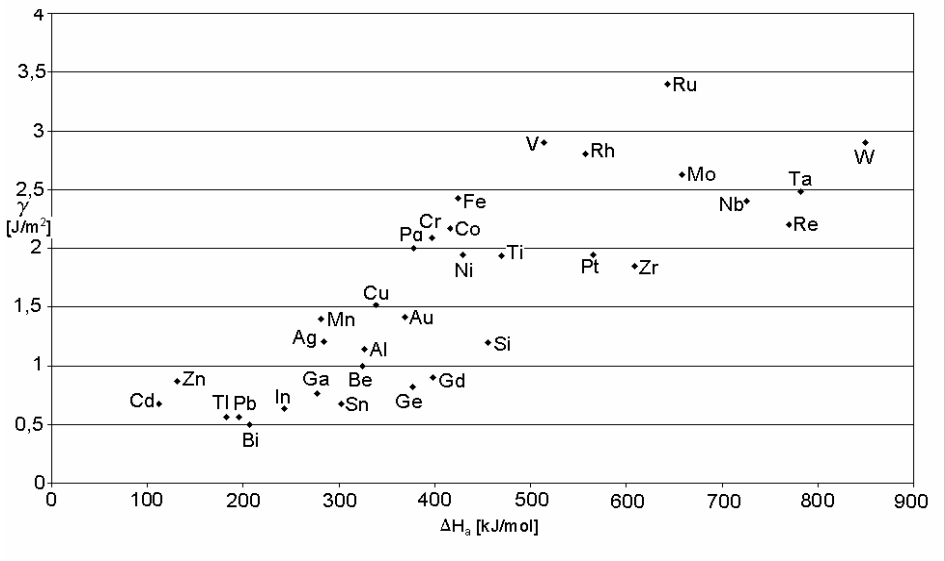

Figure 2.
Surface free energies of solid metals versus enthalpies of atomization

Experimental values for the surface free energies of solid metals were plotted versus melting points T_m in Figure 1. The two properties appear to be related, but there is not a strong linear correlation. Particularly, metals with high melting points (Nb, Mo, Ta, Re, W) don't have correspondingly high γ-values. The same is the case for the semi-metals Ge and Si. On the other hand, the surface free energy for Ga is unexpectedly high for its melting point. The correlation line for 33 experimental values corresponds to the equation:

$$\gamma\,[mJ/m^2] = (313\pm157) + (0.791\pm0.083)T_m[K], \quad r = 0.864 \qquad (5)$$

Another measure of cohesion forces in the metal lattice could be the standard enthalpy of atomization, ΔH_a (the values are also given in Table 1). As in the case of the temperature dependence, an increase of the free surface energies with increasing ΔH_a-values is evident from Figure 2, but there is no linear correlation, the scatter of the points is even higher than in Fig.1. The equation of the correlation line, passing through the origin, is:

$$\gamma[mJ/m^2] = (3.80\pm0.18)\ \Delta H_a[kJ/mol] \quad r = 0.819,\ n = 33 \qquad (6)$$

One of the reasons for the poor correlation is that, while surface free energies refer to the surface unit, the enthalpies of atomization are molar quantities. Therefore, „molar" surface tensions $\gamma.V^{2/3}$ should be used, where V stands for the molar volume of the solid metal, calculated as the ratio of the atomic weight to the density of the solid, M/ρ_S. Calculated values for the molar volumes are given in Table 1. The plot of this quantity versus melting point is given in Figure 3. The correlation is somewhat better as in Fig.1 (eq. 5), but not satisfactory. The equation of the correlation line is:

$$10^4\gamma.V^{2/3}\,[mJ] = (2160\pm580) + (3.16\pm0.31)\,T_m \quad r = 0.880 \quad n = 33 \qquad (7)$$

The greatest deviations form the fitting line are those for Be and Re (negative deviations) and for V, Ru (positive deviations). Excluding the evidently wrong values for Be and Re, the equation of the new correlation line is:

$$10^4\gamma.V^{2/3}\,[mJ] = (950\pm460) + (3.44\pm0.25)\,T_m \quad r = 0.931 \quad n = 31 \qquad (7a)$$

and without the uncertain values for V and Ru also:

$$10^4\gamma.V^{2/3}\,[mJ] = (2100\pm350) + (3.22\pm0.20)\,T_m \quad r = 0.953 \quad n = 29 \qquad (7b)$$

i.e. a quite good correlation.

Subsequently „molar“ surface tensions were plotted versus enthalpies of atomization (Figure 4). The correlation line is given by the equation:

$$10^4\gamma.V^{2/3}\ [\mathrm{mJ}] = (17.12\pm0.57)\ \Delta H_a[\mathrm{kJ/mol}] \quad r = 0.894 \quad n = 33 \qquad (8)$$

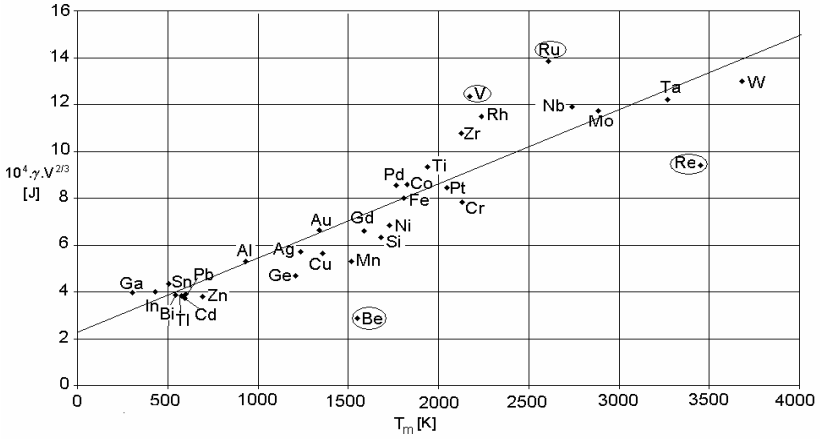

Figure 3.
„Molar“ surface tensions of solid metals versus melting points

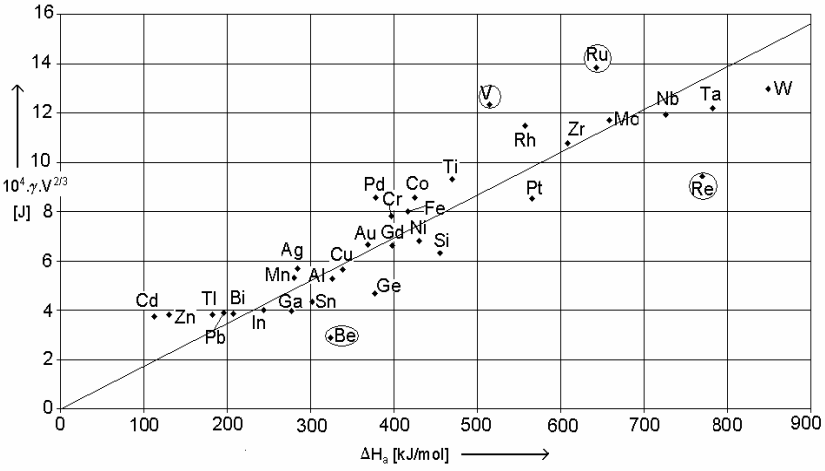

Figure 4.
„Molar“ surface tensions of solid metals versus enthalpies of atomization

The most important deviations are caused by the same elements as in the previous representation. Without Be and Re, the equation becomes:

$$10^4\gamma.V^{2/3}\ [mJ] = (17.70\pm0.51)\ \Delta H_a[kJ/mol] \quad r = 0.923,\ n = 31 \qquad (8a)$$

and letting apart V and Ru too:

$$10^4\gamma.V^{2/3}\ [mJ] = (17.14\pm0.45)\ \Delta H_a[kJ/mol] \quad r = 0.946,\ n = 29 \qquad (8b)$$

The general appearance of the plot is very similar to that on Figure 3, the correlation is quite the same. The introduction of molar surface tensions leads therefore to a better correlation as compared to surface tensions, but the scatter of the points is still important. Some reasons could be the imprecision of experimental values, the different types of crystal lattices in different metals, the fact that the experimental data were measured at temperatures sometimes quite far from the standard temperature, and the nature of molar surface tensions, these being essentially *free* energies, other than the enthalpies of atomization.

Two metals giving here deviations (but not in Fig.2) are Zn and Cd: their $\gamma V^{2/3}$-values appear to be too high as compared to their enthalpies of vaporization. This could be related to peculiarities of their crystal structure. They have a hexagonal closest packed structure, but the height of their unit cell is some 15% larger than normal for this type of crystals, i.e. the 6 adjacent atoms in the basal plane are nearer to one another as the other 6, in the next planes above or bellow. The interatomic distances are 2.660 and 2.907 Å for Zn, respectively 2.973 and 3.287 for Cd [7]. This could diminish the cohesion energy, i.e the enthalpy of atomization, while in the surface layer, these greater distances probably vanish. Besides, $V^{2/3}$ could give here a too large evaluation for the molar surface.

For comparison, the correlations were tested also with the values proposed by Tyson and Miller (Table 1). The corresponding „molar" quantities $\gamma^{TM}V^{2/3}$ were calculated for 45 elements and plotted versus melting points (Figure 5). The correlation line is described by the equation:

$$10^4\gamma^{TM}V^{2/3}\ [mJ] = (1350\pm330) + (3.42\pm0.18)\ T_m \quad r = 0.944,\ n=45 \qquad (9)$$

The corresponding representation against standard enthalpies of atomization is given in Figure 6. The equation of the correlation line is:

$$10^4\gamma^{TM}V^{2/3}\ [mJ] = (16.60\pm0.31)\ \Delta H_a[kJ/mol] \quad r = 0.969,\ n = 45 \qquad (10)$$

The much better correlation in both cases is a consequence of the higher precision of experimental data for liquid metals, the values of Tyson and Miller are based on, and of the disappearance of differences contingent on the crystal lattice near the melting point as well. Some larger deviations are those for Be, Ge and Si, accountable by their semi-metallic character and the presence of covalent binding. In Fig. 5 the large deviation for U is striking; caused by the unusual high melting temperature of this metal. In Fig. 6 this point is not longer an outlier; enthalpies of atomisation are better correlated to surface tensions than melting points.

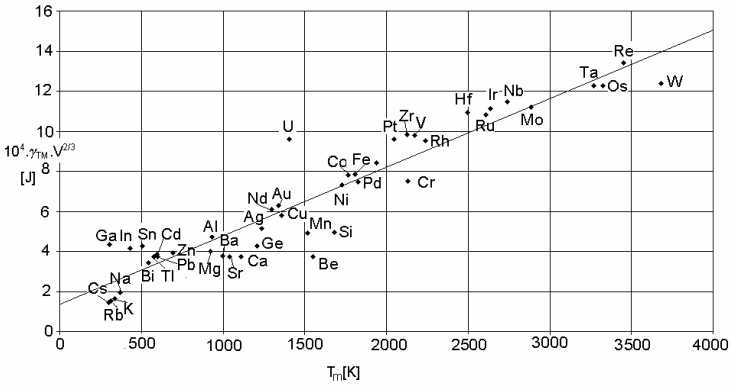

Fig.5.
Molar surface tensions (Tyson and Miller) versus melting points

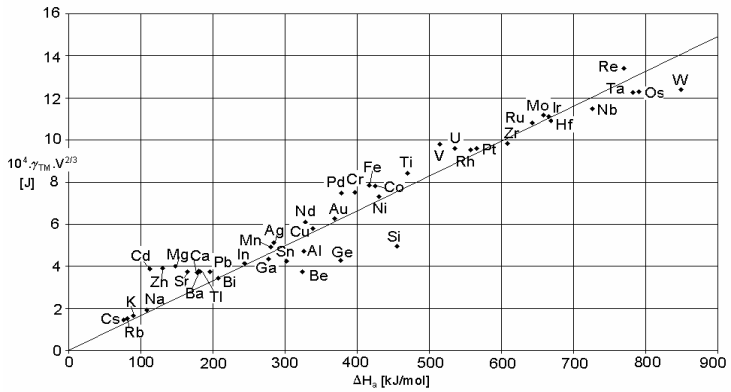

Fig.6.
Molar surface tensions (Tyson and Miller) versus enthalpies of atomization

The points for 2nd group elements in the periodic system (Mg, Ca, Sr, Ba) and for 12th group elements (Zn, Cd) are somewhat apart, over the correlation line; they all correspond to nearly the same value of „molar" surface tension. Such deviations appear also for the melts of these metals, in the correlation of their molar surface tensions with enthalpies of vaporization [8].

The experimental value for berrylium (γ = 1000 mJ/m^2) is evidently to low; it was determined by a single method [5] and is much under the value given by Tyson and Miller (1298). But even with this value, the point is clearly under the correlation line. Mezey and Giber [9] calculated for Be a γ-value of 1117; the value of Tyson and Miller extrapolated for 0 K is 1628, Boer et al. [10] estimated a value as high as 2700, while an *ab initio* calculation [11] gives γ = 1834.

The point for rhenium in Fig. 3 and 4 is far under the line, while the calculated value of Tyson and Miller gives a point near the line (Fig. 5, 6). The experimental value (2200 mJ/m^2) coming from a single determination (FEM) [5] is apparently wrong, the value extrapolated by Tyson and Miller (3133), and that calculated by Mezey [9] (3109) are much higher. Even larger are the values given by Boer [10]: 3600 and calculated ab initio [11]: 4214.

For V and Ru the points in Fig. 3 and 4 are far above the correlation line, while with the values of Tyson and Miller there are not such deviations. For both metals the experimental γ-values [5] are much higher than those given by Tyson and Miller and even than those given by Boer, but are in good agreement with the calculations of Mezey and ab initio (for V), while the results of the ab initio calculation for Ru are still higher. Therefore, our linear regression calculations were conducted as well without these four elements.

As a measure for the area occupied by an atom in the surface layer, we could select also the square of the metallic radius of the element R (Table 1), even though in the surface shell the positions of the atoms are somewhat different to those inside the metal lattice. The differences resulted from the reconstruction of the surface should however affect interatomic distances between different planes rather than distances within the same plane. The product $\gamma.R^2$ as an alternative to the "molar" surface tension, was thus plotted against the enthalpy of atomization in Figure 7, with experimental γ-values. The equation of the correlation line is:

$$10^{24}.\gamma.R^2[J] = (71.9 \pm 2.9)\Delta H_a[kJ] \quad r = 0.86,\ n = 33 \qquad (11)$$

This correlation is slightly worse than the corresponding one with $\gamma.V^{2/3}$ (Fig. 4, eq. 8), but the distribution of the points is very similar. The great deviations of the point for Ge and Si from the correlation line are evident. The reason could consist in the use of covalent radii for these elements, while metallic radii were used for all the other elements.

Excluding again Be, Re, V and Ru, the equation becomes:

$$10^{24}.\gamma.R^2[J] = (71.7 \pm 2.8)\Delta H_a[kJ] \quad r = 0.88,\ n = 29 \qquad (11a)$$

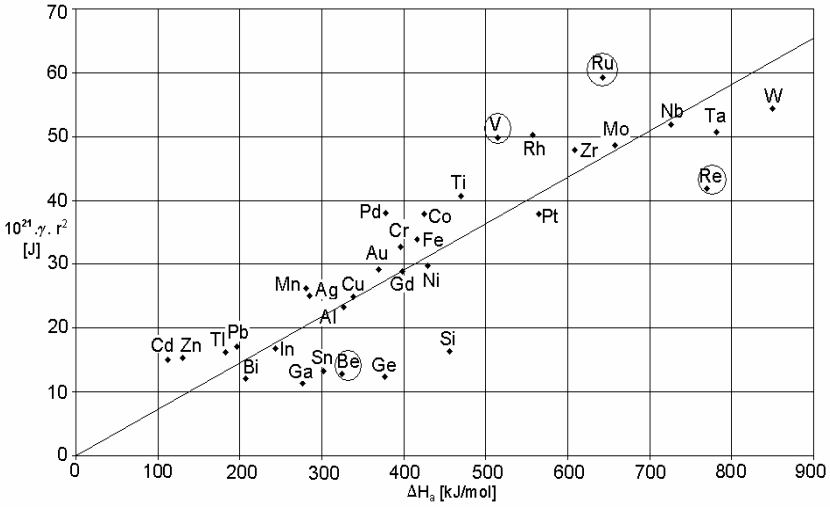

Fig.7.
$\gamma.R^2$ products against enthalpies of atomization

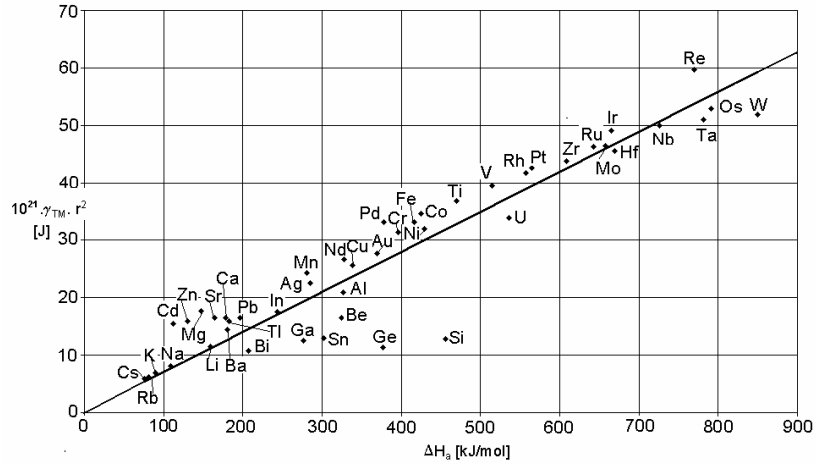

Fig. 8.
$\gamma.R^2$ products against enthalpies of atomization (γ from Tyson and Miller)

without a significant improvement for this once.

The similar plot with the values given by Tyson and Miller (Figure 8) corresponds to the correlation line:

$$10^{24}\gamma^{TM}.R^2[J] = (67.9 \pm 2.2)\Delta H_a[kJ] \quad r = 0.90,\ n = 45 \qquad (12)$$

The correlation is also somewhat worse than for „molar“ surface tensions (Fig. 6, eq. 10), while the general form is the same. The greater deviations correspond again to elements whose radii don't fit the pattern of metallic radii (Ge, Si).

Many approaches in the evaluation of surface energy make use of the broken-bond rule, according to which the surface energies scale with the number of broken bonds between first neighbours, when bulk atoms become surface atoms [12]. If only interactions between pairs of adjacent atoms are considered, the energy needed to bring atoms from the bulk to the surface should be proportional to the fraction α of broken bonds. Usually the ratio of surface energy (or enthalpy) to the enthalpy of vaporization for liquids or the enthalpy of atomization for solids is considered to be given by α. But above, we had free surface energies correlated to bulk energies. In order to have the same kind of quantities, we could either use instead of the molar surface free energies (surface tensions) the molar surface enthalpies (3) or energies

$$U_{sM} = \gamma_M + T.S_{sM} \qquad (13)$$

or instead of standard enthalpies of atomisation the corresponding free enthalpies

$$\Delta G_a = \Delta H_a - T\Delta S_a \qquad (14)$$

S_{sM} is the molar surface entropy (cf. Eq.(2)). In correlating surface and bulk properties of melted metals, the first way was chosen [8], since the temperature coefficients of the surface tension were reasonable well known and the molar surface entropy is nearly a constant, whatever the metal or the temperature were [13]. However for solid metals the temperature coefficient of surface tension was rarely determined and its constancy is questionable. For liquids, this constancy is related to constant value of the entropies of vaporization (Trouton's rule), while melting entropies are not constant, and atomization entropies should not be expected to be constant. The calculation of surface energies of solid metals would thus be very intricate. We preferred therefore the second way, to estimate free enthalpies of atomization (10).

The standard atomization entropy for solid metals can be calculated as the difference:

$$\Delta S_a = S_{298}^0 \text{ (gas)} - S_{298}^0 \text{ (solid)} \quad (15)$$

Standard entropies of solid metals are well known quantities and are given in Table 2. The entropies for gaseous metals can be calculated

Table 2.
Experimental and calculated properties of solid metals

Element	$S_{298,s}^0$ [J.mol^{-1}.K^{-1}]	$S_{298,g}^0$ [J.mol^{-1}.K^{-1}]	ΔS_a [J.mol^{-1}.K^{-1}]	ΔG_a [kJ/mol]	γ_{298} [mJ/m^2]	ΔG_a^i [kJ/mol]	k	γ_M [kJ]	$\alpha/f = \gamma_M/\Delta G_a^i$
Li	29.1	138.8	109.7	126.7	---	---	---	---	---
Be	9.5	142.0	132.5	284.8	1096	305.92	10.30	26.62	0.087
Na	51.3	153.7	102.4	77.9	---	---	---	---	---
Mg	32.7	154.4	121.7	111.4	---	---	---	---	---
Al	28.3	155.7	127.4	288.4	1180	307.77	17.78	46.22	0.150
Si	18.8	156.2	137.4	414.7	1200	433.53	14.55	53.26	0.123
K	64.7	160.3	95.6	60.7	---	---	---	---	---
Ca	41.6	160.6	119.0	142.7	---	---	---	---	---
Sc	34.6	162.1	127.5	339.8	---	---	---	---	---
Ti	30.7	162.8	132.1	430.5	2211	449.72	23.64	89.78	0.200
V	28.9	163.6	134.7	474.1	2900	493.71	25.00	104.24	0.211
Cr	23.76	163.9	140.1	354.8	2488	374.98	24.81	78.55	0.209
Mn	32	164.6	132.6	241.2	1400	261.28	20.33	44.87	0.172
Fe	27.3	164.8	137.5	375.3	2550	395.52	23.80	79.50	0.201
Co	30	165.4	135.4	384.3	2859	404.69	24.90	85.11	0.210
Ni	29.9	165.4	135.5	389.3	2304	409.69	19.77	68.41	0.156
Cu	33.2	166.4	133.2	298.6	1770	318.78	20.55	55.33	0.174
Zn	41.6	166.7	125.1	93.4	976	112.96	37.83	36.08	0.319
Ga	40.9	167.5	126.6	239.3	762	258.20	15.21	33.16	0.128
Ge	31.1	168.0	136.9	335.8	966	354.40	15.57	46.60	0.131
Rb	76.8	170.1	93.3	53.1	---	---	---	---	---
Sr	52.3	170.4	118.1	129.2	---	---	---	---	---
Y	44.4	170.6	126.2	383.7	---	---	---	---	---
Zr	39	170.9	131.9	569.5	2215	587.99	22.01	109.27	0.186
Nb	36.4	171.1	134.7	685.8	2667	704.84	18.78	111.79	0.159
Mo	28.7	171.5	142.8	615.5	3124	635.02	21.92	117.59	0.185
Tc	33.5	171.8	138.3	636.8	---	---	---	---	---
Ru	28.5	172.2	143.7	599.9	3400	619.70	22.15	116.91	0.189
Rh	31.5	172.4	140.9	514.9	2800	534.71	21.46	96.91	0.181
Pd	37.6	172.8	135.2	337.9	2000	357.54	23.96	72.36	0.202
Ag	42.6	173.0	130.4	245.7	1393	265.01	24.83	55.58	0.210
Cd	51.8	173.5	121.7	75.7	745	94.42	43.59	34.76	0.368
In	57.8	173.7	115.9	208.8	668	226.95	18.58	35.61	0.157
Sn	51.2	174.2	123.0	265.4	727	283.47	17.36	39.48	0.139
Cs	85.2	175.6	90.4	49.2	---	---	---	---	---
Ba	62.8	176.0	113.2	146.3	---	---	---	---	---

La	56.9	176.1	119.2	391.5	---	---	---	---	---
Nd	71.5	176.6	105.1	296.7	---	---	---	---	---
Pm	---	176.7	---	---	---	---	---	---	---
Sm	69.6	177.1	107.5	174.7	---	---	---	---	---
Eu	77.8	177.2	99.4	148.4	---	---	---	---	---
Gd	68.1	177.7	109.6	365.3	900	382.96	17.28	55.88	0.146
Yb	59.9	178.9	119.0	116.5	---	---	---	---	---
Lu	51	179.0	128.0	389.9	---	---	---	---	---
Hf	43.6	179.3	135.7	628.6	---	---	---	---	---
Ta	41.5	179.4	137.9	740.9	2957	760.01	19.13	122.76	0.162
W	32.76	179.6	146.9	805.6	3198	825.10	17.36	120.95	0.147
Re	36.9	179.8	142.9	727.3	2679	746.95	15.35	96.81	0.130
Os	32.6	180.1	147.5	746.9	---	---	---	---	---
Ir	35.5	180.2	144.7	622.1	---	---	---	---	---
Pt	41.6	180.4	138.8	523.9	2318	543.51	18.58	85.31	0.157
Au	47.4	180.5	133.1	329.3	1641	348.62	22.15	65.20	0.187
Tl	64.2	180.9	116.7	147.4	616	165.32	25.33	35.37	0.214
Pb	64.8	181.1	116.3	161.3	619	179.17	23.96	36.26	0.202
Bi	56.7	181.2	124.5	170.0	547	187.45	22.43	35.50	0.189
Ra	71.1	182.0	110.9	128.9	---	---	---	---	---
Th	51.8	182.5	130.7	559.3	---	---	---	---	---
Pa	51.9	---	---	---	---	---	---	---	---
U	50.2	182.8	132.6	496.1	---	---	---	---	---

Standard entropies of solid, $S_{298,s}^0$, and gas, $S_{298,g}^0$; ΔS_a - standard entropies of atomization, ΔG_a – free enthalpies of atomization, γ_{298} - γ values extrapolated for 298 K, ΔG_a^i – internal free enthalpies of atomization, $k = \gamma_{298} V^{2/3} / \Delta G_a^i$, γ_M – molar surface free energy.

by the methods of statistical thermodynamics. Since gaseous metals are monoatomic, the equation of Sackur und Tetrode [14] can be applied:

$$S(T, p) = \frac{5}{2} R \ln T - R \ln p + \frac{5}{2} R + R \ln \frac{(2\pi m)^{3./2} k^{5/2} g_0}{h^3} \qquad (16)$$

The entropies calculated by this formula are given in Table 2, together with the calculated values for the entropy of atomization (15) and the standard free enthalpies of atomization (14)

The plot of molar free surface energy against these calculated free enthalpies of atomization is similar to that in Fig. 4. The correlation line corresponds to the equation:

$$10^4 \gamma V^{2/3} \text{ [mJ]} = (18.53 \pm 0.66) \Delta G_a \text{[kJ/mol]} \quad r = 0.893, n = 33 \qquad (17)$$

The correlation is just the same as for enthalpies of atomisation (8), the introduction of free enthalpies did not improve it. The most important deviations are again for Be and Re (wrong experimental data) and for V and Ru (uncertain experimental values). Without the first two elements we obtain:

$$10^4\gamma V^{2/3}\ [\text{mJ}] = (19.20\pm0.60)\Delta G_a[\text{kJ/mol}] \quad r = 0.922,\ n = 31 \qquad (17a)$$

and excluding all the 4 elements:

$$10^4\gamma V^{2/3}\ [\text{mJ}] = (18.60\pm0.56)\Delta G_a[\text{kJ/mol}] \quad r = 0.945,\ n = 29 \qquad (17b)$$

The same correlation was verified for the values proposed by Tyson and Miller. The equation of the correlation line is:

$$10^4\gamma^{TM} V^{2/3}\ [\text{mJ}] = (17.92\pm0.39)\Delta G_a[\text{kJ/mol}] \quad r = 0.969,\ n = 45 \qquad (18)$$

The image is very similar to the one in Figure 6 and the coefficient of correlation is just the same.

The correlation with free enthalpies of atomization was also tested using R^2 as a measure of atomic surface. The correlation described by the equation:

$$10^{24}\gamma.R^2[\text{J}] = (77.89 \pm 3.23)\Delta G_a[\text{kJ}] \quad r = 0.860,\ n = 33 \qquad (19)$$

does not differ from the one using ΔH_a (Fig. 7, eq. 11). The exclusion of the 4 doubtful values (for Be, Re, V. Ru) does not result in an obvious improvement:

$$10^{24}\gamma.R^2[\text{J}] = (77.85 \pm 3.20)\Delta G_a[\text{kJ}]\ r = 0.881,\ n = 29 \qquad (19a)$$

Even though correlation is not improved by using free enthalpies of atomization instead of enthalpies of atomization, this treatment is theoretically legitimate.

The experimental values of surface free energies for solid metals were determined at very different temperatures. In order to compare them with ΔG_a it would be appropriate to refer them all to the standard temperature (298K). On the basis of the theory of corresponding states, Digilov [15] deduced an equation for the temperature dependence of surface tensions for solid metals, starting with the surface tension of the liquid at the melting point:

$$\gamma_s(T) \cong 1{,}2\gamma_L\left[1 - 0{,}229\left(\frac{T}{T_m} - 1\right) + 0.01\left(\frac{T}{T_m} - 1\right)^2\right] \qquad (20)$$

Actually, this relation should hold only for medium temperatures, about 0,6 T_m, but one may assume that the errors should not be important if extrapolated to the standard temperature. Thus the experimental data were recalculated for 298 K, inasmuch the temperature of their determination was found in literature, by an extension of equation (20):

$$\gamma_s(298) \cong \gamma_s(T)\frac{1-0{,}229\left(\frac{298}{T_m}-1\right)+0.01\left(\frac{298}{T_m}-1\right)^2}{1-0{,}229\left(\frac{T}{T_m}-1\right)+0.01\left(\frac{T}{T_m}-1\right)^2} \qquad (21)$$

These values were also enlisted in Table 2; of course, they are somewhat higher than the experimental values, determined at higher temperatures.

The values of free surface energies, recalculated for the standard temperature, were used to calculate the "molar" quantities $\gamma_{298}\ V^{2/3}$. These were plotted against free enthalpies of atomization (Fig. 9) and the correlation line has the equation:

$$10^4\gamma_{298}V^{2/3}\ [\text{mJ}] = (20.66\pm0.65)\Delta G_a[\text{kJ/mol}] \quad r = 0.916,\ n = 33 \qquad (22)$$

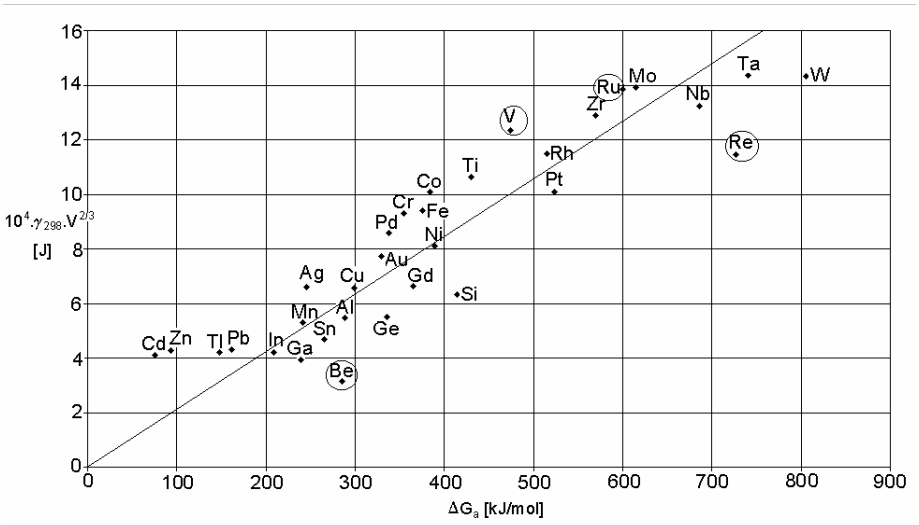

Fig.9.
„Molar" free surface enthalpy (standard temperature) against free enthalpy of atomization

Now the correlation is somewhat improved, but not in such a degree to justify all the amount of calculations necessary. The points for Be and Re remain here also far from the field of the other values, and without them the equation becomes:

$$10^4\gamma_{298}V^{2/3}\ [\mathrm{mJ}] = (21.28\pm0.61)\Delta G_a[\mathrm{kJ/mol}]\ r = 0.936,\ n = 31 \qquad (22a)$$

and after exclusion of V and Ru also:

$$10^4\gamma_{298}V^{2/3}\ [\mathrm{mJ}] = (20.92\pm0.63)\Delta G_a[\mathrm{kJ/mol}]\ r = 0.940,\ n = 29 \qquad (22b)$$

Among the other elements, higher deviations are observed for Si (nonmetal), Zn and Cd (their specific structure was discussed above) and W, whose very high free enthalpy of atomization should demand a higher value for the free surface energy also.

A possible improvement according to Mezey and Giber [9], is to use so-called "internal" free enthalpies of atomisation ΔG_a^i. These values are enthalpies of atomization corrected for the expansion work of the gas resulted by splitting all the bonds in the metal, from the (very small) volume of the metallic crystal to the volume of the monoatomic ideal gas. This work is missing in the case of the partial splitting of the bonds, associated with the conversion of a bulk atom into a surface atom. Since this work of expansion is negative, internal free enthalpies of atomisation have larger numerical values than ΔG_a:

$$\Delta G_a^i = \Delta G_a + RT\ln\frac{V_G}{V_S} = \Delta G_a + RT\ln\frac{RT}{p_0 V_S}. \qquad (23)$$

The molar volume of the gas was calculated from the law of ideal gases for the standard state, and the molar volume of the solid metal from the atomic mass and density, in the same state. These ΔG_a^i values are given in Table 2. The difference to the uncorrected values of the enthalpy of atomization is not important (some 10%) and it does not affect substantially the sequence of these values.

The plot of „molar" free surface enthalpies at 298K against the corrected ΔG_a^i-values is almost the same as in Fig. 9, and the correlation coefficient is also nearly unchanged.

$$10^4\gamma_{298}V^{2/3}\ [\mathrm{mJ}] = (19.90\pm0.60)\Delta G_a^i\ [\mathrm{kJ/mol}]\ \ r = 0.917,\ n = 33 \qquad (24)$$

The corresponding equations without Be and Re:

$$10^4\gamma_{298}V^{2/3}\ [\mathrm{mJ}] = (20.48\pm0.55)\ \Delta G_a^i\ [\mathrm{kJ/mol}]\ r = 0.937,\ n = 31 \qquad (24a)$$

and when V and Ru are also excluded:

$$10^4\gamma_{298}V^{2/3}\ [\text{mJ}] = (20.13\pm0.57)\ \Delta G_a^i[\text{kJ/mol}]\ r = 0.941,\ n = 29 \qquad (24b)$$

remain also quite unchanged.

It is interesting, that for both, the highest and the lowest values of free enthalpy of atomization, there are important deviations from the line of correlation. A sigmoidal curve seems to fit better the experimental points than a straight line (Fig. 10). Only the points for Be, Si and Re are now far outside

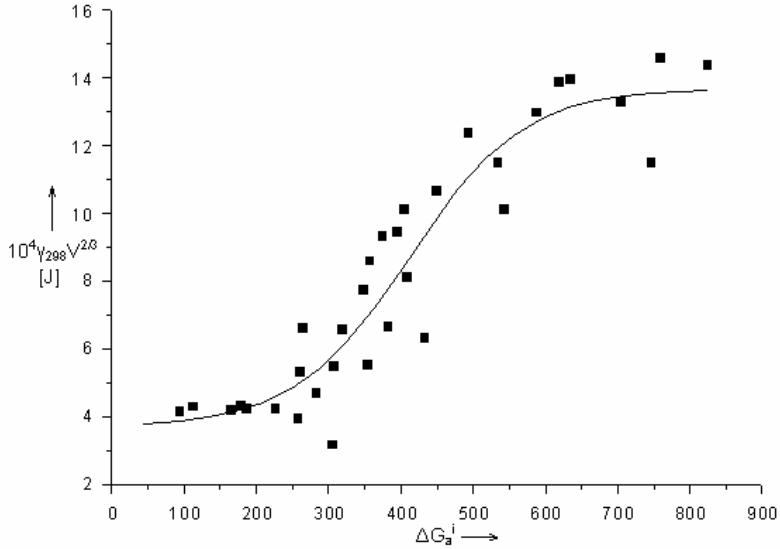

Fig.10.
Sigmoidal representation of $\gamma_{298}V^{2/3}$-values versus internal enthalpy of atomization

the curve. It may be assumed that for high values of the surface energy, a more important surface relaxation and reconstruction process takes place, in order to reduce tensions, so that the surface energy represents a smaller fraction of the bulk energy than the average for all metals. For low energies, the rearrangement of the atoms on the surface occurs to a lower degree and surface energy is a higher fraction of bulk energy.

Estimation of Surface Free Energies for Solid Elements

In order to compare for different metals the ratio of „molar" surface free enthalpy to the enthalpy of atomization, its value: $k = \dfrac{\gamma_{298}V^{2/3}}{\Delta G_a^i}$ was calculated (Table 2). The values are quite different, between 10.3 for Be and 43.6 for Cd.

The mean value is 21.57, the standard deviation 6.15, and the standard error of the mean 1.07. By excluding the extreme values for Be, Si (semi-metals), Re (uncertain value), Zn, Cd (exceptional cases), the span of the remaining 28 values is much narrower (from 15.6 to 25.3); the mean value is 21.08, the standard deviation 2.98 and the standard error of the mean: 0.56.

The "molar" surface quantities used above were conventional ones. In order to estimate the actual molar surface free energies, let us consider the atomic volume in the solid, Ω as the molar volume of the solid divided to Avogadro's number, V_S/N_A. The area assigned to an atom in the surface layer is:

$$s = f\Omega^{2/3} = f\,\frac{V_S^{2/3}}{N_A^{2/3}} \tag{25}$$

and the area occupied by a mole of atoms of this kind is $A_M=N_As$. The molar surface free energy is therefore given by:

$$\gamma_M=fN_A^{1/3}\gamma V^{2/3} \tag{26}$$

f is a packing coefficient, a little greater then 1, depending on the crystalline structure. Ignoring this factor, the $\gamma V^{2/3}$-values should be multiplied by $N_A^{1/3}$ = $8{,}445.10^7$ to give molar surface free energies. The ratio of these values to the enthalpies of atomization, α, should represent, according to the model of broken bonds, the fraction of broken bonds with the nearest neighbours, when an bulk atom goes to the surface of the crystal. Actually, for unknown f-values, the ratio of the two energies is equal to α/f. These values are also given in Table 2.

The statistical analysis of the results is similar to that of the *k*-values. The extreme values are 0.087 (Be) and 0.368 (Cd). For the 33 elements, the mean value is 0.182, the standard deviation 0.052, and the standard error of the mean 0.09. Without the values for Be, Si, Re, Zn and Cd, the range of the remaining 28 values is restrained to 0.128… 0.214; the mean value is 0.177, the standard deviation 0.026 and the standard error of the mean 0.005.

The α-value is therefore about 1/5. If we assume, with Mezey and Giber [16], that the effect of the relaxation and reconstruction in the surface layer were equivalent to the recovery of one of the broken bonds, the transition of an atom from the bulk to the surface should thus bring about the splitting of about ¼ of its bonds to the nearest neighbours.

In the case of melted metals, for 64 elements, the average ratio found between molar surface energy and enthalpy of vaporization was 0.18 [8], i.e. the same as here for α/f. This speaks for the model of the broken bonds, and shows that the situation is similar in the case of metal melts and of polycrystalline solid metals.

Among the metals with different crystal structures, no significant differences were found: the mean α/f-value is 0.182 for the 7 metals with

body centred cubic lattice and 0.181 for the 9 metals with cubic close packed lattice. There are probably too few available data. According to the theoretical estimations of Mezey and Giber [9] the ratio should be in these two cases 0.184 and 0.192 respectively.

The same ratios calculated from the data of Tyson and Miller [6], the range of values is narrower: the k-values go from 11.40 (Si) to 40.86 (Cd). Other values far from the average are those for Ge (12.06), Be (12.20) and Zn (34.72). For the other elements k varies between 15.00 and 30.72 (α/f between (0.127 and 0.260). The mean value is somewhat lower: k = 19.52 and α/f = 0.165 for 46 elements. Without the extreme values for Si, Ge, Be, Zn and Cd, the mean values become 19.186 and respectively 0.162. These lower ratios can be explained by the fact that the values of the surface free energies refer to the melting point of the solid elements, while the internal free enthalpies of atomization were calculated at 298 K. According to Mezey [9], this ratio should not vary with the temperature, but both quantities should refer to the same temperature.

On the basis of the relations found here, free surface energies for 69 elements were estimated, in three variants:

- from $\gamma_M = k\Delta G_a^i$, with the mean value k = 21
- from $\gamma_M = k\Delta G_a^i$, taking for k the slope of the straight line in eq. (20b): k = 20,1
- from the γ_M-values read on the sigmoidal representation (Fig. 14).

These free surface energies are given as γ_1, γ_2 and γ_3 in Table 3.

By comparison with experimental data (if available) and with calculated values from different authors (cf. Table 1), the most plausible values were selected (as recommended values printed in bold characters in Table 3). Insofar as possible, for elements of the same group in the periodic table the same kind of values was selected.

For non-metals and semi-metals, as Si, Ge, Be, Sb, Te none of the calculated values are suitable. The sigmoidal correlation gives better values for elements of the main groups: group 2 (Mg - Ra), groups 13 (Al - Tl), 14 (Sn - Pb), but also for groups 12 (Zn,Cd) and 15 (V - Ta), or for transition metals with highest values of surface tensions: W, Re. This correlation works also for the bivalent lanthanoides Yb and Eu, whose similarities to elements of the groups 2 and 12 are known, and also for Th and U.

For alkali metals (1st main group) the linear correlation with the lower k-value (γ_2) seems to fit the best; as well as for lanthanoides (except Eu and Yb), elements of group 15 (Sb, Bi) and for Ni and Mo.

The linear correlation with the higher k-value (γ_1) seems to work best for transition metals of the groups 3 (Sc, Y), 4 (Ti - Hf), Mn, groups 8-10 (except Ni), 11 (Cu - Au).

For some elements (Po, At, Ac) there is no possibility to select the best values, since both experimental and calculated values are missing.

Table 3.
Free surface energies (mJ/m^2) of solid metals at standard temperature, estimated from linear correlations for k=21 (γ_1) and for k = 20,1 (γ_2) and from sigmoidal correlation (γ_3). Recommended are the bold values

Element	Li	Be	Na	Mg	Al	Si	K	Ca	Sc
γ_1	550	2230	240	470	1390	1730	130	380	**1230**
γ_2	**530**	2140	**230**	450	1330	1660	**120**	370	1180
γ_3	730	2030	470	**690**	**1280**	1780	300	**470**	1162
Element	Ti	V	Cr	Mn	Fe	Co	Ni	Cu	Zn
γ_1	**1960**	2440	**2110**	**1450**	**2250**	**2410**	2450	**1810**	540
γ_2	1880	2330	2020	1380	2150	2310	**2340**	1730	520
γ_3	2050	**2610**	2020	1320	2220	2390	2450	1640	**900**
Element	Ga	Ge	Rb	Sr	Y	Zr	Nb	Mo	Tc
γ_1	1050	1300	100	290	**1150**	**2120**	2980	2990	**3310**
γ_2	1010	1250	**95**	280	1100	2030	2850	**2860**	3170
γ_3	**960**	1220	260	**390**	1150	2180	**2710**	2950	3180
Element	Ru	Rh	Pd	Ag	Cd	In	Sn	Sb	Te
γ_1	**3200**	**2740**	**1750**	**1180**	360	750	930	730	500
γ_2	3060	2620	1680	1130	340	720	890	700	480
γ_3	3200	2910	1650	1080	**700**	**730**	**830**	690	570
Element	Cs	Ba	La	Ce	Pr	Nd	Sm	Eu	Gd
γ_1	80	300	1140	1140	950	880	550	370	1090
γ_2	**75**	283	**1090**	**1090**	**910**	**840**	**530**	350	**1050**
γ_3	220	**360**	1140	1140	880	790	590	**440**	1060
Element	Tb	Dy	Ho	Er	Tm	Yb	Lu	Hf	Ta
γ_1	1100	820	860	910	670	330	1260	**2390**	3250
γ_2	**1050**	**780**	**820**	**870**	**640**	320	**1200**	2290	3110
γ_3	1060	740	770	830	640	**470**	1260	2330	**2750**
Element	W	Re	Os	Ir	Pt	Au	Tl	Pb	Bi
γ_1	3870	3660	**3870**	**3220**	**2620**	**1560**	510	540	510
γ_2	3700	3510	3700	3080	2510	1490	490	520	**490**
γ_3	**3040**	**3160**	3260	3140	2760	1440	**610**	**610**	560
Element	Po	At	Ra	Ac	Th	U			
γ_1	330	220	240	1010	1650	2010			
γ_2	320	210	230	970	1580	1920			
γ_3	500	530	**320**	990	**1710**	**2150**			

Conclusions

The scarcity of direct experimental data for the surface tensions or surface free energies of solid metals make necessary their semi-empirical estimation or the theoretical calculation. Using selected experimental values, their correlation with melting points and standard enthalpies of atomization was verified. „Molar“

surface free energies, calculated by means of molar volumes or metallic radii gave acceptable linear correlations with the enthalpies of atomization. With standard free enthalpies of atomization, calculated with the entropies of atomization, obtained as differences between the entropies of gaseous and solid metals, the correlations are almost the same as with standard enthalpies.

In order to improve the calculations, surface free energies at standard temperature were estimated from the experimental values and internal free enthalpies of atomization were calculated, but not significantly better correlations were obtained. The deviations of some elements from the correlation lines can be explained by errors in the experimental data or by peculiarities in their structure.

The results can be interpreted in terms of the theory of broken bonds between neighbouring atoms in the metallic crystals. The correlations found here could be used to estimate values of free surface energies for 69 solid elements.

REFERENCES

1. O. Horovitz, E. M. Pică, A. L. Popoviciu, *Acta Technica Napocensis,* Series: Applied Mathematics & Mechanics, **2005**, *48*, 7-12.
2. A. W. Adamson, A. P. Gast, "Physical Chemistry of surfaces", 6.Ed., Wiley, New York, 1997.
3. R. Shuttleworth, *Proc.Roy.Soc.London* Ser.A, **1950,** *63*, 444.
4. O. Horovitz, E. M. Pică, A. L. Popoviciu, *Acta Technica Napocensis,* Series: Applied Mathematics & Mechanics **2005**, *48*, 13-22.
5. V. K. Kumikov, Kh. B. Khokonov, *J.Appl.Phys.,* **1983,** 54, 1346-1350.
6. W. R. Tyson, W. A. Miller, *Surface Science*, **1977**, *62*, 267-276.
7. L. Pauling, "The Nature of the Chemical Bond", Cornell Univ.Press, Ithaca, NewYork, 1960; p.412.
8. O. Horovitz, E. M. Pică, *Analele Ştiinţifice ale Universităţii de Stat din Moldova: Seria „Ştiinţe chimico-biologice"*, Chişinău, 2005, p..561-570.
9. L. Z. Mezey, J. Giber, *Jpn.J.Appl. Phys.*, **1982**, *21*, 1569-1571.
10. F. R. de Boer, R. Boom, W. C. M. Mattens, A.. R. Miedema, A. K Niessen, "Cohesion in Metals", North-Holland Ed., Amsterdam, 1988
11. L. Vitos, A. V. Ruban, H. L. Skriver, J. Kollár, *Surface Science,* **1998**, *411*, 186-202.
12. A. S. Skapski, *J. Chem. Phys.*, **1948**, *16*, 386,389; C. Herring, in "Structure and Properties of Solid Surfaces" (Ed. R.Gomer & C.S.Smith), Univ.of Chicago Press, 1952, p. 5 ; C. Herring, "Metal Interfaces", ASM, Cleveland, 1952.
13. O. Horovitz, E.M. Pica, *Arta Technica Napocensis,* Series: Machines Constructions Materials, **2003**, *46*, 131-138.
14. I. Cădariu, „Chimie fizică. Stările de agregare şi termodinamica chimică", EDP Bucureşti, 1971, p. 372-3.
15. R. M. Digilov, *J.Crystal Growth*, **2003**, *249*, 363-371.
16. L. Z. Mezey, J. Giber, *Surface Science*, **1990**, *234*, 210-219.

STUDIA UNIVERSITATIS BABEŞ-BOLYAI, CHEMIA, LI, 1, 2006

ADSORPTION KINETICS OF STEARIC ACID AT THE BENZENE/WATER INTERFACE

MARIA TOMOAIA-COTISEL*

ABSTRACT. The adsorption kinetics of stearic acid from benzene solutions at the benzene/water interface was studied by using the pendant drop method. Kinetic equations for diffusion controlled adsorption and for Langmuir adsorption were tested. A theoretical approach to the dynamic interfacial pressures is developed and a new kinetic equation for the diffusion controlled kinetics is proposed, based on Ward and Tordai's diffusion equation associated with a two dimensional van der Waals state equation. It is shown that this approach describes the dynamic interfacial pressures within the limits of the experimental errors and the new equation is valid over a wide range of time and for different surfactant concentrations in oil solutions. It is also concluded that this new approach allows the calculation of diffusion coefficients, subsurface concentrations and intermolecular interaction parameters within adsorbed layers of biosurfactants at the oil/water interfaces. Obtained results are in substantial agreement with similar earlier reported data for the surfactant adsorption at liquid/liquid interfaces.

Keywords: Diffusion controlled adsorption; Langmuir adsorption kinetics; Dynamic interfacial pressures; Pendant drop method; Stearic acid; Benzene/water interface

Introduction

The adsorption of surfactant molecules at the air/water and oil/water interfaces has attracted a considerable attention in the last several decades (1-28) due to its fundamental and industrial importance (1-4, 25) as well as to its biological significance (29-32). These studies have involved various experimental techniques as well as the formulation of theoretical models for describing the adsorption kinetics of surfactants at liquid interfaces.

Generally, the adsorption of surfactant molecules from a solution to a liquid/gas (1-15) or to a liquid/liquid interface (1, 5, 16-24) occurs in two steps. Surfactant is first transported from the bulk to the subsurface by diffusion (the subsurface is a liquid layer just below the interface, belonging still to the bulk). The second step is the transfer from the subsurface to the interface, implying sometimes a transfer through a potential barrier (22, 25-28). In miscellaneous systems the controlling rate may be either the diffusion (i.e. the adsorption may be diffusion controlled), or the transfer (i.e. the adsorption is barrier-controlled). Several theoretical models have

* "Babes-Bolyai" University of Cluj-Napoca, Department of Physical Chemistry, 400028 Cluj-Napoca, Romania; mcotisel@yahoo.com

been developed for both processes, as well as for mixed adsorption mechanisms in which both steps are considered (1-6).

In the case of adsorption to a liquid/liquid interface (1, 16-24), the situation is analogous to that for the air/water interface if the solute is soluble only in one liquid phase. If the solute is soluble in water and in oil phases, then the adsorption process includes also the solute transfer across the interface into the other liquid bulk phase (16).

For example, the adsorption kinetics of some aliphatic carboxylic acids and aliphatic alcohols (6-9), like 1, 9 nonane dicarboxylic acid and 1, 9 nonane diol (6), was studied at the air/water interfaces and described by Langmuir kinetic equation, considering the adsorption and desorption rate constants. Another example is related to the adsorption of some salts of fatty acids, like sodium laurate (10-13), sodium myristate (10-12), and sodium oleate (14), from aqueous solutions to the air/water interface, which was analyzed by means of diffusion controlled kinetics. However, the very slow adsorption of fatty acids from oil phase to the oil/water interface has received only a limited attention (5).

The main goal of this work is to focus on the experimental dynamic data for the adsorption of stearic acid at the benzene/water interface and to discuss the theoretical aspects of adsorption kinetics at the oil/water interface. The experimental data are recorded in terms of the time dependent interfacial pressures, which are also known as dynamic interfacial pressures. These interfacial pressures are dependent of time and of the surfactant bulk concentration and of the surfactant interfacial adsorption. An equilibrium state is reached when the interfacial pressure is constant (18, 23, 24).

Stearic acid is a fatty acid widely used in model biomembranes (29-32) as well as in Langmuir-Blodgett films due to its increased stability in monolayers at fluid interfaces (33-35). The understanding of the adsorption kinetics of stearic acid at fluid interfaces is important for the description of its dynamic surface properties. This is not only an interesting subject in basic research, but also very important for fabricating stable, homogeneous and ordered molecular films.

Further, we examine the diffusion approach, its simplifying assumptions, and Langmuir adsorption kinetics for the adsorption of stearic acid at the oil/water interface. As a first step, we apply the theory of diffusion controlled kinetics on ideal interfacial layers and the Langmuir adsorption kinetics to experimental data of the adsorption of stearic acid at the oil/water interface.

Furthermore, we extend the diffusion theory for non-ideal adsorbed layers at liquid/liquid interfaces (24) and we develop a theoretical approach based on the Ward and Tordai's diffusion equation associated with a two dimensional state equation of van der Waals type and a new diffusion equation is derived and used to describe the dynamic interfacial pressures.

This approach is developed and an analytical procedure of calculation is proposed to solve the resulting new diffusion controlled equations for the surfactant adsorption at liquid/liquid interfaces.

Finally, a mathematical procedure is formulated to determine the diffusion coefficient, the subsurface concentration and the molecular interaction parameters within the adsorbed layers of surfactant at liquid/liquid interface.

Theoretical Models of Adsorption Kinetics

Diffusion Controlled Kinetic Model

Diffusion controlled adsorption was analyzed quantitatively by Ward and Tordai (5, 24) using the following equation:

$$\Gamma(t) = 2\left(\frac{D}{\pi}\right)^{1/2}\left\{c_0 t^{1/2} - \int_0^{t^{1/2}} c_s(t-\tau)d\tau^{1/2}\right\} \qquad [1]$$

where $\Gamma(t)$ is the dynamic adsorption of the surfactant from an infinite bulk phase at the interface up to the time t, *i.e.*, $\Gamma(t)$ is the amount of the solute which has diffused across the subsurface into the interface, up to the time t; D stands for the bulk diffusion coefficient of the surfactant (defined by Fick's equation); π is 3.1415; c_0 is the surfactant bulk concentration far from the surface; $c_s(t)$ is the subsurface concentration and τ stands for a dummy variable ranging from 0 to t. At zero time, $c_s(t) = 0$. Later, it begins to increase and $c_s(t)$ becomes equal to c_0, when the adsorption equilibrium is attained.

In Eq. [1] the second term on the right side contains the back diffusion integral taking into account the desorption process. Practically, at the beginning this integral vanishes and the second term may be neglected, obtaining the short time approximation:

$$\Gamma(t) = 2\left(\frac{D}{\pi}\right)^{1/2} \cdot c_0 t^{1/2} \qquad [2]$$

Another approximation has been derived for long time by presuming that at long time $c_s(t)$ is almost constant. In this approach one obtains:

$$\Gamma(t) = 2(c_0 - c_s(t))\left(\frac{D}{\pi}\right)^{1/2} t^{1/2} \qquad [3]$$

Both Eqs. [2] and [3] suggest a proportionality of the adsorption with $t^{1/2}$. Generally, the dynamic interfacial tension, σ(t), or the dynamic interfacial pressure, Π(t), is measured and used as a tool to investigate the surfactant adsorption at the fluid interfaces.

In order to establish a correlation between the adsorption Γ(t) and the dynamic interfacial tension σ(t) or the dynamic interfacial pressure Π(t) = σ_o – σ(t), frequently, the surface state equation:

$$\Pi(t)\, A(t) = kT \quad \text{or} \quad \Pi(t) = \Gamma(t)kT \qquad [4]$$

is used, which is the two dimensional analog of the perfect gas state equation (22, 27); σ_0 represents the interfacial tension of the pure interface in the absence of the surfactant. It is argued that the state equations apply whether the monolayer is in equilibrium with the subsurface or whether it is not.

Combining Eq. [4] with Eqs. [2] and [3], respectively, one obtains:

$$\Pi(t) = 2kT\left(\frac{D}{\pi}\right)^{1/2} c_0 t^{1/2} \qquad [5]$$

$$\Pi(t) = 2kT\left(\frac{D}{\pi}\right)^{1/2} (c_0 - c_s(t))t^{1/2} \qquad [6]$$

Both Eqs. [5] and [6] show a linear relationship between the dynamic interfacial pressure, Π(t), and $t^{1/2}$. Details on this approach will be presented further on in this investigation.

Langmuir Kinetic Model

On the other hand, by presuming that the molecular diffusion is very fast and the transfer from the subsurface to the surface is the rate limiting step and it follows a *Langmuir kinetics* (6-9), one obtains:

$$y = \ln \frac{\Delta\sigma_0}{\Delta\sigma} = \ln \frac{\sigma_0 - \sigma_e}{\sigma(t) - \sigma_e} = K\, t \qquad [7]$$

where σ(t) stands for the actual and σ_e for the equilibrium interfacial tension and σ_0 for the interfacial tension in the absence of the surfactant. Further, the rate constant K is given by:

$$K = \frac{k_1}{\Gamma_\infty} c_0 + \frac{k_2}{\Gamma_\infty} \quad [8]$$

where k_1 is the rate constant of adsorption (cm s^{-1}), k_2 stands for the rate constant of desorption (mole cm^{-2} s^{-1}) and Γ_∞ is the maximum adsorption (mole cm^{-2}) at the saturation of the liquid/liquid interface with surfactant molecules.

In the present paper the dynamic interfacial pressures, $\Pi(t) = \sigma_o - \sigma(t)$, at the benzene/water interface have been measured for benzene solutions of stearic acid (octadecanoic acid: SA) of various SA concentrations. The validity of the above equations has been tested and an attempt is made to derive a new equation for the diffusion controlled adsorption, taking into account the non-ideal behavior of adsorbed films at liquid interfaces, particularly for high bulk surfactant concentrations. The results of the analysis of the experimental data performed on the basis of the new equation shows that the latter allows a better description of the adsorption kinetics, than the other equations given above.

Experimental

Stearic acid (octadecanoic acid: SA) was a synthetic commercial product of high purity (minimum 99%) purchased from Sigma. Benzene pro-analysis was purchased from Merck. All chemicals were used without an additional purification. Twice-distilled water of pH 2 was used, containing 0.01 mole/dm^3 of hydrochloric acid, as the aqueous phase. Volumetric aqueous solutions of HCl pro-analysis were purchased from Reactivul Bucharest.

Stearic acid at pH 2 forms uncharged adsorbed monolayer, the molecules being completely unionized (29). Due to the very low solubility of stearic acid in water of pH 2, any transport across the benzene/water interface can be neglected. The pH of the aqueous solutions was constant during all experiments and it was measured by an MV-84 type pH-meter by using a glass electrode.

Dynamic surface tensions in the time range from 1 minute up to 120 minutes were measured by pendant drop and by ring method for pure benzene and benzene solutions of various stearic acid concentrations at the interface with aqueous solutions of pH 2.

The pendant drop technique was described by us elsewhere (23). The shape of drops was recorded on a highly quality film in order to determine the characteristic drop diameters. By using an appropriate computer program the dynamic interfacial tension values were finally determined.

Experimental data obtained by the pendant drop technique were compared with the data obtained by ring method described by us previously (36). The agreement between the two methods is excellent and the deviations

do not exceed the error of the individual method. The accuracy of interfacial tension measurements was ± 0.1 mN/m, in agreement with literature data (20, 37). All measurements were performed at constant temperature of 20 ± 0.1 ^{o}C.

Results and Discussions

Dynamic interfacial tension σ(t) values obtained by means of the pendant drop method, allowed us to calculate the corresponding Π(t) = σ_0 – σ(t) interfacial pressure values. The Π(t) *versus* time (t) curves, characterizing the adsorption process of SA from benzene at the benzene/water (pH 2) interface is presented in Fig.1.

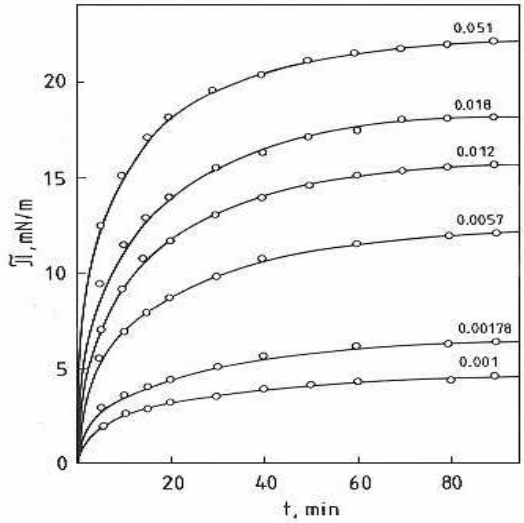

Fig. 1.

Experimental dynamic interfacial pressures, Π(t) = σ_0 – σ(t) in mN/m, of stearic acid (SA) benzene solutions as function of time, t in min, at the benzene/water of pH 2 interface. Figures indicate the bulk concentration C_0 of stearic acid in benzene, in mole dm^{-3}. Solid lines calculated by Eq. [18].

As can be seen, the interfacial pressures vary with surfactant bulk concentrations and with time over a wide range of time, from 0 to 90 min. Generally, the equilibrium interfacial pressures (Π_e in mN/m) are recorded at 120 min when the adsorption equilibrium is completely attained and it is demonstrated by the constant value of the interfacial pressures.

The validity of Eq. [7] has been tested by calculating the left hand side (denoted y) of this equation, by using the σ(t) and σ_e values (the latter ones being measured at 120 min) and the interfacial tension of the pure benzene/

water interface in the absence of surfactant was taken σ_o = 34.7 mN/m.

Inspecting the experimental data, it is found that y *versus* t data exhibit a quite good linearity, although the straight lines do not pass through the origin of the coordinate system, *i.e.* actually instead of Eq. [7] one has:

$$y = \ln \frac{\sigma_0 - \sigma_e}{\sigma - \sigma_e} = B + K t \qquad [7']$$

By performing a linear regression, the parameters B and K have been determined. Results are presented, together with the correlation coefficients, *r*, in Table I. In the last column *n* indicates the number of experimental points used in the linear regression.

Table I.
The B and K parameters of Eq. [7**'**].

C_0 mole dm^{-3}	B	K min^{-1}	r	n
0.001	0.430	0.0397	0.9991	7
0.00178	0.374	0.0396	0.9977	7
0.0057	0.395	0.0406	0.9990	8
0.012	0.439	0.0415	0.9978	8
0.018	0.568	0.0431	0.9994	9
0.051	0.566	0.0501	0.9949	10

As seen from Table I, the B values are rather far from zero. This means that the basic hypothesis used to derive Eq. [7] is not perfectly valid, presumably the diffusion equilibrium is not yet established, and consequently the boundary condition $c_s(t) = c_0$ is not fulfilled. Nevertheless, from the K values reported in Table I, some conclusions can be drawn. As seen, with increasing c_0 the K values derived also increase, as expected on the basis of Eq. [8] and the dependence of K with c_0 exhibits indeed a quite good linearity. The relative adsorption k_1/Γ_∞ and desorption k_2/Γ_∞ rate constants derived by means of linear regression Eq. (8) and the corresponding correlation coefficients are presented in Table II.

Table II.
Relative adsorption, k_1/Γ_∞, and desorption, k_2/Γ_∞, rate constants derived by Eq. [8] from K values listed in Table I.

Surfactant	k_1/Γ_∞ mole $^{-1}$ dm^3 min $^{-1}$	k_2/Γ_∞ min $^{-1}$	r	k_1/k_2 mole $^{-1}$ dm^3
Stearic acid	0.212	0.0392	0.9990	5.4
Dibucaine	7.25	0.159	0.9914	45.6
Tetracaine	4.99	0.149	0.9988	33.5

Table II contains also the same magnitudes previously obtained for two anesthetics, *viz*. dibucaine and tetracaine, under similar working conditions (24).

The analysis of data in Table II shows the quite good validity of Eq. [8], reflected by the correlation coefficient values. The relative rate constant values are rather reasonable and their k_1/k_2 ratios are in substantial agreement with published data (6-8) for the adsorption of various surfactants at liquid/liquid interfaces. These ratios represent the equilibrium adsorption constants and characterize the interfacial activity of these biocompounds at the oil/water interface. In this respect, the k_1/k_2 value for dibucaine is higher than the corresponding value for tetracaine suggesting a higher interfacial activity of the dibucaine in agreement with the interfacial pressure measurements at the oil/water interface.

Generally, the relative rate constant values (Table 2) for anesthetics are much higher than those corresponding to stearic acid. These values are not easy to compare because the mechanism of adsorption and desorption of these two types of biocompounds (i.e. anesthetics and fatty acids) is completely different and consequently the rate constants are determined by different factors. In spite of the different mechanism for adsorption, both fatty acid and anesthetics strongly adsorb at the oil/water interface and show a certain type of similarity in their adsorption behavior.

In the case of stearic acid, molecules adsorb from oil phase to the oil/water interface immersing their unionized polar groups into the water phase. The driving force for the adsorption of stearic acid molecules is the change in enthalpy due to the hydration of their adsorbed hydrophilic groups, when they immerse into the water phase being accompanied by conformational rearrangements in the hydrocarbon chains. Unlike stearic acid, anesthetics are ionized water soluble compounds. They adsorb from water to the oil/water interface by penetrating their hydrophobic chains into

the oil phase. Their adsorption is controlled by the hydrophobic effect, by the electrostatic interactions among the ionized polar groups, and by the hydrophobic interactions among the hydrophobic chains and the oil phase. According to the hydrophobic effect, the hydrocarbon chains in water phase are surrounded with structured water. Therefore, the adsorption of anesthetics is also accompanied by the increase of the entropy of the system because of the destruction of the ordered structure of water molecules formed around the hydrophobic chains in aqueous phase.

Although these results seem to be reasonable, the quite high B values reported in Table I show that Eq. [7], successfully used to describe the adsorption at the air/water interface (6-8), in our case is an approximation and the diffusion might play an important part in the overall adsorption process. Consequently, we further test the validity of Eqs. [5] and [6].

For this purpose, the experimental Π(t) values calculated from σ_0 and σ(t) values are presented *versus* $t^{1/2}$ in Fig. 2.

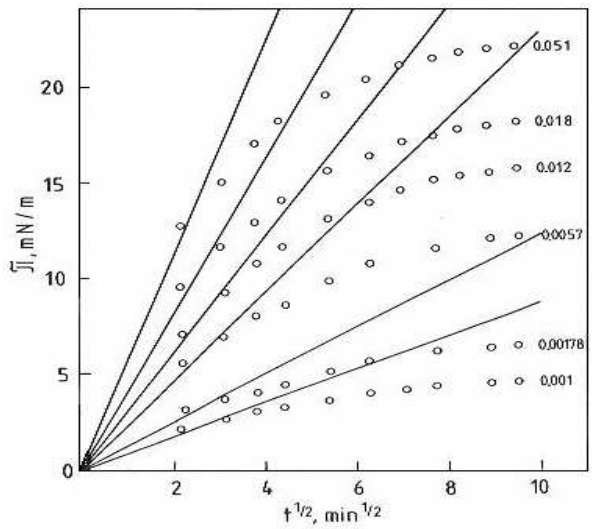

Fig. 2.
Experimental dynamic interfacial pressures of stearic acid benzene solutions at the interface with water of pH 2 as function of $t^{1/2}$. (Symbols as in Fig. 1).

If the Eq. [5] or Eq. [6] was valid, the Π(t) *versus* $t^{1/2}$ curves would exhibit a linear portion at least at small t values. This is why the tangencies to the experimental curves for t = 0 were constructed (Fig. 2). Although, the experimental curves exhibit an important negative deviation from these straight lines, certain linearity may be observed. In order to obtain a clear

image, a linear regression analysis has been performed by adding successively the experimental data, one by one, and by calculating every time the parameters of the following equation:

$$\Pi(t) = mt^{1/2} + p \qquad [9]$$

The general picture is the following, by adding the experimental data in the order of increasing t values, the slope of the straight line (*i.e.,* the m value) diminishes, and the ordinate intercept p increases. In the same time the correlation coefficient diminishes.

Results are presented in Table III, where the limits of m and p values are given. Those obtained by means of the first three experimental points (noted m_i and p_i, respectively), as well as the values obtained with a final number, n_f, of experimental points (noted m_f and p_f, respectively), for which one had still $r > 0.99$, r being the correlation coefficient. In Table III are also listed the total number, n_{max}, of the experimental points obtained for every bulk concentration of SA.

Being more specific, Eq. [9] is a general form of Eqs [5] and [6].

Table III.
Limits of the m (m_i and m_f) and p (p_i and p_f) parameters of Eq. [9] for $r > 0.99$. For symbols see the text.

C_0 mole dm^{-3}	m_i mN m^{-1} $min^{-1/2}$	m_f mN m^{-1} $min^{-1/2}$	p_i mN m^{-1}	p_f mN m^{-1}	n_f	n_{max}
0.001	0.47	0.33	1.16	1.59	10	10
0.00178	0.63	0.48	1.59	1.72	7	9
0.0057	1.47	1.26	2.23	2.85	6	9
0.012	2.27	2.08	1.96	2.48	4	11
0.018	2.14	1.88	4.64	5.92	5	11
0.051	2.68	2.50	6.57	7.06	4	11

The analysis, of the data given in Table III, shows that Eqs. [5] and [6] are very rough approximations, because p from Eq. (9) is very far from the expected zero value, especially in the case of higher SA concentrations. Further, the decrease of the m values with increasing time ($m_i > m_f$) indicates negative deviations from the linearity predicted by Eq. [5] or Eq. [6], both being consistent with the case of diffusion adsorption for the ideal

behavior, given by Eq. (4), of the interfacial film of adsorbed surfactant.

As a first approximation let us presume that at low t values Eq. [5] is valid and consequently in Eq. [9] one has p = 0 and m_i, the coefficient of $t^{1/2}$, is given by the following equation:

$$m_i = 2kT\left(\frac{D}{\pi}\right)^{1/2} c_0$$

By expressing D, one obtains:

$$D = \frac{\pi m_i^2}{(2kTc_0)^2} \qquad [10]$$

We mention that in Eq. [1] c_0 means the bulk concentration expressed in surfactant molecules/volume. Consequently, if one gives m_i in dyne cm^{-1} $s^{-1/2}$ (see Table IV), k in erg/(molecule grade) and c_0 in molecules cm^{-3}, D will be obtained in cm^2 s^{-1}. Obviously, if the bulk concentration is given as C_0 mole/L, one has $c_0 = 10^{-3}$ N_A C_0, where N_A stands for Avogadro's constant. Diffusion coefficients, D values, calculated by means of Eq. [10] from m_i values, listed in Table III, are given in Table IV.

Table IV.

Diffusion coefficients, D and D_0 calculated by Eq. [10], and C_s values calculated by Eq.[12] from the slopes m_i taken from Table III.

C_0 mole dm^{-3}	m_i dyne cm^{-1} $s^{-1/2}$	D 10^{11} cm^2 s^{-1}	D_0 cm^2 s^{-1}	C_s 10^3 mole dm^{-3}
0.001	0.0607	0.492		0
0.00178	0.0813	0.278		0.44
0.0057	0.1900	0.148	4.92 10^{-12}	2.57
0.012	0.2930	0.0796		7.17
0.018	0.2760	0.0314		13.4
0.051	0.3460	0.00614		45.3

As seen, in Table IV, D diminishes with increasing bulk concentration, suggesting the idea that Eq. [6] might be a better approach than Eq. [5]. One may take, then, from Eq. [6] for m_i the following expression:

$$m_i = 2kT\left(\frac{D}{\pi}\right)^{1/2}(c_0 - c_s) \qquad [11]$$

It is reasonable to presume that the subsurface concentration C_s (expressed in mole/L) increases with increasing bulk concentration C_0. Let us presume as a first approach that $C_s = 0$ for $C_0 = 0.001$ mole/L. In this case a D_0 value can be obtained by means of Eq. [10]. Further, by using this D_0 value and Eq. [11], C_s values may be derived, from the m_i slopes obtained for higher concentrations, *viz*., by means of the following relation:

$$C_s = C_0 - \frac{\pi^{1/2} m_i}{2kT \cdot 10^{-3} N_A D_0^{1/2}} \qquad [12]$$

The values of subsurface concentrations (C_s, calculated by Eq.[12]) and diffusion coefficient D_0 are also given in Table IV.

As seen, C_s increases with increasing C_0, as one might expect. However, the diffusion coefficient is with several orders of magnitude less than real ones ($D = 5\ 10^{-6}$ cm^2 s^{-1}) assumed for surfactants diffusing through aqueous phase to the air/water interface (7). This means, that Eqs. [5] and [6] are extremely rough approximations to fit these experimental data.

The remarkable low values of the diffusion coefficients are probably due to a slow orientation (7, 38) of the polar head groups of SA molecules at the interface and to a slow conformational transition in the long hydrocarbon chains of SA molecules to finally achieve their correct orientation at the adsorption equilibrium. These effects can also explain the slow interfacial pressure increase to reach its equilibrium value. As an alternative, the long time dependence of the interfacial pressure can be attributed to the interactions among SA molecules at the oil/water interface, where these SA molecules relax and reorient leading to their proper molecular arrangement characteristic for the adsorption equilibrium.

Modeling of the New Diffusion Kinetic Equation

Eqs. [5-6] and [9-12] have been obtained by presuming the state equation [4] to be valid. But interfacial monolayers obey Eq. [4] only at very small Π values, practically for $\Pi \rightarrow 0$. One of the best state equations, proposed for non-ionic monolayers (39) and quoted and used by others (40-42), is of the following shape:

$$\left(\Pi + \frac{\alpha}{A^{3/2}}\right)(A - A_0) = kT \qquad [13]$$

where A stands for the mean molecular area, A_0 for the own molecular area of the surfactant and α is an interaction parameter. Eq. [13] was found to describe very well the compression isotherm of miscellaneous monolayers (40, 41), especially if the interaction parameter α and the own molecular area A_0 are treated as adjustable parameters.

From state equation [13], Π may be expressed as:

$$\Pi = \frac{kT}{A - A_0} - \frac{\alpha}{A^{3/2}} = \frac{kT\Gamma}{1 - \Gamma A_0} - \alpha\Gamma^{3/2} \qquad [14]$$

Let us denote:

$$x = 2(c_0 - c_s)\left(\frac{D}{\pi}\right)^{1/2} \qquad [15]$$

Thus, the long time approximation of diffusion, given by Eq. [3], may be written as $\Gamma(t) = xt^{1/2}$. Then, combining Eqs. [3], [13] and [15], one obtains:

$$\Pi = \frac{kTxt^{1/2}}{1 - A_0 xt^{1/2}} - \alpha x^{3/2} t^{3/4} = kTx\left[\frac{t^{1/2}}{1 - A_0 xt^{1/2}} - \frac{\alpha x^{1/2}}{kT} t^{3/4}\right] \qquad [16]$$

Therefore, one may expect Eq. [16] to describe better the time dependence of Π, than Eq. [6] does.

Introduction of Dimensionless Variables

In order to study the properties and possibilities of Eq. [16], let us introduce a reduced time scale. If in an experiment Π has been followed from t = 0 up to a maximum time t_m, a reduced time (noted τ) can be defined as:

$$\tau = \frac{t}{t_m} \qquad [17]$$

Combining Eqs. [16] and [17] one obtains:

$$\Pi = kTxt_m^{1/2}\left[\frac{\tau^{1/2}}{1 - A_0 xt_m^{1/2}\tau^{1/2}} - \frac{\alpha x^{1/2}}{kT} t_m^{1/4}\tau^{3/4}\right]$$

The Eq. [17] may be written as:

$$\Pi = a\left[\frac{\tau^{1/2}}{1-b\tau^{1/2}} - c\tau^{3/4}\right] = a\varphi(\tau) \qquad [18]$$

with:

$$a = 2kT(c_0 - c_s)\left(\frac{Dt_m}{\pi}\right)^{1/2}$$

$$b = 2A_0(c_0 - c_s)\left(\frac{Dt_m}{\pi}\right)^{1/2}$$

$$c = \frac{2^{1/2}\alpha(c_0 - c_s)^{1/2}}{kT}\left(\frac{Dt_m}{\pi}\right)^{1/4}$$

From the expression of the parameters *a, b* and *c* one obtains:

$$D = \left[\frac{a}{2kT(c_0 - c_s)}\right]^2 \frac{\pi}{t_m}; \quad A_0 = \frac{kTb}{a}; \quad \alpha = \frac{c}{a^{1/2}}(kT)^{3/2} \qquad [19]$$

Obviously, if $t = t_m$, from Eq. [17] one has $\tau = 1$ and Eq. [18] becomes:

$$\Pi_m = a\varphi(1) = a\left[\frac{1}{1-b} - c\right] \qquad [20]$$

Let us introduce also for the interfacial pressure a reduced scale:

$$\Pi^* = \frac{\Pi}{\Pi_m}$$

where Π_m stands for the maximum interfacial pressure, corresponding to $t = t_m$. By using the Eqs. [18] and [20], this reduced interfacial pressure is expressed as:

$$\Pi^* = \frac{\Pi}{\Pi_m} = \frac{\varphi(\tau)}{\varphi(1)} \qquad [21]$$

Thus one obtains finally for the time dependence of the interfacial pressure:

$$\Pi = \frac{\Pi_m}{\varphi(1)}\varphi(\tau) \qquad [22]$$

By comparing Eq. [22] with Eq. [18] it is obvious that:

$$a = \frac{\Pi_m}{\varphi(1)} \qquad [23]$$

Procedure of Calculations

In order to test the utility of Eq. [22] or of Eq. [18], we studied the influence of the parameters *b* and *c* upon the shape of the Π/a *versus* τ and Π^* *versus* τ curves. For this purpose theoretic curves have been constructed. Some examples are given in Figs. 3-6.

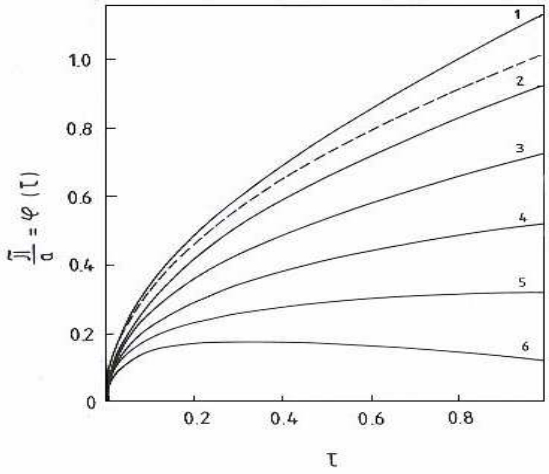

Fig. 3.

Influence of the *c* parameter upon the theoretical $\varphi(\tau)$ *versus* τ curves, given by Eq. [18], for *b* = 0.1. The *c* values: curve (1) 0; (2) 0.2; (3) 0.4; (4) 0.6; (5) 0.8; (6) 1.0. Dashed line curve: *b* = *c* = 0.

In Fig. 3 the influence of the *c* parameter, upon the shape of the $\Pi/a = \varphi(\tau)$ *versus* the dimensionless τ curves, is illustrated by taking the constant *b* = 0.1 value. Fig. 4 illustrates the influence of the *b* parameter for the constant *c* = 0.6 value.

Since parameters *b* and *c* influence also the $\varphi(1)$ value (see Eq. [20]), the shift of the calculated curves makes their comparison rather difficult. The influence of these parameters is more clear if the $\Pi^* = \varphi(\tau)/\varphi(1)$ *versus* τ curves are constructed. These are shown in Figs. 5 and 6.

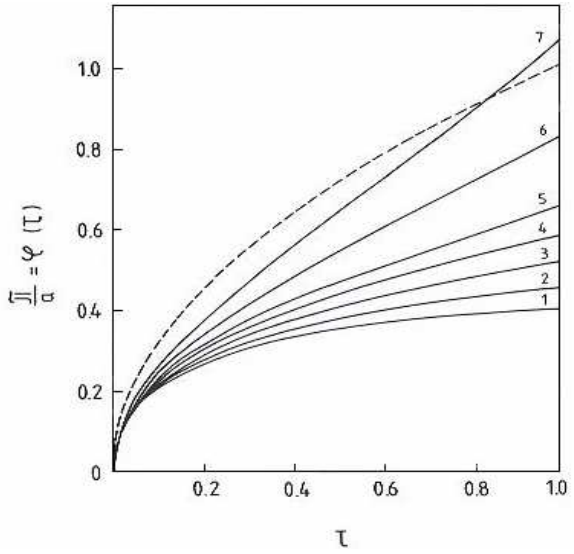

Fig. 4.

Influence of the *b* parameter upon the theoretical φ(τ) *versus* τ curves, given by Eq. [18], for *c* = 0.6. The *b* values: curve (1) 0; (2) 0.05; (3) 0.1; (4) 0.15; (5) 0.2; (6) 0.3; (7) 0.4. Dashed line curve: *b* = *c* = 0.

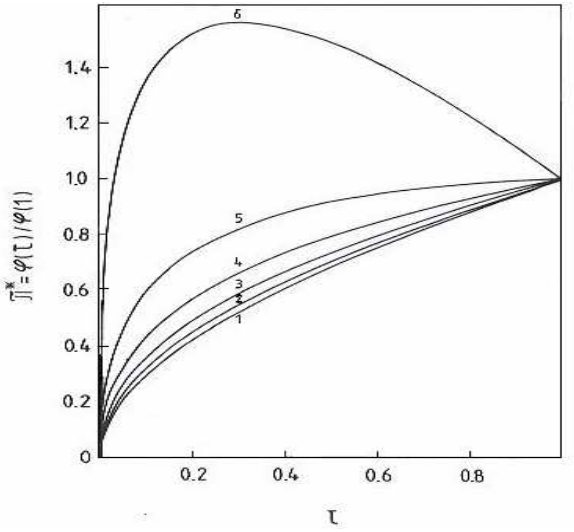

Fig. 5.

Influence of the *c* parameter upon the theoretical $\prod^{*}$ *versus* τ curves, given by Eq. [21]. The *b* and c values as in Fig. 3.

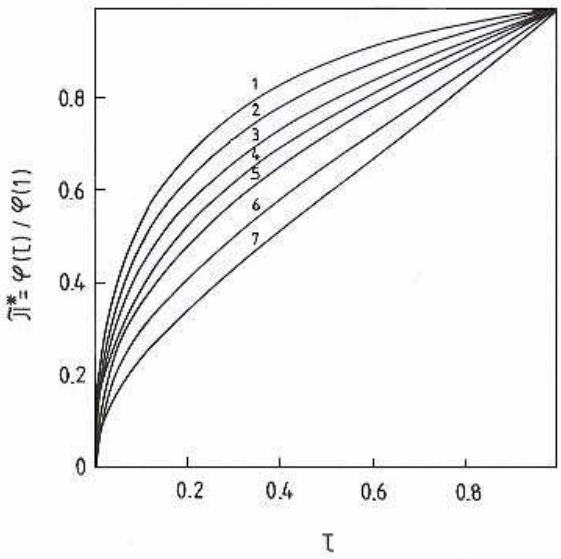

Fig. 6.
Influence of the *b* parameter upon the theoretical Π^* *versus* τ curves, given by Eq. [21]. The *b* and *c* values as in Fig. 4.

It is worth mentioning that for $b = 0.1$ and $c = 1.0$ both $\varphi(\tau)$ (curve 6 in Fig. 3) and Π^* (curve 6 in Fig. 5) exhibit a maximum for about $\tau = 0.3$. This would imply the appearance of a maximum interfacial pressure at a certain time, followed by the diminution of Π. This is of course unrealistic. Therefore, it is obvious that not all *b* and *c* pairs can describe the real adsorption kinetics. Further, the curve for $b = 0.4$, $c = 0.6$ (curve 7 in Fig. 4) indicates the adsorption rate to decrease down to a minimum value, followed by the acceleration of the adsorption. This also cannot happen in a real adsorption process, since the more occupied the adsorption sites, the less will be the adsorption rate, becoming zero at the adsorption equilibrium.

Although, not all calculated $\varphi(\tau)$ functions correspond to real adsorption behavior of surfactants, the main feature is that in the case of *diffusion controlled adsorption* the own molecular area A_0 and the intermolecular interactions expressed by the parameter α may count for both positive and negative deviations from the $t^{1/2}$ law (see Fig. 2).

Since according to the $t^{1/2}$ law expressed by Eq. [6] one has $\Pi^* = \tau^{1/2}$, the deviation of the reduced surface pressure from the $t^{1/2}$ law may be expressed by the function:

$$\Delta = \frac{\varphi(\tau)}{\varphi(1)} - \tau^{1/2} \qquad [24]$$

The influence of the *c* and *b* parameters upon the theoretical Δ vs. τ curves is illustrated in Figs. 7 and 8, respectively. It is obvious that both positive and negative Δ values may appear and the deviation from the $t^{1/2}$ law may be very important.

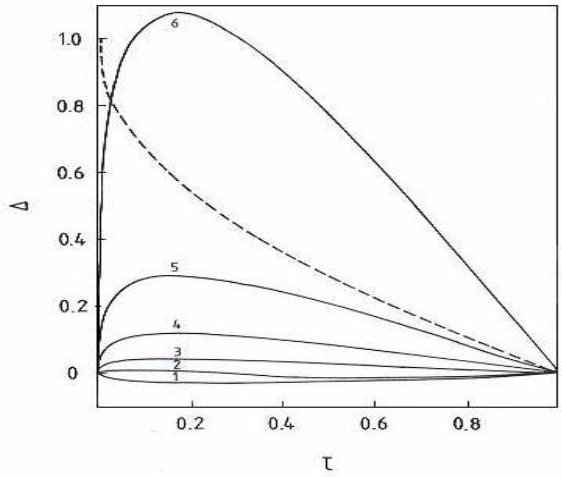

Fig. 7.
Influence of the *c* parameter upon the theoretical Δ *versus* τ curves, given by Eq. [24].The *b* and *c* parameters as in Fig. 3.

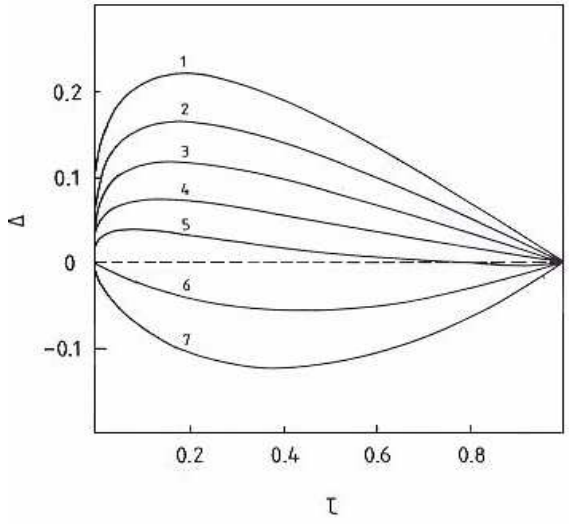

Fig. 8.
Influence of the *b* parameter upon the theoretical Δ *versus* τ curves, given by Eq. [24]. The *b* and *c* parameters as in Fig. 4.

In real systems, as seen in Fig. 2, with increasing time negative deviations from the $t^{1/2}$ law appear. In a Π^* vs. τ plot this means that the curve is more convex (has a higher curvature) as compared to $\tau^{1/2}$, i.e. Δ has positive values. Consequently, negative Δ values indicate unrealistic theoretical curves. Even the positive values have an upper limit, it is easy to see that the Π vs. t curve passes through a maximum if $\Delta > 1 - \tau^{1/2}$. The dashed line curve in Fig. 7 indicates this upper limit $\Delta = 1 - \tau^{1/2}$.

Since the Δ vs. τ curves exhibit important shifts if *b* or *c* is modified, in order to illustrate the influence of the parameters b and c upon the shape of the curves, we choose a set of *b* – *c* pairs which oblige the Δ vs. τ curves to pass through a common point. If we impose the condition that at a certain τ_0 value the Δ function must be equal to Δ_0, Eq. [24] becomes:

$$\Delta_o = \frac{\varphi(\tau_0)}{\varphi(1)} - \varphi_0^{1/2}$$

From this relation one might express the *c* parameter and one obtains:

$$c = \frac{1}{\Delta_0 + \tau_0^{1/2} - \tau_0^{3/4}} \left[\frac{(\tau_0^{1/2} - \tau_0)b}{(1-b)(1-\tau_0^{1/2}b)} + \frac{\Delta}{1-b} \right] \qquad [25]$$

Table V.
The *b* and *c* pairs, calculated by Eq. [26],
ensuring $\Delta = 0.2$ for $\tau = 0.2$.

No.	b	c
1	0	0.575
2	0.02	0.601
3	0.05	0.643
4	0.10	0.721
5	0.15	0.810
6	0.20	0.913
7	0.25	1.033
8	0.30	1.172
9	0.35	1.337
10	0.40	1.534

Eq. [25] allows us to calculate for a given Δ_0 - τ_0 pair the *c* parameter as function of *b*. Thus, for $\Delta_0 = \tau_0 = 0.2$ one obtains:

$$c = \frac{0.71b}{(1-b)(1-0.447b)} + \frac{0.574}{1-b} \qquad [26]$$

Some illustrative examples of *c* – *b* pairs ensuring $\Delta = 0.2$ for $\tau = 0.2$, calculated by means of Eq. [26] are given in Table V.

For cases 1, 3, 4, 6, 7 and 8 whole Δ vs. τ curves are given in Fig. 9.

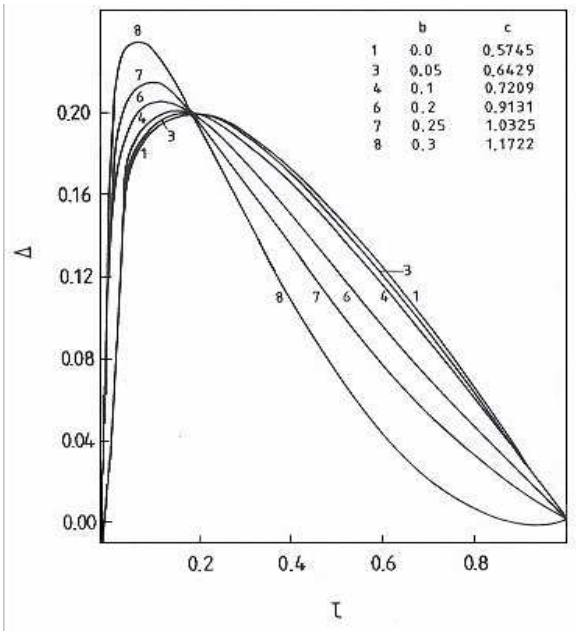

Fig. 9.
Some Δ *versus* τ curves passing through the point $\Delta = \tau = 0.2$. Figures indicate the *b* and *c* pairs given in Tab. 5.

It is clear that Eq. [18] corresponds to a very flexible function able to describe well a great variety of curves. Since for *b* = 0.3 the deviation Δ arrives in the negative region for $\tau > 0.85$, Eq. [26] may give *b* – *c* pairs corresponding to real experimental curves only if *b* < 0.3.

Deriving of the Parameters of Eq. [18] from Experimental Data

In order to derive the parameters *a, b* and *c* of Eq. [18] we adopted the following procedure of working up the experimental data given in Fig. 1. We have chosen t_m = 90 min and calculated for each experimental point the reduced parameters τ and Π^*. Further we calculated, for the found τ values, the theoretical Π^* values by taking certain *b* – *c* pairs. In the first approach we took *b* = 0 and calculated theoretical Π^* values for different *c* ones. In the case of each *c* value the standard deviation (SD) of the experimental Π^* values from the theoretical ones was calculated. By means of a systematic variation of *c* the minimum standard deviation $(SD)_m$ was sought for. Then, the calculations were repeated for other *b* values, too. Thus, a double minimization of the standard deviation has been performed and the *b* – *c* pair ensuring the least value for the standard deviation has been taken for the most realistic parameter values.

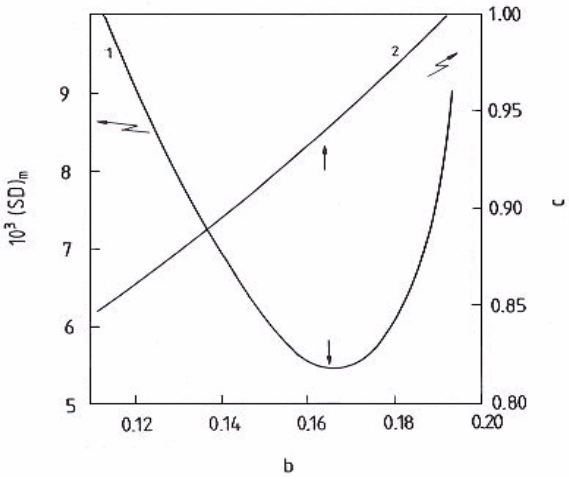

Fig. 10.

Deriving of *b* and *c* parameters for the stearic acid benzene solution of C_0 = 0.051 mole dm^{-3} at the interface with water phase of pH 2.

This calculation procedure is visualized in Fig. 10 for the stearic acid oil solution of 0.051 mole/L. Curve 1 gives the minimum standard deviation $(SD)_m$ obtained for different b values presumed and curve 2 indicates the corresponding *c* value. Let us take, e.g. *b* = 0.12. Eq. [21] allows us to calculate theoretical Π^* values corresponding to *b* = 0.12 and to different *c* values. In each case, i.e. with each *c* value presumed, the standard deviation:

$$SD = \sqrt{\frac{1}{n}\sum\left(\Pi_t^* - \Pi_e^*\right)^2} \qquad [27]$$

is calculated where n stands for the number of points used, and Π_t^* and Π_e^* stand for the theoretical and for the experimental reduced interfacial pressure, respectively. By trying different *c* values, one observed that the standard deviation will be the less for *c* = 0.86, viz. it will be equal to $(SD)_m$ = 0.00928. Thus, we obtained a point on curve 1 and a point on curve 2.

By repeating these calculations for other *b* values, eventually one obtains the whole curve 1 and curve 2. As seen, curve 1 has a minimum (indicated by a downward vertical arrow), corresponding to *b* = 0.163, this minimum $(SD)_m$ is ensured by a *c* value equal to 0.937 (indicated on the curve 2 by an upward vertical arrow).

By using the *b* and *c* values obtained, φ(1) may be easily calculated according to Eq. [20], as well as the corresponding parameter *a* by means of Eq. [23]. Results obtained by means of this procedure are presented in Table VI.

Table VI.
Parameters of Eq. [18] derived from the experimental dynamic interfacial pressures for SA at the benzene/water of pH 2 interface.

C_0 mole dm^{-3}	t_m min	Π_m mN m^{-1}	φ(1)	a	b	c	$(SD)_m$ mN m^{-1}
0.001	90	4.5	0.3820	11.78	0.0813	0.706	0.0060
0.00178	90	6.4	0.4096	15.62	0	0.590	0.0046
0.0057	90	12.1	0.3682	32.86	0.0039	0.635	0.0019
0.012	90	15.6	0.3506	44.50	0	0.649	0.0019
0.018	90	18.1	0.3367	53.76	0.0019	0.665	0.0022
0.051	90	22.0	0.2575	85.43	0.163	0.937	0.0054

The parameter values given in Table VI allow us to construct by means of Eq. [18] theoretical Π vs. t curves. These curves are given in Fig. 1 as full line curves. Thus, it is demonstrated that Eq. [18] describes very well the experimental Π vs. t data within the experimental errors.

Inspection of Table VI shows that the *a* parameter increases with increasing bulk concentration C_0 of stearic acid. The *c* parameter shows

also a clear increasing tendency. The *b* parameter has very small values frequently vanishing ones and cannot be correlated with C_0.

With respect to the meaning of the parameter *a*, according to Eq. [19] it allows us to calculate the diffusion coefficient D. Let us assume as a first approach that $C_s = 0$ at all bulk concentrations C_0. By taking into account that $c_0 = C_0\ 10^{-3}\ N_A$, Eq. [19] becomes:

$$D = \left(\frac{a}{2kT \cdot 10^{-3} \cdot N_A \cdot C_0} \right)^2 \frac{\pi}{t_m} \qquad [28]$$

Diffusion coefficients calculated by means of Eq. [28], and by using the *a* values listed in Table VI, are presented in Table VII.

Table VII.

Diffusion coefficients, D and D_0, calculated by Eq. [28], subsurface concentrations C_s, calculated by Eq. [29], and interaction parameters α calculated by Eq. [19], from the a and c parameters of Eq. [18]. Symbols are defined in the text.

C_0 mole dm^{-3}	D 10^{10} cm^2 s^{-1}	D_0 10^{10} cm^2 s^{-1}	C_s 10^3 mole dm^{-3}	α 10^{22} dyne cm^2
0.001	0.3430		0	16.7
0.00178	0.1900		0.45	12.1
0.0057	0.0821	0.343	2.91	9.02
0.012	0.0840		8.22	7.92
0.018	0.0220		13.4	7.38
0.051	0.0069		43.7	8.24

By analyzing the D values listed in Table VII and by comparing them with the values given in Table IV, one can see that the general picture is similar, since D values show a decreasing tendency with increasing bulk concentration of stearic acid and seem to be more realistic, their values being higher with about one order of magnitude as compared to the previous approach (Eqs. [5] and [6]).

As a second approach we shall presume that $C_s = 0$ only in the case of the surfactant solution of 0.001 mole/L and it increases with increasing bulk concentration, but the diffusion coefficient remains the same D_0 as obtained from the a value for the 0.001 mole/L solution. In this assumption C_s may be calculated from the expression of D given in Eq. [19] and one obtains:

$$C_s = C_0 - \frac{\pi^{1/2} \cdot a}{2kT \cdot 10^{-3} \cdot N_A \cdot D_0^{1/2} \cdot t_m^{1/2}} \quad [29]$$

The C_s values calculated by Eq. [29] are presented in Table VII and they increase linearly with increasing C_0 as in the case of those C_s values presented in Table IV, but the correlation coefficient is better, r = 0.9994, as compared to r = 0.9983 obtained with C_s values from Table IV. Although the D_0 value (Table VII) is higher with almost one order of magnitude than D_0 value (Table IV), it is far from being realistic. This situation is similar with the adsorption of palmitic acid at the hexane/water interface, for which D = 5.66 10^{-13} cm^2 s^{-1} was reported (5) and the authors consider that the anomalous D value is due to the existence of an activation barrier for the adsorption between the subsurface and the interface.

Generally, the diffusion coefficient obtained for SA is with at least one order of magnitude smaller than its value previously determined for the two anesthetics, e.g. dibucaine and tetracaine (24, 43). This finding is probably related with the structure of anesthetic molecules, since dibucaine and tetracaine have much shorter hydrocarbon chains and are quite rigid molecules, and their diffusion through the bulk phase and penetration into the oil/water interface might occur easier than for stearic acid molecules.

Eq. [19] allows also the calculation of the interaction parameter α from the parameters *a* and *c* of Eq. [18]. The α values are presented also in Table VII. As seen one does not obtain the same value in the case of differing bulk concentrations, viz. a decreasing tendency is observed with increasing C_0. This indicates, similarly to the too low D_0 value, that the process is not purely diffusion controlled and the potential energetic barrier to adsorption (43, 44) and an interfacial reorientation (45-47) of surfactant molecules could play an important part.

By calculating the mean value of the interaction parameter one obtains α = 1.02 10^{-21} dyne cm^2. It is worth mentioning that for stearic acid monolayers spread at the air/water interface we obtained 4.3 10^{-21} dyne cm^2 (42). In the case of the air/water interface in the air phase strong hydrophobic interactions appear between the long hydrocarbon chains, which are almost absent at the benzene/water interface, when the hydrocarbon chains are solvated with benzene molecules hindering the direct interaction between the neighboring SA molecules. Consequently the α value must be much less as compared to the air/water interface. Thus, the above α value seems to be in substantial agreement with our earlier results (42).

The low values of the diffusion coefficients can be further correlated with the presence of an energy barrier of adsorption due to a slow reorientation

(7, 38) of the polar head groups of SA molecules at the interface to finally achieve their proper arrangement or their correct orientation at the adsorption equilibrium. This effect can also explain the slow interfacial pressure increase to reach its equilibrium value.

Therefore, these data represent strong experimental evidence about the non-ideal behavior of adsorbed SA layers at the oil/water interface and about the interfacial reorientation of SA molecules at the oil/water interface, which apparently operates for the adsorption of fatty acids from oil solution to an oil/water interface. It seems that the adsorption of SA from benzene to the benzene/water interface is of this type in agreement with the adsorption of palmitic acid at the hexane/water interface reported earlier (5). Hence, the adsorption process is controlled by the molecular diffusion in the oil phase associated with the surface reorientation and the molecular interactions of stearic acid molecules at the oil/water interface.

Conclusions

A theoretical approach to the dynamic interfacial pressures is developed and a new kinetic Eq. [18] for the diffusion controlled kinetics is proposed, based on Ward and Tordai's diffusion equation associated with a two dimensional van der Waals state equation. This approach is consistent with the case of the non-ideal behavior of the adsorbed films widely used in the kinetic of adsorption of surfactants from concentrated bulk solutions to the liquid interfaces. This provides a possibility for one to determine the diffusion coefficients, subsurface concentrations and intermolecular interaction parameters within adsorbed films of surfactants at the liquid/liquid interfaces. The theory is applied to describe and fit the experimental data of the dynamic interfacial pressures for the adsorption of stearic acid (SA) at the benzene/water interface. Obtained results are in general agreement with similar earlier reported data for the adsorption of palmitic acid (5) and the adsorption of chlorophyll (22) at the different oil/water interfaces.

The adsorption of stearic acid (SA) at the benzene/water interface seems to be a process in which the rate is controlled both by the molecular diffusion from the bulk to the subsurface and by the molecular interactions in adsorbed SA layer at the liquid/liquid interface since both Eqs. [7] and [18] yield interesting pieces of information, but none of them gives a perfect description of the phenomenon.

The low D values for SA further suggest the presence of an energy barrier of adsorption between the subsurface and the oil/water interface. This barrier might be attributed to the steric restraints on the stearic acid molecules, in the proximity of the oil/water interface, and therefore, the molecules need to achieve a correct orientation to adsorb at the interface. This barrier of adsorption can be also due to a slow reorientation of the

polar head groups of SA molecules at the oil/water interface. This will cause an increase in the timescale for the dynamic interfacial pressure to reach out its equilibrium value.

Eq. [18] proposed in the present paper is better than Eq. [6] and it allows a more correct description of the experimental data of the dynamic interfacial pressures for a large interval of surfactant concentrations in oil solutions and over a period of time that can range up to two hours, depending on the stearic acid bulk concentration. In this period of time, the dynamic interfacial tension, σ(t), will decay to reach its equilibrium value and, consequently, the dynamic interfacial pressure, Π(t), will increase to attain its equilibrium value.

In future studies we intend to extend this investigation by using the diffusion adsorption theory associated with the surface reorientation of the fatty acid molecules at the oil/water interface.

REFERENCES

1. F. Ravera, M. Ferrari and L.Liggieri, *Adv. Colloid Interface Sci.,* **2000***,* 88, 129.
2. J. Eastoe and J. S. Dalton, *Adv. Colloid Interface* Sci., **2000,** 85, 103.
3. B. A. Noskov, *Adv. Colloid Interface* Sci., **1996,** 69, 63.
4. C. -H. Chang and E. I. Franses, *Colloids Surf. A*, **1995**, 100, 1.
5. A. F. H. Ward and L. Tordai, *J. Chem.* Phys., **1946,** 14, 453.
6. P. Joos, G. Bleys and G. Petre, *J. Chim. Phys*., **1982**, 79, 387.
7. G. Bleys and P. Joos, *J. Phys. Chem.,* **1985***,* 89, 1027.
8. P. Joos and G. Serrien, *J. Colloid Interface* Sci., **1989**,127, 97.
9. V. B. Fainerman, S. A. Zholob, R. Miller and P. Joos, *Colloids Surf. A*, **1998**,143, 243.
10. R. Van den Bogaert and P. Joos, *J. Phys. Chem*., **1979,** 83, 2244.
11. R. Van den Bogaert and P. Joos, *J. Phys. Chem*., **1980***,* 84**,** 190.
12. E. Rillaerts, and P. Joos, *J. Colloid Interface* Sci., **1982,** 88, 1.
13. K. A. Coltharp and E. I. Franses, *Colloids Surf. A,* **1996,** 108, 225.
14. K. Theander and R. J. Pugh, *J. Colloid Interface Sci.*, **2001,** 239, 209.
15. G. Czichocki, A.V. Makievski, V. B. Fainerman and R. Miller, *Colloids Surf. A*, **1997**,122, 189.
16. M. Vermeulen and P. Joos, *Colloids* Surf., **1988***,* 33, 337.
17. G. Tomoaia, A. Tomoaia-Cotisel, M. Tomoaia-Cotisel and A. Mocanu, *Cent. Eur. J. Chem.,* **2005**, 3, 347.
18. L. Liggieri, F. Ravera and A. Passerone, *J. Colloid Interface Sci*., **1995***,* 169**,** 238.
19. J. Li, R. Miller and H .Mohwald, *Colloids Surf. A,* **1996,** 114, 113.
20. J. Li, V. B. Fainerman and R. Miller, *Langmuir,* **1996,** 12, 5138.
21. C. J. Beverung, C. J. Radke and H. W. Blanch, *Biophys. Chem*., **1999***,* 81, 59.
22. J. F. Baret, *J. Chim. Phys*., **1968,** 65, 895.

23. E. Chifu, M. Salajan, J. Demeter-Vodnár and M. Tomoaia-Cotisel, *Rev. Roum. Chim*., **1987***,* 32, 683.
24. M. Tomoaia-Cotisel, J. Zsako, G. Tomoaia, A. Mocanu, V. D. Pop, and E. Chifu, *Rev. Roum. Chim*., **2004,** 49, 443.
25. J. Chatterjee and D. T. Wasan, *Chem. Eng. Sci*., **1998,** 53, 2711.
26. L. Liggieri, F. Ravera and A. Passerone, *Colloids Surf. A,* **1996,** 114, 351.
27. F. Ravera, L. Liggieri and A. Steinchen, *J. Colloid Interface* Sci., **1993***,* 156**,** 109.
28. A. Yousef and B. J. McCoy, *J. Colloid Interface Sci.,* **1983,** 94**,** 497.
29. M. Tomoaia-Cotisel, J. Zsako, A. Mocanu, M. Lupea and E. Chifu, *J. Colloid Interface* Sci., **1987***,* 117, 464.
30. J. Zsako, M. Tomoaia-Cotisel, E. Chifu, A. Mocanu and P. T. Frangopol, *Biochim. Biophys. Acta,* **1990,** 1024, 227.
31. M.Tomoaia-Cotisel, *Progr. Colloid Polym.* Sci., **1990**, 83, 155.
32. M. Tomoaia-Cotisel and D. A. Cadenhead, *Langmuir,* **1991**, 7, 964.
33. L. J. Noe, M. Tomoaia-Cotisel, M. Casstevens and P. N. Prasad, *Thin Solid Films*, **1992,** 208, 274.
34. Z. Lu, B. Zhang, Z. Ai, J. Huang and H. Nakahara, *Thin Solid Films,* **1996,** 284-285**,** 127.
35. E. Gyorvary, J. Peltonen, M. Linden and J. B. Rosenholm, *Thin Solid Films,* **1996.** 284-285**,** 368.
36. E. Chifu, M. Tomoaia and A. Ioanette, *Gazz. Chim.* Ital., **1975***,* 105, 1225.
37. R., Miller, P. Joos and V. B. Fainerman, *Adv. Colloid Interface* Sci., **1994***,* 49, 249.
38. A. Sanfeld, A. Steinchen and R. Defay, *J. Phys. Chem*., **1969**, 73, 4047.
39. J. Guastalla, *J. Chim. Phys.,* **1946**, 43, 184.
40. E. Ter Minassian-Saraga, *J. Chim.* Phys., **1955***,* 52, 80.
41. E. Chifu, J. Zsakó and M. Tomoaia-Cotisel, *J. Colloid Interface* Sci., **1983**, 95, 346.
42. M. Tomoaia-Cotisel, E. Chifu, A. Mocanu, J. Zsakó, M. Salajan and P.T. Frangopol, *Rev. Roum.* Biochim., **1988***,* 25, 227.
43. M. Tomoaia-Cotisel, J. Zsako, A. Mocanu, M. Salajan, Cs. Racz, S., Bran and E. Chifu, *Stud. Univ. Babes-Bolyai, Chem*., **2003***,* 48*,* 201.
44. V. G. Babak and F. Boury, *Colloids Surfaces A: Physicochem. Eng. Aspects,* **2004**, 243, 33.
45. M. Tomoaia-Cotisel and P. Joos, *Rev. Roumaine Chim*., **2004,** 49, 539.
46. M. Tomoaia-Cotisel and P. Joos, *Studia, Univ. Babes-Bolyai, Chem*., **2004***,* 49 (1), 35.
47. P. Joos, A. Tomoaia-Cotisel, A. J. Sellers and M. Tomoaia-Cotisel, *Colloids Surfaces. B. Biointerfaces,* **2004,** 37, 83.

STUDIA UNIVERSITATIS BABEŞ-BOLYAI, CHEMIA, LI, 1, 2006

ERRATUM

KINETICS AND MECHANISM OF *P*-XYLENE OXIDATION BY CE(IV) IN AQUEOUS ACID MEDIUM. LFER AS AN ARGUMENT TO THE OXIDATION MECHANISM

GABRIELA-CRISTINA BUCŞA AND IOAN BÂLDEA

(Article appeared in Studia Univ. Babeş-Bolyai. Chem. L (1), 2005, 157-168)

Some errors were discovered in the article mentioned concerning the mechanism of the title reaction (p.165) and the rate law from the mechanism (eqn. 13). The correct mechanism and rate law are as follows:

$$Ce^{4+} + H_2O \Leftrightarrows CeOH^{3+} + H^+ \qquad k_1, k_{-1}, \quad K_h$$

$$Ce(OH)^{3+} + CH_3C_6H_4CH_3 \Leftrightarrows Adduct^{3+} \qquad k_2, k_{-2}, \quad K_f$$

$$Adduct^{3+} + H^+ \xrightarrow{r.d.s.} [CH_3C_6H_4(H)CH_2^o]^+ + Ce^{3+} + H_2O \qquad k_3$$

$$[CH_3C_6H_4(H)CH_2^o]^+ + Ce(OH)^{3+} \xrightarrow{fast} Ce^{3+} + CH_3C_6H_4CH_2^+H_2O$$

$$CH_3C_6H_4CH_2^+ + H_2O \xrightarrow{fast} CH_3C_6H_4CH_2OH + H^+$$

$$r = \frac{d[Ce(IV)]_t}{d_t} = \frac{k_3K_2[p-xylene][H^+]}{1 + K_h^{-1}[H^+] + K_2[p-xylene]}[Ce(IV)]_t \quad (13)$$

The rate law has the same form as the published one and the conclusions remain the same.